technische universität
dortmund

Arbeit zur Erlangung des akademischen Grades
Dr. rer. nat.

Dynamic mean-field theory for simulating the infinite-temperature dynamics of spin ensembles

---

Timo Gräßer
geboren in Lüdenscheid

2024

Uhrig Group - Condensed Matter Theory
Fakultät Physik
Technische Universität Dortmund

Erstgutachter: Prof. Dr. Götz S. Uhrig
Zweitgutachter: Prof. Dr. Frithjof Anders
Drittgutachter: Prof. Dr. Matthias Ernst

Abgabedatum: 12. August 2024

Kurzfassung

Die Hochtemperaturdynamik von Spinsystemen ist für einige moderne Forschungsbereiche wie zum Beispiel Stickstoff-Fehlstellen-Zentren in Diamant oder Kernspinresonanz zentral. Diese theoretische Doktorarbeit befasst sich mit einer dynamischen Molekularfeldtheorie, genannt spinDMFT, mit welcher solche Systeme simuliert werden können. Der geringe numerische Aufwand der Methode erlaubt eine systematische Erweiterung auf Spincluster (CspinDMFT), was die Genauigkeit, allerdings auch den numerischen Aufwand, erhöht. Mit Hilfe von CspinDMFT wird die Dynamik von räumlich ungeordneten Defektspins auf einer Diamantoberfläche simuliert. Das Zusammenspiel von effektiver dipolarer Anisotropie und räumlicher Unordnung führt zu einem erheblichen Unterschied zwischen den Zeitskalen der longitudinalen und transversalen Relaxation. Dieses Phänomen ist auch experimentell beobachtet worden. In einem weiteren Teil dieser Arbeit werden spinDMFT und eine Erweiterung auf nicht-lokale Korrelationen (nl-spinDMFT) verwendet, um Kernspinresonanzmessungen wie zum Beispiel den freien Induktionszerfall oder Spinechos zu simulieren. Die Übereinstimmung mit experimentellen Daten für Kalziumfluorid (CaF_2) und Adamantan ($C_{10}H_{16}$) ist hervorragend. Ein interessanter Ausblick in diesem Kontext ist die Erweiterung auf Magic-Angle-Spinning Experimente, die heutzutage sehr relevant für die Festkörper-Kernspinresonanzspektroskopie mit hoher Präzision sind. Die zentrale Schlussfolgerung dieser Arbeit ist, dass spinDMFT einschließlich der Erweiterungen zwar auf hohe Temperaturen beschränkt sind, in diesem Grenzfall aber numerisch günstige und sehr flexible Methoden darstellen, die auf viele Systeme anwendbar sind.

Abstract

The high-temperature dynamics of spin systems is crucial in a number of modern research areas such as nitrogen-vacancy centers in diamond and nuclear magnetic resonance. This doctoral thesis deals with a dynamic mean-field theory, dubbed spinDMFT, that allows for the simulation of such systems. The relatively modest computational expense of the method permits an extension to spin clusters (CspinDMFT), which increases both the accuracy and the computational effort. CspinDMFT is employed to simulate the dynamics of randomly-distributed defect spins on a diamond surface. The interplay between effective dipolar anisotropy and positional disorder results in a significant difference between the timescales of longitudinal and transverse relaxation. This phenomenon has also been observed experimentally. In another part of this work, spinDMFT and an extension to non-local correlations (nl-spinDMFT) are used to simulate nuclear magnetic resonance experiments such as the free induction decay and spin echoes. The agreement with experimental data for calcium fluoride (CaF_2) and adamantane ($C_{10}H_{16}$) is excellent. An interesting outlook in this context is the extension to magic-angle-spinning experiments which are highly relevant in solid-state nuclear magnetic resonance spectroscopy with high precision. The central conclusion of this thesis is that spinDMFT and its extensions are limited to high temperatures, but offer computationally cheap and highly flexible numerical methods which are applicable to a wide range of systems in this limit.

Contents

List of publications

Related to this work:

- T. Gräßer, P. Bleicker, D.-B. Hering, M. Yarmohammadi, and G. S. Uhrig. *Dynamic mean-field theory for dense spin systems at infinite temperature.* Physical Review Research **3**, 043168 (2021). DOI: 10.1103/PhysRevResearch.3.043168
- T. Gräßer, K. Rezai, A. O. Sushkov, and G. S. Uhrig. *Understanding the dynamics of randomly positioned dipolar spin ensembles.* Physical Review Research **5**, 043191 (2023). DOI: 10.1103/PhysRevResearch.5.043191
- T. Gräßer. T. Hahn, and G. S. Uhrig. *Microscopic understanding of NMR signals by dynamic mean-field theory for spins.* Solid State Nuclear Magnetic Resonance **132**, 101936 (2024). DOI: 10.1016/j.ssnmr.2024.101936

Not related to this work:

- M. Yarmohammadi, K. Bolsmann, Y. Ribbeheger, T. Gräßer, and G. S. Uhrig. *Truncated Wigner approximation for the bosonic model of large spin baths.* Physical Review B **107**, 125421 (2023). DOI: 10.1103/PhysRevB.107.125421

1 Introduction

The objective of condensed-matter physics is to measure, understand and predict the behavior of solid and liquid matter. As such, it is a vast field of research with interdisciplinary links to a plethora of other sciences including chemistry, electrical engineering, biology and medicine. In essence, matter consists of electrons and nuclei. Their microscopic motions and interactions are well captured by the Schrödinger equation which is known since 1926 [Sch26]. In a realistic solid-state system, this equation has to account for the dynamics of $\propto 10^{23}$ electrons and nuclei. Therefore, although the problem can be formulated straightforwardly, it cannot be solved by hand or even by machine without substantial simplifications. This is what makes condensed-matter physics a challenging, yet fascinating research area: The remarkable variety of materials, substances and phases of matter that we encounter in our daily lives, that form the basis of many technologies, and that even constitute our own bodies, can be boiled down to a comparably simple microscopic description. The phenomenon whereby the collective behavior of many entities differs considerably from the behavior of an individual entity is known as "emergence". It is summarized simply yet accurately by Anderson's famous quote "More is different" [And72] and forms the basis of condensed-matter physics.

An important part of physics is to bridge the gap between experiment and theory. Hence, it is essential to find a minimal yet sufficiently accurate theoretical model to capture the experimentally observed behavior. This thesis is devoted to a specific class of models, namely ensembles of interacting localized spins in the high-temperature limit. In the strict sense, the term "spin" refers to an intrinsic particle property that interacts with the observable reality through an associated magnetic moment. Nevertheless, the term is often employed as a placeholder for the corresponding particle itself, especially in scenarios where other properties, such as charge, are unimportant. In this case, an ensemble of localized spins can be imagined as a collection of tiny magnets being nailed down on a board. They cannot move, but they are allowed to rotate, which is inevitable due to their mutual interactions resulting from their magnetic moments. The term "high-temperature limit" corresponds to the regime where the thermal energy is significantly larger than the interaction energies. Consequently, we consider no phase transitions and the spins are disordered, i.e., randomly oriented. Where do we encounter localized spin ensembles in nature?

While electrons do carry a spin, they are often either entirely delocalized, as in a metal, or their spins effectively cancel each other out, as is the case in closed atomic shells or covalent or ionic bonds. Nevertheless, there are rare systems where the electrons should be delocalized according to band theory, but remain stationary due to their mutual Coulomb interaction. Such materials are termed Mott insulators and can be effectively described by a model of localized spins [Mot49]. Other examples of localized spin ensembles include unpaired electrons or holes hosted by crystal defects, for instance, at dangling bonds or color centers. Besides this, also the atomic nuclei often carry a well-localized spin resulting from the comprised protons and neutrons.

The dynamics of spin ensembles can be very subtle, even at high temperatures. But why should we study them?

1.1 Nitrogen-vacancy centers and paramagnetic defect spins in diamond

As a first example, we consider the experimental platform of nitrogen-vacancy (NV) centers in diamond. This research area was pushed forward in the past decades due to promising areas of application such as nanoscale magnetometry [Bal+08; Maz+08; Sch+11; Sch+17] or quantum-information processing [Doh+13; Tam+14; Bra+19]. In their negative charge state, NV centers carry a spin of $S = 1$ and can be manipulated and read out by optically detected magnetic resonance [JW06; Sch+14]. Due to their stability even at room temperature, they serve as excellent quantum reporters of their local environment. In order for the NV center to sense targets outside of the diamond, it must be located close to the surface. However, the coherence time of shallow NV spins is reduced because they interact with paramagnetic spins at the surface [Gro+11; Gri+14; Rom+15], as illustrated in Fig. 1.1. The latter likely result from localized defects at the surface termination [San+19; Sta+19], but their precise nature remains a topic of discussion [Dwy+22]. Although they have been considered deleterious because they cause decoherence, they can assist in sensing applications if they are appropriately manipulated [Sus+14; Coo+19; Rez22; Rez+23]. A detailed understanding of the surface-spin dynamics could, for instance, help to clarify the nature of the underlying defects, which is certainly important for technological applications. But this system is also relevant from another perspective: Stemming from defects, the surface spins are randomly located at the diamond surface. Such extrinsic randomness is fundamentally interesting because it can hamper or even disrupt the process of thermalization in a quantum many-body system as will be discussed in the next section.

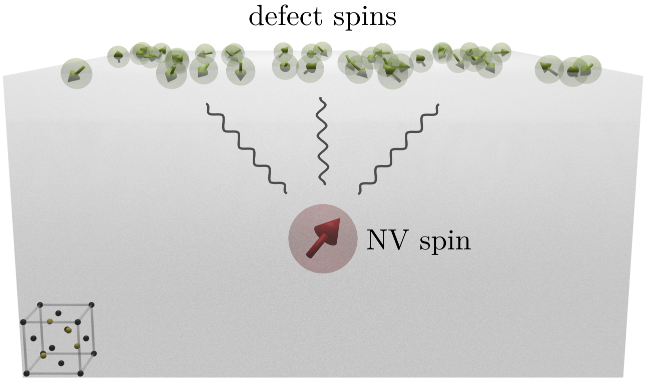

Figure 1.1: Cutout of a diamond surface. The spin of a shallow NV center interacts with an ensemble of spins stemming from randomly located surface defects.

1.2 Thermalization and localization

Thermalization is a fundamental principle in statistical physics stating that an excited many-body system evolves in time to arrive at a very generic ensemble of states called thermal equilibrium. We can observe this phenomenon in everyday life, for example, when we pour milk into our coffee and wait for the liquids to mix. The final state, a brown broth, appears to be independent of the specific manner in which the milk was poured, for example, the orientation of the cup or the trajectory of the milk as it entered the surface of the coffee. Thermalization is generic and can be observed in far more abstract scenarios such as spin ensembles. Despite its generality, the occurrence of thermalization is particularly subtle from a microscopic point of view. In classical systems, it can be understood by means of chaos theory and in quantum systems, it is partly explained by the eigenstate thermalization hypothesis (ETH) [Deu91; Sre94].

Nevertheless, there exist also rare systems in which thermalization is unexpectedly slow or completely absent. In some of these, the presence of an extrinsic randomness plays a pivotal role. In 1958, Anderson showed that transport properties in a lattice of non-interacting electrons are considerably affected by a random on-site potential [And58]. Under certain circumstances, the electrons become exponentially localized as indicated in Fig. 1.2, panel (b), which leads to an insulator. The analogous phenomenon in the presence of interactions is referred to as many-body localization (MBL) and has been extensively studied in the past two decades [ŽPP08; Yao+14; ASK15; NH15; Sch+15; Cho+16; WRC18; Aba+19].

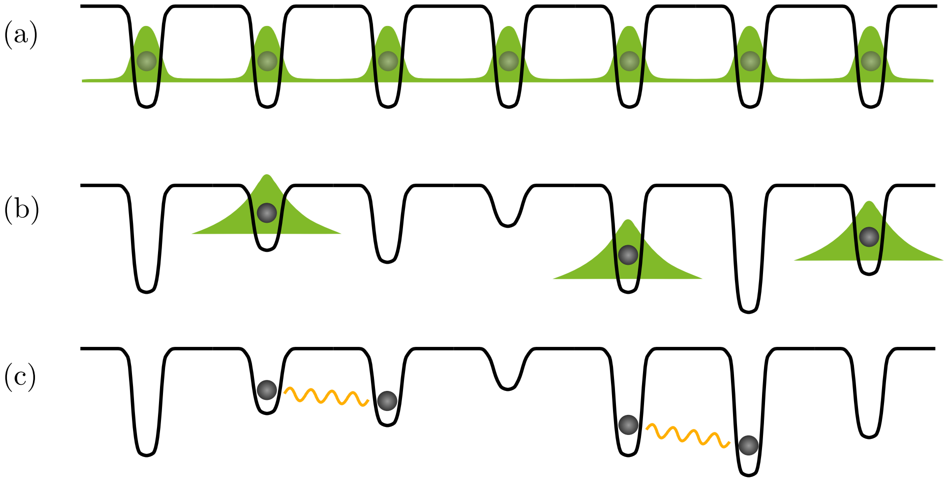

Figure 1.2: Electrons (gray spheres) in a potential landscape (black line) generated by a one-dimensional (1D) crystal. **(a)** In a homogeneous crystal without electron-electron interactions the eigenstates are delocalized Bloch waves (green). **(b)** Adding a random potential leads to exponentially localized single-particle wave functions (also green). The system describes an Anderson insulator. **(c)** Adding an electron-electron interaction (orange wiggly lines) to the Anderson model. Can localization persist? *Figure inspired by* Ref. [Aba+19].

Amongst others, MBL manifests in the infinite lifetime of local excitations [SPA13a; HNO14]. It is, in fact, challenging to experimentally confirm such behavior, since the system under study must be very well isolated for a long time [Aba+19; Pan+20]. In theory, a particular issue is that finite-size calculations may not be representative of the thermodynamic limit [EMB23; Pan+20]. It is therefore debated nowadays, whether or where true MBL, in the sense of a complete absence of thermalization, exists [EMB23; SP23]. But it is undebated that an extrinsic randomness can immensely slow down the process of thermalization which is sometimes referred to as "critical" [Kuc+18] or "prethermal MBL" [Lon+23] behavior. The defect-spin ensemble at the diamond surface forms an experimental playground for studying this phenomenology. It should be noted that a microscopic understanding of thermalization is of interest not only from a purely theoretical perspective. Thermalization is closely related to decoherence [Dav+23] which remains one of the main challenges in the realization of quantum devices that are required, for example, for a quantum computer [DiV00; Jaz+19]. Hence, it is very beneficial to study systems that thermalize unexpectedly slow or not at all.

1.3 Nuclear magnetic resonance

As previously mentioned, spins can also be carried by the atomic nuclei. Since nuclear gyromagnetic ratios are smaller by a factor of about 10^{-3} relative to the electron gyromagnetic ratio, their influence on the physical and chemical properties of a material or substance is negligible. Conversely, they allow for "spying" on the microscopic structure, which is the principle of nuclear magnetic resonance (NMR) spectroscopy [Lev01]. Since its foundation around 1940 [Rab+38; BHP46; PTP46], the field of NMR has continuously developed and become extremely valuable in various contexts, such as structural biology where NMR spectroscopy provides detailed information about the structure of proteins [Cas+02; PV19], or diagnostic medicine where the NMR-related magnetic resonance imaging (MRI) is used to examine tissue, for example, to detect cancer cells [Gro+15; LD17; Zha+24].

Particular strengths of NMR spectroscopy are its non-destructive nature and its ability to reveal not only the compounds, but also the chemical structure of a substance, for example, through the chemical shifts [LBJ02; Mar+17; PV19]. The schematic experimental setup for this is illustrated in Fig. 1.3. In addition to the growing relevance of NMR, also the demand for simulation software complementing the NMR spectrometer has increased [Con20]. Corresponding numerical algorithms face the notoriously difficult task of simulating large ensembles of interacting localized spins[1].

One of the most important interactions governing the dynamics of nuclear spins is the direct dipole-dipole interaction. It is considered deleterious for NMR spectroscopy because it broadens the spectral lines thus reducing the intrinsic resolution. Intrinsic molecular motions in liquids [Lev01] or manually applied motions as in magic-angle spinning (MAS) of solids [ABE58; Low59; Meh83] reduce this effect significantly, but cannot eliminate it entirely [Mal+19; Pen+19; Chá+21; Sim+23]. In this context, a detailed microscopic understanding of the dynamics of dipolar spin ensembles is very beneficial. It is noteworthy that nuclear spins are fully disordered at room temperature due to their gyromagnetic ratios being small. Hence, the restriction to high temperatures

---

[1] It should be noted that "localized" in this context refers to the locality of the spatial wave function of the spins at a fixed time. Therefore, molecular motions are actually not ruled out when we refer to localized spins.

in the framework of this thesis does not exclude NMR spectroscopy provided that the sample under study is not considerably cooled down.

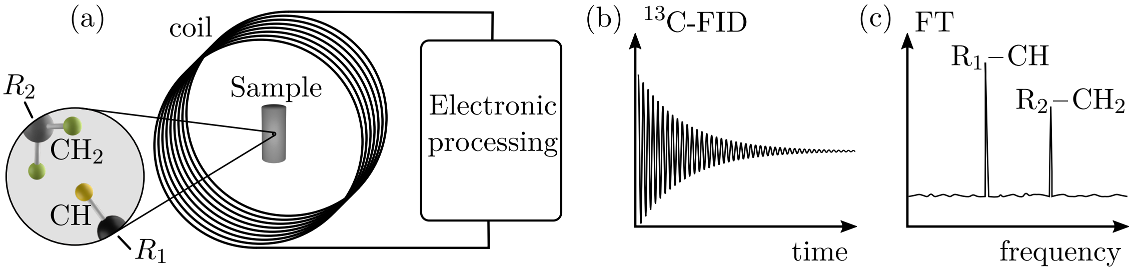

Figure 1.3: Schematic and strongly-simplified procedure of structure determination via NMR spectroscopy. **(a)** The sample comprises molecules that contain carbon and hydrogen atoms. One possible NMR measurement is the free induction decay (FID) of ^{13}C. To this end, a strong static field and dynamic fields at resonance with the ^{13}C-spins are applied (the fields are not shown in the figure). The carbon spins respond by inducing a measurable oscillating current in the depicted coil. **(b)** Sketch of the FID signal obtained by processing the current. **(c)** The Fourier transformation (FT) of the FID yields the NMR spectrum. The electrons in the sample induce local variations of the magnetic field at the locations of the nuclei shifting the resonance frequencies. This effect is called chemical shift. Different structure components, here R_1-CH and R_2-CH_2, correspond to different chemical shifts and, thus, to different peaks in the spectrum.

1.4 Dynamic mean-field theory for spins at infinite temperature

The considered examples illustrate the relevance of high-temperature spin dynamics for both fundamental physics and technological applications. As previously stated, the theoretical study of quantum many-body systems is notoriously difficult due to the sheer number of particles involved. Since this problem is long-standing and has been extensively studied over many decades, a variety of approximation methods have been developed over time[2]. Mean-field theories form a special category of approximations which are justified in high-dimensional systems, see Fig. 1.4. The potential success of a mean-field approximation is exemplified by the dynamic mean-field theory (DMFT) for itinerant lattice fermions developed in the nineties [KV04].

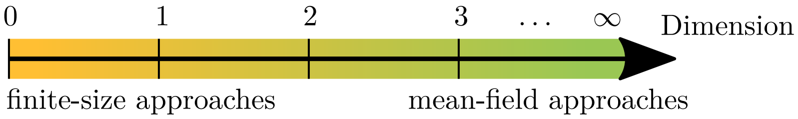

Figure 1.4: In contrast to approaches that operate on finite-size systems, mean-field approaches perform better if the system is high-dimensional.

This thesis presents a dynamic mean-field theory for spin ensembles at infinite temperature, which is dubbed spinDMFT. The key idea is to substitute a large spin ensemble by an effective model describing a single spin in a dynamic Gaussian mean field. The variability and efficiency of spinDMFT allow for extending it to spatial fluctuations. The extended

---

[2] Several approximation schemes for spin ensembles will be listed in Ch. 3 and in the beginning of Ch. 6.

method, designated as CspinDMFT, describes the dynamics of a cluster of spins in a mean-field background and captures, for example, systems with positional disorder, see Fig. 1.1. Besides this, spinDMFT is also capable of simulating NMR experiments. To this end, it needs to be extended in order to access non-local quantities such as spin pair correlations. This extension is referred to as non-local spinDMFT, or nl-spinDMFT for short. The main objective of this thesis is to derive and benchmark spinDMFT and its extensions and apply them to the scenarios portrayed earlier.

The thesis is structured as follows. In Ch. 2, we introduce several spin models and discuss experimental setups relevant for the chapters to come. We explain some fundamental NMR measurements and present a recent experiment, which probes the spin dynamics on a diamond surface by means of an NV center. Subsequently, in Ch. 3, we explain the key idea of a mean-field and compare some important mean-field theories to one another and to spinDMFT. Furthermore, we list and discuss some related approaches. In Ch. 4, we derive spinDMFT and present its generic results for a Heisenberg, Ising and XXZ model. Subsequently, we perform a benchmark by comparing spinDMFT to brute-force methods. The extension to CspinDMFT is presented in Ch. 5. In Secs. 5.1 and 5.2, we derive and benchmark CspinDMFT for lattices and inhomogeneous systems. Subsequently, we apply it to the aforementioned experimental scenario dealing with dipolar defect spins on a diamond surface in Sec. 5.3. Thereby, we explicitly compare the experimental measurements with the theoretical results and discuss them in the context of MBL. Section 6 is devoted to NMR. We explain how spinDMFT and nl-spinDMFT can be used to simulate NMR signals such as the FID or spin echoes. The methods are tested by applying them to the examples of calcium fluoride and adamantane. Finally, we conclude the thesis, provide an outlook and summarize the advantages and disadvantages of the dynamic mean-field approach in Ch. 7.

2 Measurement and modeling of spin systems

The objective of this thesis is to establish spinDMFT and its extensions, which simulate the dynamics of localized spin ensembles at high temperatures. In principle, the results of such simulations can be compared to experimental findings in order to understand phenomena from a microscopic point of view. However, performing such a comparison can already be a challenge. We highlight two crucial aspects that must be considered: First, it is essential to identify appropriate quantities that are accessible in both experiment and theory. Second, one must find a model that adequately captures the experimental situation. In this chapter, we aim to bridge the gap between experiment and theory, or, similarly, between *measurement and modeling*. We explain different experimental scenarios and highlight which quantities are important and can be measured. Concurrently, we present spin models that capture the main physics in these scenarios.

The expectation value of an operator $\mathbf{O}$ is generally defined as

$$\langle \mathbf{O} \rangle_\rho \coloneqq \mathrm{Tr}\left(\mathbf{O}\rho\right), \tag{2.1}$$

where ρ is the density operator. For brevity, we will omit ρ as an index, if the state we are referring to is either not specified or automatically clear from the context. This and further conventions are summarized in App. A. Generally, we consider the canonical ensemble, which is given by

$$\rho_\mathrm{th} \coloneqq \frac{1}{\mathcal{Z}} \mathrm{e}^{-\beta \mathbf{H}}, \qquad \beta = (k_\mathrm{B} T)^{-1}, \qquad \mathcal{Z} = \mathrm{Tr}\left(\mathrm{e}^{-\beta \mathbf{H}}\right). \tag{2.2}$$

Very important throughout this thesis is the case of infinite temperature, where the thermal state simply reduces to

$$\rho_0 \coloneqq \frac{1}{d} \mathbf{1}, \tag{2.3}$$

with d being the Hilbert space dimension.

This chapter is set up as follows. In Sec. 2.1, we introduce the microscopic quantities important for this thesis. Subsequently, we discuss some fundamental spin models in Secs. 2.2 and 2.3 and derive the effective dynamics in case of a strong external magnetic field in Sec. 2.4. Section 2.5 is devoted to NMR experiments and in Sec. 2.6, we consider an experiment measuring the spin relaxation on a diamond surface.

2.1 Microscopic quantities

The most important quantities considered in this thesis are the spin expectation values

$$S_i^\alpha(t) \coloneqq \langle \mathbf{S}_i^\alpha(t) \rangle, \qquad \alpha \in \{x, y, z\}, \tag{2.4}$$

as well as the spin correlations

$$g_{ij}^{\alpha\beta}(t_1,t_2) := \langle \mathbf{S}_i^\alpha(t_1)\mathbf{S}_j^\beta(t_2)\rangle, \qquad \alpha,\beta \in \{x,y,z\}. \tag{2.5}$$

Both carry crucial information about the static and dynamic behavior of a spin system: The spin expectation value $S_i^\alpha(t)$ measures the average polarization of the spin component α at site i and time t. The spin correlation $g_{ij}^{\alpha\beta}(t_1,t_2)$ tells us how much the spin component α at site i and time t_1 is correlated to another spin component β at site j and time t_2. Its maximum possible value is $S(S+1)/3$ assuming a single spin species with length S. We distinguish between diagonal ($\alpha=\beta$) and off-diagonal correlations ($\alpha\neq\beta$), as well as between autocorrelations ($i=j$) and pair correlations ($i\neq j$). In case of an easy-axis anisotropy, i.e., cylindrical symmetry, we distinguish between transverse correlations ($\alpha=\beta$ perpendicular to the easy axis) and longitudinal correlations ($\alpha=\beta$ parallel to the easy axis). In case of infinite temperature ($\rho=\rho_0$), some important properties can be deduced:

- The spins are disordered so that any spin expectation value vanishes,

$$S_i^\alpha(t) = 0. \tag{2.6a}$$

- Any correlation is invariant under time translation,

$$g_{ij}^{\alpha\beta}(t_1,t_2) = g_{ij}^{\alpha\beta}(t_1-t_2,0) =: g_{ij}^{\alpha\beta}(t_1-t_2), \tag{2.6b}$$

  if the Hamiltonian is not explicitly time dependent.

- Any correlation is real,

$$\operatorname{Im}\left(g_{ij}^{\alpha\beta}(t)\right) = 0. \tag{2.6c}$$

- Any correlation is symmetric except for time reversal,

$$g_{ij}^{\alpha\beta}(t) = g_{ji}^{\beta\alpha}(-t). \tag{2.6d}$$

  If the Hamiltonian is bilinear in spin operators, time-reversal symmetry (T-symmetry) holds in addition.

- Of all correlations, only diagonal autocorrelations are non-zero at $t=0$,

$$g_{ij}^{\alpha\beta}(0) = \delta_{ij}\delta^{\alpha\beta}\frac{S(S+1)}{3}, \tag{2.6e}$$

  assuming a single spin species S.

For later purposes, we define the normalized spin correlations

$$G_{ij}^{\alpha\beta}(t_1,t_2) := \frac{3}{S(S+1)}\, g_{ij}^{\alpha\beta}(t_1,t_2), \qquad -1 \leq G_{ij}^{\alpha\beta}(t_1,t_2) \leq 1. \tag{2.7}$$

and the matrix representations

$$\underline{\underline{g}}_{ij}(t_1,t_2) := \begin{pmatrix} g^{xx} & g^{xy} & g^{xz} \\ g^{yx} & g^{yy} & g^{yz} \\ g^{zx} & g^{zy} & g^{zz} \end{pmatrix}_{ij} (t_1,t_2), \qquad \underline{\underline{G}}_{ij}(t_1,t_2) := \frac{3}{s(s+1)}\,\underline{\underline{g}}_{ij}(t_1,t_2). \tag{2.8}$$

We intentionally use the letters "g" or "G" for the spin correlations because they are linked to **G**reen's functions. The retarded Green's function, for example, describes the linear response of a system to an external perturbation according to Kubo's formalism [Nol15]. In this context, it is defined as

$$\mathcal{G}^{\text{ret}}_{\mathbf{A}|\mathbf{B}}(t_1, t_2) = -\mathtt{i}\Theta\left(t_1 - t_2\right) \langle [\mathbf{A}(t_1), \mathbf{B}(t_2)] \rangle_{\rho_{\text{eq}}} \tag{2.9}$$

where $\mathbf{B}$ is the perturbation operator, $\mathbf{A}$ is the considered perturbed observable and ρ_{eq} is the equilibrium state. Setting $\mathbf{B} = \mathbf{S}_j^\beta$ and $\mathbf{A} = \mathbf{S}_i^\alpha$, the retarded Green's function can be directly related to spin correlations according to

$$\mathcal{G}^{\text{ret}}_{\mathbf{S}_i^\alpha|\mathbf{S}_j^\beta}(t_1, t_2) = -\mathtt{i}\Theta\left(t_1 - t_2\right) \left(g_{ij}^{\alpha\beta}(t_1, t_2) - g_{ji}^{\beta\alpha}(t_2, t_1)\right) \xrightarrow[T\to\infty]{} 0. \tag{2.10}$$

In case of infinite temperature, this expression is zero due to Eq. (2.6d). Physically, this means that a weak magnetic field applied to a single site j does not affect the average spin polarization at the same or at any other site. The situation may change when the temperature is lowered, but spinDMFT and its extensions are developed exclusively for infinite temperature. Hence, we do not consider Green's functions, but work directly with the spin correlations in the framework of this thesis.

The spin expectation values and the spin correlations are microscopic quantities, which is immediately clear from their definitions Eqs. (2.4) and (2.5), which involve only one or two sites. In practice, measuring such quantities is challenging, because the applied magnetic fields in experiment usually cannot address single spins exclusively. In Sec. 2.6, we consider an experiment, where single electron spins on a diamond surface are addressed indirectly through a shallow NV center. By means of this technique, the microscopic spin autocorrelations are indeed measurable, but such setups are rather special. Often, one has to let go of the microscopic quantities and instead consider macroscopic observables such as the global magnetization

$$\mathbf{m}^\alpha := \frac{1}{N}\sum_{i=1}^{N} \mathbf{S}_i^\alpha, \qquad\qquad \alpha \in \{x, y, z\}. \tag{2.11}$$

An example for this is the free induction decay in NMR, see Sec. 2.5. Before explicitly discussing experiments, we introduce some fundamental spin models in the following sections.

2.2 Heisenberg, XXZ and Hubbard model

The Heisenberg model is one of the simplest models for describing the quantum-mechanical interaction of localized spins. The interaction is given by the scalar product of the involved spin operators making the model fully spin isotropic. The Hamiltonian reads [Nol15]

$$\mathbf{H}_{\text{iso}} = \frac{1}{2}\sum_{i,j} J_{ij} \vec{\mathbf{S}}_i \cdot \vec{\mathbf{S}}_j = \frac{1}{2}\sum_{i,j} J_{ij} \left(\frac{1}{2}\mathbf{S}_i^+\mathbf{S}_j^- + \frac{1}{2}\mathbf{S}_i^-\mathbf{S}_j^+ + \mathbf{S}_i^z\mathbf{S}_j^z\right), \tag{2.12}$$

with arbitrary prefactors J_{ij} defining the coupling strength. In this thesis, the Heisenberg model is used as a toy model for establishing spinDMFT and CspinDMFT. We will also consider the more general XXZ model. It is an extension of the above Hamiltonian by an easy-axis anisotropy into the z-direction,

$$\mathbf{H}_{\mathrm{XXZ}} = \frac{1}{2}\sum_{i,j} J_{ij}\left(\mathbf{S}_i^x\mathbf{S}_j^x + \mathbf{S}_i^y\mathbf{S}_j^y + \lambda\mathbf{S}_i^z\mathbf{S}_j^z\right), \tag{2.13}$$

aquired by a prefactor $\lambda \in \mathbb{R}$. Depending on the respective purpose, we will consider these models with different geometries, e.g., nearest-neighbor (NN) couplings, $J_{ij} \propto \delta_{\langle i,j\rangle}$, or dipole-like couplings, $J_{ij} \propto |\vec{R}_i - \vec{R}_j|^{-3}$. Besides the methodological benefit, the Heisenberg model has direct physical relevance. It is employed, for example, to describe spin glasses [BM80; GR98] and many insulating magnetic materials such as the antiferromagnet Manganese(II)-Oxide (MnO) [Nol15]. The antiferromagnetic Heisenberg model is a limiting case of the Hubbard model, which is used to describe correlated electrons in a crystal. We discuss the Hubbard model and the transition briefly in the following paragraph.

If the electrons in a solid-state system are tightly bound at the nuclei[1], their mutual Coulomb interaction becomes important. This situation can be modeled by the one-band Hubbard model. Its Hamiltonian in Wannier representation reads [Nol15]

$$\mathbf{H}_{\mathrm{Hubb}} = -t\sum_{\langle i,j\rangle,\sigma} \mathbf{c}_{i\sigma}^\dagger\mathbf{c}_{j\sigma} + U\sum_i \mathbf{n}_{i\uparrow}\mathbf{n}_{i\downarrow}. \tag{2.14}$$

with $\sigma \in \{\uparrow,\downarrow\}$ denoting the spin, t being the NN hopping amplitude and U being the local strongly-screened Coulomb-interaction strength. The operator $\mathbf{c}_{i\sigma}^{(\dagger)}$ annihilates (creates) an electron at site i and $\mathbf{n}_{i\sigma} := \mathbf{c}_{i\sigma}^\dagger\mathbf{c}_{i\sigma}$ measures the occupation number at site i. Increasing the interaction strength U means reducing the probability of finding two electrons at the same site. In case of half filling, that is, one electron per lattice site, one expects a metal-insulator transition for decreasing ratio t/U. In the limit $t/U \to 0$, each site is only occupied by a single electron. The remaining dynamics consists of virtual hopping-processes which allow two adjacent electrons of opposite spin to switch sites. Since the electrons themselves are indistinguishable, one could alternatively say the spin states of two adjacent electrons are exchanged. This is also called “flip-flop” process and it is precisely what the terms $\mathbf{S}_i^+\mathbf{S}_j^-$ and $\mathbf{S}_i^-\mathbf{S}_j^+$ in the Heisenberg model in Eq. (2.12) represent. By perturbation theory in t/U, it can be rigorously shown that the half-filled Hubbard model maps to the Heisenberg model with $J_{ij} = -4t^2/U\delta_{<i,j>}$ [Czy08]. Due to the negative sign, this transition leads to an antiferromagnetic ground-state. In this thesis, we exclusively consider the high-temperature regime, where a global sign in the Hamiltonian in Eq. (2.12) hardly matters. It is not relevant at all for the spin correlations $g_{ij}^{\alpha\beta}(t)$.

For later purposes, we briefly comment on the symmetries of the Heisenberg and XXZ model. The Heisenberg model is spherically symmetric in spin space, which leads to the following important properties[2]:

- All components of the global magnetization are conserved,

$$[\mathbf{H}_{\mathrm{iso}}, \mathbf{m}^\alpha] = 0, \qquad\qquad \alpha \in \{x,y,z\}. \tag{2.15a}$$

---

[1] For example, in d-orbitals of transition metals.

[2] We consider the canonical ensemble and no spontaneous spin-symmetry breaking.

- All off-diagonal correlations vanish,

$$g_{ij}^{\alpha\beta}(t) = 0, \qquad \alpha \neq \beta. \tag{2.15b}$$

- All diagonal correlations are equivalent,

$$g_{ij}^{xx}(t) = g_{ij}^{yy}(t) = g_{ij}^{zz}(t). \tag{2.15c}$$

The prefactor λ in the XXZ model breaks the spherical symmetry if it deviates from one, but rotational symmetry around z holds independent of the value of λ. Some important properties of the XXZ model are:

- The z-component of the global magnetization is conserved,

$$[\mathbf{H}_{\mathrm{XXZ}}, \mathbf{m}^z] = 0. \tag{2.16a}$$

- All off-diagonal correlations vanish,

$$g_{ij}^{\alpha\beta}(t) = 0, \qquad \alpha \neq \beta. \tag{2.16b}$$

- The transverse diagonal correlations are equivalent,

$$g_{ij}^{xx}(t) = g_{ij}^{yy}(t). \tag{2.16c}$$

The Heisenberg model describes the exchange interaction resulting from movable electrons in case of very strong mutual interactions as captured by the Hubbard model. In fact, there exist many more examples of localized spin ensembles. In some systems, the spin-carrying particles cannot move at all, but still interact with one another through their associated magnetic moments. This scenario is captured by the dipole-dipole interaction which will be discussed in the following section.

2.3 Dipole-dipole model

The direct dipole-dipole interaction is relevant, for example, in solid-state NMR [Lev01]: A nuclear spin is spatially fixed at a certain lattice site i and generates a dipolar magnetic field at the site j of another nuclear spin and *vice versa*. The interaction energy depends on the orientation of the spin vectors, $\vec{\mathbf{S}}_i$ and $\vec{\mathbf{S}}_j$, and the relative distance vector $\vec{R}_{ij} := \vec{R}_j - \vec{R}_i$. This is captured by the Hamiltonian [Czy08; Sli90; Lev01]

$$\mathbf{H}_{\mathrm{DD}} = \frac{1}{2} \sum_{i,j} J_{ij} \left(3 \left(\vec{\mathbf{S}}_i \cdot \vec{n}_{ij} \right) \left(\vec{\mathbf{S}}_j \cdot \vec{n}_{ij} \right) - \vec{\mathbf{S}}_i \cdot \vec{\mathbf{S}}_j \right). \tag{2.17}$$

with long-range couplings

$$J_{ij} := -\frac{\mu_0 \gamma_i \gamma_j}{4\pi R_{ij}^3}, \qquad R_{ij} := |\vec{R}_{ij}|, \qquad \vec{n}_{ij} := \frac{\vec{R}_{ij}}{R_{ij}}. \tag{2.18}$$

Note that the spins are not necessarily of the same kind, i.e., the gyromagnetic ratios γ_i and γ_j may not be the same.

For describing magnetic phenomena of electrons in solids, the direct dipole-dipole interaction is often neglected because it is weak compared to the exchange interaction described in the previous section [Czy08]. There are, however, also materials with unpaired and spatially separated electrons where the dipole-dipole interaction is relevant. Defect electrons on a diamond surface are an example for this, see Sec. 2.6.

The Hamiltonian in Eq. (2.17) is anisotropic, but in a different way than the XXZ model. In the XXZ model, the z-direction is distinguished from x and y, but the anisotropy itself does not change from pair to pair of spins, i.e., λ is independent of i and j. In the dipole-dipole model, no direction is *per se* distinguished. Indeed, performing a rotation in spin and real space leaves the Hamiltonian in Eq. (2.17) invariant. If the spins have fixed positions, however, the rotational symmetry in real space is broken. Therefore, the coupling is anisotropic and, in contrast to the XXZ model, the anisotropy varies from pair to pair of spins. This lack of rotational symmetries can lead to all nine spin autocorrelations being non-zero. In experimental setups, the spins are typically subject to a strong external magnetic field. This leads to an effective interaction in which some symmetries are recovered again. We discuss how this is modeled in the following section.

2.4 External magnetic fields and rotating-wave approximation

In the models presented so far, an external magnetic field can be easily added. To this end, the Hamiltonian is extended by the Zeeman term $\mathbf{H}_\mathrm{Z}$, which couples each spin operator linearly to the external field. Usually, the field axis is chosen parallel to the z-axis yielding

$$\mathbf{H}_\mathrm{Z} = -B \sum_i \gamma_i \mathbf{S}_i^z = -\sum_i \omega_i \mathbf{S}_i^z. \tag{2.19}$$

Here, B is the absolute of the magnetic field, γ_i is the gyromagnetic ratio and ω_i is the Larmor frequency of spin i.

If the strength of the field significantly exceeds the spin-spin interactions, one can make use of the so-called rotating-wave approximation[3] (RWA) [Lev01]. This can be understood best in the Larmor-rotating frame, which rotates at the Larmor frequency of the spins. To this end, we transform each spin vector according to

$$\vec{\mathbf{S}}_i(t) \to \vec{\mathbf{S}}_{i,\mathrm{rf}}(t) := \underbrace{\mathbf{U}^\dagger(t)\mathbf{U}_\mathrm{Z}(t)}_{\mathbf{U}^\dagger_\mathrm{eff}(t)}\, \vec{\mathbf{S}}_i(0)\, \underbrace{\mathbf{U}^\dagger_\mathrm{Z}(t)\mathbf{U}(t)}_{\mathbf{U}_\mathrm{eff}(t)}, \qquad \mathbf{U}_\mathrm{Z}(t) := \mathrm{e}^{-\mathrm{i}\mathbf{H}_\mathrm{Z} t} \tag{2.20}$$

where "rf" stands for rotating frame. The operator $\mathbf{U}(t)$ describes the time evolution in the laboratory frame. It is generated by $\mathbf{H} = \mathbf{H}_0 + \mathbf{H}_\mathrm{Z}$, where $\mathbf{H}_0$ is the unperturbed Hamiltonian, containing for example spin-spin interactions. Using the Schrödinger

---

[3] Also called secular approximation.

equation, it can be shown that the effective time evolution $\mathbf{U}_{\text{eff}}(t)$ is generated by the effective Hamiltonian

$$\mathbf{H}_{\text{eff}}(t) = \mathbf{U}_{\text{Z}}^{\dagger}(t)\mathbf{H}\mathbf{U}_{\text{Z}}(t) - \mathbf{H}_{\text{Z}} = \mathbf{U}_{\text{Z}}^{\dagger}(t)\mathbf{H}_0\mathbf{U}_{\text{Z}}(t). \tag{2.21}$$

We eliminated the Zeeman term, but obtained an explicit time dependence which, at the first glance, makes the situation much more complicated. We obtain couplings with oscillating prefactors, for example,

$$\mathbf{H}_{\text{eff}}(t) \ni \cos(\omega_i t)\cos(\omega_j t)\mathbf{S}_i^x\mathbf{S}_j^x. \tag{2.22}$$

If the magnetic field and thus the Larmor frequencies ω_i are very large, the time scale of these oscillations is much shorter than the time scale associated with the spin-spin interactions. In this case, the two types of dynamics can be separated. Aiming at the slower, more relevant dynamics, it is justified to perform a time average of the effective Hamiltonian. This corresponds to a first order truncation of the Magnus expansion [Mag54; Bla+09; AF11] and, in case of a single Larmor frequency, induces an error in the order of E/ω, where E is the typical energy scale of the system [ASK15; Sli90]. Starting from the spin-spin couplings in the laboratory frame, we obtain

$$\mathbf{S}_i^x\mathbf{S}_j^y + \mathbf{S}_i^y\mathbf{S}_j^x, \quad \mathbf{S}_i^z\mathbf{S}_j^x, \quad \mathbf{S}_i^z\mathbf{S}_j^y \quad \longrightarrow \quad 0 \tag{2.23a}$$

$$\mathbf{S}_i^x\mathbf{S}_j^x, \quad \mathbf{S}_i^y\mathbf{S}_j^y \quad \xrightarrow[\omega_i=\omega_j]{} \quad \frac{1}{2}\left(\mathbf{S}_i^x\mathbf{S}_j^x + \mathbf{S}_i^y\mathbf{S}_j^y\right) \tag{2.23b}$$

$$\mathbf{S}_i^x\mathbf{S}_j^x, \quad \mathbf{S}_i^y\mathbf{S}_j^y \quad \xrightarrow[\omega_i\neq\omega_j]{} \quad 0 \tag{2.23c}$$

$$\mathbf{S}_i^z\mathbf{S}_j^z \quad \longrightarrow \quad \mathbf{S}_i^z\mathbf{S}_j^z. \tag{2.23d}$$

In Eqs. (2.23b) and (2.23c), we distinguished between the homogeneous case, i.e., the spins are of the same species and the heterogeneous case, i.e., the spins are different[4]. The Heisenberg model with homogeneous couplings is invariant under the transformation in Eq. (2.23). For the dipole-dipole Hamiltonian in Eq. (2.17), we obtain

$$\mathbf{H}_{\text{hom}}^{\text{rf}} = \frac{1}{2}\sum_{i,j} d_{ij}\left(2\mathbf{S}_i^z\mathbf{S}_j^z - \mathbf{S}_i^x\mathbf{S}_j^x - \mathbf{S}_i^y\mathbf{S}_j^y\right) = \frac{1}{2}\sum_{i,j} d_{ij}\left(3\mathbf{S}_i^z\mathbf{S}_j^z - \vec{\mathbf{S}}_i\cdot\vec{\mathbf{S}}_j\right) \tag{2.24}$$

in the homogeneous case and

$$\mathbf{H}_{\text{het}}^{\text{rf}} = \frac{1}{2}\sum_{i,j} d_{ij} 2\mathbf{S}_i^z\mathbf{S}_j^z \tag{2.25}$$

in the heterogeneous case [Lev01]. The secular couplings are given by[5]

$$d_{ij} \coloneqq \frac{J_{ij}}{2}\left(3n_{z,ij}^2 - 1\right) = \frac{J_{ij}}{2}\left(3\cos^2(\vartheta_{ij}) - 1\right) \tag{2.26}$$

where ϑ_{ij} refers to the angle between magnetic field and distance vector $\vec{R}_{ij}$. The dipolar dynamics become considerably simpler in the rotating frame after applying the RWA.

---

[4] We do not use the standard NMR nomenclature ("homonuclear" and "heteronuclear") because the transformations are also used for electron spins in this thesis.

[5] The letter "d" is conventionally used for the secular couplings in NMR.

We end up with an XXZ model for the homogeneous and with an Ising model for the heterogeneous case. Note that the Hamiltonians in Eqs. (2.24) and (2.25) refer to the rotating frame. If one is interested in the dynamics in the laboratory frame, one can use the simple back transformation

$$\vec{\mathbf{S}}_i(t) = \mathbf{U}^\dagger_{\text{eff}}(t)\mathbf{U}^\dagger_{\text{Z}}(t)\vec{\mathbf{S}}_i(0)\mathbf{U}_{\text{Z}}(t)\mathbf{U}_{\text{eff}}(t) = \underline{\underline{\Omega}}_i(t)\vec{\mathbf{S}}_{i,\text{rf}}(t), \tag{2.27a}$$

$$\underline{\underline{\Omega}}_i(t) = \begin{pmatrix} \cos\omega_i t & \sin\omega_i t & 0 \\ -\sin\omega_i t & \cos\omega_i t & 0 \\ 0 & 0 & 1 \end{pmatrix}. \tag{2.27b}$$

The Hamiltonians in Eqs. (2.24) and (2.25) are fundamental for NMR, which will be briefly introduced in the section below. It is noteworthy that the error induced by the RWA has been studied for spinDMFT in Ref. [Grä+21] (Sec. IV).

2.5 Nuclear magnetic resonance spectroscopy

NMR spectroscopy naturally falls into the scope of applications of spinDMFT, since it deals with high-temperature spin dynamics. We will use spinDMFT and nl-spinDMFT to simulate and understand NMR signals in Ch. 6. As a preparation, we briefly explain the meaning of longitudinal and transverse relaxation and present some basic NMR experiments in the following. This part of the section is based on Ref. [Lev01] which provides a comprehensive introduction to the basics of NMR. Subsequently, we relate the quantities measured in an NMR experiment to microscopic spin correlations.

We use the notation $(\varphi)_\alpha$ to refer to a radio-frequency (RF) pulse rotating by φ around one of the main axes $\alpha \in \{x, y, z\}$. Applying this to a single spin corresponds to the unitary transformation [SS04]

$$D_\alpha(\varphi) := \mathrm{e}^{-\mathtt{i}\varphi\mathbf{S}^\alpha} \underset{S\,=\,1/2}{=} \cos(\varphi/2)\sigma^0 - \mathtt{i}\sin(\varphi/2)\sigma^\alpha, \tag{2.28}$$

where σ^α represents the Pauli matrix in α-direction.

2.5.1 Measuring the lifetime of a spin state: T_1 and T_2

The fundamental gist of NMR spectroscopy is to obtain information about the composition and structure of a sample by resonantly addressing the contained nuclear spins. These serve as reporters of their local environment due to several kinds of electro-magnetic interactions. Important interactions in NMR are for example the chemical shift, the dipole-dipole interaction, the J-coupling and the quadrupolar interaction (see Ref. [Lev01] for details). Useful initial information about a sample can be gathered by measuring relaxation processes, which are, in turn, connected to characteristic times. The most important ones are (i) the longitudinal relaxation time (T_1) and (ii) the transverse relaxation time (T_2).

Nuclear spins are completely disordered at ambient conditions, since the available thermal energy exceeds the dipolar interaction by far[6]. Hence, without any external perturbations,

---

[6] To grasp the orders of magnitude, we will provide an example below, see Eq. (2.29).

there is no nuclear spin magnetization in the considered sample. Longitudinal relaxation can be observed for instance, if the sample is suddenly brought into an external magnetic field, which causes the spins to align along the field axis. The characteristic time required for the alignment is called T_1, see Fig. 2.1 for an illustration[7].

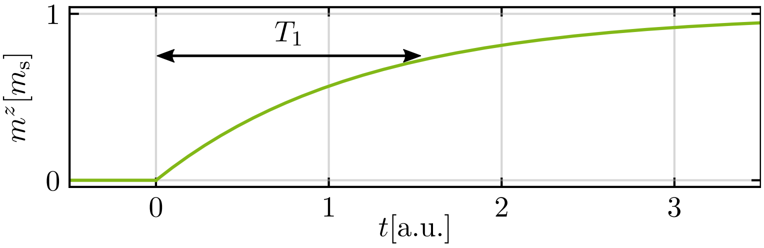

Figure 2.1: Schematic plot of T_1 relaxation. The magnetic field is switched on at $t = 0$ and m_s is the saturation magnetization.

In a transverse relaxation measurement, one considers the nuclear spins to be initially polarized through an external magnetic field. Then, a $\left(\frac{\pi}{2}\right)_y$-pulse in resonance with the Larmor frequency of the nuclear spins is used to rotate the magnetization vector into the transverse plane. There, it precesses around the field direction, which can be measured as a current in a wire coil. Decoherence causes the amplitude of the measured oscillation to decrease over time, see Fig. 2.2. The resulting signal is referred to as the free induction decay.

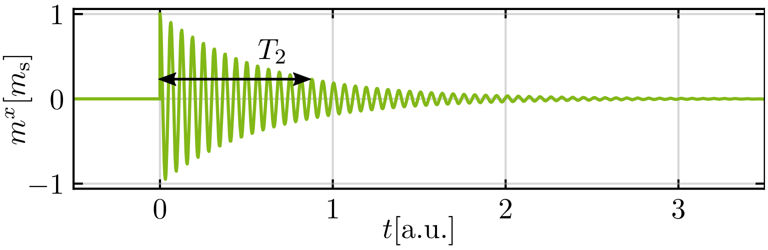

Figure 2.2: Schematic plot of T_2 relaxation. The pulse is applied at $t = 0$ and m_s is the saturation magnetization. The signal oscillates at the Larmor frequency.

T_1 and T_2 relaxation are fundamentally different. In T_1 relaxation, the longitudinal magnetization changes, which inevitably requires an energy exchange between the considered spins and some environment[8]. Therefore, longitudinal relaxation usually contains information about the motion and rotation of molecules or atoms. T_2 relaxation, on the other hand, may occur without any energy exchange, since the transverse magnetization is no conserved quantity. Therefore, T_2 relaxation is often much faster than T_1 relaxation. The FID includes dephasing processes due to time-dependent fluctuations, gathered under the term homogeneous broadening, and due to static field inhomogeneities, gathered under the term inhomogeneous broadening. Homogeneous broadening results, for example, from the flip-flop processes involved in the direct spin-spin interactions. Inhomogeneous

---

[7] One should note that the presented direct measurement of T_1 relaxation is impractical, because the induced magnetization of the nuclei is a lot smaller than the diamagnetism of the electrons in the sample. In practice, the method of inversion-recovery is used instead [Lev01].

[8] This is because the secular homonuclear Hamiltonian in Eq. (2.24) commutes with the longitudinal magnetization. Hence, the latter is conserved if the system contains no additional environments.

broadening results from spatial fluctuations of the magnetic field, for example, due to the chemical-shift anisotropy [Lev01].

By performing a spin-echo measurement[9], the inhomogeneous broadening can be eliminated. The idea is to flip the nuclear spins after some time in order to revert the effect of the static dephasing. An exemplary pulse sequence is presented in Fig. 2.3. A complete spin-echo experiment requires several measurements for different pulse spacings $\tau/2$. Subsequently, one plots the resulting signal at $t=\tau$ versus the total sequence time τ. While static inhomogeneities are completely eliminated, the induced decoherence by time-dependent fluctuations is typically slowed down relative to the FID signal. In this context, the literature often distinguishes between the FID relaxation time T_2^* (which includes inhomogeneous broadening) and the spin-echo relaxation time T_2, see for example Ref. [WD06].

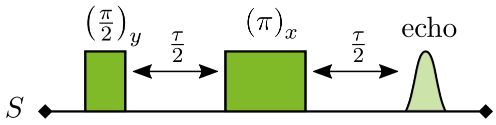

Figure 2.3: Exemplary spin-echo pulse sequence.

The concept of T_1 and T_2 relaxation originates from the field of NMR, but it is also applied to electron magnetic moments. In Sec. 2.6, we consider dipolar defect electrons on a diamond surface, where NMR-related methods are applied to investigate the spin dynamics. In Ch. 6, we want to access the above presented measurements within the mean-field framework of spinDMFT and its extensions. To this end, we need to express the measurements by infinite-temperature expectation values, which will be done in the following paragraph.

2.5.2 Expectation values in NMR experiments

Within a typical NMR experiment, three energy scales are well separated: the thermal energy is much larger than the magnetic field energy which is, in turn, much larger than the spin-spin interaction energy. Consider for example ^{1}H spins with dipolar interactions and a spacing of 0.2 nm. Given that the typical fields used in NMR are in the order of 10 T, the energy scales differ by several orders of magnitude according to

$$E_{\mathrm{th}}(300\,\mathrm{K}) \approx 2.6\times 10^{-2}\,\mathrm{eV} \quad \gg \quad \gamma_{\mathrm{H}} B \approx 1.8\times 10^{-6}\,\mathrm{eV} \quad \gg \quad J \approx 6.2\times 10^{-11}\,\mathrm{eV}. \tag{2.29}$$

This allows for several simplifications in a theoretical description. The difference between the time scale of the Larmor precession and the spin-spin interaction allows one to apply the RWA, which we presented in Sec. 2.4. Moreover, since the thermal energy is immensely large, the density operator can be approximated by a first order Taylor expansion according to [Cho+05; ASK15; SF18]

$$\mathcal{Z}\rho_{\mathrm{th}} = \exp\left(\sum_\mu h_\mu \sum_{i=1}^{N_\mu} \mathbf{S}^z_{\mu,i}\right) \approx \mathbf{1} + \sum_\mu h_\mu \sum_{i=1}^{N_\mu} \mathbf{S}^z_{\mu,i}, \qquad h_\mu := \gamma_\mu B\beta \ll 1, \tag{2.30}$$

---

[9] Sometimes also referred to as Hahn echo [Hah50].

where N_μ is the number of spins and γ_μ is the gyromagnetic ratio of the spin species μ. In the following consideration, we provide the mathematical expressions for the presented measurements and relate them to microscopic spin correlations. Conventionally, NMR signals such as the FID are normalized to one at $t = 0$. Hence, we leave out static prefactors in the following consideration.

Homonuclear free induction decay

We consider a single spin species S. A measurement of the FID corresponds to a measurement of the transverse polarization over time considering the spins to be initially polarized into the transverse plane due to the $\left(\frac{\pi}{2}\right)_y$-pulse. Therefore, the FID is given by

$$\mathcal{F}(t) \propto \langle \mathbf{m}^x(t) \rangle_{\rho_{\mathrm{th},\perp}} \propto \sum_i \langle \mathbf{S}_i^x(t) \rangle_{\rho_{\mathrm{th},\perp}}, \qquad \rho_{\mathrm{th},\perp} := \frac{1}{\mathcal{Z}} \left(\mathbf{1} + h \sum_i \mathbf{S}_i^x \right). \tag{2.31}$$

We consider the FID in the rotating frame, i.e., the time evolution is generated by the secular Hamiltonian in Eq. (2.24). Using that the trace of a single spin operator vanishes, see Eq. (2.6a), the above expression can be simplified to

$$\mathcal{F}(t) \propto \sum_{i,j=1}^{N} \langle \mathbf{S}_i^x(t) \mathbf{S}_j^x(0) \rangle_{\rho_0}, \tag{2.32}$$

which relates the FID to microscopic spin correlations at infinite temperature.

Heteronuclear free induction decay

We consider several spin species with pairwise different gyromagnetic ratios. The $\left(\frac{\pi}{2}\right)_y$ -pulse addresses only one of these species, which is henceforth denoted by S_1. Since off-diagonal correlations vanish, see Eq. (2.16b), the polarization of the remaining species of spins (S_μ with $\mu \neq 1$) can be neglected in the FID. We conclude

$$\mathcal{F}(t) \propto \sum_{i,j=1}^{N_\mu} \langle \mathbf{S}_{1,i}^x(t) \mathbf{S}_{1,j}^x(0) \rangle_{\rho_0} \tag{2.33}$$

which is equivalent to Eq. (2.32), but the time evolution now involves any secular couplings between the different species of spins, see Eqs. (2.24) and (2.25).

Spin echo

The spin echo is distinguished from the FID due to the additional $(\pi)_y$-pulse. The resulting signal cannot be related to equilibrium spin correlations as above, but we will see later that an explicit time dependence can be incorporated in spinDMFT and its extensions. The action of the $(\pi)_y$-pulse onto the addressed spin species S_1 can be formally included by adding

$$\mathbf{H}_{\text{pulse}}(t) = \sum_{i=1}^{N_1} \pi\delta\left(t - \frac{\tau}{2}\right) \mathbf{S}^y_{1,i} \tag{2.34}$$

to the Hamiltonian. The spin echo is the result of Eq. (2.33), evaluated at $t = \tau$ and considering the adapted Hamiltonian for the time evolution.

2.6 Dipolar spin relaxation on a diamond surface

We consider a recent experiment [Rez22; Rez+23; Grä+23], which uses a near-surface NV center to probe the dynamics of defect spins on a diamond surface. The results of this experiment will be compared to simulations by spinDMFT and extensions in Ch. 5. Here, we briefly present the experimental setup and the measurement methods.

2.6.1 Experimental setup

The experimental setup essentially comprises the sample, a permanent magnet, a RF setup and an optical setup. The sample under examination is ^{12}C-enriched diamond with shallow NV centers (located around $2 - 7\,\text{nm}$ below the surface). The diamond surface hosts a dipolar ensemble of spins with $S = 1/2$ and $g_\text{S} \approx -2$, which likely result from localized defects [Gro+11; Gri+14; San+19; Sta+19]. Candidates are for example electrons from dangling bonds [Dwy+22; Cho+23]. Henceforth, we refer to these spins as surface spins (S). In addition to them, there is a significant protonic noise source (P) at the surface, which likely results from an intrinsic layer of surface water and/or hydrocarbons [Häb+15; Sta+15]. In experiment, a single NV center is employed as a magnetic sensor to probe the surface spin dynamics. An exemplary cutout of the system is displayed in Fig. 2.4.

The sample is subject to external magnetic fields during the measurements. A permanent magnet establishes a static field of about $0.1\,\text{T}$ at the surface. For any measurement presented below, the field encloses the magic angle

$$\vartheta_\text{m} = \arccos \frac{1}{\sqrt{3}} \approx 54.7^\circ \tag{2.35}$$

with the normal vector of the surface plane[10]. In the experimental framework, the NV spin and the surface spins are treated as two-level systems, each possessing distinct transition frequencies. By means of the RF setup, the NV spin and the surface-spin ensemble can be addressed independently by applying proper pulse sequences. The

---

[10] The secular couplings in Eq. (2.26) vanish at the magic angle which gives the latter a special meaning in NMR [Lev01]. In the context of the considered experiment, however, the magnetic field is applied along the axis of the NV center, which, coincidentally, encloses the magic angle with the surface normal vector (the magic angle is also the angle enclosed by the diagonal of a cube and one of its edges).

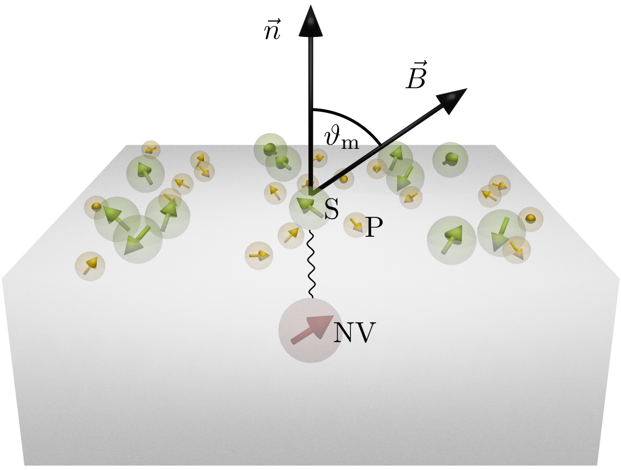

Figure 2.4: Cutout of the diamond surface. The NV spin is displayed in red, the surface spins in green and the proton spins in orange. The external magnetic field $\vec{B}$ encloses the magic angle ϑ_m with the normal vector $\vec{n}$ of the surface. All the spins interact dipolarly with one another. The coupling of the NV spin to its most important interaction partner is indicated by the wiggly line.

optical setup consists of a scanning confocal microscope which allows for addressing and reading-out the spin state of the NV center. This forms the basis for all measurements.

The goal of the experiment is to employ the NV center to measure the autocorrelations of a single surface spin. In the particular scenario considered in the experiment, the NV spin couples primarily to this specific surface spin as indicated in Fig. 2.4. The autocorrelations of the surface spin are accessed by probing it through the NV spin using the RF setup[11]. The dipolar coupling required for this procedure is determined using a double-electron-electron-resonance (DEER) sequence (not shown here). When the coupling is known, the to-us relevant surface-spin measurements can be performed using the correlation-spectroscopy sequence depicted in Fig. 2.5. The gray box is a placeholder for different pulse sequences with which different autocorrelations of the strongest-coupled surface spin can be measured. Before discussing this in detail, we set up the model Hamiltonian for the surface-spin dynamics in the following section.

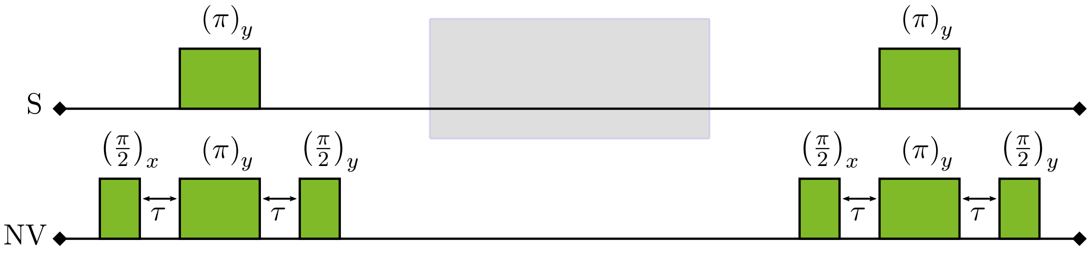

Figure 2.5: Correlation-spectroscopy sequence for probing an individual surface spin using an NV center. The pulse spacing τ is determined from the coupling between the surface spin and the NV spin. The gray box between the pulse sandwiches is a placeholder for different surface-spin measurements.

---

[11] This complicates the experimental procedure, but it is inevitable for measuring the autocorrelations because the RF setup cannot address individual surface spins in contrast to the NV center.

2.6.2 Hamiltonian in the rotating frame

We emphasize that the experiment is carried out at ambient conditions so that all the spins are randomly oriented in the beginning. The total Hamiltonian of the spin dynamics includes the dipolar interactions between the NV spin, the surface spins and the proton spins as well as any couplings to external fields. It is experimentally verified that the influence of the NV spin on the surface spins plays only a minor role during the time evolution of the gray box in Fig. 2.5. Therefore, we neglect the NV spin for a description of the surface-spin dynamics. The static field applied in all measurements is significantly stronger than the dipolar fields experienced by the surface spins which allows to apply the RWA to them[12], see Eqs. (2.24) and (2.25).

The microscopic nature of the proton noise is not entirely clear. Its effect on the surface spins may be modeled by a semiclassical fluctuating field $b_i^z(t)$ according to

$$\mathbf{H}^{\mathrm{rf}}_{\mathrm{S-P}} = \sum_i b_i^z(t)\mathbf{S}_i^z, \tag{2.36}$$

which entails at least two additional parameters[13], the correlation time τ and the noise variance W^2. In the framework of this thesis, we focus on those experimental measurements where the proton noise is essentially canceled out by the applied pulses. The reason for this restriction is that we want to have as few unknown degrees of freedom as possible when comparing experiment and theory. The corresponding measurements and their translation into observables are presented in the next section.

Without proton noise, only the dipolar interactions between the surface spins remain. The rotating-frame Hamiltonian then reads

$$\mathbf{H}^{\mathrm{rf}}_{\mathrm{S}} = \mathbf{H}^{\mathrm{rf}}_{\mathrm{hom}} = \frac{1}{2}\sum_{i,j} d_{ij}\left(2\mathbf{S}_i^z\mathbf{S}_j^z - \mathbf{S}_i^x\mathbf{S}_j^x - \mathbf{S}_i^y\mathbf{S}_j^y\right) \tag{2.37}$$

with the secular couplings d_{ij} given in Eq. (2.26). Since the spins are spatially constrained to the surface, it is useful to introduce surface polar coordinates (R_{ij}, φ_{ij}), see Fig. 2.6.

This allows the couplings to be rewritten as

$$d_{ij} = -\frac{J_{ij}}{2}\cos\left(2\varphi_{ij}\right) = \frac{1}{2}\frac{\mu_0\gamma_{\mathrm{S}}^2}{4\pi R_{ij}^3}\cos\left(2\varphi_{ij}\right). \tag{2.38}$$

For theoretical considerations it is clearly important to know, how the surface-spins are spatially distributed. Their density strongly depends on the surface preparation [San+19; Dwy+22]. For the diamond sample in the considered experiment, the surface-spin spacing is measured to be $r_0 = 8(1)\,\mathrm{nm}$[14]. The locations of the surface defects depend on the underlying diamond lattice, but since the lattice constant, $a \approx 0.36\,\mathrm{nm}$, is much smaller than r_0, the lattice structure is not expected to be directly important for the spin dynamics. In theoretical considerations, the surface-spin locations are drawn randomly. More details on this will be provided in Sec. 5.3.2.

---

[12] E.g., for a relative distance of 5 nm, the dipolar coupling between two surface spins is about 3-4 orders of magnitude smaller than the external field.

[13] Note that these parameters are explicitly measured in Ref. [Rez+23].

[14] The spacing is related to the density by $n_0 = r_0^{-2} = 0.016(4)\,\mathrm{nm}^{-2}$.

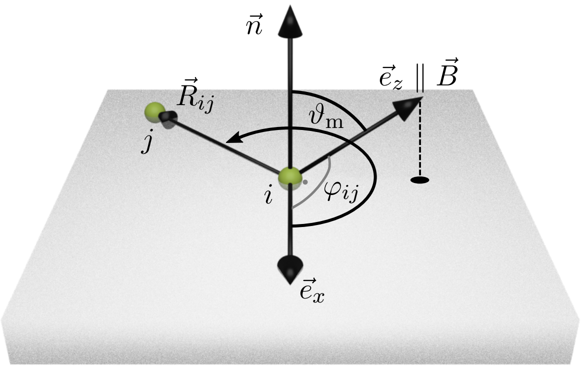

Figure 2.6: Sketch of the surface geometry. The distance vector between the spins i and j is denoted by $\vec{R}_{ij} = \vec{R}_j - \vec{R}_i$ and φ_{ij} is the angle between $\vec{R}_{ij}$ and the x-direction.

2.6.3 Measuring the surface-spin autocorrelations

In this section, we briefly present the measurements including the applied pulse sequences and translate them into observables. The relaxation processes and the characteristic times are named in the same way as in NMR, see Sec. 2.5. However, one has to keep in mind that the considered experiment measures the relaxation of a single surface spin instead of the global spin polarization. As pointed out in the previous section, we focus on those measurements, where the proton noise is essentially eliminated.

T_2 relaxation

The T_2 relaxation is measured using the spin-echo sequence in Fig. 2.7a. The π-pulse flips the surface spins relative to the proton noise so that the effect of the latter is reduced[15]. Then, the measurement approximately corresponds to the transverse autocorrelation $\langle \mathbf{S}_i^x(t)\mathbf{S}_i^x(0)\rangle^{\mathrm{rf}}$ considering the time evolution generated by $\mathbf{H}_{\mathrm{S}}^{\mathrm{rf}}$. The relaxation process takes place on the characteristic time scale T_2, which is usually obtained by fitting, e.g., using a Gaussian or an exponential function depending on the shape of the signal[16].

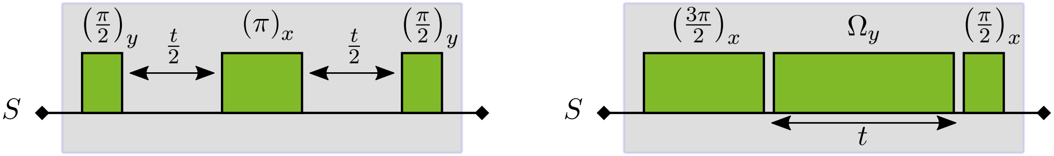

(a) Sequence for the T_2 measurement.

(b) Sequence for the $T_{1\rho}$ measurement.

Figure 2.7: Pulse sequences applied to the surface spins in different relaxation measurements. The sequences can be inserted into the placeholder of the correlation-spectroscopy sequence in Fig. 2.5.

---

[15] Due to its time dependence, the proton noise is not completely eliminated by the spin echo. Its remainder leads approximately to a modulation of the experimental data, which will be briefly discussed in Sec. 5.3.3.

[16] The fit functions will be also provided in Sec. 5.3.

$T_{1\rho}$ relaxation

Within a spin-lock driving measurement, the proton noise can also be eliminated from the longitudinal surface-spin dynamics. It should be noted that due to the strong static field B in experiment, only the z-coupling between the surface spins and the noise persists in RWA. The idea of spin-lock driving is to reduce this remaining coupling by applying a drive field B_{drive} perpendicular to B. This additional field rotates at the Larmor frequency ω_{L} around B and is thus static in the rotating frame according to

$$\mathbf{H}_{\text{drive}}(t) = \Omega_y \sum_i \left(-\sin(\omega_{\text{L}} t)\mathbf{S}_i^x + \cos(\omega_{\text{L}} t)\mathbf{S}_i^y\right) \xrightarrow[\text{rot. frame}]{} \mathbf{H}_{\text{drive}}^{\text{rf}} = \Omega_y \sum_i \mathbf{S}_i^y. \tag{2.39}$$

with $\Omega_y := \gamma_{\text{S}} B_{\text{drive}}$. We added the index y to Ω_y because for our choice of coordinates, the drive field points in the y-direction of the rotating frame. If a spin is polarized into this direction, the drive field “locks” the spin in its direction by decreasing the spin-noise coupling. Varying the strength of Ω_y allows one to adjust the effective strength of the noise. If Ω_y is chosen large, the spin-noise coupling is eliminated. Then, we can employ the RWA once more and describe the surface-spin dynamics elegantly in the doubly-rotating frame. Using the transformations in Eq. (2.23) (with y and z swapped), we obtain

$$\mathbf{H}_{\text{S}}^{\text{drf}} = \frac{1}{2} \sum_{i,j} d_{ij} \left(\frac{1}{2} \mathbf{S}_i^x \mathbf{S}_j^x - \mathbf{S}_i^y \mathbf{S}_j^y + \frac{1}{2} \mathbf{S}_i^z \mathbf{S}_j^z \right). \tag{2.40}$$

As a consequence of the drive field, we obtain a surface-spin coupling similar to the one in the original rotating frame. The only difference is that, now, the y-direction is the easy axis and the couplings are globally reduced by a factor of 2. By means of the pulse sequence shown in Fig. 2.7b, the longitudinal autocorrelation $\langle \mathbf{S}_i^y(t)\mathbf{S}_i^y(0)\rangle^{\text{drf}}$ can be measured. The relaxation process happens on the characteristic time scale $T_{1\rho}$, which can be extracted by an appropriate fit.

Summary of the surface-spin measurements

Due to the similarity of the Hamiltonians in Eqs. (2.37) and (2.40), the transverse autocorrelation is essentially the same in the singly-rotating and in the doubly-rotating frame except for a factor of 2 in the time scale. The experimental setup also allows for measuring T_1 relaxation, i.e., the longitudinal relaxation in the singly-rotating frame. But this relaxation is significantly affected by the proton noise so that we do not consider it in the framework of this thesis. The main pieces of information from this section are summarized in Tab. 2.1.

Table 2.1: Summary of the surface-spin relaxation processes. The autocorrelations refer to the infinite-temperature state.

	transverse relaxation			longitudinal relaxation		
frame	Hamiltonian	time	autocorr.	Hamiltonian	time	autocorr.
rf	$\mathbf{H}_{\text{S}}^{\text{rf}}$	T_2	g^{xx}	$\mathbf{H}_{\text{S}}^{\text{rf}} + \mathbf{H}_{\text{S-P}}^{\text{rf}}$	T_1	g^{zz}
drf	$\mathbf{H}_{\text{S}}^{\text{drf}}$	$2T_2$	g^{xx}	$\mathbf{H}_{\text{S}}^{\text{drf}}$	$T_{1\rho}$	g^{yy}

3 Overview of mean-field and related approaches

As pointed out in the introduction, the theoretical treatment of quantum many-body systems is a notoriously difficult task. Mean-field theories form a prominent class of approaches that are particularly successful in high-dimensional systems. Historically, the first mean-field theories have been considered in classical systems, long before quantum mechanics was established. An example for this is the mean-field approach by Curie [Cur95] and Weiss [Wei07] around 1900 to describe the emergence of magnetic ordering phenomena. Since the discovery of the Schrödinger equation in 1926, mean-field theories have been applied also to quantum systems, see for example the Hartree-Fock theory developed in the following decade [Har28; Foc30]. The Ginzburg-Landau theory for superconductivity from 1950 [Gin04] demonstrates the success of mean-field theories in qualitatively describing phase transitions. A first microscopic understanding of superconductivity was provided a few years later by Bardeen, Cooper and Schrieffer based on Hartee-Fock-related methods [BCS57]. With the computational resources available nowadays, extended mean-field theories can capture many-body physics even on a quantitative level, see for example the DMFT for strongly correlated fermion systems developed in the nineties [Mül89; MV89; Geo+96]. Unexpectedly, the concept of a mean field is also used in sciences unrelated to physics and chemistry, such as opinion formation [Koz22]. This chapter is devoted to the general ideas of a mean-field theory in condensed-matter physics and shall give an overview over mean-field and related approaches.

In the first section, we discuss how a mean-field theory can be derived and justified in general. Two examples for static mean-field theories and the DMFT for fermions are presented in Secs. 3.2 to 3.4. Subsequently, we discuss several attempts to a DMFT for spins and classify our own approach (spinDMFT) and its extensions in Sec. 3.5. In Sec. 3.6, we list and briefly discuss several approaches related to spinDMFT.

3.1 Mean-field theories in condensed-matter physics

The starting point is a many-body Hamiltonian, $\mathbf{H}$, which describes interacting particles, for instance, electrons hopping from site to site on a lattice. Due to the mutual interactions, the problem usually cannot be solved exactly and requires the application of approximations such as a mean-field approach. Although there is no unique construction scheme, most mean-field theories can be summarized by the two ingredients listed in Fig. 3.1.

(1) The environment of a single site is replaced by an averaged field, the so-called **mean field**. This reduces the many-body problem to a single-site problem, which is much easier to solve.

(2) The mean field represents the averaged action of a large number of sites. Its dynamics are linked to those of the effective site which entails a **self-consistency problem**, because the latter are known only *a posteriori*.

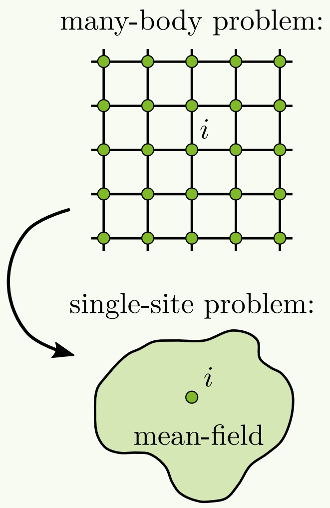

Figure 3.1: Key ingredients of a mean-field approach.

Mean-field approaches can be formally derived from a variational principle [Kuz15; Czy08; BF04]. To this end, one replaces the original many-body Hamiltonian $\mathbf{H}$ by a simpler, soluble Hamiltonian $\mathbf{H}_0$, which has to be expressed in terms of variational parameters. The Bogoliubov inequality provides an upper bound for the free energy of $\mathbf{H}$,

$$F \leq F_0 + \langle \mathbf{H} - \mathbf{H}_0 \rangle_0, \tag{3.1}$$

where F_0 is the free energy of $\mathbf{H}_0$ and $\langle \dots \rangle_0$ is an expectation value with respect to the thermal state of $\mathbf{H}_0$. The strategy is, to minimize the right-hand-side of the inequality by varying $\mathbf{H}_0$. The minimal result is considered the mean-field approximation of $\mathbf{H}$. This procedure can be connected to the two key ideas presented in Fig. 3.1. The soluble Hamiltonian $\mathbf{H}_0$ can describe the single-site problem and the minimization procedure the self-consistency problem. The formulation via a variational principle appears to be very general, but it should be noted that choosing a proper $\mathbf{H}_0$ and carrying out the minimization is not necessarily straightforward.

Static mean-field approaches can be alternatively derived by neglecting any two-particle correlations in the full many-body Hamiltonian $\mathbf{H}$. This strategy automatically leads to an effective model and a self-consistency condition as we will see in Secs. 3.2 and 3.3. In a static mean-field approach, the environment of an individual site is automatically frozen due to neglecting the two-particle correlations. In contrast to this, a *dynamic* mean-field approach allows for time-dependent fluctuations of the environment. The corresponding derivation and the resulting effective model is more involved as we will see in Sec. 3.4.

Mean-field theories are successful if the system dimension D is large, which can be understood by a rather simple argument. Consider for example a lattice of localized spins: From the perspective of an individual spin, the collective field of all of its neighbors is very important, no matter the dimension. If D is large, the number of spins in this field is also large. This implies that the fraction of this field resulting from a single neighbor spin is rather unimportant compared to the rest of the field. Thus, it is plausible that the removal of a single spin from the lattice has only a minor effect on its former neighbors. This qualitative argument justifies decoupling a single spin from the rest of the lattice, which is precisely what is done in a mean-field theory. Note that the crucial quantity in this argument is the number of nearest neighbors, which is also referred to as the coordination number and represented by the letter z. The dimension and the coordination number are related, for example, $z = 2D$ in a simple-cubic lattice. If z or, equivalently, D is sent to infinity, the mean-field description often becomes exact. However, for this limit to be physically meaningful, the Hamiltonian usually needs to be rescaled. We will come back to this, when discussing specific examples in the following sections.

3.2 Weiss mean-field theory for the Ising model

The Ising model describes a system of classical spins $S_i \in \{-1, 1\}$ on a lattice [Isi25; Pav+11]. Considering nearest-neighbor interactions, the Hamiltonian can be written as[1]

$$H_{\text{Ising}} = -\frac{J}{2}\sum_{\langle i,j\rangle} S_i S_j = \frac{1}{2}\sum_i S_i B_i, \qquad B_i := -J\sum_j \delta_{\langle j,i\rangle} S_j, \tag{3.2}$$

where we consider ferromagnetic couplings ($J > 0$). The field B_i describes the local environment of spin S_i. One way to derive a static mean-field model is to replace this field by its expectation value. Alternatively, as described in the previous section, one can neglect the two-particle correlations which entails

$$\begin{aligned} S_i S_j &= \underbrace{(S_i - \langle S_i\rangle)(S_j - \langle S_j\rangle)}_{\text{two-particle correlation}} + S_i\langle S_j\rangle + \langle S_i\rangle S_j - \langle S_i\rangle\langle S_j\rangle \\ &\approx S_i\langle S_j\rangle + \langle S_i\rangle S_j - \langle S_i\rangle\langle S_j\rangle. \end{aligned} \tag{3.3}$$

Applying this directly to the Hamiltonian leads to a simple effective model with a static mean field B^{mf} and decoupled spins,

$$H^{\text{mf}}_{\text{Ising}} = B^{\text{mf}}\sum_i S_i + E_0, \qquad B^{\text{mf}} := -zJ\langle S\rangle, \qquad E_0 := \frac{1}{2}zNJ\langle S\rangle^2. \tag{3.4}$$

From this, one can derive the self-consistency condition

$$\langle S\rangle = \tanh\left(zJ\beta\langle S\rangle\right). \tag{3.5}$$

which implies a critical temperature $T_{\text{crit}} := J/k_{\text{B}}$ separating a paramagnetic from a ferromagnetic phase, see Fig. 3.2. The results are qualitatively the same, if the mean-field approach is applied to the quantum Heisenberg model [BF04; Czy08]. For realistic systems, the approach overestimates T_{crit} and the critical exponents are incorrect [Czy08]. Furthermore, the Mermin-Wagner theorem is not obeyed. However, despite its simplicity, the Weiss mean-field theory does provide a first qualitative description of the magnetic phase transition.

---

[1] The factor $1/2$ accounts for double countings of the coupling.

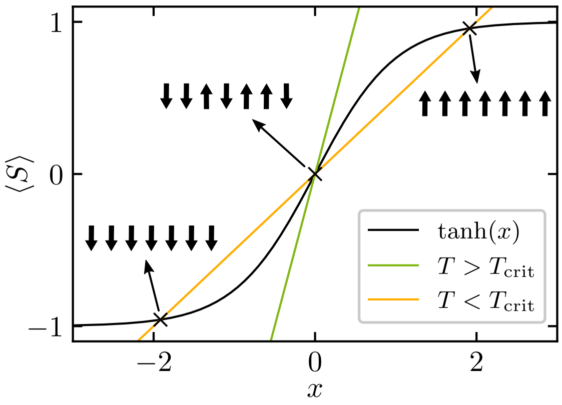

Figure 3.2: Graphical solution of the self-consistency problem described by Eq. (3.5) for two different temperatures. The left-hand side and the right-hand side of the equation are plotted versus $x := zJ\beta\langle S\rangle$. The black crosses indicate the intersections, which correspond to solutions of Eq. (3.5). For $T < T_\mathrm{crit}$, the ordered phase corresponds to a minimum of the free energy and is thus favored.

For a physically meaningful limit $z \to \infty$, the couplings need to be rescaled by $^1/_z$ so that the mean field remains finite[2]. Then, it can be shown that the neglect of two-particle correlations in Eq. (3.3) is, indeed, exact for $z \to \infty$ [Bro60].

3.3 Hartree-Fock mean-field theory for the Hubbard model

The Hartee-Fock theory is a static mean-field theory for itinerant particles. Applied to the fermionic Hubbard model, it is also known under the name Stoner model in the literature [Nol15]. We recap the one-band Hubbard Hamiltonian from Sec. 2.2,

$$\mathbf{H}_\mathrm{Hubb} = -t \sum_{\langle i,j\rangle,\sigma} \mathbf{c}^\dagger_{i\sigma}\mathbf{c}_{j\sigma} + U\sum_i \mathbf{n}_{i\uparrow}\mathbf{n}_{i\downarrow}. \tag{3.6}$$

Similar to Eq. (3.3), the interaction term can be approximated neglecting the two-particle correlations according to

$$\mathbf{n}_{i\uparrow}\mathbf{n}_{i\downarrow} \approx \mathbf{n}_{i\uparrow}\langle\mathbf{n}_{i\downarrow}\rangle + \mathbf{n}_{i\downarrow}\langle\mathbf{n}_{i\uparrow}\rangle - \langle\mathbf{n}_{i\uparrow}\rangle\langle\mathbf{n}_{i\downarrow}\rangle, \tag{3.7}$$

which results in the effective Hamiltonian

$$\mathbf{H}^\mathrm{mf}_\mathrm{Hubb} - E_0 = \sum_{\langle i,j\rangle,\sigma}\left[t + \delta_{ij}U\langle\mathbf{n}_{\overline{\sigma}}\rangle\right]\mathbf{c}^\dagger_{i\sigma}\mathbf{c}_{j\sigma} = \sum_{\vec{k},\sigma}\left[\epsilon(\vec{k}) + U\langle\mathbf{n}_{\overline{\sigma}}\rangle\right]\mathbf{c}^\dagger_{\vec{k}\sigma}\mathbf{c}_{\vec{k}\sigma}, \tag{3.8}$$

where $\overline{\sigma}$ denotes the opposite spin direction of σ, $\epsilon(\vec{k})$ is the one-particle energy and E_0 is a constant energy. The average occupation number can be determined self-consistently by

$$\langle\mathbf{n}_{\overline{\sigma}}\rangle = \frac{1}{N}\sum_{\vec{k}}\left(1 + \mathrm{e}^{\beta(\epsilon(\vec{k})+U\langle\mathbf{n}_\sigma\rangle)}\right)^{-1}. \tag{3.9}$$

This equation implies a ferromagnetic state below a critical temperature, if the Stoner criterion $1 \leq U\rho(\epsilon_\mathrm{F})$ is met. The Stoner model captures itinerant ferromagnetism and

---

[2] The rescaling factor should be chosen in dependence on the phase of interest. If the focus lies on the paramagnetic phase, the couplings should be scaled as $1/\sqrt{z}$ to obtain a non-trivial limit $z \to \infty$ [Geo+96].

the Stoner criterion captures the trend for some metals [Nol15]. However, the derived effective model in Eq. (3.8) can be only valid if U is small. As discussed already in Sec. 2.2, one expects a metal-insulator transition for increasing U in case of half filling. This is clearly not captured by the one-particle model in Eq. (3.8). In fact, even the limit $z \to \infty$ does not make the approximation in Eq. (3.7) exact because in the Hubbard model each electron has at maximum a single interaction partner per site, independent of the coordination number. The situation changes, if one alters the model so that U couples instead the electrons of neighboring sites to one another. Then, the Hartee-Fock mean-field theory is indeed exact for $z \to \infty$, analogous to the Weiss mean-field theory for localized spins [Mül89]. It is noteworthy that the Hartree-Fock theory and extensions of it are still applied in quantum chemistry nowadays [HJO00; EA07].

Itinerant-fermion models contain a non-trivial one-particle dynamics which fundamentally separates them from spin models. For instance, there is no direct analogue to the Weiss mean field B^{mf} from Eq. (3.4) in the Stoner model. The fact that the mean-field approach is static can be read off the self-energy[3] $\Sigma_\sigma = U\langle \mathbf{n}_{\overline{\sigma}} \rangle$, which does not depend on the frequency. This is different in the DMFT, which will be discussed in the next section.

3.4 Dynamic mean-field theory for strongly correlated fermion systems using the example of the Hubbard model

The transition from static mean fields to dynamic mean fields complicates the mean-field framework considerably. But it is necessary for an adequate description of systems, in which the two-particle correlations are not negligible as assumed in Hartee-Fock theory. Such *strongly correlated* electron systems are characterized by a competition between the hopping and the mutual interaction of the electrons. In the Hubbard model, this means that neither t nor U are dominating. In this case, an effective one-particle picture is not valid anymore so that even the otherwise very successful density-functional theory (DFT) is not adequate[4]. Here, the DMFT can help out. Below, we briefly summarize its main ingredients.

The first ingredient is again the limit $z \to \infty$ or, equivalently, $D \to \infty$. In 1989, Metzner and Vollhardt showed that, if the hopping amplitude is scaled as $t/\sqrt{D}$, the Hubbard model maintains a competition between hopping and interaction in the limit $D \to \infty$ [MV89]. At the same time, the computation of ground-state properties greatly simplifies because the self-energy becomes site-local,

$$\Sigma_{i\sigma|j\sigma}(\omega) = \delta_{ij}\Sigma_\sigma(\omega) \tag{3.10}$$

or, equivalently, momentum-independent.

---

[3] The self-energy summarizes the effect of the interaction. In the Stoner model, it corresponds to a constant shift of the one-particle energies, see Eq. (3.8).

[4] DFT is widely used in physics and chemistry and its foundation by Walter Kohn has been awarded with the Nobel prize in 1998 [Koh99]. The basic idea of DFT is to minimize an energy functional of the electron density. The interaction energy in this functional consists of the classical interaction term (Hartree) as well as an “exchange and correlation” term, which has to be guessed.

The second ingredient is the mapping of the Hubbard model on a lattice to a single-impurity Anderson model (SIAM) [And61]: Instead of the intractable lattice model, one considers an effective model which captures a single site, the impurity, that couples to a bath representing the remainder of the lattice. This is schematically displayed in Fig. 3.3 and formally described by the Hamiltonian

$$\mathbf{H}_{\mathrm{SIAM}} = U\mathbf{c}_{\uparrow}^{\dagger}\mathbf{c}_{\uparrow}\mathbf{c}_{\downarrow}^{\dagger}\mathbf{c}_{\downarrow} + \sum_{\nu\sigma} \varepsilon_{\nu}\, \mathbf{a}_{\nu\sigma}^{\dagger}\mathbf{a}_{\nu\sigma} + \sum_{\nu\sigma} V_{\nu} \left(\mathbf{a}_{\nu\sigma}^{\dagger}\mathbf{c}_{\sigma} + \mathbf{c}_{\sigma}^{\dagger}\mathbf{a}_{\nu\sigma}\right), \tag{3.11}$$

where $\mathbf{c}_{\sigma}$ and $\mathbf{c}_{\sigma}^{\dagger}$ are the fermionic ladder operators of the impurity and $\mathbf{a}_{\nu\sigma}$ and $\mathbf{a}_{\nu\sigma}^{\dagger}$ are the ladder operators of the bath with ν being the index of the bath orbitals. Note that ε_{ν} is distinguished from the one-particle energies $\epsilon(\vec{k})$ of the Hubbard model. The SIAM and the Hubbard model have the same *local* self-energy in the limit $D \to \infty$, if the parameters ε_{ν} and V_{ν} are chosen appropriately [GK92]. The condition for equivalence of the models is given by [Geo+96; KV04]

$$\mathcal{G}_{\sigma}(\omega)\,[\Delta] = \sum_{\vec{k}} \frac{1}{\omega - \Sigma_{\sigma}\big(\Delta(\omega)\big) - \epsilon\big(\vec{k}\big)}, \qquad \Delta(\omega) := \sum_{\nu} \frac{|V_{\nu}|^{2}}{\omega - \varepsilon_{\nu}}, \tag{3.12}$$

where $\mathcal{G}$ is the local one-particle Green's function. This formula clearly entails a self-consistency problem because it contains the self-energy Σ, which is known only *a posteriori*. It can be solved iteratively, if an impurity solver such as exact diagonalization (ED) [CK94], numerical renormalization group (NRG) [AS05; BCP08], quantum Monte-Carlo (QMC) [Gul+11] or dynamic density matrix renormalization group (DMRG) [Geb+03; KRU08] is provided.

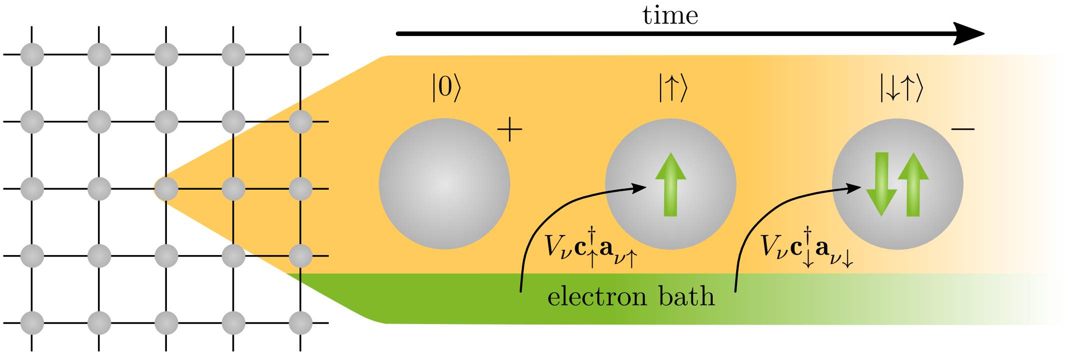

Figure 3.3: DMFT replaces the lattice of the Hubbard model by a single impurity atom embedded in a bath of electrons as described by the SIAM. By exchanging electrons with the bath, the central atom (gray) fluctuates among different configurations, shown here as snapshots in time. The allowed atomic states are $|0\rangle, |\downarrow\rangle, |\uparrow\rangle$ and $|\uparrow\downarrow\rangle$. The illustration shows an exemplary sequence of transitions between the atom and the surrounding electronic reservoir. The hybridization V_{ν} specifies how likely a transition occurs. *Figure inspired by* Ref. [KV04].

One of the great successes of DMFT is the qualitatively correct description of the Mott metal-insulator transition. While band theory only describes the metallic phase and atomic theory only describes the insulating phase, DMFT captures also the intermediate case. In realistic materials, orbitals with itinerant electrons coexist with orbitals with strongly correlated electrons. Therefore, DMFT is often combined with other approaches such as the local-density approximation (LDA[5]) [Pav+11] or Hartree method [Dat+23] in practice.

3.5 Dynamic mean-field theory for spins

As demonstrated in the above sections, it makes a considerable difference for the theoretical complexity and for the validity of the results, whether a mean-field approach is static or dynamic. Considering the step from Hartree-Fock to DMFT, the question arises if an analogous step can be made starting from the Weiss mean-field theory as sketched in Fig. 3.4.

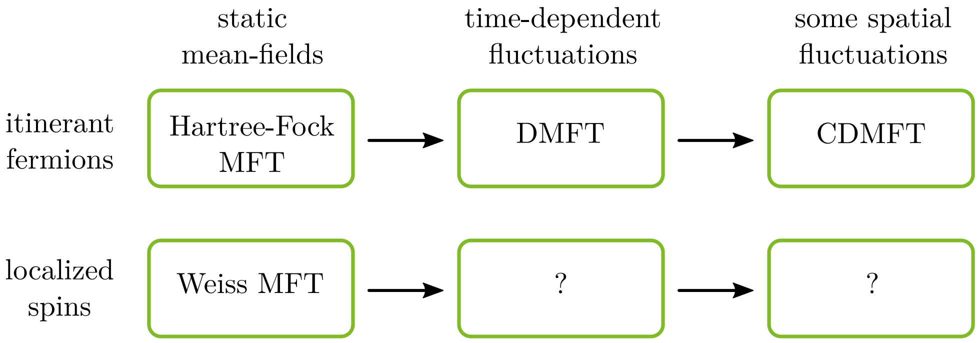

Figure 3.4: Stepping from a static to a dynamic mean-field theory and, subsequently, to a cluster dynamic mean-field theory. Similar to the fermionic case, a DMFT for localized spins and a corresponding cluster extension should exist.

Attempts and comparison to spinDMFT

We note that attempts for this have been made long ago. Related approaches have been considered in the context of the Sherrington-Kirkpatrick model (SKM) which is used to model spin glasses [SK75; EA75; Fis75; TAP77; Kle79]. In 1980, Bray and Moore considered an extension of the SKM (Heisenberg model with Gaussian-distributed couplings) and derived a self-consistency problem from a minimization principle using the replica method [BM80].

About twenty years later, this idea was taken up and reformulated slightly [GR98; GPS00]. The newer description essentially breaks down to the simulation of a spin in a Gaussian noise of which the moments are connected to the spin autocorrelations. As will be seen in the next chapter, this is very close to what is done in spinDMFT. However, one should note that the formerly considered spin-glass models are distinguished from bare spin models, since any expectation values are additionally averaged with respect to the distribution of the couplings (disordered models). The additional averaging is advantageous, because in the framework of the replica approximation it can be carried out before the quantum average which simplifies the problem. This trick cannot be used in conventional spin models, where the couplings are fixed. Still, the closeness of the

---

[5] LDA is a specific approximation of the exchange and correlation term in DFT.

resulting effective model to the one in spinDMFT is remarkable and should be kept in mind. Note that spinDMFT has not yet been extended to finite temperatures, but the approaches in Refs. [GR98; GPS00] give an idea of how this could be attempted.

As pointed out in the previous section, a key aspect of the fermionic DMFT is that the self-energy becomes local for $D \to \infty$. Similarly, a key aspect of spinDMFT is that the two-spin correlations become local, that is, pair correlations are suppressed versus autocorrelations for $D \to \infty$ at infinite temperature. The subdominant role of pair correlations has been recognized already in 1988 by Zobov [Zob88].

After the development of the fermionic DMFT, Kuramoto and Fukushima proposed a DMFT for spins (s-DMFT), which includes also finite temperatures and accesses distinct phases [KF98]. Their method is very general, but the mean-field description via bosons makes it rather cumbersome. A solution of the self-consistency appears to be computationally demanding without applying further approximations [OK13].

In view of the above approaches, the constraint of infinite temperature is certainly a disadvantage of spinDMFT. We emphasize, however, that due to the smallness of dipolar couplings there are many experimental platforms, where infinite temperature is a valid assumption. Being tailored to this regime makes spinDMFT computationally cheap and, thus, open for extensions.

Cluster DMFT

Conventional mean-field theories result in an effective single-site model so that spatial fluctuations are neglected by construction. It is possible to recover these fluctuations to some extent, see for example the cellular DMFT which extends the fermionic DMFT to clusters [Kot+01]. As indicated in Fig. 3.4, this is also a natural extension of mean-field theories for spins [OK13; Jin+16] and explicitly carried out for spinDMFT in Ch. 5.

Bosonic DMFT

For the sake of completeness, we mention that there exist also DMFTs for bosonic systems, for example, B-DMFT [BV08; HT09; And+11]. A particular challenge of this approach is that the hopping amplitude has to be rescaled differently in the limit $D \to \infty$ depending on whether the system is in the Bose-Einstein condensate or not.

3.6 Mean-field-related methods

The main issue of dealing with a quantum many-body system is the exponential growth of the Hilbert space. To tackle this, a common strategy is to decouple the system at the quantum level. This can be, for example, a decoupling into cluster and environment, but also a decoupling into many distinct clusters. Besides spinDMFT and its extensions, there are many other examples for such kinds of approaches [Mai+05].

For example in 2005, Witzel, de Sousa and Das Sarma considered the spectral diffusion decay of an electron spin in a nuclear spin bath using a cluster-expansion (CE) method [WSD05; WD06]. The method involves a recursive strategy that separates the nuclear spin bath into different clusters that independently contribute to the spin-echo signal. Related to this approach are also the linked cluster-expansion (LCE) [SYS07; Rig14] and the cluster-correlation expansion (CCE) [YL08; YL09; WYD14; ZML20]. We note that these methods focus on approximately star-like topologies, while mean-field theories are justified for dense geometries, which is the opposite case. For the sake of completeness, we mention that exactly star-like topologies are also accessible by DMRG although the reachable maximum time is limited [Sch05; SRU13].

Closely related to spinDMFT and its extensions is the hybrid quantum-classical simulation by Starkov and Fine [SF18; SF20]. Their method is tailored for NMR and accesses the FID in dense spin lattices. In essence, the surrounding spins of a selected quantum cluster are replaced by classical ones. The simulation of classical spins is, of course, far less costly than the simulation of quantum spins. Calculations with up to 10^3 classical spins and quantum cluster sizes of 9 spins are still feasible [SF18]. The approach is extended to the method of coupled quantum clusters in Ref. [SF20]. In this extension, the whole system is separated into quantum clusters, which interact with one another through their expectation values.

Related to spinDMFT are also approaches based on semi-classical Lindblad master equations [DSR21]. However, the Lindblad formalism requires that system and bath dynamics take place on different time scales. In contrast to this, the key aspect of spinDMFT is that the dynamics of a spin (system) happens on the exact same time scale as the dynamics of the mean field (environment).

From a different perspective, also the truncated Wigner approximation (TWA) bears similarities to spinDMFT [Wig32; Pol10]. The TWA is based on the computation of classical trajectories in phase space drawing the initial conditions from the Wigner function, in which the quantum-mechanical uncertainty is built in. SpinDMFT and its extensions also consider the initially correct quantum state, but due to the self-consistency, some quantumness enters also into the dynamics[6]. But, the TWA is far less constrained, for example concerning the temperature. It is applied to bosonic [Yar+23] and fermionic systems [DSP17]. Extensions of the TWA such as the generalized discrete TWA (GDTWA) can also be powerful in describing spin dynamics [ZRS19]. However, a systematic improvement of the TWA beyond classical trajectories is challenging.

Finally, we also mention the possibility to access spin systems by brute-force methods such as the ED [FSW08] and the Chebyshev-expansion technique (CET) [Wei+06; AF11]. On the one hand, the reachable maximum times are very large, but on the other hand, the results are subject to finite-size errors, especially, in high-dimensional systems. We will come back to these methods, when benchmarking spinDMFT in Sec. 4.3.

---

[6] Note that this statement does not hold for the bare spinDMFT with $S = 1/2$, since the effective mean-field model maps to a fully classical one. This is discussed in Sec. 4.1.7.

4 Dynamic mean-field theory for dense spin systems at infinite temperature

This chapter is devoted to the derivation of spinDMFT followed by some benchmarking. In the previous chapter, we discussed several mean-field and related theories that are applicable to various physical systems. The scope of applications of spinDMFT is limited to spin systems that are (i) *dense* and (ii) prepared at *infinite temperature*. The first aspect is simply a rewording of the very general requirement that each particle must have a large number of interaction partners. The dimension d or the coordination number z serve as measures for this. In a manner analogous to the mean-field approaches presented in the previous chapter, we demonstrate that our approach becomes exact for $z \to \infty$. The second aspect entails considering the spins to be completely disordered, i.e., $\rho = \rho_0 \propto \mathbf{1}$. This assumption applies, for example, to generic NMR experiments.

First, we present the derivation of spinDMFT for a Heisenberg model with $S = 1/2$. In Sec. 4.2, we show the generic numerical results considering different spin models. Subsequently, we benchmark spinDMFT by comparing its results to the ones of several brute-force methods for a Heisenberg model in Sec. 4.3. Afterwards, we briefly discuss the application of the method to dipolar defect spins on a diamond surface in Sec. 4.3.1 and conclude the chapter in Sec. 4.4. Several contents of this chapter are based on Ref. [Grä+21].

4.1 Derivation of spinDMFT for the Heisenberg model

4.1.1 Preparation

We consider an ensemble of N localized spins with $S = 1/2$ and Heisenberg couplings. The spins are subject to a global magnetic field h and the system is considered completely disordered. The Hamiltonian is given by

$$\mathbf{H} = \frac{1}{2} \sum_{i,j} J_{ij} \vec{\mathbf{S}}_i \cdot \vec{\mathbf{S}}_j + h \sum_i \mathbf{S}_i^z, \tag{4.1}$$

with general couplings $J_{ij} = J_{ji}$ and $J_{ii} = 0$. The moments of the coupling constants are defined as

$$(\mathcal{J}_{m,i})^m := \sum_j (J_{ij})^m, \qquad m \in \mathbb{N}^+. \tag{4.2}$$

Of particular importance are the quadratic coupling constant, $J_{\mathrm{Q},i} := \mathcal{J}_{2,i}$, and the quartic coupling constant, $J_{\mathrm{T},i} := \mathcal{J}_{4,i}$. Their ratio defines the effective coordination number

$$z_{\mathrm{eff},i} = \left(\frac{J_{\mathrm{Q},i}}{J_{\mathrm{T},i}}\right)^4, \qquad z_{\mathrm{eff}} := \frac{1}{N}\sum_i z_{\mathrm{eff},i}. \tag{4.3}$$

It should be noted that by maintaining the index i, these definitions encompass lattices with polyatomic bases or inhomogeneous systems. For spins on a lattice with a one-atomic basis and nearest-neighbor (NN) couplings $J_{ij} = \delta_{\langle i,j\rangle} J$, one obtains $z_{\mathrm{eff},i} = z_{\mathrm{eff}} = z$, where z is the conventional coordination number. Consequently, $z_{\mathrm{eff},i}$ may be regarded as a generalization of z to long-range couplings. We consider $z_{\mathrm{eff},i}$ to be a measure of the density of a spin system, as illustrated in Fig. 4.1[1]. The coupling sums in Eq. (4.3) are sometimes defined with a sum over the different directions considering J^x_{ij}, J^y_{ij} and J^z_{ij} in the literature [EF15]. This affects $z_{\mathrm{eff},i}$ only, if the couplings are anisotropic and the anisotropy varies from one pair of spins to another, for example, as in the bare dipole-dipole model presented in Sec. 2.3.

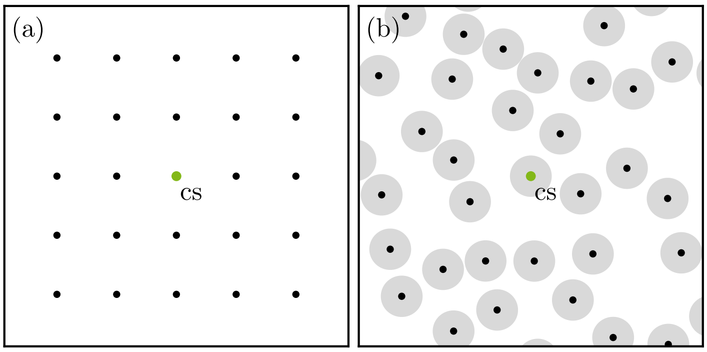

Figure 4.1: Cutout of a square lattice (a) and an inhomogeneous spin system (b) with dipolar couplings $J \propto R^{-3}$. The inhomogeneous system is generated by randomly drawing the spin positions, with a constraint for the minimum distance between two spins (gray circles cannot overlap). The effective coordination number of the central spin (cs) is $z_{\mathrm{eff,cs}} = z_{\mathrm{eff}} \approx 5.3$ for the square lattice and $z_{\mathrm{eff,cs}} \approx 3.5$ ($z_{\mathrm{eff}} \approx 3$) for the inhomogeneous system in this example. This indicates that the square lattice is denser than the inhomogeneous system. In contrast, the formal spin density, or the number of spins per area, is identical in both cases.

Next, we define the operators of the local spin environments (henceforth local-environment operators) of each spin,

$$\vec{\mathbf{V}}_i := \sum_j J_{ij} \vec{\mathbf{S}}_j. \tag{4.4}$$

With the help of the above definitions, we can rewrite the Hamiltonian according to

$$\mathbf{H} = \frac{1}{2}\sum_i \vec{\mathbf{S}}_i \cdot \vec{\mathbf{V}}_i + h \sum_i \mathbf{S}^z_i, \tag{4.5}$$

---

[1] Note that there are various ways to define an effective coordination number, see Ref. [Grä+21]. According to the subsequent derivation, Eq. (4.3) is the most reasonable definition.

where the prefactor of $1/2$ is required to avoid double counting.

We divide the derivation of spinDMFT into three steps:

(i) We identify the local spin environments and substitute them by classical dynamic mean fields. We demonstrate that back actions of a single spin are negligible, allowing the mean-field dynamics to be treated independently of the dynamics of the considered single spin. The mean fields are defined as stochastic time-dependent variables drawn from a random distribution. (Sec. 4.1.2)

(ii) We show that the random distribution is Gaussian. Furthermore, we explain how local expectation values are computed in the mean-field framework. (Sec. 4.1.3)

(iii) We link the defining moments of the normal distributions to spin expectation values, which, in turn, leads to a closed self-consisteny problem. (Sec. 4.1.4)

At several points in the derivation, statements about the scaling of spin correlations are required. These statements are derived in Ref. [Grä+21] (App. A) using the example of a Bethe lattice with NN interactions. We do not repeat this analysis here, but we provide a summary of the findings in Tab. 4.1.

Table 4.1: Scaling of correlations on a Bethe lattice of disordered spins with $S = 1/2$ and NN interactions [Grä+21]. In this scenario, $z = z_{\mathrm{eff},i}$ for all sites i. The local-environment operators $\vec{\mathbf{V}}_i$ have been rescaled by a factor of $1/\sqrt{z}$ for the entirety of this analysis. The expression $\lambda(i,j)$ represents the taxicab distance between site i and j. It is reasonable to posit that these scalings are also valid for other lattices and larger spins.

correlation		scaling
$\langle \mathbf{S}_i^\alpha(t_1)\mathbf{S}_i^\beta(t_2)\rangle$		1
$\langle \mathbf{S}_i^\alpha(t_1)\mathbf{S}_j^\beta(t_2)\rangle$,	$i \neq j$	$z^{-\lambda(i,j)}$
$\langle \mathbf{V}_i^\alpha(t_1)\mathbf{V}_i^\beta(t_2)\rangle$		1
$\langle \mathbf{V}_i^\alpha(t_1)\mathbf{V}_j^\beta(t_2)\rangle$,	$\lambda(i,j) = 1$	z^{-1}
$\langle \mathbf{V}_i^\alpha(t_1)\mathbf{V}_j^\beta(t_2)\rangle$,	$\lambda(i,j) > 1$	$z^{-\lambda(i,j)+1}$
$\langle \mathbf{S}_i^\alpha(t_1)\mathbf{V}_i^\beta(t_2)\rangle$		$z^{-1/2}$
$\langle \mathbf{S}_i^\alpha(t_1)\mathbf{V}_j^\beta(t_2)\rangle$,	$i \neq j$	$z^{-\lambda(i,j)+1/2}$

A remark on the rescaling of the local-environment operators in this consideration is in order. As previously mentioned in Ch. 3, the Hamiltonian usually needs to be rescaled before performing the limit $z \to \infty$ or $z_{\mathrm{eff},i} \to \infty$. In the disordered regime, a physically meaningful limit necessitates finite values for $J_{\mathrm{Q},i}$, which represents the energy scale of the system[2]. This is ensured by the rescaling [Geo+96]

$$\mathbf{H} \longrightarrow \frac{1}{\sqrt{z_{\mathrm{eff}}}}\mathbf{H}, \tag{4.6}$$

---

[2] Conventionally, the rescaling is chosen such that free energy per site remains finite [Pav+11]. However, this approach is not successful here because the free energy is independent of the Hamiltonian at $T = \infty$.

which can be directly transferred to the local-environment operators contained in **H**. Note that for inhomogeneous systems or systems with polyatomic basis, we require that $z_{\text{eff},i} \propto z_{\text{eff}}$ for all sites i. If this is not the case, it is necessary to distinguish between different types of spins in the mean-field framework. In the following section, we present the first step of the derivation.

4.1.2 Step (i): Mean-field substitution and single-site problem

In the initial step of spinDMFT, the local-environment operators are replaced by classical fields similar to what is done in Weiss mean-field theory, see Sec. 3.2. This substitution is justified, if each $\vec{\mathbf{V}}_i$ contains a multitude of contributions of comparable strength. Analogous to the consideration in Ref. [SRU13] for the central spin model (CSM), this can be substantiated further by means of the Frobenius norm of an operator,

$$\|\mathbf{A}\|^2 := \frac{1}{d} \operatorname{Tr}\left(\mathbf{A}^\dagger \mathbf{A}\right) = \langle \mathbf{A}^\dagger \mathbf{A} \rangle, \tag{4.7}$$

which is equivalent to the $T = \infty$ autocorrelation of **A**. We compute the Frobenius norms of a spin component and a component of the local-environment operator for arbitrary spin S. For comparability, we consider the rescaled operator

$$\tilde{\mathbf{V}}_i^\alpha = \frac{1}{J_{\mathrm{Q},i}} \mathbf{V}_i^\alpha. \tag{4.8}$$

Using this definition, the norms of the components yield the same result,

$$\|\mathbf{S}_i^\alpha\|^2 = \|\tilde{\mathbf{V}}_i^\alpha\|^2 = \frac{S(S+1)}{3}. \tag{4.9}$$

For a classical angular momentum, any commutator vanishes. Therefore, it is reasonable to examine the commutator norms,

$$\|\left[\mathbf{S}_i^\alpha, \mathbf{S}_i^\beta\right]\|^2 = (1-\delta^{\alpha\beta}) \frac{S(S+1)}{3}, \tag{4.10a}$$

$$\|\left[\tilde{\mathbf{V}}_i^\alpha, \tilde{\mathbf{V}}_i^\beta\right]\|^2 = (1-\delta^{\alpha\beta}) \frac{S(S+1)}{3} \frac{1}{z_{\text{eff},i}}, \tag{4.10b}$$

in order to identify classical behavior. In contrast to the component norms, the spin and local-environment operator behave differently in this respect. The additional factor $1/z_{\text{eff},i}$ clearly vanishes in the limit $z_{\text{eff},i} \to \infty$ making $\vec{\mathbf{V}}_i$ a classical field. This is undoubtedly a compelling argument, but statements about the magnitude of the error of a classical substitution can only be made on the basis of explicit benchmarks.

The phenomenon of the commutator norm being suppressed is related to the correspondence principle in quantum mechanics. Quantities containing a large number of constituents exhibit classical behavior. However, this does not imply that these quantities necessarily have to be static, as is assumed for the mean fields in standard Weiss mean-field theory. Therefore, in spinDMFT, we consider *time-dependent*, classical mean fields, denoted by $\vec{V}_i(t)$.

Prior to establishing the dynamics, it is essential to discuss the impact of *back actions* of a spin on its local environment. If these are substantial, the dynamics of $\vec{V}_i(t)$ are dependent of the dynamics of $\vec{\mathbf{S}}_i$, which would significantly complicate the mean-field framework. However, we recall that spinDMFT has been developed for dense spin systems, where each spin has many interaction partners. In this case, a single spin is not important for the dynamics of its surrounding spins and can, in principle, be left out. This is a standard mean-field argument and also discussed, for example, in the cavity method [Geo+96]. Nevertheless, a rigorous mathematical formulation of this argument is challenging. We provide a rigorous argument based on the observation that correlations between $\mathbf{S}_i^\beta$ and $\mathbf{V}_i^\alpha$ over time are suppressed by $1/z$, as detailed in Tab. 4.1. This implies that a spin is completely uncorrelated with its local environment for infinite coordination number. Consequently, we conclude that in a dense spin system, *back actions* are negligible and the mean-field dynamics can be treated independently of the particular dynamics of a single spin. We emphasize that if the system is inhomogeneous, the effective coordination number $z_{\text{eff},i}$ needs to be large for all sites i. A counterexample to this is the CSM, where $z_{\text{eff},i}$ is large for the central spin, but equal to 1 for the bath spins. The omission of back actions of the central spin inevitably results in a completely frozen bath. This assumption is only valid for very short times [MER02; SRU13; SRU14; Sta14].

Based on the above arguments, we replace each local-environment field in the Hamiltonian in Eq. (4.5) by an *a priori* given mean field $\vec{V}_i(t)$, which leads to

$$\mathbf{H}^{\text{mf}}\left[\vec{V}_1(t),\ldots,\vec{V}_N(t)\right] = \sum_i \mathbf{H}_i^{\text{mf}}\left[\vec{V}_i(t)\right], \tag{4.11a}$$

$$\mathbf{H}_i^{\text{mf}}\left[\vec{V}_i(t)\right] = \vec{V}_i(t)\cdot\vec{\mathbf{S}}_i + h\mathbf{S}_i^z. \tag{4.11b}$$

Note that the factor $1/2$ has been removed, since each spin-spin coupling contributes to the mean field of both involved spins. The values $\vec{V}_i(t)$ cannot be deterministic, as this would automatically break time translation invariance[3], which is not physical. Therefore, we treat $\vec{V}_i(t)$ as a random variable and perform a stochastic average in all physical expectation values. In this way, time translation invariance can be ensured, while allowing for fluctuations of the mean fields.

We use the shorthand $\vec{\mathcal{V}}_i(t_2,t_1)$ to denote a single time series of the mean field at site i from time t_1 to t_2. The series $\vec{\mathcal{V}}_i(t_2,t_1)$ contains a specific value of $\vec{V}_i$ at all possible times in the interval $t\in(t_1,t_2)$. For the sake of brevity, we use $\vec{\mathcal{V}}_i \coloneqq \vec{\mathcal{V}}_i(\infty,-\infty)$ henceforth. Clearly, there is an infinite number of single time series, which have to be taken into account. In a stochastic average, they are weighted by a probability functional $p[\vec{\mathcal{V}}_1,\ldots,\vec{\mathcal{V}}_N]$, which is yet unknown. We will later compute the moments of this functional by linking them to expectation values of the local-environment operators. In principle, the functional could be constructed from its moments, but without any specification, the number of non-trivial moments required for this is infinite. However, as will be demonstrated in the next section, the functional is Gaussian, which means that only the first two moments need to be known.

It is important to note that the mean-field Hamiltonian given by Eq. (4.11) is decoupled with respect to the sites. The original, 2^N-dimensional lattice problem has been mapped

---

[3] Except for the trivial case, where the mean fields are static, but this scenario is ruled out here.

to N two-dimensional single-site problems. Each of them describes a single spin evolving under its own mean-field and the external field. In the next section, we will explain how local averages can be computed in this framework.

4.1.3 Step (ii): Probability functional

The central argument in this step is that two spins at sites i and j are only weakly correlated. This assertion is particularly compelling for a dense spin system, in line with the observation that the back actions of a single spin are negligible. To substantiate this claim, we consider the Bethe lattice with NN interactions again, see Tab. 4.1. For this system, it can be shown that the pair correlation $\langle \mathbf{S}_i^\alpha(t)\mathbf{S}_j^\beta(0)\rangle$ scales like $z^{-\lambda(i,j)}$, where $\lambda(i,j)$ is the number of NN links needed to go from site i to j. This entails that in the limit $z \to \infty$ two distinct spins are not correlated to each other, even if they are neighbors in the lattice. In light of this observation and the definition of the local-environment operators in Eq. (4.4), we conclude that each mean field consists of a large number of essentially independent contributions. Consequently, we can utilize the central limit theorem and deduce that their probability functional is Gaussian[4]. Having identified the mean-field distribution, we can now set up a strategy for computing averages.

We restrict ourselves to averages of operators $\mathbf{O}_i$ that are local at a single site i. In the framework of spinDMFT, the computation of any physical average requires two separate averaging procedures. First, one computes the expectation value of the local quantum degrees of freedom assuming a disordered state $\rho_{0,i} \coloneqq \mathbf{1}_i/d_{\text{loc}}$, where $d_{\text{loc}} = 2S+1$ is the Hilbert space dimension. This entails tracing over the local Hilbert space according to

$$O_i \coloneqq \langle \mathbf{O}_i \rangle_{\rho_{0,i}} = \frac{\mathrm{Tr}_{(i)}\left(\mathbf{O}_i\right)}{d_{\text{loc}}}. \tag{4.12}$$

The operator $\mathbf{O}_i$ may contain time propagators which are computed from the local mean-field Hamiltonian in Eq. (4.11b) employing the Schrödinger equation

$$\frac{\mathrm{d}}{\mathrm{d}t}\mathbf{U}_i\Big[\vec{\mathcal{V}}_i(t,t_0)\Big] = -\mathrm{i}\mathbf{H}_i^{\text{mf}}\left[\vec{\mathcal{V}}_i(t)\right]\mathbf{U}_i\Big[\vec{\mathcal{V}}_i(t,t_0)\Big]. \tag{4.13}$$

In this notation, $\mathbf{U}_i[\vec{\mathcal{V}}_i(t,t_0)]$ describes the time propagator that propagates from t_0 to t. In the following, we will consider the quantity $\mathbf{O}_i$ to contain a single time evolution, so that $O_i = O_i[\vec{\mathcal{V}}_i(t,t_0)]$.

In order to obtain a physical result, the quantum average must be followed by an average with respect to the mean fields. This is achieved by integrating over the probability space spanned by *all* mean fields at *all* times according to

$$\overline{O_i}^{\text{mf}} = \left(\prod_{k=1}^{N}\int \mathrm{D}\vec{\mathcal{V}}_k\right) p\left[\vec{\mathcal{V}}_1,\ldots,\vec{\mathcal{V}}_N\right] O_i\Big[\vec{\mathcal{V}}_i(t,t_0)\Big], \tag{4.14}$$

---

[4] We note that this is not strictly rigorous, since two spins being uncorrelated does not necessarily imply that they are independent. Moreover, since there is no defining equation for $V_i(t)$, it is not clear how the central limit theorem is applied precisely. A rigorous mathematical proof of this may be conducted in the future, for example, by considering a Bethe lattice.

where mf stands for **m**ean-**f**ield average. For a Gaussian probability functional, any degrees of freedom that are not contained in O_i can be integrated out easily, which leads to

$$\overline{O_i}^{\mathrm{mf}} = \int \mathrm{D}\vec{\mathcal{V}}_i(t,t_0)\, p_{\mathrm{mar}}\Big[\vec{\mathcal{V}}_i(t,t_0)\Big]\, O_i\Big[\vec{\mathcal{V}}_i(t,t_0)\Big]\,. \tag{4.15}$$

The marginal distribution p_{mar} is also Gaussian and contains only the first and second moments of the local mean field at site i from time t_0 to t. No moments of other times or other mean fields are mixed into it. For the sake of completeness, we mention that the correlations $\langle \mathbf{V}_i^\alpha(t_1)\mathbf{V}_j^\beta(t_2)\rangle$ for $i \neq j$ are suppressed by at least $1/z$ relative to $\langle \mathbf{V}_i^\alpha(t_1)\mathbf{V}_i^\beta(t_2)\rangle$ on a Bethe lattice, see Tab. 4.1. Thus, the Gaussian probability functional is separable with respect to the sites for $z \to \infty$. It turns out that this property is not required to make the mean-field average local.

If the first two mean-field moments are known, local averages can be computed by means of Eqs. (4.12) and (4.15). The time-dependent spin expectation values vanish,

$$\langle \vec{\mathbf{S}}_i(t)\rangle^{\mathrm{mf}} = 0, \tag{4.16}$$

which is the exact result at infinite temperature. The spin autocorrelations can be computed from

$$\begin{aligned}\langle \mathbf{S}_i^\alpha(t_1)\mathbf{S}_i^\beta(t_2)\rangle^{\mathrm{mf}} &= \int \mathrm{D}\mathcal{X}\, \frac{p_{\mathrm{mar}}[\mathcal{X}]}{d_{\mathrm{loc}}}\, \mathrm{Tr}_{(i)}\Big(\mathbf{U}_i^\dagger[\mathcal{X}]\,\mathbf{S}_i^\alpha \mathbf{U}_i[\mathcal{X}]\,\mathbf{S}_i^\beta\Big)\,,\\ \mathcal{X} &:= \vec{\mathcal{V}}_i(t_1,t_2),\end{aligned} \tag{4.17}$$

for $t_1 > t_2$. We recall that a single time series of the mean field breaks time translation invariance. This implies that the trace in the integral explicitly depends on t_1 and t_2 and not solely on the difference $t_1 - t_2$. However, if the first and second moments in p_{mar} are time translation invariant, then so is the entire integral which ultimately yields physical results. Furthermore it should be noted that numerical calculations of the path integral are done for discretized times. In the next section, we present the remaining ingredient of spinDMFT, i.e., the procedure to determine the moments of p_{mar}.

4.1.4 Step (iii): Self-consistency

The marginal distribution $p_{\mathrm{mar}}[\mathcal{X}]$ describes the probability for each single time series of the mean field $\vec{V}_i$. As previously demonstrated, p_{mar} is Gaussian so that only the first two moments are required to fully determine it. The idea is to link these moments to expectation values of the local-environment field $\vec{\mathbf{V}}_i$, from which the mean field $\vec{V}_i$ originated. Due to the considered infinite temperature, the first moments yield zero,

$$\overline{V_i^\alpha(t)}^{\mathrm{mf}} = \langle \mathbf{V}_i^\alpha(t)\rangle = 0. \tag{4.18}$$

This condition can be easily fulfilled. For the second moment, we obtain

$$\overline{V_i^\alpha(t_1)V_i^\beta(t_2)}^{\text{mf}} = \langle \mathbf{V}_i^\alpha(t_1)\mathbf{V}_i^\beta(t_2)\rangle = \sum_{j,k} J_{ij}J_{ik}\langle \mathbf{S}_j^\alpha(t_1)\mathbf{S}_k^\beta(t_2)\rangle \tag{4.19a}$$

$$\approx \sum_j J_{ij}^2 \langle \mathbf{S}_j^\alpha(t_1)\mathbf{S}_j^\beta(t_2)\rangle \tag{4.19b}$$

$$\approx \sum_j J_{ij}^2 \langle \mathbf{S}_j^\alpha(t_1)\mathbf{S}_j^\beta(t_2)\rangle^{\text{mf}}. \tag{4.19c}$$

In Eq. (4.19b), we neglect pair correlations, since they are suppressed by the coordination number in accordance with Tab. 4.1 [Zob88]. Note that this step requires not only that z is large, but also that the number of shared neighbors of two spins is small, see App. B for details. To obtain Eq. (4.19c), we replaced the exact autocorrelations with autocorrelations in mean-field approximation which ultimately closes the self-consistency loop: The spin autocorrelations are given by Eq. (4.17), which contains the distribution p_{mar} and hence the mean-field moments. In turn, the computation of the moments requires the knowledge of the spin autocorrelations according to Eq. (4.19). This situation can be solved numerically by an iteration procedure. This terminates the derivation of spinDMFT. We discuss some properties of the formalism in the following sections.

4.1.5 Homogeneity in space

Once a mean field at a specific site is known, any local averages at this site can be computed independently of the other sites according to Eq. (4.15). A single evaluation of the path integral is computationally cheap. Note, however, that the derived self-consistency condition links the dynamics of different sites with each other. Consequently, for a general solution, N single-site problems have to be solved in parallel which is computationally challenging for large N. In the case of translational invariance in space, this issue is straightforwardly solved by setting the mean-field moments and spin correlations at different sites equal. Then, only one single-site problem remains and the self-consistency reduces to

$$\overline{V^\alpha(t_1)V^\beta(t_2)}^{\text{mf}} = J_{\text{Q}}^2 \langle \mathbf{S}^\alpha(t_1)\mathbf{S}^\beta(t_2)\rangle^{\text{mf}}, \tag{4.20}$$

where we omitted the site indices, since they are redundant. The time evolution is generated by the mean-field Hamiltonian

$$\mathbf{H}\left[\vec{V}(t)\right] = \vec{V}(t)\cdot\vec{\mathbf{S}} + h\mathbf{S}^z. \tag{4.21}$$

Thus, the original lattice model has been finally reduced to a single-site model, see Fig. 4.2 for an illustration. It should be noted that this reduced model can also be a valid description if the spins do not sit on a regular lattice. In order for the self-consistency to be reduced to a single site, the standard deviation of the quadratic coupling constant needs to be small, that is,

$$\sqrt{\frac{1}{N}\sum_i \left(J_{\text{Q},i} - J_{\text{Q}}\right)^2} \ll J_{\text{Q}}. \tag{4.22}$$

This can also be valid in an inhomogeneous system, for example, if a strong repulsion ensures a minimum distance between any pair of spins, see panel (b) in Fig. 4.1. If Eq. (4.22) is not fulfilled, spatial dependencies are important and different sites need to be distinguished. In this case, the coordination number may be too small for the entire approximation to be valid. This issue will be discussed in Sec. 4.3.1.

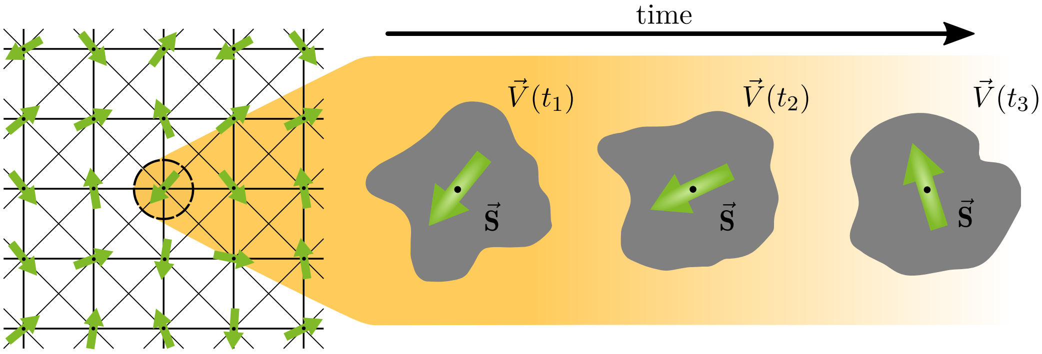

Figure 4.2: In approximately homogeneous systems, spinDMFT reduces the full lattice model to a single-site model with explicit time dependence. The single-site model describes the evolution of a single spin $\vec{\mathbf{S}}$ under a dynamic Gaussian mean field $\vec{V}(t)$, which represents the effect of the remainder of the lattice.

In the context of this thesis, we consider only the spatially homogeneous self-consistency condition in Eq. (4.20) for spinDMFT. This implies that the only energy constant governing the spin dynamics is the quadratic coupling constant J_Q. It encompasses the whole information about the geometry of the system.

4.1.6 Homogeneity in time

If the moments entering the distribution p_mar in Eq. (4.17) fulfill time translation invariance, then so do the resulting autocorrelations. It is evident that the self-consistency condition preserves this property so that solutions homogeneous in time exist. It is probable that these are the only conceivable solutions, but this thesis does not investigate, whether exceptions can occur. We stress that in the numerical evaluation, time translation invariance should be enforced as it reduces the computational effort. This entails that, effectively, any correlation function depends only on a single time, $t := t_1 - t_2$, according to

$$\langle \mathbf{S}^\alpha(t_1)\mathbf{S}^\beta(t_2)\rangle = \langle \mathbf{S}^\alpha(t_1 - t_2)\mathbf{S}^\beta(0)\rangle = \langle \mathbf{S}^\alpha(t)\mathbf{S}^\beta(0)\rangle. \tag{4.23}$$

It should be noted that the formalism can be extended to systems where time translation invariance is explicitly broken. In fact, the presented derivation is identical if we replace $h \to h(t)$. An application of this is presented in the context of NMR in Ch. 6.

4.1.7 Classical spins

Another noteworthy observation is that the derived mean-field model would be identical if we initially considered classical spins of the same average length. This is due to the fact that the mean-field Hamiltonian defined in Eq. (4.11b) contains the spin operator in a linear fashion as does the equation of motion

$$\frac{\mathrm{d}}{\mathrm{d}t}\vec{\mathbf{S}}(t) = \vec{V}(t) \times \vec{\mathbf{S}}(t). \tag{4.24}$$

Employing the Ehrenfest theorem, we can deduce that the classical spin vector, $\vec{S}(t) := \langle \vec{\mathbf{S}}(t) \rangle$, has the exact same equation of motion. Since the mean field is already classical, the derived mean-field model maps to a fully classical one. This entails that the classical and quantum mechanical spin system converge to the same spinDMFT for infinite coordination number. We emphasize, however, that this is not always the case. For spins with $S > 1/2$, non-linear local terms can arise in the Hamiltonian, for example from quadrupolar interactions [Lev01; Gla18]. In this scenario, the quantum spinDMFT is different from the classical one. It is worth noting that the semiclassical description has a clear advantage over a fully classical one. It is straightforward to incorporate quantum degrees of freedom into a model that still contains some quantumness. This is the key idea of CspinDMFT which will be presented in Ch. 5.

4.1.8 Larger spins

Related to the above observation is that according to spinDMFT, the spin length S is unimportant for the form of the autocorrelations in a dense spin system with bilinear spin-spin interactions (considering no external fields or quadrupolar terms). Changing S means changing the maximum value $S(S+1)/3$ of the autocorrelations. This value clearly affects the strength of the mean fields, but it can be completely hidden in the quadratic coupling constant according to

$$\tilde{J}_\mathrm{Q}^2 := J_\mathrm{Q}^2 \frac{S(S+1)}{3}. \tag{4.25}$$

The corresponding self-consistency condition reads

$$v^{\alpha\beta}(t) = \tilde{J}_\mathrm{Q}^2 \, G^{\alpha\beta}(t), \tag{4.26}$$

where $G^{\alpha\beta}$ is the normalized autocorrelation introduced in Eq. (2.7) and we assumed time translation invariance. If we measure the time in units of $\tilde{J}_\mathrm{Q}^{-1}$, the normalized autocorrelation looks exactly the same for any geometry and any spin length S. Note that this is the case only if the single-site Hamiltonian is linear in spin operators. In case of non-linear terms, e.g., $\mathbf{S}^\alpha \mathbf{S}^\alpha$, the time evolution of a spin operator depends on its length as elucidated in Sec. 4.1.7.

4.1.9 Summary of the self-consistency

To solve the self-consistency problem in Eq. (4.20), we additionally need the single-site mean-field Hamiltonian in Eq. (4.21) and the path integral for computing spin autocorrelations in Eq. (4.17). For a summary of the self-consistency, we restrict ourselves to models homogeneous in time and space. Analogous to the spin autocorrelations $g^{\alpha\beta}(t)$, we introduce the shorthands

$$v^{\alpha\beta}(t) := \overline{V^\alpha(t)V^\beta(0)}^{\mathrm{mf}}, \qquad \underline{\underline{v}}(t) := \begin{pmatrix} v^{xx} & v^{xy} & v^{xz} \\ v^{yx} & v^{yy} & v^{yz} \\ v^{zx} & v^{zy} & v^{zz} \end{pmatrix}(t). \tag{4.27}$$

The iterative procedure for solving the self-consistency is presented in Fig. 4.3. Any details of the considered spin model are encoded in the self-consistency condition through the matrix $\underline{\underline{P}}$, which simply reads $\underline{\underline{P}} = J_{\mathrm{Q}}^2\underline{\underline{1}}$ for the Heisenberg model. The procedure outlined in Fig. 4.3 is applicable to any spin model that contains only spin-spin interactions of the form $\mathbf{S}_i^\alpha\mathbf{S}_j^\beta$ with $i \neq j$ including the homogeneous Zeeman term. In the case of multi-linear or local bilinear terms, the formalism must be adapted. In the following section, we will provide a brief overview of the numerical details.

(1) Make a guess for the second moments $v^{\alpha\beta}(t)$.

(2) Compute the required autocorrelations from

$$g^{\alpha\beta}(t) = \int \mathrm{D}\mathcal{X}\, \frac{p_{\mathrm{mar}}[\mathcal{X}]}{d_{\mathrm{loc}}}\, \mathrm{Tr}\left(\mathbf{U}^\dagger[\mathcal{X}]\,\mathbf{S}^\alpha\mathbf{U}[\mathcal{X}]\,\mathbf{S}^\beta\right)$$

with $\mathcal{X} := \vec{\mathcal{V}}(t,0)$, $t > 0$ and p_{mar} being Gaussian with zero mean and second moments $v^{\alpha\beta}(t_1,t_2)$. The time propagators are generated from

$$\mathbf{H}\left[\vec{V}(t)\right] = \vec{V}(t)\cdot\vec{\mathbf{S}} + h\mathbf{S}^z.$$

(3) Determine the second mean-field moments from the self-consistency condition

$$\underline{\underline{v}}(t) = \underline{\underline{P}}\,\underline{\underline{g}}(t)$$

Go back to step (2) or …

(4) … stop, if the autocorrelations are sufficiently converged.

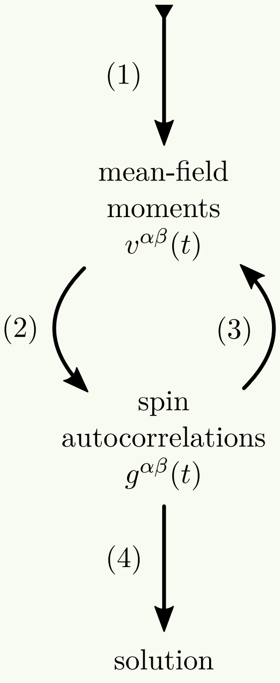

Figure 4.3: General iteration procedure to solve the self-consistency problem in case of a time translation invariant model.

4.1.10 Numerical implementation and error sources

The main ingredients of the numerical implementation are listed below.

- The time is discretized into equidistant time points.
- The path integral in step (2) of Fig. 4.3 is evaluated by Monte-Carlo simulation. For this purpose, the mean fields over time are drawn from the multivariate Gaussian

distribution p_{mar}. This involves constructing and diagonalizing the corresponding covariance matrix.

- For each mean-field sample, we compute the time-varying Hamiltonian and, based on this, the time evolution operator, which is required for the trace under the path integral in step (2). The usage of commutator-free exponential time propagators (CFET) can be helpful [AF11].
- A suitable convergence criterion for stopping the iteration considers if the absolute difference between the current autocorrelations and those of the previous iteration step is below a predefined threshold.

Further details are provided in App. C.1 and Ref. [Grä+21] (Section II., D.).

There are three distinct sources of numerical error in the above steps: the statistical error from the Monte-Carlo simulation, the error from the time discretization, and the iteration error from the self-consistency not being exactly converged. These errors are defined in App. C.1 and have been analyzed for different models in Ref. [Grä+21] (App. B). Since the computational cost of estimating these errors is small, they are tracked during each individual simulation. This allows one to provide the numerical results along with an absolute numerical error tolerance ϵ. For optimal efficiency, the numerical parameters such as the step width, δt, or the number of samples, M, should be chosen such that the various numerical errors are of the same order of magnitude. The choice of these parameters is also discussed in App. C.1.

Finally, we stress that time translation invariance and symmetries of the considered spin model should be always exploited in the implementation. This not only reduces the computational effort, but also enhances the numerical accuracy. With all these factors built in, the runtime for a spinDMFT simulation is remarkably low. The algorithm converges already after about 4 iteration steps requiring only a few minutes to finish on a single CPU.

4.2 Generic results of spinDMFT for $S = 1/2$

In this section, we explain how spinDMFT is applied to various models and present the results considering homogeneity in space and time. It is important to note that these results are universal for different geometries because only a single energy scale, namely, the quadratic coupling constant J_{Q}^2, occurs. The procedure is always the one from Fig. 4.3, but with an adapted self-consistency condition. For all plots shown in this and the next section, the absolute numerical error tolerance of the data from spinDMFT is $\epsilon = 10^{-3}$.

4.2.1 Heisenberg model

We begin by considering the Heisenberg model, for which the self-consistency condition is given in Eq. (4.20). For zero magnetic field, we find that the off-diagonal autocorrelations are zero while the diagonal ones are all equivalent. This is consistent with the symmetry relations for the Heisenberg model presented in Sec. 2.2. The diagonal autocorrelation, $G_0 := G^{xx} = G^{yy} = G^{zz}$, is plotted in Fig. 4.4 versus the time together with a Gaussian fit, which yields a standard deviation of $\sigma = 1.480(2)\, J_\mathrm{Q}^{-1}$. The fit describes the behavior at short times well. At $t \approx 3J_\mathrm{Q}^{-1}$, the actual decay weakens a bit relative to the fit, which is clearly visible in the log-vs-t^2 panel on the right-hand side.

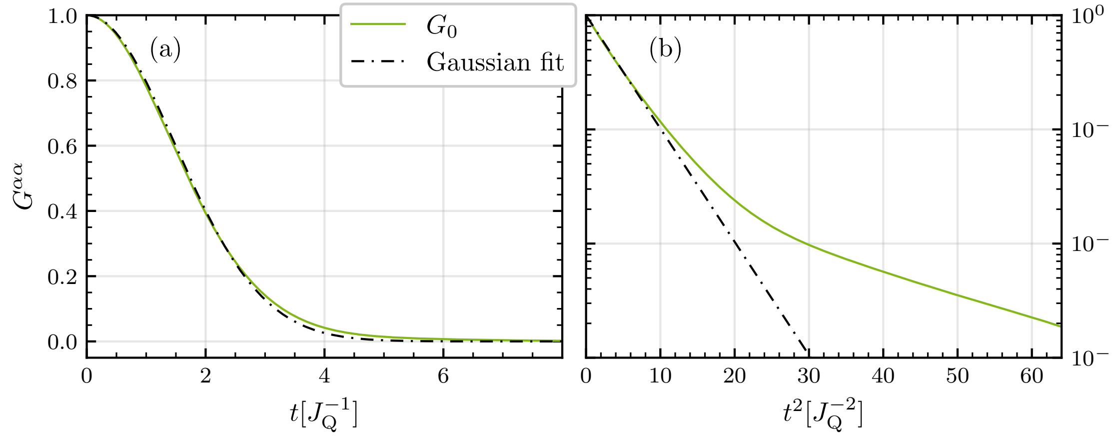

Figure 4.4: Universal diagonal autocorrelation of the Heisenberg model according to spinDMFT and Gaussian fit in linear (a) and log-vs-t^2 representation (b).

We refrain from presenting the results for finite external field h, as they are directly connected to the case without field. This is due to the fact that the field can be eliminated in the Larmor rotating frame resulting in identical outcomes as those in Fig. 4.4. Equation 2.27 describes the process of transitioning from the rotating frame back to the laboratory frame. Utilizing this, we obtain

$$\underline{\underline{G}}_\mathrm{rf}(t) = G_0(t)\underline{\underline{\Omega}}^\top(t), \qquad \underline{\underline{\Omega}}^\top(t) = \begin{pmatrix} \cos(ht) & -\sin(ht) & 0 \\ \sin(ht) & \cos(ht) & 0 \\ 0 & 0 & 1 \end{pmatrix}, \tag{4.28}$$

where $\underline{\underline{G}}_\mathrm{rf}$ denotes the autocorrelation tensor for finite external field and in the rotating frame and G_0 denotes the autocorrelation in the zero-field case, see Fig. 4.4. This behavior is precisely reproduced by spinDMFT.

4.2.2 Ising model

We proceed to examine the Ising model, which is described by

$$\mathbf{H}_\mathrm{Ising} = \frac{1}{2}\sum_{i,j} J_{ij}\mathbf{S}_i^z\mathbf{S}_j^z. \tag{4.29}$$

The dynamics induced by this Hamiltonian are entirely classical, but by using spin operators, we can apply our formalism in the exact same way as before. We obtain the very simple self-consistency condition

$$v^{zz}(t) = J_\mathrm{Q}^2\, g^{zz}(t) = \frac{J_\mathrm{Q}^2}{4}, \qquad J_\mathrm{Q}^2 = \sum_j J_{ij}^2, \tag{4.30}$$

while any other second mean-field moments are zero. The mean fields are entirely static because the z-component of each spin is conserved. This allows the mean-field integral in Eq. (4.17) to be solved analytically yielding

$$G^{xx}(t) = \exp\left(-\frac{1}{8}J_{\mathrm{Q}}^2 t^2\right). \tag{4.31}$$

This result is consistent with the transverse autocorrelation for the Ising model on complete graphs in the limit $N \to \infty$, see Ref. [DL91].

4.2.3 Dipolar spins with rotating-wave approximation

In the presence of a strong magnetic field, the dipolar interaction reduces to the secular Hamiltonian in Eq. (2.24) in the Larmor rotating frame. The effective model corresponds to the XXZ model with anisotropy $\lambda = -2$ as detailed in Sec. 2.2. The application of spinDMFT is straightforward. We redefine the local-environment fields according to

$$\vec{\mathbf{V}}_i := \sum_j d_{ij} \underline{\underline{D}}\, \vec{\mathbf{S}}_j, \qquad \underline{\underline{D}} := \begin{pmatrix} 1 & 0 & 0 \\ 0 & 1 & 0 \\ 0 & 0 & -2 \end{pmatrix}. \tag{4.32}$$

Then, we carry out the mean-field substitution ending up with the same single-site Hamiltonian as before, see Eq. (4.11b) (for $h = 0$). Any arguments that lead to the use of Gaussian mean fields are also valid for the XXZ model. Assuming homogeneity in space, we obtain

$$v^{\alpha\alpha}(t) = J_{\mathrm{Q}}^2 \left(D^{\alpha\alpha}\right)^2 g^{\alpha\alpha}(t), \qquad J_{\mathrm{Q}}^2 = \sum_j d_{ij}^2, \tag{4.33}$$

while any off-diagonal autocorrelations and moments vanish. The self-consistency condition implies two different autocorrelations, $G^{xx} = G^{yy}$ and G^{zz}, see Fig. 4.5.

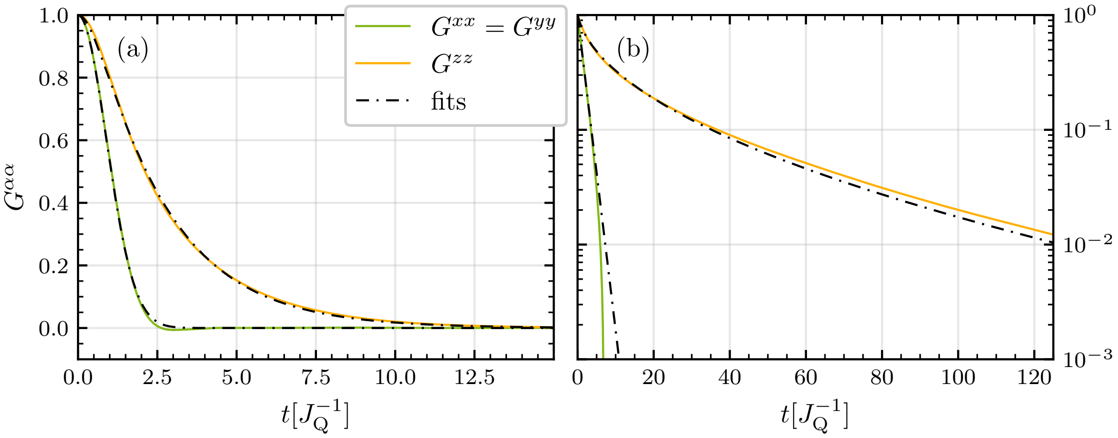

Figure 4.5: Universal diagonal autocorrelations for dipolar spins in a strong magnetic field according to spinDMFT and fits according to Eq. (4.34) in normal (a) and logarithmic representation (b).

These are well captured by the fit functions

$$F^{xx}(t) = \exp\left(-\frac{1}{2}\left[\frac{t}{\sigma}\right]^2\right), \qquad \sigma = 0.8891(3)\,J_{\mathrm{Q}}^{-1}, \tag{4.34a}$$

$$F^{zz}(t) = \exp\left(-\rho\left[\sqrt{t^2+\kappa^2}-|\kappa|\right]\right), \quad \rho = 0.4327(6)\,J_{\mathrm{Q}}, \quad \kappa = 0.647(3)\,J_{\mathrm{Q}}^{-1}. \tag{4.34b}$$

We emphasize the qualitative difference in the long-time behavior of F^{xx} and F^{zz}, Gaussian versus exponential. In the following section, we benchmark spinDMFT by comparing it to other approaches.

4.3 Benchmarks for the Heisenberg model

As with other mean-field theories, spinDMFT is most accurate when applied to high-dimensional systems. In such cases, purely classical spin simulations on finite-size systems can be successful. These simulations consider up to $10^3 - 10^4$ spins, so that errors from finite-size effects are unimportant [EF15]. However, a comparison between a classical simulation and spinDMFT would not be a useful benchmark, as both approaches are essentially classical. Our objective is to gain insight into the error resulting from neglecting quantum fluctuations. Therefore, we prefer a comparison with brute-force quantum algorithms, which are reliable for low-dimensional systems. This is the opposite case of where spinDMFT is justified, but it is the best option for a benchmark at hand. Before presenting the results, we will briefly list the employed methods.

The exact diagonalization method is well known: The Hamiltonian of a finite-size system is directly diagonalized to obtain the time evolution, see Ref. [Ble21] for details. The Chebyshev expansion technique expands the time-evolution operator in terms of Chebyshev polynomials. It also operates on a finite-size system, but it is more efficient than the ED in accessing larger system sizes. A brief description of the CET is provided in Ref. [Grä+21], while more details can be found in Refs. [Wei+06; Ble21]. The iterated equations of motion (iEoM) method iteratively approximates the time dependence of an operator in the Heisenberg picture [Grä+21; Ble21]. The approach operates on the infinite-size system, but the computational cost increases exponentially with the number of iterations which constrains the achievable accuracy for long times.

We begin by considering the Heisenberg model on a chain and a square lattice with NN interaction J captured by the Hamiltonian

$$\mathbf{H} = J\sum_{\langle i,j\rangle}\vec{\mathbf{S}}_i\cdot\vec{\mathbf{S}}_j. \tag{4.35}$$

Note that each NN coupling occurs exactly once in the summation. The quadratic coupling constant reads

$$J_{\mathrm{Q}}^2 = 2DJ^2, \tag{4.36}$$

where $D \in \{1,2\}$ is the system dimension. We display the autocorrelations from CET, iEoM, ED and spinDMFT in Fig. 4.6 versus the time in units of J_{Q}^{-1}.

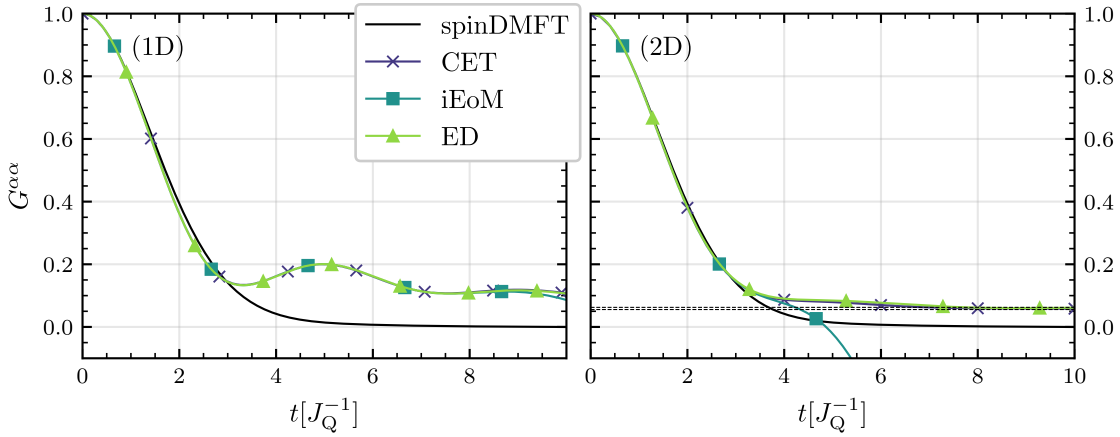

Figure 4.6: Autocorrelation results from different approaches for the Heisenberg model on a chain (1D) and on a square lattice (2D) with NN interactions, see Eq. (4.35). The CET results [Ble24] were computed considering $N = 18$ sites, periodic boundary conditions (PBC) and a relative error tolerance of $\epsilon = 10^{-3}$. The iEoM results [Her24] were produced by performing $m = 13$ (1D) and $m = 7$ (2D) iterations. The ED results were computed for $N = 16$ sites and PBC.

The CET and ED results were computed for distinct system sizes, $N = 18$ and $N = 16$. Since they agree excellently in 1D and 2D (ND = N dimensions), it may be assumed that finite-size effects are small for the considered scenarios. This is certainly a valid conclusion in 1D because, in this case, the CET and the ED results match also with the iEoM, which operates on the infinite-size system. In 2D, the iEoM diverges at $t \approx 3.5 J_\mathrm{Q}^{-1}$ due to the insufficient iteration order. The proximity of the CET and ED can be attributed to a slow convergence of these approaches with the system size, rather than finite-size effects being negligible. This statement is supported by Mazur's inequality, which provides a lower bound for the long-time average of the autocorrelation [Uhr+14]. Considering the conservation of a component of the total spin, it can be shown that

$$\lim_{T\to\infty} \frac{1}{T} \int_0^T \mathrm{d}t\, G^{\alpha\alpha}(t) \geq G_\mathrm{low} = \frac{1}{N}. \tag{4.37}$$

This bound value describes the equilibrium state, where the initial polarization of a single spin has spread over the whole system. As can be seen on the dashed line in Fig. 4.6 (2DD), the ED and CET results rapidly approach the corresponding limit, i.e., it is plausible that they are converged in time but not in N. Therefore, the non-existent decay after $t \approx 6 J_\mathrm{Q}^{-1}$ is likely a finite-size effect. We anticipate that the autocorrelations will diminish further if N is increased to ∞.

Finally, we also compare the findings to spinDMFT. The initial decay of the autocorrelation up to about $t \approx 3 J_\mathrm{Q}^{-1}$ matches well with the other approaches in 1D and 2D. However, after that time, the autocorrelation from spinDMFT displays a rapid decoherence, while the genuine results in 1D contain revivals and a rather slow decay. Clearly, the mean-field approximation is not justified for the spin chain, since the approach is based on a $1/z$-expansion and the chain corresponds to $z = 2$ only. In 2D, the discrepancy between spinDMFT and the other approaches is already much smaller, even after $t \approx 3 J_\mathrm{Q}^{-1}$. This tendency is expected since the coordination number is increased to $z = 4$. As previously stated, the ED and CET results likely encompass finite-size effects so that the remaining discrepancy should not be attributed solely to the mean-field approximation. In fact, only the result from spinDMFT describes complete decoherence until $G^{\alpha\alpha} = 0$, which is in principle expected in the infinite-size system according to thermalization. A more quantitative picture of how well spinDMFT captures this decay will be presented in Sec. 5.2, where we compare it to CspinDMFT.

As a second test, we consider the Heisenberg model on complete graphs, i.e., graphs where all sites are connected to one another. In spinDMFT, this scenario leads to the same autocorrelation as before except for a renormalized quadratic coupling constant. To benchmark this, we also compute the autocorrelation by CET on a finite-size graph. Note that if all couplings are considered to be identical, the model is highly symmetric which leads to rather special autocorrelations. Consequently, the couplings J_{ij} are randomly drawn from a Gaussian distribution with zero first moments and the value of the second moments chosen such that $J_{\mathrm{Q},i} = J_\mathrm{Q}$ for all sites i. The dynamics are then computed by considering the Hamiltonian

$$\mathbf{H}_\mathrm{CG} = \sum_{i<j} J_{ij} \vec{\mathbf{S}}_i \cdot \vec{\mathbf{S}}_j. \tag{4.38}$$

For a fixed graph size N, the CET results are averaged over 100 sets of random couplings. In order to ensure comparability, the couplings are always normalized such that J_Q is the same in all individual calculations. The results from the CET for different values of N are displayed in Fig. 4.7 together with those from spinDMFT.

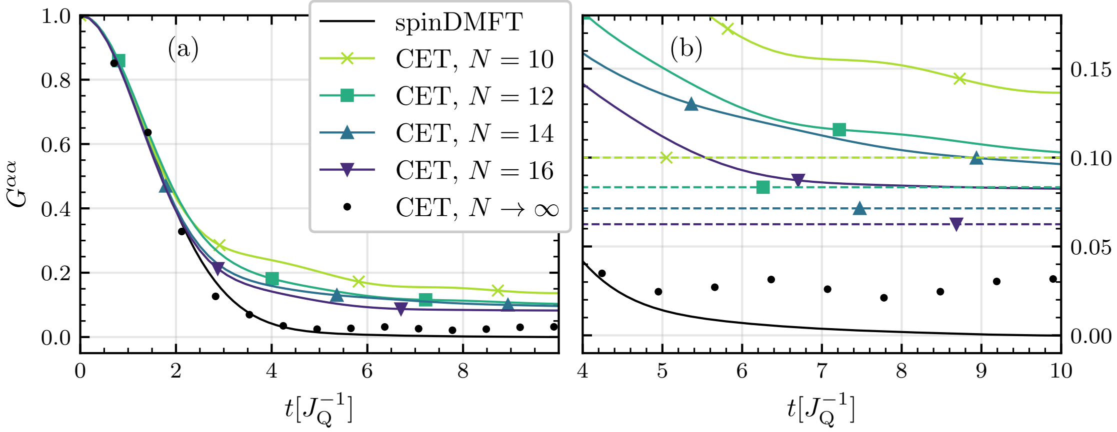

Figure 4.7: **(a)** Autocorrelation results from CET [Ble24] for the Heisenberg model on complete graphs compared to spinDMFT, see Eq. (4.38). The relative error tolerance of each CET computation is $\epsilon = 10^{-3}$. **(b)** Zoomed inset of panel (a). The lower bounds of the long-time limits according to Eq. (4.37) are shown by dashed lines of the corresponding color.

As N is increased, the results converge to those of spinDMFT. The circles represent the CET data extrapolated to $N = \infty$ using a fit according to $N^{-3/2}$ of the data for the three largest values of N. In fact, spinDMFT is not the exact result for $N \to \infty$ ($z \to \infty$), since the contribution of pair-correlations to the mean-field is not suppressed by the coordination number as explained in App. B. Still, the extrapolated CET result matches relatively well with spinDMFT. This further corroborates the foundation of spinDMFT.

In the next section, we come back to the experiment described in Sec. 2.6 and discuss the results of spinDMFT for this scenario.

4.3.1 Dipolar relaxation of defect spins on a diamond surface

In Sec. 2.6, we presented a recent experiment [Rez+23; Grä+23] measuring the relaxation of defect spins on a diamond surface. The measurement takes place in the doubly-rotating frame, which corresponds essentially to the dynamics considered in Sec. 4.2.3, except for a factor of 2 in the global time scale. We will present and discuss the results of the experiment in detail in Sec. 5.3. At this point, it is sufficient to note that the experiment observed an intriguing phenomenon: the transverse and longitudinal relaxation processes occur on completely separated time scales. This behavior is attributed to the inhomogeneous distribution of the spins on the surface.

In spinDMFT, the relative time scale between the two relaxation processes is completely independent of the system geometry. This is because the geometry is entirely hidden in the coupling constant J_{Q}, which affects only the global time scale. As can be seen in Fig. 4.5, spinDMFT generally predicts the two decays to happen approximately on the same time scale[5], which disagrees qualitatively with the experiment.

One potential solution to this issue is to revisit the complete self-consistency problem in Eq. (4.19) and attempt to solve it without assuming homogeneity in space. This approach would allow for the spin dynamics to vary from site to site, thereby allowing the geometry to influence relaxation in a more nuanced manner. While this sounds like a reasonable approach, we remind the reader that spinDMFT requires large coordination numbers to be justified. If a considered inhomogeneous system exhibits strongly site-dependent spin dynamics, this may coincide with each spin having only very few interaction partners. To corroborate this, we present histograms of the effective coordination number in an inhomogeneous system in Fig. 4.8. For the scenario in panel (a), the majority of spins essentially have a single interaction partner. Therefore, spinDMFT is not justified, even in the absence of spatial homogeneity in Eq. (4.19). However, if the effective model is fundamentally modified, a mean-field description may be valid again, see Ch. 5.

Note that by including a sizable minimum distance between each pair of spins, the inhomogeneous system can be made much denser, see panel (b) of Fig. 4.8. But such a strong constraint is not realistic for the experiment considered in Sec. 2.6 and Sec. 5.3.

---

[5] Yet, there is a difference in the form of the decay, Gaussian versus exponential.

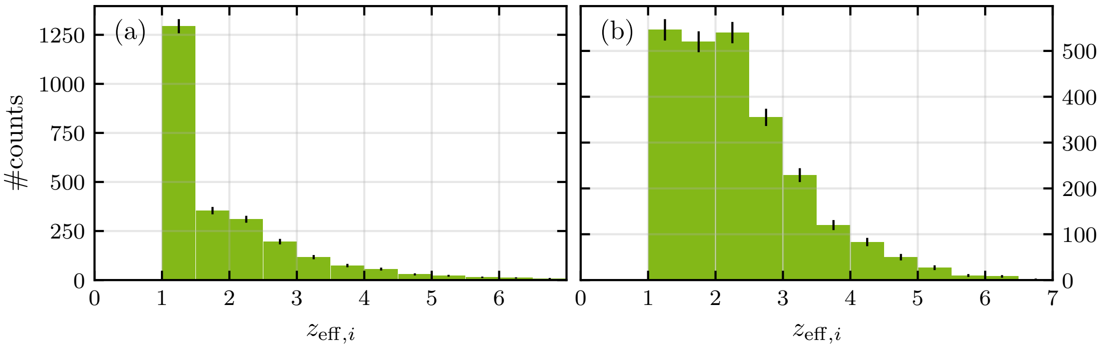

Figure 4.8: Histograms of the effective coordination number for inhomogeneous spin systems with dipole-like interactions, $J \propto R^{-3}$, in two dimensions. Panel (a) refers to completely randomly drawn spin positions and panel (b) to randomly drawn positions with a constraint for the minimum distance, $R_{\mathrm{min}} = 0.5 n_0^{-1/2}$, where n_0 is the spin density.

4.4 Chapter conclusion and outlook

SpinDMFT is a numerical method for accessing the infinite-temperature dynamics of dense spin ensembles. Its validity has been analyzed by the benchmarks presented in Sec. 4.3. One-dimensional systems are clearly not in the scope of the approach. In two dimensions, it already provides a satisfactory approximation which has been demonstrated for the square lattice with $z = 4$. In higher dimensions or for higher coordination numbers, respectively, we expect it to be more accurate since it is justified by a $1/z$-expansion. However, the particularly interesting scenario of a system with positional disorder involves rather small coordination numbers as explained in the previous section. Hence, the experiment introduced in Sec. 2.6 is not captured by spinDMFT. It should be noted, however, that the computational cost of spinDMFT is minimal. Consequently, there is significant scope for extensions that enhance it, such as CspinDMFT or nl-spinDMFT, which will be introduced in subsequent chapters. Comparisons of spinDMFT with its extensions and with experimental data will serve as additional benchmarks.

We recall that spinDMFT is formulated exclusively for infinite temperature, i.e., completely disordered spins. This regime is relevant in several contexts such as NV centers in diamond or NMR, see Ch. 1. Yet, it is very desirable to consider also finite-temperatures and phase transitions in particular. Whether spinDMFT can be extended to this regime is not clear, but related mean-field-approaches for spin glasses provide an idea of how this might be accomplished [GR98; GPS00].

Besides this, it is already interesting to leave the regime of completely disordered spins. Applying a strong magnetic field to a spin system can lead to a measurable polarization even at high temperatures, i.e., far away from any spontaneous symmetry breaking. The study of such a scenario is relevant, e.g., in NMR, see Ch. 6, or in the context of spin diffusion [Zu+21]. However, a particular issue of spinDMFT is that global conservation laws, for example, the conservation of a global polarization, are not automatically accounted for. In App. F, we discuss this in detail and present a proposal and preliminary results for an extension of spinDMFT that respects conservation laws.

5 Cluster extension of spinDMFT

As pointed out in the previous chapter, spinDMFT is justified for dense spin systems, that is, for large effective coordination numbers. The benchmarks for the square lattice indicated that spinDMFT still captures $z = 4$ to a good approximation. If the considered spin system is inhomogeneous or has, for example, a dimer structure, the coordination number can be much smaller, $z_{\mathrm{eff}} = 1 - 2$. In such cases, the mean-field approximation by spinDMFT is not justified anymore. Here, the extended approach, “CspinDMFT”, can help out.

In the first section, we present a brief derivation of CspinDMFT. The approach is benchmarked on homogeneous and inhomogeneous systems in Sec. 5.2. In Sec. 5.3, we use it to compute the dynamics of dipolar defect spins on a diamond surface and compare the results to measurements from the experiment described in Sec. 2.6. While interpreting the results, we also furnish a brief overview over the subject of thermalization and MBL in Sec. 5.3.6. A chapter conclusion and an outlook is given in Sec. 5.4. Several contents of this chapter are based on Ref. [Grä+23][1].

5.1 Derivation of CspinDMFT

5.1.1 Preparation

The idea of CspinDMFT is to improve the mean-field approach by considering more than a single spin on the quantum level. This entails extending the single-site model in spinDMFT to a multi-site model. The quantum-mechanically treated subset of spins is termed *cluster*, hence the name **C**luster-spinDMFT or short CspinDMFT. We present the derivation for a spin ensemble with $S = 1/2$ at infinite temperature, described by a Heisenberg model

$$\mathbf{H} = \frac{1}{2} \sum_{i,j} J_{ij} \vec{\mathbf{S}}_i \cdot \vec{\mathbf{S}}_j \tag{5.1}$$

with general couplings $J_{ij} = J_{ji}$ and $J_{ii} = 0$. Our main goal is to compute the autocorrelations of a specific spin $\vec{\mathbf{S}}_1$, henceforth referred to as the central spin. The first step is to choose the cluster of spins, which we denote by Γ. We require that $\vec{\mathbf{S}}_1$ is part of the cluster, but there are no strict rules for the remaining spins[2]. Of course, it makes sense to include the spins in the proximity of $\vec{\mathbf{S}}_1$ in Γ, but this can be done in many different ways. We discuss and compare specific strategies for choosing the cluster in App. D. In the following, we assume the cluster to be given.

---

[1] We highlight the different naming of the cluster size, n vs. N_Γ, in this thesis and in the cited article.

[2] Note, for example, that Γ does not need to retain any symmetries of the system.

The derivation of CspinDMFT is presented in three steps similar to the ones of spinDMFT:

(i) We identify the environments of each spin in the cluster and substitute them by stochastic classical dynamic mean fields. We discuss, how CspinDMFT improves spinDMFT if the cluster is chosen properly. (Sec. 5.1.2)

(ii) We show that the mean fields follow a multivariate Gaussian distribution and define expectation values in the mean-field framework. (Sec. 5.1.3)

(iii) The defining moments of the Gaussian distribution are linked to spin expectation values. We close the self-consistency by replacing out-of-cluster correlations by in-cluster correlations. (Sec. 5.1.4)

The first step is presented in the following section.

5.1.2 Step (i): Mean-field substitution and multi-site model

For a given cluster Γ, the Hamiltonian can be divided into three parts,

$$\mathbf{H} = \frac{1}{2}\sum_{i,j\in\Gamma} J_{ij}\vec{\mathbf{S}}_i \cdot \vec{\mathbf{S}}_j \tag{5.2a}$$

$$+\sum_{i\in\Gamma}\vec{\mathbf{S}}_i \cdot \sum_{j\notin\Gamma} J_{ij}\vec{\mathbf{S}}_j \tag{5.2b}$$

$$+\frac{1}{2}\sum_{i,j\notin\Gamma} J_{ij}\vec{\mathbf{S}}_i \cdot \vec{\mathbf{S}}_j. \tag{5.2c}$$

The first term contains the intra-cluster couplings, which are treated exactly in CspinDMFT. The second term contains the couplings between the spins in the cluster and the spins in the environment, henceforth called *border*. We treat this kind of couplings on the mean-field level. The third term contains only couplings between spins of the environment. Since they are decoupled from the cluster, they do not explicitly show up in CspinDMFT.

In Eq. (5.2b), the local-environment operators of the spins in the cluster can be identified,

$$\vec{\mathbf{V}}_i := \sum_{j\notin\Gamma} J_{ij}\vec{\mathbf{S}}_j. \tag{5.3}$$

Analogous to spinDMFT, we replace them by time-dependent mean fields $\vec{V}_i(t)$. We consider a separate mean field for each spin of the cluster, hence the subscript i.

In spinDMFT, we justified the mean-field substitution by the large effective coordination number of the system. Employing the Frobenius norm, we showed that the local-environment operators behave classically in the limit $z_{\mathrm{eff},i} \to \infty$. Moreover, we argued that in the same limit back actions of the spin onto its environment can be neglected. In principle, these arguments work as well for the adapted operators in Eq. (5.3), but the moments of the couplings must be redefined such that they do not contain any intra-cluster couplings,

$$(\mathcal{J}_{m,i})^m := \sum_{j\notin\Gamma} (J_{ij})^m, \qquad m \in \mathbb{N}^+, \qquad i \in \Gamma. \tag{5.4}$$

This may increase or decrease $z_{\mathrm{eff},i}$ depending on the systems geometry. Consider, for instance, a lattice of spin dimers as depicted in Fig. 5.1, panels (b1) and (b2).

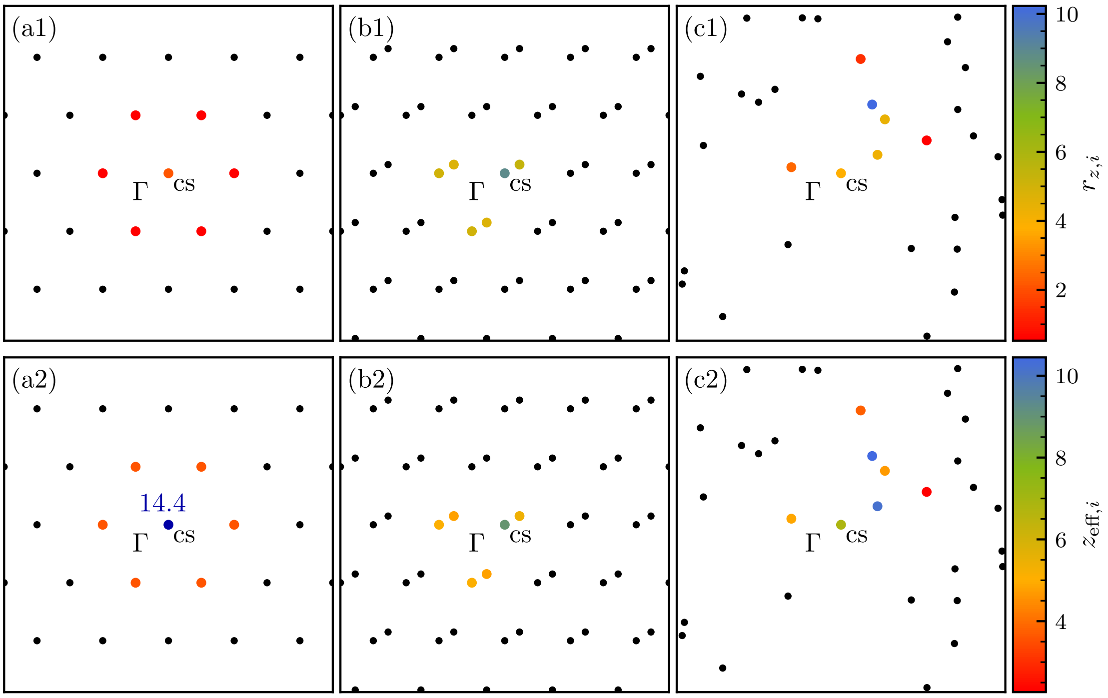

Figure 5.1: Two-dimensional spin ensembles and exemplary clusters Γ considering dipole-like interactions $J = R^{-3}$. The spins that are not part of Γ are shown by the smaller, black dots. Both plot rows show the same three geometries, but encode different information. In panels (a1-c1), the spins of the cluster are shown in color depending on the ratio $r_{z,i}$ of $z_{\mathrm{eff},i}$ in CspinDMFT (Γ contains the colored spins) over $z_{\mathrm{eff},i}$ in spinDMFT (Γ contains only spin i). Accordingly, $r_{z,i}$ measures the improvement of the effective coordination number, when extending spinDMFT to CspinDMFT. In panels (a2-c2), the colors represent the absolute values of $z_{\mathrm{eff},i}$ in CspinDMFT. The central spin in the triangular lattice (a2) is not captured by the color map, since its effective coordination number, $z_{\mathrm{eff},i} \approx 14.4$, is very large.

In this scenario, the application of spinDMFT is not justified because $z_{\mathrm{eff}} \approx 1$ due to the close neighbor spin in each dimer. However, for a dimer cluster ($n = 2$) the close neighbor is treated quantum-mechanically and, thus, left out in the local-environment operators leading to a much higher $z_{\mathrm{eff},i}$. This advantage of CspinDMFT only pays out, if the cluster is chosen cleverly, see App. D. In regular lattices, this is only possible to a limited extent. Here, $z_{\mathrm{eff},i}$ is increased for the central spin and decreased at the edge of Γ compared to $z_{\mathrm{eff},i}$ in spinDMFT. This can be well seen in the example of a triangular lattice, see Fig. 5.1, panels (a1) and (a2). However, as the effective number of spins in a local-environment field is reduced, also its strength and the strength of the corresponding mean-field is weakenend, which clearly improves the approximation. This weakening can be tracked by means of the ratios of the quadratic coupling constants, see Fig. 5.2. We conclude that the mean-field substitution can be well justified even if the corresponding $z_{\text{eff},i}$ is not very large. A more quantitative picture requires explicit benchmarks.

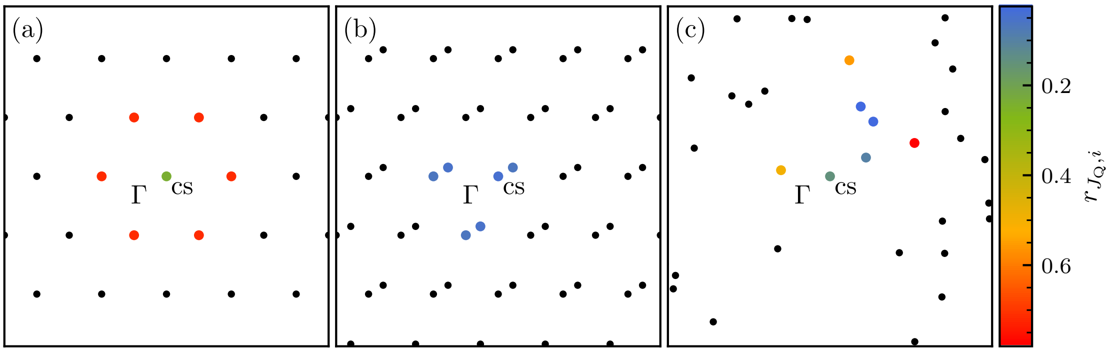

Figure 5.2: Same as Fig. 5.1, but the colors represent the ratio $r_{J_{\mathrm{Q}},i}$ of $J_{\mathrm{Q},i}$ in CpinDMFT (Γ contains the colored spins) and $J_{\mathrm{Q},i}$ in spinDMFT (Γ contains only spin i). Accordingly, $r_{J_{\mathrm{Q}},i}$ measures the weakening of the mean-fields, when extending spinDMFT to CspinDMFT.

Generally, we expect a better performance of CspinDMFT, if the system consists of well-separable clusters of proximate spins. This is clearly the case for systems with dimer or multi-spin bases, but inhomogeneous systems can also have this tendency, see Fig. 5.1, panels (c1) and (c2), and Fig. 5.2, panel (c). In regular lattices, where the spatial separability is not given, the effective coordination number is not very large at the edge of the cluster. Hence, the improvement by passing from spinDMFT to CspinDMFT is not expected to be considerable. But, we remind the reader that lattices in $D > 1$ are already well captured by spinDMFT. From that perspective, it is obvious that the improvement cannot be enormous.

One should note that for the relevance of back actions, the environments of the spins contained in $\vec{\mathbf{V}}_i$ and *not* the environments of the spins contained in Γ are crucial. This should be considered particularly in inhomogeneous systems, where the local environments vary strongly from site to site. We emphasize, however, that the cluster can be considered well separated from the environment if the values for $z_{\text{eff},i}$ for the spins in Γ are large. Even in inhomogeneous systems, this coincides with the cluster being unimportant for the dynamics of the environment. A counterexample for this would be a CSM with the central spin replaced by a cluster of spins. In this case, $z_{\text{eff},i}$ can be large, while at the same time back actions are important. But such special systems are not considered in the framework of this thesis.

Carrying out the mean-field substitution $\vec{\mathbf{V}}_i \to \vec{V}_i(t)$, we arrive at a multi-site model described by the Hamiltonian

$$\mathbf{H}_\Gamma^{\text{mf}}\left[\vec{V}_1(t), \dots, \vec{V}_n(t)\right] = \frac{1}{2}\sum_{i,j\in\Gamma} J_{ij}\vec{\mathbf{S}}_i \cdot \vec{\mathbf{S}}_j + \sum_{i\in\Gamma}\vec{\mathbf{S}}_i \cdot \vec{V}_i(t). \tag{5.5}$$

The remaining degrees of freedom are the 2^n dimensions of the Hilbert space of the spins and the continuous probability space of the n vector-valued mean fields, where n is the cluster size. We proceed with the next step of the derivation.

5.1.3 Step (ii): Probability functional

This step is essentially the same as in spinDMFT, see Sec. 4.1.3. Each mean field consists of a large number of uncorrelated spins and thus follows a Gaussian distribution functional according to the central limit theorem. In systems that consist of spatially well-separated groups of spins, this argument has to be generalized. Some pairs of spins may be strongly correlated, see for example the dimers in Fig. 5.1, panels (b1) and (b2). In such cases, the Gaussian approximation is still valid, if we replace "uncorrelated spins" by "uncorrelated contributions", where a contribution may result from several spins.

As in spinDMFT, expectation values are computed by averaging over the quantum and mean-field degrees of freedom. Note that any conceivable expectation value on the cluster can be accessed. This includes, for example, pair correlations between two spins in Γ. Formally, the equation for computing spin-spin correlations in mean-field approximation reads

$$\begin{aligned} \langle \mathbf{S}_i^\alpha(t_1)\mathbf{S}_j^\beta(t_2)\rangle^{\mathrm{mf}} = &\left(\prod_{i=1}^{n}\int \mathrm{D}\chi_i\right)\frac{p_{\mathrm{mar}}[\chi_1,\dots,\chi_n]}{d_\Gamma} \\ &\times \mathrm{Tr}_{(\Gamma)}\left(\mathbf{U}_\Gamma^\dagger[\chi_1,\dots,\chi_n]\,\mathbf{S}_i^\alpha\mathbf{U}_\Gamma[\chi_1,\dots,\chi_n]\,\mathbf{S}_j^\beta\right), \\ \chi_i := \vec{\mathcal{V}}_i(t_1,t_2), \qquad & i,j\in\Gamma, \end{aligned} \tag{5.6}$$

where p_{mar}[3] is the Gaussian probability functional, $d_\Gamma = 2^n$ is the local Hilbert space dimension and $\mathbf{U}_\Gamma$ is the time evolution operator generated by the Hamiltonian in Eq. (5.5). It should be noted that the mean fields can be correlated to one another, i.e., p_{mar} is not necessarily separable with respect to the different χ_i. Below, we carry out the last step of CspinDMFT.

5.1.4 Step (iii): Self-consistency

Eventually, we need to determine the first and second moments of the mean-field probability functional p_{mar}. In analogy to spinDMFT, we link these moments to quantum expectation values of the local-environment operators, from which the mean fields originate. Again, the first moments are zero due to infinite temperature,

$$\overline{V_i^\alpha(t)}^{\mathrm{mf}} = \langle \mathbf{V}_i^\alpha(t)\rangle = 0. \tag{5.7}$$

For the second moments, we obtain

$$\overline{V_i^\alpha(t_1)V_j^\beta(t_2)}^{\mathrm{mf}} = \langle \mathbf{V}_i^\alpha(t_1)\mathbf{V}_j^\beta(t_2)\rangle = \sum_{p,q\notin\Gamma} J_{ip}J_{jq}\langle \mathbf{S}_p^\alpha(t_1)\mathbf{S}_q^\beta(t_2)\rangle. \tag{5.8}$$

The double sum contains correlation functions of spins outside of Γ, henceforth *out-of-cluster* correlations, which are not directly accessible in the mean-field framework. This issue also occurs in spinDMFT and is solved by neglecting pair correlations and

---

[3] As with spinDMFT, the index "mar" indicates the use of the marginal distribution, i.e., only the moments of mean-fields on the cluster at times $t \in [t_1, t_2]$ are relevant for it.

by replacing any autocorrelation by the one of the central spin assuming translational invariance in space.

The first of these approximations is not necessary here because, in principle, pair correlations can be accessed in CspinDMFT. In fact, CspinDMFT is designed particularly for systems with smaller coordination numbers where spinDMFT is not justified and pair correlations are relevant. Consequently, it is reasonable to drop this oversimplification.

The second approximation can be extended by approximating out-of-cluster correlations by correlations of spins on the cluster (*in-cluster* correlations). To this end, we explicitly distinguish lattices from inhomogeneous systems.

Self-consistency in lattice systems

In lattices, we can exploit translational invariance and map the out-of-cluster correlations to their exact replicas in Γ, see for example Fig. 5.3. Clearly, this mapping leads to ambiguities due to the occurrence of several correlation replicas in Γ. One way to tackle this is to replace out-of-cluster correlations by the average of all of their replicas[4]. This is termed “correlation replica average” (CRav) and presented in Ref. [Grä+23] (App. C, 2.).

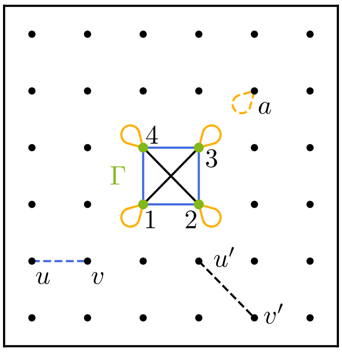

Figure 5.3: Sketch of a square spin lattice with isotropic interactions (J depends solely on the relative distance of two spins) and an exemplary cluster Γ. We represent in-cluster correlations by solid and out-of-cluster correlations by dashed lines between the involved spins. Autocorrelations are shown in orange, NN pair correlations in blue and NNN pair correlations in black. Each out-of-cluster correlation has several correlation replicas in Γ.

It should be noted, however, that the calculation of correlations requires significant computational effort so that it is preferable to compute each kind of correlation only once. Hence, we suggest the following alternative procedure:

(a) Categorize the correlations that are accessible in Γ by different indices $c \in C$. For example in Fig. 5.3, there are three categories: autocorrelations ($c = 0$), NN pair correlations ($c = 1$) and NNN pair correlations ($c = 2$).

(b) For each category, find a pair of spin indices in the cluster that represent the category. We summarize this with the function $f : C \to \Gamma^2$ which assigns a category index $c \in C$ to a pair index $\{k, l\} \in \Gamma^2$. Clearly, $k = l$ for an autocorrelation and $k \neq l$ for a pair correlation. For example in Fig. 5.3, the representative correlations could be $kl = 11, 12, 13$ for $c = 0, 1, 2$.

---

[4] In practice, these replicas are not always exactly the same because the cluster explicitly breaks some symmetries of the lattice.

(c) Employ translational invariance to replace each out-of-cluster correlation by the respective in-cluster correlation that represents the corresponding category. This implies a function $g : \overline{\Gamma}^2 \to C$, assigning a pair index $\{p, q\} \in \overline{\Gamma}^2$ to a category index $c \in C$. Here, $\overline{\Gamma}$ is the complement of Γ, i.e., all spins that are not part of the cluster. Out-of-cluster correlations that are not represented by any category are replaced by zero. Considering Fig. 5.3, for example, $pq = aa$ is mapped to $c = 0$, $pq = uv$ is mapped to $c = 1$ and $pq = u'v'$ is mapped to $c = 2$.

Applying this to Eq. (5.8), we obtain

$$\overline{V_i^\alpha(t_1) V_j^\beta(t_2)}^{\mathrm{mf}} = \sum_{c \in C} \left(J_{ij,c}^{\mathrm{CR}} \right)^2 \langle \mathbf{S}_k^\alpha(t_1) \mathbf{S}_l^\beta(t_2) \rangle^{\mathrm{mf}} \Big|_{\{k,l\} = f(c)}, \tag{5.9a}$$

$$\left(J_{ij,c}^{\mathrm{CR}} \right)^2 := \sum_{p,q \notin \Gamma : R} J_{ip} J_{jq}, \qquad R : \; g(\{p, q\}) = c, \tag{5.9b}$$

where CR stands for **C**orrelation **R**eplica and R is a sum condition to ensure the correct mapping. This closes the self-consistency because the sum in Eq. (5.9a) contains only in-cluster correlations, which can be accessed through Eq. (5.6). Note that in case of a bilinear Hamiltonian, the correlation functions are symmetric with respect to the sites, see Eq. (2.6d). In this case, only one of the two in-cluster correlations, that is, $\{k, l\}$ or $\{l, k\}$ should be considered for the categorization, as indicated in the example.

There are mostly several possibilities to choose the representative correlation in step (b). In this thesis, we number the spins ascending according to the order in which they were added to the cluster. Then, the representative correlation with pair index $\{k, l\}$ is always chosen by minimizing k and, subsequently, if there are still several options, by also minimizing l.

Self-consistency in inhomogeneous systems

To access inhomogeneous systems, we pursue an analogous strategy by identifying approximate replicas for each out-of-cluster correlation. This is not straightforward because the correlations are *a priori* unknown. One way to tackle this is to find a suitable quantity that classifies a correlation based on the *a priori*-given couplings. In this way, the similarity between two different correlations can be roughly quantified. In Ref. [Grä+23] (App. C, 1.), we analytically derive such quantities for the Heisenberg model from the leading order derivatives of the correlations, i.e., their short-time behavior. In conclusion, pair correlations can be classified by the direct couplings of the involved spins and autocorrelations by the quadratic coupling constant[5],

$$s_{pq}^{\mathrm{pair}} := J_{pq}^2, \qquad\qquad s_p^{\mathrm{auto}} := \sum_r J_{rp}^2. \tag{5.10}$$

The similarity of two pair correlations or two autocorrelations, respectively, can be simply measured by the modulus or squared difference of the corresponding coupling constant.

---

[5] Note that in this definition of the quadratic coupling constant, the sum runs over all spins in contrast to the sum in Eq. (5.4).

To map an out-of-cluster correlation $g^{\alpha\beta}_{pq}(t_1, t_2)$, to an in-cluster correlation $g^{\alpha\beta}_{kl}(t_1, t_2)$, we use the function $f : \overline{\Gamma}^2 \to \Gamma^2$ with

$$f(\{p,q\}) = \begin{cases} \min_{\{k,l\}\in\Gamma^2} \left(s^{\text{pair}}_{pq} - s^{\text{pair}}_{kl}\right)^2, & p \neq q \\ \min_{k\in\Gamma} \left(s^{\text{auto}}_{p} - s^{\text{auto}}_{k}\right)^2, & p = q. \end{cases} \tag{5.11}$$

In addition, we define a lower cutoff for s^{pair}_{pq} by

$$s^{\text{pair}}_{\text{cut}} := \frac{1}{2} \min_{\{k,l\}\in\Gamma} s^{\text{pair}}_{kl}. \tag{5.12}$$

Any pair correlation in $\overline{\Gamma}^2$ with $s^{pq}_{\text{pair}} < s^{\text{cut}}_{\text{pair}}$ is considered too small to be relevant and is thus set to zero. This prevents an over-weighting of the weakest pair correlation in Γ. Summarizing this and Eq. (5.11), the final closed self-consistency condition reads

$$\overline{V_i^{\alpha}(t_1) V_j^{\beta}(t_2)}^{\text{mf}} \approx \sum_{k,l\in\Gamma} \left(J^{\text{CRA}}_{ij,kl}\right)^2 \langle \mathbf{S}^{\alpha}_k(t_1) \mathbf{S}^{\beta}_l(t_2)\rangle, \tag{5.13a}$$

$$\left(J^{\text{CRA}}_{ij,kl}\right)^2 =: \sum_{p,q\notin\Gamma:R} J_{ip} J_{jq}, \qquad R:\ f(\{p,q\}) = \{k,l\},\ s^{\text{pair}}_{p\neq q} > s^{\text{pair}}_{\text{cut}} \tag{5.13b}$$

where CRA stands for **C**orrelation-**R**eplica **A**pproximation and R ensures the correct mapping. It should be noted that in contrast to Eq. (5.9), the sum in Eq. (5.13) runs over all correlations in the cluster. Hence, the computational cost is increased compared to a lattice system. As mentioned above, the correlation functions are symmetric with respect to the two site indices, i.e., one should consider only one of the two in-cluster correlations, $\{k,l\}$ or $\{l,k\}$.

It is debatable whether the mapping induced by the CRA is indeed a good approximation. The quantities in Eq. (5.10) provide a reasonable classification of correlations, but it is not realistic that each correlation is replaced by an appropriate replica, i.e., that the difference between the replica and the true correlation is really small. We emphasize, however, that the mean fields consist of large sums of correlations if the cluster is chosen properly. Thus, errors from individual false mappings are expected to average out to some extent. Moreover, we stress that the mean fields only make up for a part of the dynamics. The other part is made up by the mutual interactions of the spins in the cluster. Thus, deviations in the mean-field distribution translate into smaller deviations in the correlation functions computed by Eq. (5.6). An explicit benchmark and an idea to improve the CRA is proposed in Sec. 5.4.3.

Analogous to spinDMFT, the self-consistency problem of CspinDMFT is closed by Eq. (5.9) or Eq. (5.13). The full spin system is effectively reduced to a multi-site model as shown in Fig. 5.4, which can be solved numerically by iteration. Thus, the derivation of CspinDMFT is completed. We comment on the properties of the formalism in the following subsection.

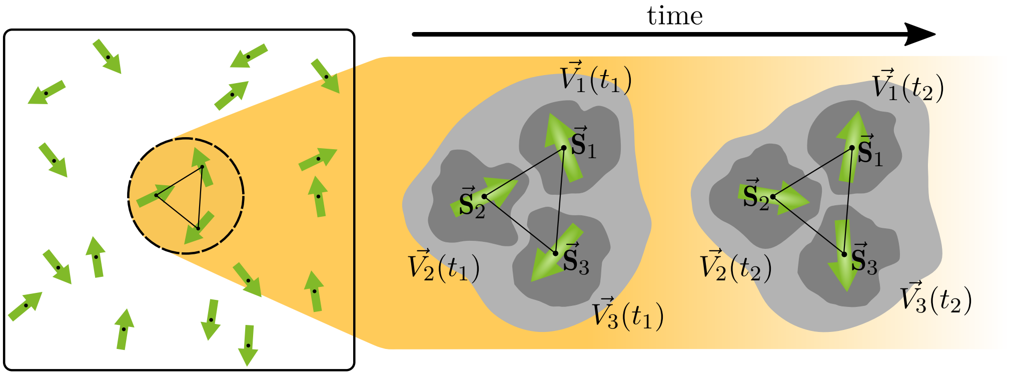

Figure 5.4: CspinDMFT reduces the full spin system (here inhomogeneous) to a multi-site model with explicit time dependence. The latter describes the evolution of a few interacting spins $\vec{\mathbf{S}}_i$, represented by green arrows, under dynamic Gaussian mean fields $\vec{V}_i(t)$, represented by dark-gray clouds. These are correlated to one another, which is indicated by the light-gray clouds. Due to the inclusion of several sites, CspinDMFT retains some spatial fluctuations in contrast to spinDMFT, which is illustrated in Fig. 4.2.

5.1.5 Remarks and procedure

As in spinDMFT, the autocorrelations of CspinDMFT fulfill time translation invariance, if the distribution p_{mar} does. Therefore, solutions homogeneous in time exist. To reduce the computational cost, time translation invariance should be enforced in any numerical implementation. We stress that in contrast to spinDMFT, CspinDMFT does not map to a model of classical spins. The cluster is treated exactly so that local quantum effects are accounted for. Due to the self-consistency, these effects also influence the mean fields. CspinDMFT can be extended to spins with $S > 1/2$. In contrast to spinDMFT, the spin length cannot be completely "hidden" in coupling constants anymore. Due to the explicit treatment of the cluster, we expect a generically different behavior for different spin lengths S.

The procedure to compute the spin dynamics by CspinDMFT runs as follows:

(1) Choose an appropriate cluster Γ according to the hybrid strategy, see App. D. The maximum cluster size $n^{\max}$ is limited by the available numerical resources.

(2) Define the mapping from out-of-cluster correlations to in-cluster correlations, which is required for closing the self-consistency. By means of this mapping, compute the coupling constants that occur in the self-consistency condition, see Eq. (5.9) for lattices and Eq. (5.13) for inhomogeneous systems.

(3) Solve the self-consistency problem by iteration analogous to spinDMFT, see Fig. 4.3. Obviously, one needs to consider adapted equations in CspinDMFT. This includes the effective Hamiltonian in Eq. (5.5), the expectation value in Eq. (5.6) and the self-consistency condition established in the previous step.

Note that the steps (1) and (2) are independent of any expectation values and thus numerically cheap. The computational cost of the iteration in step (3) increases rapidly with the cluster size (approximately as 2^{3n}). However, as in spinDMFT, the algorithm converges after only ≈ 4 iteration steps so that simulations with cluster sizes of $n = 10$ are feasible. Differences compared to spinDMFT regarding numerical details are discussed in App. C.2. One key aspect is that the numerical error tolerances we will provide apply solely to the explicitly depicted correlations and not to all correlations that enter the self-consistency equations. Another aspect is that the statistical error decreases upon increasing the cluster size. Hence, the simulation of a large cluster requires a much smaller sample size M than in spinDMFT.

So far, the derivation of CspinDMFT has been carried out particularly for the Heisenberg model. Extending it to the XXZ model requires to include the easy-axis anisotropy in the effective Hamiltonian and in the self-consistency condition. This is done, for example, in Sec. 5.3, where we consider dipolar spins on a diamond surface. It is worth mentioning that, analogous to spinDMFT, the mean-field framework is very versatile. The effective Hamiltonian in Eq. (5.5) can be altered considering different spin models and extended to static or time-dependent magnetic fields. We emphasize, though, that for such modifications one needs to reconsider the strategies used in steps (1) and (2). For example, the quantities for the CRA, see Eq. (5.10), may need to be rederived.

The need for a cluster extension of spinDMFT has been noted also in Ref. [Mar+23]. The authors present an alternative cluster extension of spinDMFT, which they term “cDMFT”. The main differences between the approaches are that in cDMFT

- the whole spin ensemble is separated into clusters,
- no mapping of correlations is performed, i.e., all clusters of spins are simulated in parallel,
- the approach is carried out on the dimer level, i.e., the cluster size is 2.

Advantageously in CspinDMFT, the self-consistency demands the simulation of a single cluster only so that simulations with considerably larger cluster sizes are feasible. Disadvantageously in CspinDMFT, the mapping of correlations by means of the CRA forms an additional approximation, which is not required in cDMFT.

5.2 Benchmarks for the Heisenberg model in two dimensions

We can check the validity of CspinDMFT by comparing it to brute-force methods. Furthermore, the possibility to vary the cluster size allows for another kind of benchmark. We can track the convergence of CspinDMFT as n is increased because the method becomes exact for $n \to \infty$. In this section, we consider both kinds of benchmarks for a Heisenberg model on different geometries. We restrict ourselves to 2D systems, since the dynamics in 1D is strongly constrained (see Sec. 4.3) and three or more dimensions are too demanding for the brute-force methods CET or ED.

At first, we consider the square lattice with NN interactions. In contrast to Sec. 4.3, we consider only the CET for comparison, since the iEoM results are not sufficiently converged and ED is indistinguishable from CET for comparable system sizes. The results from CET and CspinDMFT are presented in Fig. 5.5 versus the time in units of $J_{\mathrm{Q}}^{-1} = 2J$, where J is the NN coupling.

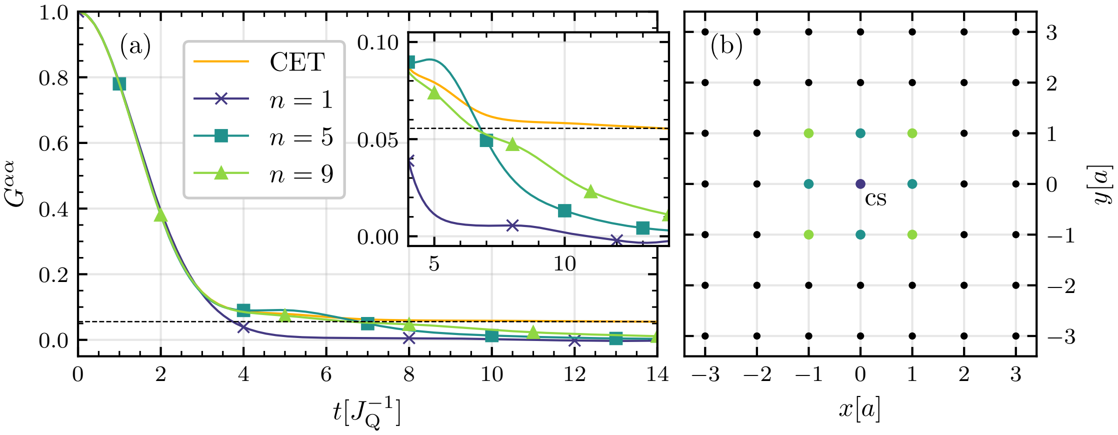

Figure 5.5: **(a)** Autocorrelations from CET [Ble24] and CspinDMFT for the Heisenberg model on a square lattice with NN interactions. The CET results were computed considering $N = 18$ sites (PBC) and a relative error tolerance of $\epsilon = 10^{-3}$. The black dashed line represents the lower bound $1/N$ of the long-time limit of the CET results according to Mazur's inequality. The CspinDMFT results are shown for the cluster sizes $n = 1$ (spinDMFT), $n = 5$ and $n = 9$, all with an absolute numerical error tolerance of $\epsilon = 3 \times 10^{-3}$. **(b)** Cutout of the square lattice around the central spin (cs). The spins in the clusters are displayed by the large colored dots. A cluster always contains the next-smaller cluster plus some additional spins, which are shown in the color of the respective curve in panel (a).

The striking part is that in contrast to spinDMFT ($n = 1$), the autocorrelations from CspinDMFT ($n = 5, 9$) do not immediately decay to zero. Instead, the initial rapid decay is slowed down considerably after $t \approx 3.5\, J_\mathrm{Q}^{-1}$. Correspondingly, CspinDMFT is relatively close to CET up to about $t \approx 7\, J_\mathrm{Q}^{-1}$. Afterwards, the CET does not decay any further which is obvious from Mazur's inequality providing a rigorous bound for the long-time average in the finite-size system, see Eq. (4.37). This inequality does not apply to CspinDMFT, since polarization is not preserved in the cluster due to the interaction with the mean fields. Therefore, the autocorrelations decay to zero in CspinDMFT, which is qualitatively correct in the thermodynamic limit. The extent to which CspinDMFT quantitatively captures the form of this decay remains an open question. The differences between the results for $n = 5$ and $n = 9$ give an impression about the magnitude of the remaining error.

In Fig. 5.6, we plot the different kinds of pair correlations computed by CspinDMFT for $n = 9$. They all look qualitatively the same, showing one or two maxima followed by a relatively slow decay. The position and magnitude of the maxima vary considerably. This can be phenomenologically understood by assigning each maximum to a process involving a specific number of spins. For more details, we refer to Ref. [GHU24], where a similar behavior is obtained for the pair correlations in calcium fluoride. We stress that overall the pair correlations are significantly smaller than the autocorrelation and therefore less relevant for the self-consistency. This is expected from the coordination number, $z = 4$, and forms the basis for spinDMFT.

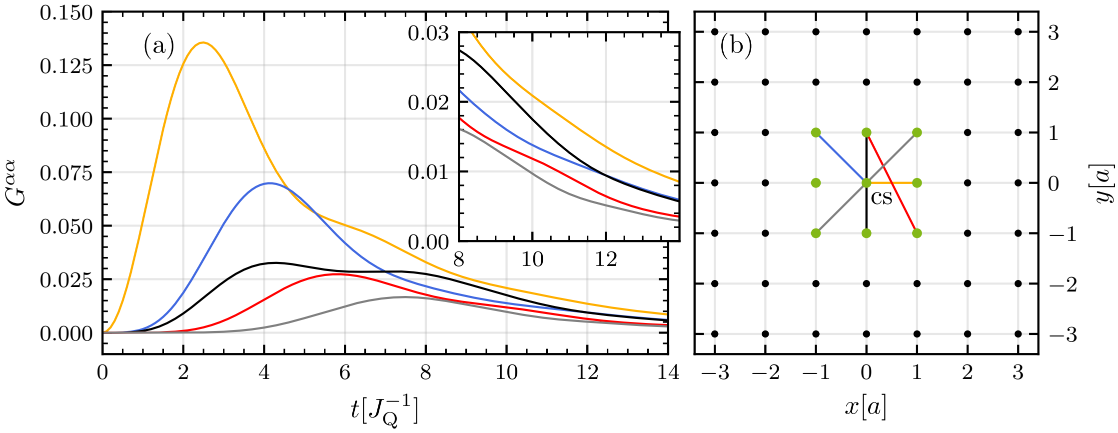

Figure 5.6: Pair correlations computed by CspinDMFT for the Heisenberg model on a square lattice with NN interactions. For a cluster of $n = 9$ spins, 5 different categories of pair correlations are accessible. Each of these categories is plotted in panel (a) and represented by a connection line of the same color in panel (b).

The results for the triangular lattice with NN interactions, see Fig. 5.7, look very similar to the ones of the square lattice. The difference between the brute-force method (ED) and CspinDMFT is larger at moderate times, $t \approx 5.5\, J_{\mathrm{Q}}^{-1}$. These differences are expected to become smaller if the cluster size is increased further. But finite-size effects in the ED can also be relevant in this time regime because the triangular lattice is more dense. The latter aspect also explains why the convergence of CspinDMFT with the cluster size is faster in this case.

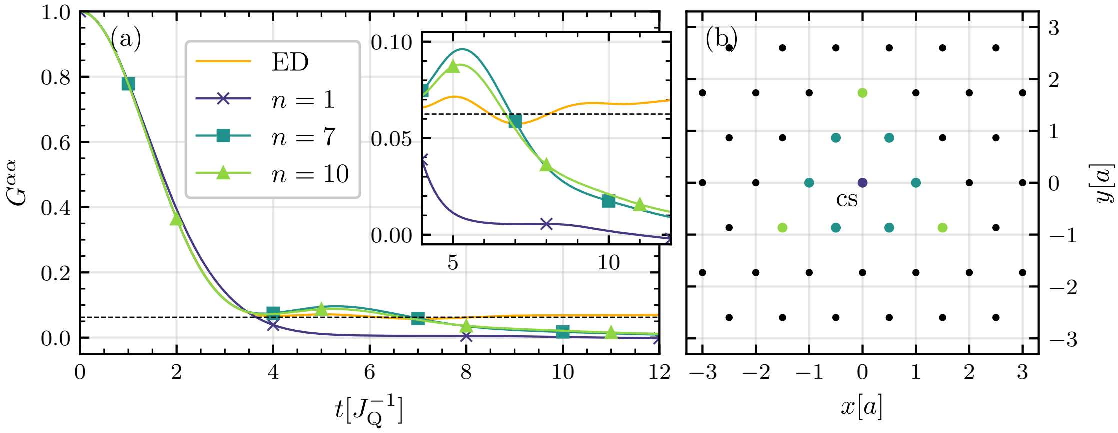

Figure 5.7: Same as Fig. 5.5, but for the triangular lattice and considering ED with $N = 16$ sites (PBC) for comparison. Note that the last shell of the largest cluster ($n = 10$) is incomplete due to the computational limitations.

Many of the spin systems considered in this thesis involve dipolar couplings, which is why this case should be benchmarked as well. This has been done already in Ref. [Grä+23] for the triangular lattice. We refrain from showing this here, but emphasize that the convergence is faster than for NN interactions, which is expected due to the higher effective coordination number $z_{\text{eff}} \approx 6.76$[6]. It is even more interesting to look at the results for an inhomogeneous spin system because its coordination numbers are sometimes much smaller. As a consequence, the specific choice of the cluster is very important. The central-spin-based and cluster-based strategy have been analyzed for an inhomogeneous system in Ref. [Grä+23]. The ensuing results are not shown here because these strategies are not used in this thesis. Instead, we consider the hybrid strategy, which is described in App. D. We consider a Heisenberg model with randomly positioned spins in 2D and couplings

$$J_{ij} = J_0 \left(\frac{r_0}{r_{ij}} \right)^3 , \tag{5.14}$$

which correspond to dipolar ones, but without anisotropy. Here, r_0 is defined via the spin density $n_0 = r_0^{-2}$ and J_0 is the unit of the inverse time.

First, we consider an example configuration, where the central spin is rather weakly coupled to the environment. The corresponding ensemble and the resulting autocorrelations are displayed in Fig. 5.8 for varying cluster size n.

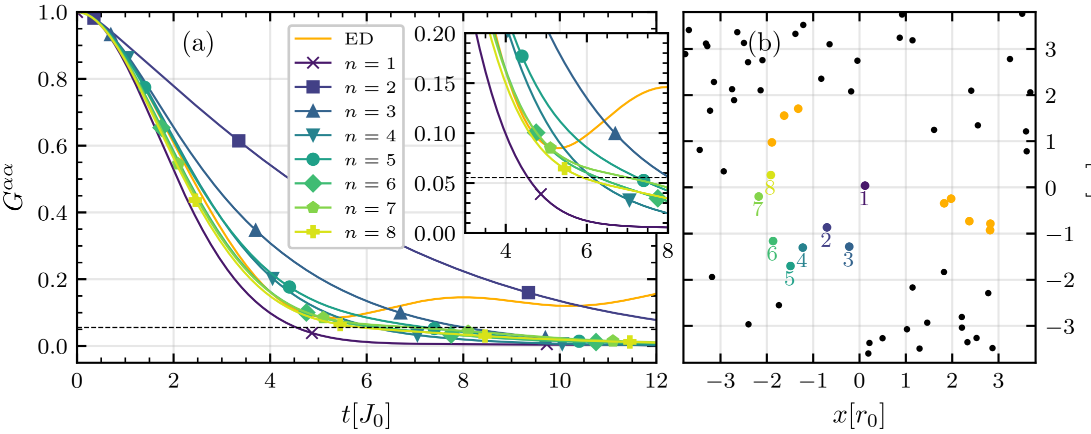

Figure 5.8: **(a)** Autocorrelation results from ED and CspinDMFT for the Heisenberg model and randomly distributed spins with dipole-like couplings, see Eq. (5.14). The central spin is rather weakly coupled to the environment, $J_Q \approx 0.8\,J_0$. The ED results were computed considering $N = 16$ spins and the black dashed line represents the lower bound $1/N$ according to Mazur's inequality. The CspinDMFT results are shown for varying cluster sizes from $n = 1$ (spinDMFT) to $n = 8$, all with an absolute numerical error tolerance of $\epsilon = 0.02$. **(b)** Cutout of the considered random ensemble. For a CspinDMFT simulation with cluster size n, the spins with numbers $1 - n$ are added to the cluster. Note particularly the spatial proximity of the spins No. 5 and 6. Cutting this dimer in half leads to considerable errors in CspinDMFT. The ED simulation includes the numbered spins as well as the spins shown by orange dots.

The central spin couples most strongly to a group of five spins with indices $2-6$, which are added successively to the cluster by the hybrid strategy. The result for $n = 2$ considerably

---

[6] Note that the effective coordination number provided in Refs. [Grä+21; Grä+23] is different from the one given here because a different definition has been used. In this thesis, we use the definition in Eq. (4.3).

deviates from the rest. This is not surprising because spin No. 2 affects the central spin most strongly and its environment consists only of a few spins. Treating them completely on the mean-field level is not a good approximation. We consider the results for $n = 6$ to be much more reliable than for $1 < n < 6$ because the whole group is included in the cluster. Adding the spins No. 7 and 8 hardly changes the result, so they can be treated just as well on the mean-field level.

For cluster sizes $n > 3$, the short time behavior of CspinDMFT matches approximately with the ED data, which indicates that the most important interaction partners of the central spin are considered. The subsequent deviations between ED and CspinDMFT are likely caused by finite-size effects in the ED. These are expected to be much stronger here than for the lattices, because we cannot consider PBC[7]. It is also worth mentioning that the overall results are relatively close to what spinDMFT ($n = 1$) predicts. This is because for the considered configuration, the central spin is only weakly coupled to the environment leading already to a moderate coordination number, $z_{\text{eff}} \approx 3.9$. Note that the results for $n = 2$ deviate quite substantially from the rest. We conclude that the border between cluster and environment has to be chosen appropriately for CspinDMFT to yield a good approximation. For the considered example, the hybrid strategy suggests a cluster size of $n = 6$, which is completely plausible from Fig. 5.8. In Fig. 5.9, some of the pair correlations computed by CspinDMFT are displayed. Note that they become very large, when the involved spins are close to each other. This is fundamentally different in lattice systems, see Fig. 5.6 for comparison.

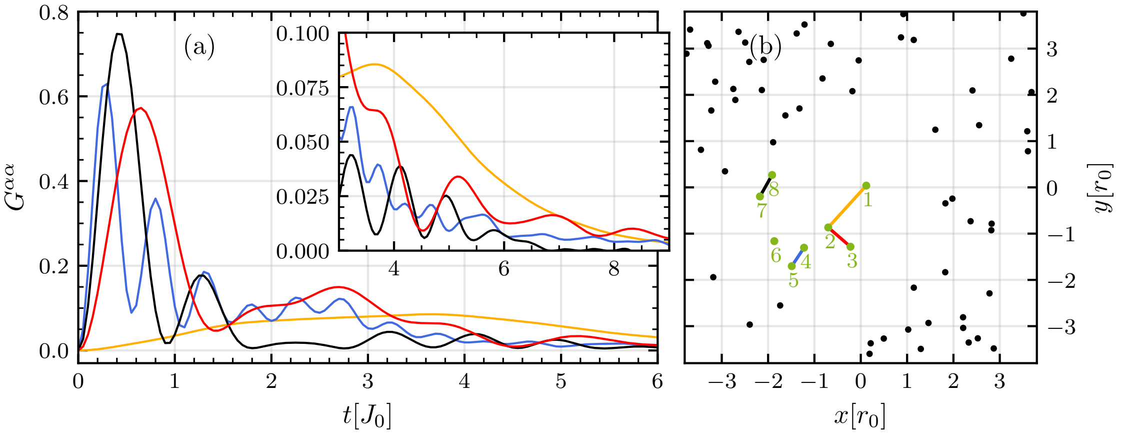

Figure 5.9: Exemplary pair correlations computed by CspinDMFT with $n = 8$ for the Heisenberg model in an inhomogeneous system with dipole-like interactions. The considered configuration is the same as in Fig. 5.8. Each pair correlation plotted in panel (a) is represented by a connecting line of the same color in panel (b).

Second, we consider an example, where the central spin is more strongly coupled to the environment, see Fig. 5.10.

---

[7] PBC could be implemented, but would not be plausible in the inhomogeneous system, since there is no translational invariance.

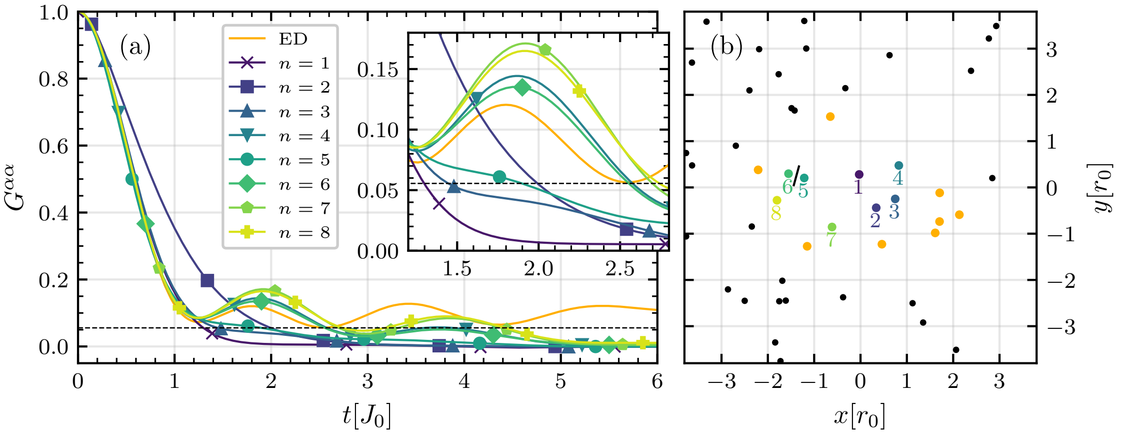

Figure 5.10: Same as Fig. 5.8, but for a different configuration with a central spin that is more strongly coupled to the environment, $J_Q \approx 2.9\,J_0$.

In this case, $z_{\text{eff}} \approx 3.4$ so that spinDMFT deviates more from ED and CspinDMFT for large n. Qualitatively, we find the same behavior as in Fig. 5.8, but the autocorrelations have a more complex structure. Overall, the autocorrelations converge more or less monotonically to the result for $n = 8$ for increasing the cluster size. The results for $n = 2$ and $n = 5$ fall out of line which is, again, not suprising because the spins No. 2 and 5 both only have a few important interaction partners. Particularly, the spins No. 5 and 6 couple very strongly to each other, $J_{56} \approx 23.1\,J_0$ so that it is not justified to draw the border between cluster and mean field between these two spins. Hence, the result for $n = 5$ deviates significantly from $n = 4$ and $n = 6$, although the spins No. 5 and 6 do not seem to be so important to be simulated quantum-mechanically for the dynamics of the central spin, see the results for $n = 4$ compared to $n \geq 6$. For the sake of completeness, we mention that cutting a strong dimer bond in half can also lead to numerical problems because the corresponding mean field becomes very strong, which can lead to large statistical and discretization errors[8]. Hence, this should be prevented. Besides this, it is noteworthy that the hybrid strategy reasonably suggests to add all $n = 8$ spins to the cluster.

We are aware that convergence plots always allow for several interpretations if no exact results are available. It should be noted, however, that our arguments are consistent with the expectation from the derivation of the mean-field approach, e.g., higher coordination numbers lead to better approximations. Overall, we conclude that the hybrid strategy for choosing the clusters performs well. Moreover, we consider the convergence of the autocorrelation with the cluster size to be a reliable measure for the validity of the approximation. Note that the creation of convergence plots is computationally cheap: The computation for the largest cluster size, which is required anyway, is typically more expensive than the computations for all smaller cluster sizes together.

---

[8] This behavior has been observed in other examples.

5.3 Dipolar relaxation of defect spins on a diamond surface

In this section, we apply CspinDMFT to the experimental scenario discussed in Sec. 2.6, which measures the dynamics of dipolar defect spins on a diamond surface [Rez22; Rez+23; Grä+23]. The main results of CspinDMFT have been published already in Ref. [Grä+23] considering the cluster-based strategy. Here, we will use the hybrid strategy given in App. D.

5.3.1 Adapted self-consistency condition

At first, we adapt the self-consistency condition to the specific problem under study. As pointed out in Sec. 2.6, the $T_{1\rho}$ measurement, our main concern, takes place in the doubly-rotating frame. In this case, the surface spins interact with one another according to the Hamiltonian

$$\mathbf{H}_{\mathrm{S}}^{\mathrm{drf}} = \frac{1}{2}\sum_{i,j} d_{ij}\left(\frac{1}{2}\mathbf{S}_i^x\mathbf{S}_j^x - \mathbf{S}_i^y\mathbf{S}_j^y + \frac{1}{2}\mathbf{S}_i^z\mathbf{S}_j^z\right), \tag{5.15a}$$

$$d_{ij} = -\frac{J_{ij}}{2}\cos\left(2\varphi_{ij}\right) = \frac{1}{2}\frac{\mu_0\gamma_{\mathrm{S}}^2}{4\pi R_{ij}^3}\cos\left(2\varphi_{ij}\right), \tag{5.15b}$$

which describes an easy-axis anisotropy in y-direction[9]. Completely analogous to the Heisenberg model, we can derive the multi-site mean-field Hamiltonian

$$\mathbf{H}_{\mathrm{S},\Gamma}^{\mathrm{drf,mf}} = \frac{1}{2}\sum_{i,j\in\Gamma} d_{ij}\,\vec{\mathbf{S}}_i^{\top}\,\underline{\underline{D}}\,\vec{\mathbf{S}}_j + \sum_{i\in\Gamma}\vec{\mathbf{S}}_i\cdot\vec{V}_i(t), \qquad \underline{\underline{D}} = \begin{pmatrix}\frac{1}{2} & 0 & 0\\ 0 & -1 & 0\\ 0 & 0 & \frac{1}{2}\end{pmatrix}, \tag{5.16}$$

as well as the self-consistency condition

$$\overline{V_i^\alpha(t)V_j^\beta(0)}^{\mathrm{mf}} = \delta^{\alpha\beta}\left(D^{\alpha\alpha}\right)^2\sum_{k,l\in\Gamma}\left(J_{ij,kl}^{\mathrm{CRA}}\right)^2\langle\mathbf{S}_k^\alpha(t)\mathbf{S}_l^\alpha(0)\rangle, \qquad \alpha,\beta\in\{x,y,z\}. \tag{5.17}$$

Note that the easy-axis anisotropy is encoded in the matrix $\underline{\underline{D}}$, of which only the diagonal matrix elements $D^{\alpha\alpha}$ are non-zero. We use the mean-field coupling tensor J^{CRA} from the CRA because the spin ensemble is inhomogeneous. This tensor is computed in the exact same manner as for the Heisenberg model, see Sec. 5.1.4. Note that any off-diagonal spin correlations ($\alpha\neq\beta$) and mean-field moments are zero according to Eq. (2.16b). In the next section, we discuss the locations of the spins, which are required to compute the dipolar couplings d_{ij} entering J^{CRA}. Note that according the definitions above, d_{ij} directly replaces J_{ij} in Sec. 5.1.4, i.e., no additional factors appear.

---

[9] The y-axis is intentionally chosen instead of the z-axis because the latter already defines the direction of the singly-rotating frame, see Sec. 2.6.

5.3.2 Locations of the surface spins

Our aim is to compute the autocorrelations of the single surface spin, which is examined in experiment. Henceforth, we refer to this spin as the central spin $\vec{\mathbf{S}}_1$. According to the discussion in Sec. 2.6.2, the positions of the surrounding spins have to be drawn randomly. To enhance the comparability between experiment and theory, we consider the following constraints:

(A) From Sec. 2.6.2, we adopt the spin density

$$n_0 = (8(1)\,\mathrm{nm})^{-2} = 0.016(4)\,\mathrm{nm}^{-2}. \tag{5.18}$$

(B) Besides the central spin, the positions of two more surface spins are determined in experiment[10],

$$\vec{r}_1 =: \begin{pmatrix} 0.22\,\mathrm{nm} \\ 0.17\,\mathrm{nm} \end{pmatrix}, \qquad \vec{r}_2 =: \begin{pmatrix} 1.7\,\mathrm{nm} \\ -3.9\,\mathrm{nm} \end{pmatrix}, \qquad \vec{r}_3 =: \begin{pmatrix} -0.1\,\mathrm{nm} \\ -5.5\,\mathrm{nm} \end{pmatrix}, \tag{5.19}$$

where $\vec{r}_1$ is the central-spin position.

(C) The spin with index 2 is the strongest-coupled neighbor of the central spin. The corresponding coupling,

$$|d_{\mathrm{max}}| = |d_{12}| \approx 1.013\,07 \times 10^{-9}\,\mathrm{eV} \approx 1.5391\,\mathrm{\mu s}^{-1}, \tag{5.20}$$

is verified to be the maximum coupling to the central spin throughout the measurements.

(D) Two spins are not allowed to have a distance smaller than

$$r_{\mathrm{min}} \approx 1\,\mathrm{nm}. \tag{5.21}$$

This value is not derived from experimental measurements and can be varied in future studies. It is beneficial to consider such a constraint because it excludes rare configurations with strongly coupled spins which are numerically difficult to investigate. The precise value of r_{min} is not a determining factor for the results, provided that it is much smaller than the spin spacing $r_0 = 8(1)\,\mathrm{nm}$. To illustrate this point, we find that on average there are only about 26(3) out of $\approx 5 \times 10^5$ pair distances smaller than r_{min} in an ensemble of 10^3 spins without any constraints.

The central spin and its two closest neighbors are fixed by constraint (B). The $N-3$ remaining spin positions are drawn successively from a uniform random distribution in a square of size $L = \sqrt{N/n_0}$ (centered around $\vec{r}^{\top} = \begin{pmatrix} 0 & 0 \end{pmatrix}$) to ensure the correct spin density according to constraint (A). If a new spin position violates the constraints (C) or (D), the position is drawn again. The majority of spins enter the actual CspinDMFT simulation only through the mean fields. Finite-size effects in the mean-field coupling tensor are discussed in Ref. [Grä+23] with the result that they are small already for $N \approx 10^3$ spins. Note that the computational cost of computing the coupling tensor

---

[10] This is realized by adapted DEER measurements [Rez22; Rez+23] and methods similar to those in Ref. [Sus+14].

is negligible and by no means comparable to the CspinDMFT simulation. Therefore, we set $N = 10^4$ to be on the safe side. An exemplary configuration created by this procedure is given in Fig. 5.11. The clover shape in gray represents the maximum-coupling constraint (C) and results from the angle dependence of the couplings $d_{ij} \propto \cos(2\varphi_{ij})$, see Eq. (5.15). It is worth mentioning that the area in which no other spins can be placed according to the constraints is several times smaller than the area that three spins occupy on average. Hence, the local density around the central spin is significantly larger than the average density. However, due to the lack of information about the precise geometry, it seems unreasonable to correct this increased density by any method.

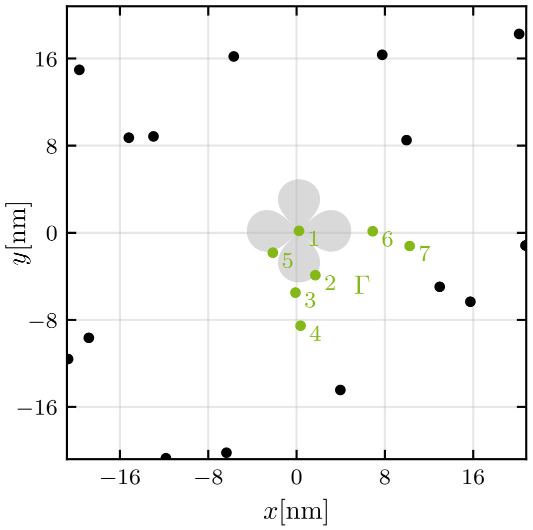

Figure 5.11: Cutout of a typical distribution of spins on the diamond surface (Seed No. 0 in the next section). Spin No. 1 is the central spin and the spins No. 2 and 3 are its fixed neighbors according to constraint (B). The remaining spins are drawn randomly considering the correct density (constraint (A)), the maximum-coupling constraint for the central spin (constraint (C)), and the minimum-distance constraint (constraint (D)). The maximum-coupling constraint is indicated by the gray area. The minimum-distance constraint is indicated by setting the dot radii of each spin to 0.5 nm. In this example seed, 4 further spins (green, No. 4-7) are added to the cluster according to the hybrid strategy ($n^{\max} = 7$).

The results of a recent experiment suggest that the surface spins can be mobile depending on the surface treatment [Dwy+22]. The corresponding hopping rate has not been investigated, but it is assumed to be much smaller than the rate of the dipolar relaxation[11]. Even in case of a small hopping rate, such processes would be relevant for any spin-relaxation signals, since each data point involves a large number of consecutive measurements during which the spin ensemble could reorganize. It should be noted that the existence of such processes does not entail that *all* of the surface spins are moving. Some spins could be better localized, for example, because the corresponding defect is located deeper below the surface. The study in Ref. [Dwy+22] provides an upper bound of about 20 % for the number of stationary surface spins. It should be noted, however, that in this work, a different diamond sample with a different surface treatment was used[12]. The experiment to which we will compare the results of CspinDMFT explicitly verifies that the central surface spin does not reorganize during the measurements. But considering the hypothesis of mobile spins, it is possible that the experiment measures the relaxation of the central surface spin in a configuration-averaged environment. We can reconstruct this situation easily in theory. For this purpose, we introduce the configuration average

---

[11] It is argued that the hopping could be driven by the laser illumination required to polarize and read out the NV spin between the measurements [Dwy+22].

[12] The defect density, for example, is about three times smaller than the one given in constraint (A).

and variance

$$\overline{G^{\alpha\alpha}}^{\mathrm{cf}}(t) := \frac{1}{K}\sum_m G^{\alpha\alpha}_{(m)}(t), \quad (\Sigma^{\alpha\alpha}(t))^2 := \frac{1}{K-1}\sum_m \left(\overline{G^{\alpha\alpha}}^{\mathrm{cf}}(t) - G^{\alpha\alpha}_{(m)}(t)\right)^2, \tag{5.22}$$

where $G^{\alpha\alpha}_{(m)}$ is the resulting autocorrelation of a specific configuration m and K is the number of considered configurations, henceforth called "seeds". The standard error of the mean defined by

$$\sigma^{\alpha\alpha}(t) := \frac{1}{\sqrt{K}}\Sigma^{\alpha\alpha}(t). \tag{5.23}$$

is also important. We present the results from CspinDMFT as well as a comparison to the experimental data in the next section. It should be noted that in the configuration averages we will consider the two closest neighbors of the central spin to be localized as well, although this has not been verified experimentally.

5.3.3 Main results

We perform CspinDMFT simulations for $K = 30$ random seeds for the ensemble surrounding the three fixed spins in experiment. The latter are always added to the cluster. Then, we add further spins according to the hybrid strategy with a given value for n^{max}. We recall that n^{max} defines the maximum possible cluster size, i.e., the considered cluster for a certain seed can contain $n \leq n^{\mathrm{max}}$ spins. At first, we track the convergence of CspinDMFT for the considered system. To this end, we consider the configuration-averaged results $\overline{G^{\alpha\alpha}}^{\mathrm{cf}}$ as n^{max} is increased, see Fig. 5.12.

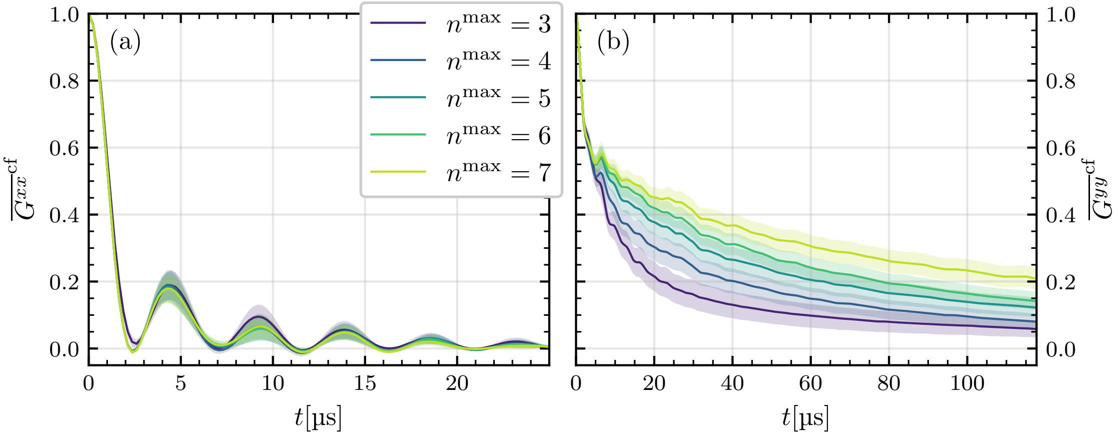

Figure 5.12: Configuration-averaged central-spin autocorrelation simulated by CspinDMFT for varying maximum cluster sizes n^{max}. Panel (a) shows the transverse and panel (b) the longitudinal autocorrelation. The transparent areas around the curves represent the standard error of the mean, see Eq. (5.23). The absolute numerical error tolerance of the configuration averages is $\epsilon = 10^{-2}$ for $n^{\mathrm{max}} = 3$ and $\epsilon = 5 \times 10^{-3}$ for $n^{\mathrm{max}} > 3$, see the main text for more details on the numerics.

The transverse autocorrelation shows a rapidly decaying oscillation and is already well converged if we only include the three spins fixed by the experiment in the cluster. In contrast, the longitudinal autocorrelation decays very slowly and shows considerable shifts to larger values as the allowed cluster size is increased. For the considered range of $n^{\max}$, the size of these shifts does not seem to decrease with increasing $n^{\max}$. However, we suspect that beyond some critical value for $n^{\max}$, the most important neighbor spins of the central spin are added to the cluster in all of the seeds. Beyond this $n^{\max}$, the shifts are expected to become smaller. Such a behavior has been already seen in the benchmarks. Consequently, we expect the results for $n^{\max} = 7$ to be closer to numerical convergence than the plot suggests at first sight. This has to be verified in future studies by considering larger cluster sizes, which can be achieved by investing more computational resources or, preferably, by revising the CRA to gain performance. The latter aspect will be discussed briefly in Sec. 5.4.3. Here, we will draw a qualitative picture. Note that the overall functional behavior of the longitudinal autocorrelation does not change upon inreasing $n^{\max}$. We obtain a rather steep drop of $\overline{G^{yy}}^{\mathrm{cf}}$ at short times followed by a considerable decelaration after about 10 µs. Before comparing this to the experiment, we make a short remark on the numerics.

We track the absolute numerical error of an individual autocorrelation included in the configuration average to be $\varepsilon < 5 \times 10^{-2}$ for $n^{\max} = 3$ and $\varepsilon < 2.5 \times 10^{-2}$ for $n^{\max} > 3$. An error of 5 % or 2.5 % relative to the initial value of an autocorrelation appears large, but only a small number of seeds actually gets close to this threshold. For example, for $n^{\max} = 7$ only 3 out of 30 seeds have a maximum error of $\varepsilon > 10^{-2}$. This error results mainly from the finite time discretization and tends to be larger if the mean fields involve rapidly oscillating correlations[13]. We can estimate the resulting error for the configuration averages to be smaller, $\Delta Q < 5 \times 10^{-3}$. This is true for all maximum cluster sizes except $n^{\max} = 3$ because here all three spins are fixed which sometimes leads to cuts of spin dimers at the edge of the cluster. In 7 out of 30 seeds, the discretization error is very large, $\Delta Q \approx 0.02 - 0.04$, which leads to a moderate error of the configuration average, $\varepsilon < 10^{-2}$. Nevertheless, the numerical errors are much smaller than the standard error of the mean shown by the transparent areas in Fig. 5.12. Hence, we conclude that they are by no means relevant for the qualitative picture we are drawing.

In the previous section, we discussed the possibility that the surface spins are moving on the surface. If this is true, the configuration average $\overline{G^{\alpha\alpha}}^{\mathrm{cf}}$ is the most appropriate quantity for a comparison between theory and experiment. The corresponding plot is displayed in Fig. 5.13. The initial drop of the transverse autocorrelation matches well with the experimental data. At larger times, CspinDMFT predicts a strongly damped oscillation, which may be driven by the strong coupling between the central spin and its neighbor (spin No. 2), since the period time of the oscillation $T \approx 4.8(5)$ µs is close to $2\pi/|d_{\max}| \approx 4.1$ µs. Because of the short time interval and the fluctuations and error bars of the experimental data, it cannot be concluded whether these oscillations are also present in experiment. The longitudinal autocorrelation matches well at short times $t < 10$ µs, i.e., the initial drop is seen in experiment and in theory and stops roughly at $\overline{G^{yy}}^{\mathrm{cf}} \approx 0.6$. Afterwards both signals decay on a much larger time scale than the transverse autocorrelation. However, the speed of this decay differs considerably between experiment and theory. Before discussing this in detail, we briefly address the scenario of completely stationary surface spins.

---

[13] Note that decreasing the step width reduces the error, but the computations can become very demanding in some cases.

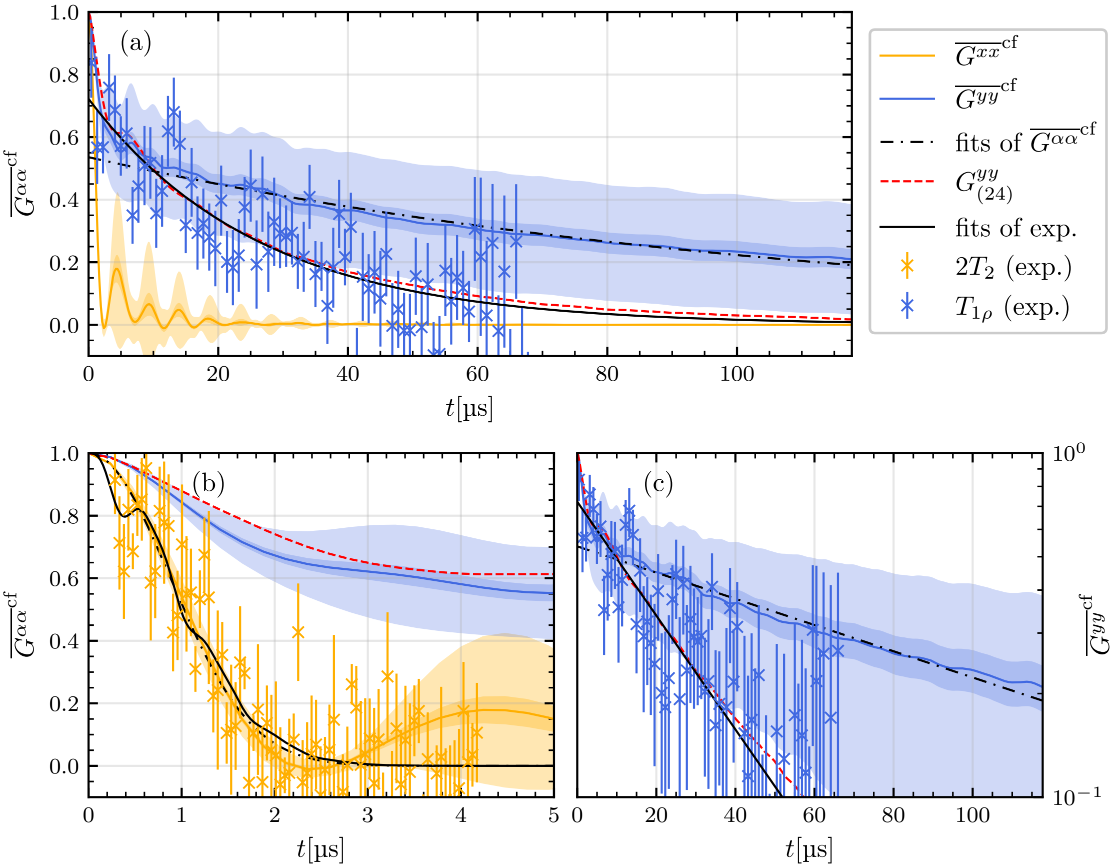

Figure 5.13: Comparison between the experimental data [RS24] (crosses with errorbars) and the results from CspinDMFT for $n^{\mathrm{max}} = 7$ (lines). The short-lived transverse correlations are shown in orange and the long-lived longitudinal correlations in blue. Panels (a) and (b) are in linear and panel (c) in logarithmic representation. For a better view, we did not include each set of data into all of the panels. The configuration averages $\overline{G^{\alpha\alpha}}^{\mathrm{cf}}$ from CspinDMFT are each surrounded by two transparent areas. The light-colored areas each represent the variance of the different seeds and the dark-colored areas the standard error of the mean, see Eqs. (5.22) and (5.23). The absolute numerical error tolerance of the configuration averages is $\epsilon = 5 \times 10^{-3}$. In addition to the configuration averages, we also show the CspinDMFT result for a specific seed (No. 24, shown in red), which matches well with the experimental data. The time scale of the echo data has been multiplied by a factor of 2 due to the conversion from singly to doubly-rotating frame as explained in Sec. 2.6.3. The fit functions and parameters are discussed in the main text, see Eqs. (5.24) to (5.28).

If the spins are not moving at all, the experiment measures a certain fixed configuration of the spins. In this case, it is not very surprising that the configuration average deviates from the experimental data because G^{yy} varies strongly from seed to seed, see the light-blue area in Fig. 5.13. Indeed, we obtain a very good agreement with the experiment, if we cherry-pick a specific seed (No. 24) as indicated by the dashed red line. This seed corresponds to the third-fastest decaying G^{yy} of the $K = 30$ seeds[14]. For a large time interval, the longitudinal result does not lie within the light-blue area which makes this seed rather special. Still, we cannot rule out that it is representative of the experiment due to the lack of knowledge about the geometry of the surrounding ensemble. We conclude that a comparison between experiment and theory cannot go beyond a very qualitative level if the spins are not moving[15].

To quantify and summarize the results, it is useful to extract the characteristic relaxation times T_2 and $T_{1\rho}$ by proper fits. As the transverse autocorrelation decays rapidly, a Gaussian fit according to

$$F^{xx}(t)[T_2] = \mathrm{e}^{-\left(\frac{t}{2T_2}\right)^2} \tag{5.24}$$

is appropriate. To account for the not completely eliminated proton noise in the singly-rotating frame, the experimental data are fitted by a modulated Gaussian,

$$F^{xx}_{\mathrm{mod}}(t)[T_2, W, \omega_{\mathrm{L,P}}] = f(t)[T_2] \exp\left\{ -\frac{40}{9} \sin^4\left(\frac{\omega_{\mathrm{L,P}} t}{4}\right) \frac{\gamma_{\mathrm{e}}^2 W^2}{\omega_{\mathrm{L,P}}^2} \right\} \tag{5.25}$$

where W^2 is the root-mean-square of the noise field and $\omega_{\mathrm{L,P}}$ is the proton Larmor frequency, which are both fit parameters. The modulation can be derived from the experimentally measured power spectrum of the noise and the filter function of the spin echo, see Ref. [Rez+23] (App. D.1) for details. The power spectrum is composed of two Lorentzians, one at zero frequency and one at the proton Larmor frequency. To derive Eq. (5.25), both Lorentzians are replaced by δ-distributions for simplicity[16]. Applying these fits to the data yields the parameters

$$\text{CspinDMFT}: \quad T_2 = 0.62(1)\,\mu\text{s}, \tag{5.26a}$$

$$\text{experiment}: \quad T_2 = 0.66(3)\,\mu\text{s}, \quad W = 37(10)\,\mu\text{T}, \quad \omega_{\mathrm{L,P}} = 36(4)\,\mu\text{s}^{-1}, \tag{5.26b}$$

and the black lines in Fig. 5.13, panel (b). The longitudinal results are fitted by an exponential function with variable prefactor according to

$$F^{yy}(t)[C, T_{1\rho}] = C\mathrm{e}^{-\frac{t}{T_{1\rho}}}, \tag{5.27}$$

which yields the fit parameters

$$\text{CspinDMFT}: \quad T_{1\rho} = 114(8)\,\mu\text{s}, \quad C = 0.536(2), \tag{5.28a}$$

$$\text{experiment}: \quad T_{1\rho} = 26(3)\,\mu\text{s}, \quad C = 0.72(5), \tag{5.28b}$$

---

[14] The speed of the decay is measured by the magnitude of G^{yy} at the last accessible point in time.

[15] However, if the experimental measurement is repeated for randomly chosen NV centers that couple to different surface-spin configurations, one could compare an unbiased configuration average instead of specific seeds.

[16] This eliminates the noise correlation time τ from the fit parameters.

along with the black lines in Fig. 5.13, panel (a). In the CspinDMFT fit, we left out the data up to $t_0 = 10\,\mu\mathrm{s}$, i.e., we fit only the tail of the autocorrelation. It is noteworthy that increasing t_0 barely changes the outcome. The extracted characteristic relaxation times are represented graphically in Fig. 5.14. The discrepancy between the experiment and the configuration average of CspinDMFT essentially boils down to a factor of 4 in the $T_{1\rho}$ times. Despite this difference, the main observation in experiment, namely, that the longitudinal autocorrelation is considerably slowed-down versus the transverse one, is qualitatively captured by CspinDMFT. The same result has been obtained in Ref. [Grä+23] using the cluster-based strategy.

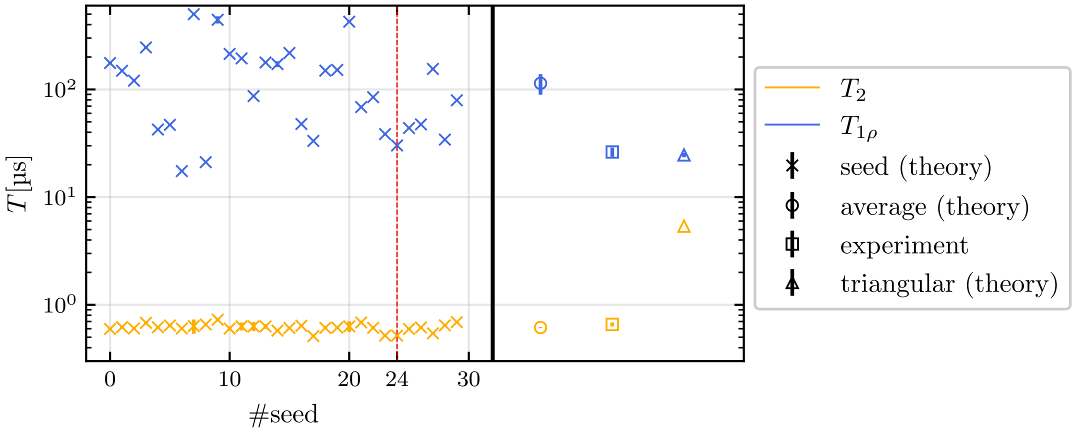

Figure 5.14: Comparison of the characteristic relaxation times between experiment [RS24] and CspinDMFT ($n^{\max} = 7$) determined by a Gaussian (T_2) and an exponential fit ($T_{1\rho}$). The relaxation times are extracted from individual seeds (crosses), from the configuration average (circles) and from the experiment (squares). In addition, we included the relaxation times for a triangular lattice with the same spin density for comparison (triangles), see Sec. 5.3.4. The results for the individual seeds are separated from the rest by the thick black line. The error bars for the individual seeds (mostly too small to be visible) and for the experimental data result directly from the fitting procedure. The error bars for the configuration averages form an estimate for the standard error of the mean, see Eq. (5.23). The error bars for the triangular lattice represent the variation resulting from changing the tilting angle. The dashed red line highlights seed No. 24, which is particularly close to the experimental results as can be seen in Fig. 5.13.

Due to the easy-axis anisotropy, a difference between $\overline{G^{xx}}^{\mathrm{cf}}$ and $\overline{G^{yy}}^{\mathrm{cf}}$ is expected and can already be seen in the results from spinDMFT, see Fig. 4.5[17]. However, in view of the anisotropy factor of only 2 in the considered Hamiltonian, see Eq. (5.15a), it is remarkable that the characteristic relaxation times T_2 and $T_{1\rho}$ differ by two orders of magnitude. Since such a large difference is not obtained by spinDMFT, we conclude that the geometry and disorder in particular play an important role for this phenomenon. To corroborate this statement, we consider the same spin model on a triangular lattice in the next section.

---

[17] The model considered for this figure is the same as the one considered in the current chapter except for a global factor of 2 in the Hamiltonian and z being the easy axis instead of y.

5.3.4 Results on the triangular lattice

We recall that the dipolar couplings are angle dependent, see Eq. (5.15b). In the inhomogeneous system, the x-axis (zero polar angle) is fixed by the provided positions of three spins close to the NV center. But for a completely random ensemble, the choice of the axis would not matter on average, because no direction is preferred. For a triangular lattice, the situation changes. Here, the spin positions are all fixed so that there are distinguishable directions. As a consequence, the results will depend on the relative angle between the lattice and the zero polar angle with respect to the couplings. In other words, the orientation of the lattice with respect to the clover matters. We capture this by introducing the *tilting angle* φ_0. For $\varphi_0 = 0$, two opposite clover leaves are parallel to one of the lattice axes, see Fig. 5.15, panel (b), for an illustration. Increasing φ_0 means rotating the clover counterclockwise which corresponds to adapting the couplings according to

$$d_{ij} = -\frac{J_{ij}}{2} \cos\left(2(\varphi_{ij} + \varphi_0)\right). \tag{5.29}$$

Making use of the symmetry of the clover[18] and the lattice, the relevant interval can be reduced to $\varphi_0 \in [0°, 15°]$, i.e., this interval is representative of any possible orientation of the clover. The autocorrelation results for $\varphi_0 = 0$ and different cluster sizes n are shown in Fig. 5.15.

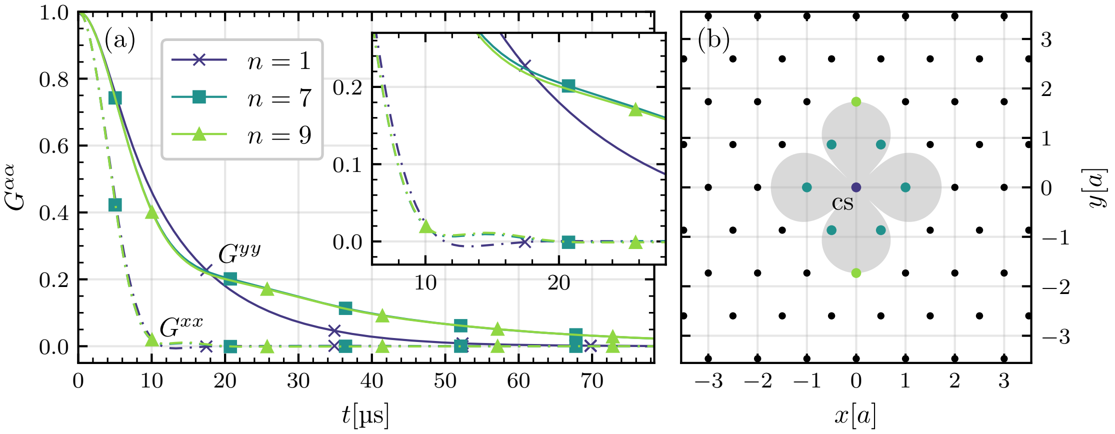

Figure 5.15: Convergence plot for the spin autocorrelations from CspinDMFT on a triangular lattice with anisotropic interaction according to Eq. (5.15a). The solid lines with markers correspond to the longitudinal autocorrelations (G^{yy}), and the dash-dotted lines with markers correspond to the transverse autocorrelations (G^{xx}). The absolute numerical error tolerance of the data is $\epsilon = 10^{-2}$. The cluster for each color in panel (a) includes all spins represented by the same color in panel (b) plus the spins of the next-smaller cluster. The x-axis is parallel to one of the lattice vectors, i.e., the tilting angle in Eq. (5.29) is $\varphi_0 = 0$. The clover in panel (b) indicates the corresponding angular dependence of the couplings.

---

[18] Note that the symmetry group of the clover defined by the couplings is D_2, because the two pairs of opposite leaves each correspond to a different sign, $\cos 2\varphi = -\cos 2(\varphi + {}^{\pi}\!/_{2})$. However, since the autocorrelations are T-symmetric, this sign does not matter globally so that we effectively arrive at D_4.

Note that passing from spinDMFT ($n = 1$) to CspinDMFT leaves the transverse decay almost untouched and makes the longitudinal decay a bit slower. The results for $n = 7$ and $n = 9$ are barely distinguishable so that we consider $n = 9$ to be close to the converged result. The spin density is set to the same value as in the inhomogeneous system (see constraint (A)) so that

$$a = \sqrt{\frac{\sqrt{3}}{2}}r_0 = 7.44\,\mathrm{nm}. \tag{5.30}$$

Thus, the time unit is fixed and the results can be provided in µs for a better comparability with the ones of the previous section.

As can be seen in Fig. 5.16, the fits from the previous section work very well for the triangular lattice. We also computed the autocorrelations for the tilting angles $\varphi_0 \in \{5°, 10°, 15°\}$, but found no qualitative differences to $\varphi_0 = 0$. The convergence is comparable and we can use the same fitting procedure.

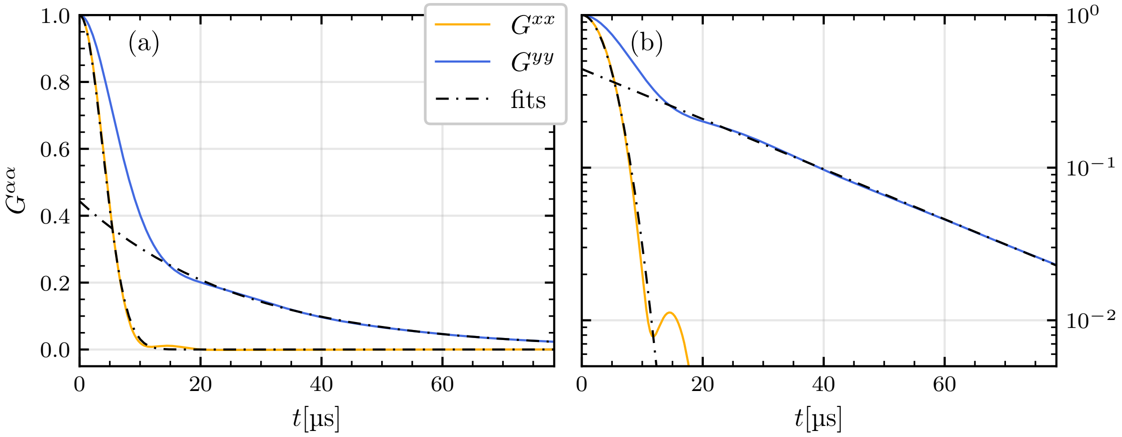

Figure 5.16: Autocorrelation results from CspinDMFT for $n^{\max} = n = 9$ on a triangular lattice with anisotropic interaction according to Eq. (5.15a) considering a tilting angle of $\varphi_0 = 0$ for the couplings in Eq. (5.29). The exponential fit for G^{yy} works very well as can be seen in the linearnormal (a) and logarithmic representation (b). The Gaussian fit for G^{xx} is also valid except for the tiny revival at about 15 µs.

The fit parameters are summarized in Tab. 5.1. From this we can estimate the average ratio between the transverse and longitudinal relaxation time to be[19]

$$\overline{\left(\frac{T_{1\rho}}{T_2}\right)} = 4.6(2). \tag{5.31}$$

Hence, the enormous difference between T_2 and $T_{1\rho}$ in the inhomogeneous system is not obtained for the triangular lattice.

---

[19] Note that this value is a bit higher than in Ref. [Grä+23]. We consider the results in this thesis to be more reliable, since the simulated clusters are larger.

Table 5.1: Fit parameters for the autocorrelations of the triangular lattice for different tilting angles φ_0 considering the fit functions Eq. (5.24) and Eq. (5.27). As in the previous section, G^{xx} is fitted by a Gaussian, see Eq. (5.24), and G^{yy} by an exponential function, see Eq. (5.27). The fits are shown graphically in Fig. 5.16.

φ_0	T_2	$T_{1\rho}$	C
0°	5.369(9)	26.46(8)	0.443(2)
5°	5.37(1)	23.7(1)	0.396(3)
10°	5.39(1)	25.0(1)	0.468(3)
15°	5.38(1)	23.49(8)	0.418(2)

5.3.5 Interpretation of the results

The takeaway of the previous section is that the geometry is pivotal for the discrepancy between the two relaxation processes. However, the precise physical cause is to be discussed. A crucial difference between the two directions is that the total longitudinal polarization, $\mathbf{m}^y$, is rigorously conserved in contrast to the transverse components $\mathbf{m}^x$ and $\mathbf{m}^z$. This conservation law holds exactly in the considered spin model, but it is only approximately fulfilled in CspinDMFT, since, over time, the cluster can lose polarization to the mean-fields, which remain zero on average. The spin autocorrelations can be interpreted as the decay of polarization of a single spin which has been polarized at $t = 0$ according to[20]

$$G_{ii}^{\alpha\alpha}(t) = 4\langle \mathbf{S}_i^\alpha(t)\mathbf{S}_i^\alpha(0)\rangle_{\rho_0} = 2\langle \mathbf{S}_i^\alpha(t)\rangle_{\rho_{i,\alpha}}, \qquad \rho_{i,\alpha} = \frac{1}{d}\left(\mathbf{1} + 2\mathbf{S}_i^\alpha\right). \tag{5.32}$$

If $\alpha \in \{x, z\}$, the polarization can decay locally due to dephasing because it is not linked to a global conservation law. In contrast, if the spin is polarized into the longitudinal direction, the local polarization can only decay by being transported away from site i. The positional disorder tends to form well-separated clusters of a few spins[21]. Transport processes may be quick within a single cluster, but are likely slowed-down beyond the cluster in comparison to a lattice. To view this in greater detail, we plot the summed-up polarization of the three fixed spins in transverse and longitudinal direction in Fig. 5.17. A considerable amount of the longitudinal polarization is transferred from the central spin to its two neighbors, which explains the previously recognized drop of $\overline{G_{11}^{yy}}^{\mathrm{cf}}$ at short times. Upon adding the time-dependent polarization of the spins No. 2 and 3 this drop is clearly smoothened as can be seen in panel (b). At the largest considered time, the three fixed spins still carry about a third of the initial polarization. In contrast, the speed of the transverse decay does not change upon adding the transverse polarization of spin No. 2 and 3. These observations indicate that the global conservation of $\mathbf{m}^y$ plays an important role for the mechanism. This could be supported in future studies by adjusting the model Hamiltonian, for example, by breaking the conservation law with an additional anisotropy between the x- and z-direction.

---

[20] While this equation is mathematically correct, it should be noted that the provided fully polarized state $\rho_{i,\alpha}$ is not realistic in experiment. But the arguments work similarly for a partly polarized spin.

[21] In this context, the term “cluster” refers to a group of proximate spins and is distinguished from the cluster in CspinDMFT. However, given that the cluster-finding algorithm in CspinDMFT explicitly considers the spatial separation of spins, these definitions are at least similar.

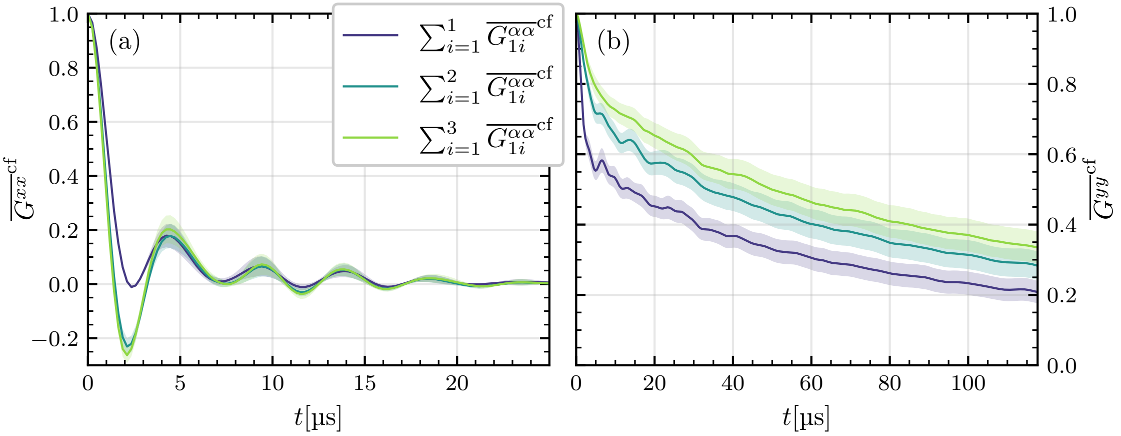

Figure 5.17: Configuration-averaged summed-up correlations of the central spin with itself and its two closest neighbors from CspinDMFT for $n^{\max} = 7$. Panel (a) shows the transverse and panel (b) the longitudinal direction. The standard error of the mean of the configuration average is represented by the colored areas.

The provided picture qualitatively explains the difference between the two decay channels and between the triangular and inhomogeneous system. It should be noted that the argument does not explicitly require the positional disorder, but only the spatial separation of the clusters. It is unclear, whether lattices of well-separated clusters would exhibit the same behavior, or whether the lack of randomness leads to a faster longitudinal relaxation. In the literature, slow transport processes in inhomogeneous systems are often explained by means of *resonance-counting* models [Bur07; Yao+14; Kuc+18; Rez22; Rez+23]. The key idea for randomly-positioned spins is the following: The ensemble is perceived as a collection of pairs of strongly-coupled spins, termed pseudospins. Two distinct pseudospins resonate with each other if the mismatch of the intra-pseudospin couplings is small compared to the inter-pseudospin couplings. By counting the number of these resonances, generic conclusions for the transport properties are made. In Ref. [Yao+14], for example, resonance counting is employed to determine under which conditions (dimension, range of interaction) MBL can occur[22].

The remarkable slowness of the longitudinal decay in experiment and in the numerical results underlines that the process of thermalization is considerably weakened. Before analyzing this further, we include a section on the state of research of the subjects thermalization and MBL.

5.3.6 Excursus: Thermalization and many-body localization

Thermalization is a fundamental principle in statistical physics. It states that an isolated many-body system out of equilibrium evolves in time to eventually arrive at a very generic state, which can be described by a few macroscopic variables only. This generic state is called thermal state and it can be mimicked, for example, by the microcanonical ensemble. Although the occurrence of thermalization is standard textbook knowledge

---

[22] According to this work, the critical dimension for random dipolar spins is $D = 1.5$, which would exclude the considered surface-spin system from MBL.

[Sch07], its microscopic origin in quantum systems is very subtle and remains subject of current research [DAl+16].

The eigenstate thermalization hypothesis proposed by Deutsch and Srednicki provides a deep understanding of how quantum thermalization may occur [Deu91; Sre94]. It entails that the expectation value of a typical observable with respect to a single eigenstate of the Hamiltonian is representative of a thermal expectation value[23]. A typical out-of equilibration state superposes and mixes the eigenstates of a small energy window in such a way that expectation values of certain observables display the out-of equilibrium situation. As time proceeds, the initial state dephases with respect to the energy eigenstates and the initial coherence is lost. Then, the expectation value of any typical observable can be described, either, by a sum of expectation values of eigenstates within a small energy window (microcanonical ensemble), or, according to the ETH, by the expectation value with respect to a single representative eigenstate of the Hamiltonian. A sketch of this principle is provided in Fig. 5.18. The ETH has been tested and confirmed in various finite-size systems [RDO08; DAl+16], but conclusions for the thermodynamic limit are never fully rigorous. Therefore, the ETH remains a hypothesis and it is not clear, whether it is a necessary condition for thermalization [NH15; DAl+16].

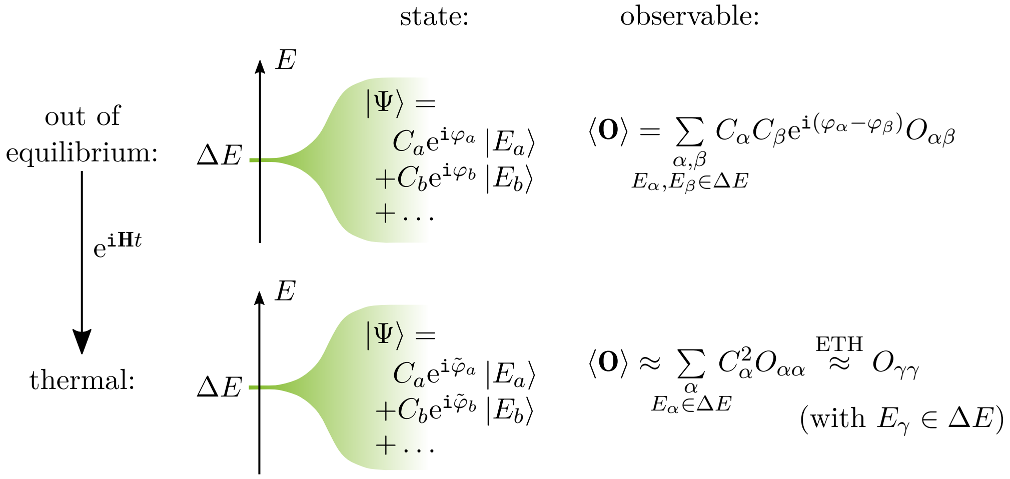

Figure 5.18: Thermalization in an isolated quantum system from the point of view of the energy eigenbasis. A typical out-of-equilibrium state (pure in this example) superposes energy eigenstates of a subextensively small energy window ΔE. The Hamiltonian time evolution does not change the occupations, but only the phases of the eigenstates. This entails that thermalization corresponds to dephasing in the energy eigenbasis. For a typical observable $\mathbf{O}$ with matrix elements $O_{\alpha\beta} = \langle E_\alpha | \mathbf{O} | E_\beta \rangle$, the initial phases may be coherent. For large enough times, this coherence is entirely lost so that only the energy-diagonal matrix elements $O_{\alpha\alpha}$ contribute to the expectation value. The ETH states that the diagonal elements do not vary much within the small energy window so that one may approximate the expectation value by a single energy-diagonal matrix element $O_{\gamma\gamma}$ within the energy window.

Aside from this, there are also several scenarios where thermalization is fundamentally absent. In integrable systems, for example, the number of conserved quantities is so

---

[23] The word “typical” is vague, but cannot be circumvented. Indeed, one can always create exotic observables for which the ETH cannot hold true, for example, the energy projectors.

large that the dynamics is too constrained for the system to thermalize. Another class of systems resists thermalization due to the existence of an extrinsic randomness or disorder. In a pioneering paper from 1958, Anderson showed that diffusion is absent in certain lattices with on-site disorder [And58]. In this scenario, the single-particle wave functions are exponentially localized so that the system is insulating. Remarkably, an arbitrarily small variance of the disorder potential suffices for this phenomenon to occur in $D \leq 2$. One should note, however, that the Anderson model considers no interactions between the particles[24], so the robustness of the phenomenon must be questioned. Adding a small perturbing interaction might lead to slow diffusion processes again [Aba+19]. Indeed, localization has been observed experimentally [Sch+07; Bil+08; Roa+08], but mostly in well-controllable, artificial systems such as optical lattices.

The absence of thermalization in presence of interactions is known as many-body localization and is subject of today's research [Aba+19]. The phenomenology of MBL can be characterized by the existence of quasi-local integrals of motion (LIOM) [SPA13a; HNO14]. The MBL phase exhibits an emergent integrability due to the existence of an extensive number of LIOMs. From this point of view, the absence of thermalization is easily understood: A local observable can have a considerable overlap with some of the LIOMs. Since the Hamiltonian time evolution leaves the latter invariant, the local observable will, at least partly, remain local even for infinite times. In contrast, we expect any local observable to delocalize entirely in a thermalizing system. Further typical signatures of the MBL phase are:

- The ETH is not fulfilled [NH15; Aba+19].
- The energy-level statistics approaches a Poisson distribution, i.e., there is no energy-level repulsion as in thermalizing systems [Aba+19].
- The entanglement entropy of highly excited energy eigenstates grows by an area law and not by a volume law as in thermalizing systems [NH15; Aba+19].
- Starting from a product state, entanglement grows logarithmically in time [SPA13b; HNO14; Luk+19; NH15; Aba+19].

A system is called fully many-body localized (FMBL) if all of the many-body eigenstates are localized. In FMBL systems, the MBL phase can, in principle, persist at arbitrarily high temperatures [Alt18].

A rich phenomenology can be derived under the initial assumption that the MBL phase exists. But rigorously proving the latter turns out to be very difficult. This is demonstrated, for example, by the immense effort put into a proof considering a 1D transverse-field Ising model in Ref. [Imb16], which still required some additional assumptions. Indeed, MBL has been studied mostly in 1D and using approximative schemes, for example real-space renormalization group (RG) [VHA15], DMRG [ŽPP08; Ser+16] or brute-force methods in finite-size systems [Yao+14; LLA16; SLZ20]. Ref. [WPS19] uses a tensor-network approach to access a Bose-Hubbard model in 2D also finding signatures of the MBL phase.

On the experimental side, it is very challenging to observe MBL because the system under study must be very well isolated from the environment [NH15; Aba+19]. The experiment

---

[24] Indeed, this makes the Anderson model integrable, since the single-particle energies are conserved.

in Ref. [Sch+15], for example, considered the time evolution of a charge-density wave in a system of ultracold fermions (Aubry-André model). For a sufficiently large disorder width, the imbalance of charges survives for long times indicating the occurrence of MBL. Another example is provided by Ref. [Cho+16], which observed non-thermalizing behavior in an optical lattice of bosons (^{87}Rb atoms) in two dimensions.

While many studies in the past two decades corroborated the existence of the MBL phase, it is highly questioned in several recent articles, whether or where the celebrated and presumably observed MBL phase indeed exists [Šun+20; SP21; SP23; Kie+22; EMB23]. For example in 2023, Evers, Modak and Bera claimed that close to the potential MBL transition, finite-size effects are expected to be very strong due to the existence of rare ergodic bubbles that are not necessarily included in a small system cutout [EMB23]. In a slow process termed "creep", these ergodic bubbles thermalize also almost localized regions of the system which ultimately leads to many-body **de**localization in the thermodynamic limit. It is stated that many previous numerical and experimental studies did not account for the occurrence of creep which partly invalidates the interpretations in these studies. Evers *et al.* considered a model of spinless fermions on a chain (t-V model with $V = 1$) according to

$$\mathbf{H} = -\frac{1}{2}\sum_{i=1}^{L-1}\left(\mathbf{c}_i^\dagger \mathbf{c}_{i+1} + \text{h.c.}\right) + \sum_{i=1}^{L}\epsilon_i\left(\mathbf{n}_i - \frac{1}{2}\right) + \sum_{i=1}^{L-1}\left(\mathbf{n}_i - \frac{1}{2}\right)\left(\mathbf{n}_{i+1} - \frac{1}{2}\right), \tag{5.33}$$

where $\epsilon_i \in [-W, W]$ represents a random on-site potential[25]. Their studies do not rule out MBL, but shift the critical disorder width at which it may occur to a rather large value[26], $W_\text{crit} \approx 10$. As detailed in Fig. 5.19, the authors predict a phase diagram with a large prethermal MBL phase, in which diffusion is slow, but not fully absent.

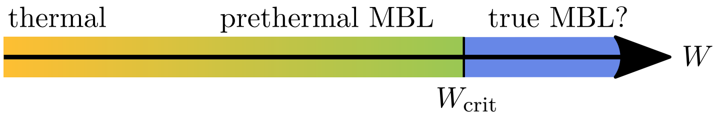

Figure 5.19: Schematic phase diagram of low-dimensional many-body systems with extrinsic disorder W [EMB23; Lon+23]. Whether true MBL exists, remains an open question.

Another interesting article in this context is Ref. [Pan+20], which questions entirely whether the MBL transition can be studied with nowadays available techniques and resources. The authors provide arguments that, in experiments, slow transport is not distinguishable from MBL at reachable times and on the numerical side, the reachable system sizes are simply too small to draw conclusions about the thermodynamic limit. Hence, the conclusion is drawn that it cannot be finally decided whether MBL exists or not and if so, in which systems. But no matter if true MBL exists or not, it is anyway interesting to look closer into the systems that exhibit at least precursors of this phase. Even if thermalization ultimately takes place, the time scale can be enormously large. This is not only interesting from a fundamental physical point of view, but perhaps also

---

[25] By means of a Jordan-Wigner transformation, this model can be mapped to an anisotropic Heisenberg model in one dimension.

[26] For comparison, earlier studies predicted half as large or even smaller values, e.g., $W_\text{crit} \approx 5.4$ [SLZ20].

for technological applications because it allows one to maintain quantum information locally for a very long time.

5.3.7 Interpretation of the results in the context of many-body localization

We note that the generic behavior of the correlations computed by spinDMFT and CspinDMFT agrees with thermalization because they ultimately decay to zero[27]. This can be well seen in Sec. 4.2 and in all benchmarks in Sec. 5.2. In the inhomogeneous system, the average correlation also decays, but the considered time window is simply too small to draw conclusions about $t = \infty$. The exponential fit we performed in Fig. 5.13 is advantageous because it works acceptably well for experiment and theory and it allows to boil the speed of the decay down to a single parameter $T_{1\rho}$. However, considering the logarithmic representation in panel (c), the curvature of the configuration average seems to be slower than exponential. To capture this, we apply a stretched exponential fit according to

$$F^{yy}_{\mathrm{str-exp}}(t)\left[\tilde{T}_{1\rho}, k\right] = \exp\left(\frac{t}{\tilde{T}_{1\rho}}\right)^{k}, \qquad \tilde{T}_{1\rho} = 36.8(2)\,\mathrm{\mu s}, \qquad k = 0.365(3), \tag{5.34}$$

which is shown graphically in Fig. 5.20.

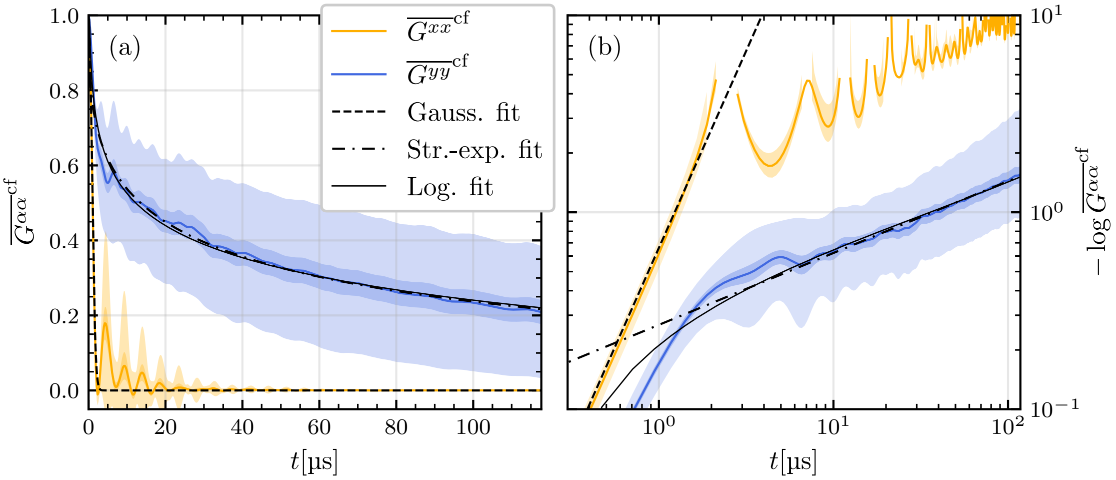

Figure 5.20: Configuration-averaged results from CspinDMFT for $n^{\max} = n = 7$ and fits. Panel (a) shows the linear and panel (b) the triple-log representation which is helpful to identify stretched-exponential behavior. The configuration averages $\overline{G^{\alpha\alpha}}^{\mathrm{cf}}$ are each environed by two transparent areas. The light-blue area represents the variance of the different seeds and the dark-blue area the standard error of the mean. The transverse autocorrelation is fitted by a Gaussian according to Eq. (5.24) and the longitudinal autocorrelation by a stretched exponential according to Eq. (5.34) and a logarithm according to Eq. (5.35). Both the stretched-exponential and the logarithmic fit work out very well and are nearly indistinguishable from one another.

---

[27] Note that this is our only indicator. It is not possible to test the ETH in the mean-field framework, since we have no access to energy eigenstates.

Note that we still only use two fit parameters and that we consider the data on the whole time interval for the fitting. Clearly the fit does not work at very short times, since $\frac{\mathrm{d}G^{yy}}{\mathrm{d}t} = 0$ in contrast to the fit function, but the subsequent decay is captured very well as can be seen in the linear and triple-log representation. In future studies, the maximum time of the simulation may be increased to see whether the stretched-exponential behavior continues for more than two powers of ten[28].

It is noteworthy that infinite-temperature autocorrelations are indeed measurable probes of thermalization and if they decay slowly, this can be a notable characteristic of a prethermal MBL regime [LBB19; Lon+23]. As such, stretched-exponential behavior has been observed numerically and experimentally in various spin systems with extrinsic and/or positional disorder [Lon+23; Dav+23; Cho+17a; Kuc+18]. Here, we obtain preliminary evidence of such behavior in a 2D system with positional disorder. We emphasize that it would be desirable to increase the maximum cluster size as well as the time interval for a better validation of our observations. Note, for example, that a logarithmic fit according to

$$F^{yy}_{\log}(t)\left[\hat{T}_{1\rho}, r\right] = -r \ln\left(\frac{t}{\hat{T}_{1\rho}}\right), \qquad \hat{T}_{1\rho} = 701(12)\,\mathrm{\mu s}, \qquad r = 0.1235(7), \tag{5.35}$$

works equally well as a stretched-exponential fit on the considered time interval as can also be seen in Fig. 5.20. A reliable distinction of logarithmic and stretched-exponential behavior requires at least one more power of ten in the time scale [Lon+23].

5.4 Chapter conclusion and outlook

5.4.1 Simulating spin dynamics by CspinDMFT

CspinDMFT extends spinDMFT by passing from a single-site to a multi-site model, as illustrated in Fig. 5.4. The latter describes a cluster of spins in a background of correlated Gaussian mean fields. A particular challenge of CspinDMFT is the formulation of a closed self-consistency problem, since the mean fields are composed of a large number of *a priori* unknown out-of-cluster correlations. In lattices, these correlations can be straightforwardly mapped to their exact replicas in the cluster, while in inhomogeneous systems, an approximate mapping scheme is given by the CRA. The benchmarks in Sec. 5.2 demonstrate the rapid convergence of CspinDMFT with the cluster size n for lattices. In inhomogeneous systems, the convergence can be slower in some cases, see for example the results for defect spins on a diamond surface in Fig. 5.12. Nevertheless, CspinDMFT is in qualitative agreement with the experiment showing a vast difference between the transverse and longitudinal relaxation of these spins. It also confirms the assumption that this difference is caused by the geometry, i.e., the positional disorder of the spins. However, it should be noted that CspinDMFT does not capture the experimental data quantitatively. In view of the fact that the difference between the

---

[28] Note that the mean-field sampling requires the diagonalization of a covariance matrix, the dimension of which increases linearly with the maximum time. At some point, this will become the computational bottleneck of the simulation.

longitudinal autocorrelation $\overline{G^{yy}}^{\mathrm{cf}}$ in CspinDMFT and the experimental data increases upon incrementing the maximum cluster size $n^{\max}$, the presence of systematic errors is very likely. These will be discussed in the following section.

5.4.2 Systematic error sources

In theory, a potential error source aside from the mean-field approximation itself is the mapping of correlations using the CRA. The latter might be tested and adapted in future studies as we will point out in the next section. Furthermore, there are several potential error sources in experiment. For instance, the surface-spin state has to be read out indirectly via optical detection of the NV spin. The latter clearly has further interaction partners, which potentially disturb the obtained signals. Furthermore, the $T_{1\rho}$ relaxation takes place in the doubly-rotating frame, which implies two nested RWAs. Imperfections in the field alignments and the applied pulses will certainly affect the experimental data.

In addition, we recall that there are many uncertainties concerning the surface properties, in particular, the geometry. For example, is it valid to place the spins one by one or could their locations be correlated (beyond a minimum distance) to one another? Are the spins mobile and, if so, which fraction of them? If some of the spins are mobile, what is the corresponding hopping rate? If the spins move at a similar speed as the speed of the dipolar relaxation, the hopping forms another relevant source of decoherence which is not yet modeled. We remind the reader that the occurrence of MBL is very unstable to weak thermalizing environments [Aba+19]. It is plausible that this property transfers also to a prethermal MBL phase. The appearance of any kind of thermal bath, for example due to some surface spins being mobile or due to a remainder of the proton noise, could lead to considerable discrepancies between experiment and the bare spin model in Eq. (5.15). In view of all of these uncertainties, we consider the qualitative agreement between experiment and theory to be fully satisfactory.

5.4.3 Testing and reformulating the correlation-replica approximation

The idea of the CRA formulated in Sec. 5.1.4 is to generate the mean fields in an inhomogeneous system by approximating the out-of-cluster correlations by in-cluster correlations. The mapping required for this relies on quantities that classify the correlations based on their short-time behavior. The CRA has two major drawbacks. The first and obvious one is that the mapping of the correlations is not really accurate. We discussed that the magnitude of the error induced by this could be small, but a numerical study for confirmation has not yet been done. There is indeed a way to test the CRA. As detailed in Fig. 5.21, one could simulate the correlation functions for a given seed A of the inhomogenous system by constructing the mean fields from correlations that have been self-consistently computed from another seed B. The geometry of the environment of a cluster is essentially independent of the geometry of the cluster itself. Therefore, if the CRA is accurate, it should not matter which set of correlations it is based on: one could equally use the correlations of the cluster from seed A or from seed B or from any other seed. The only important aspects are that the set of correlations used is sufficiently large to cover the variety of correlations occurring in the ensemble, and that the set results from a well-converged self-consistent iteration. Consequently, by comparing the spin correlations of the cluster of seed A computed in two different ways (using the correlations of seed A for the CRA or using the correlations of seed B for the CRA), we obtain an error estimate of the CRA. For a reliable test, this procedure should be repeated for several pairs of seeds. Subsequently, if the CRA turns out to be too inaccurate, one could improve it by introducing further classifying quantities, for example, based on higher time derivatives of the correlations.

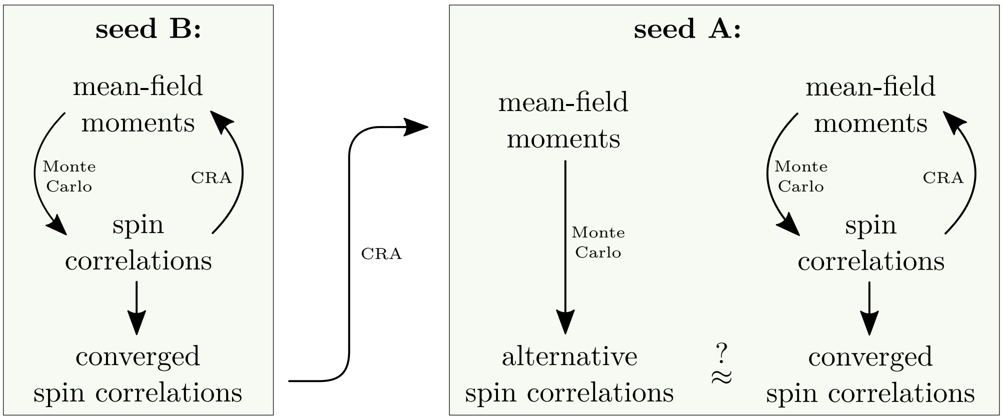

Figure 5.21: Testing procedure for the CRA. The crucial step is the arrow that connects seed B with seed A. The converged correlations from seed B are used as building blocks for the mean-fields of seed A employing the CRA. The simulated alternative spin correlations can be compared to the converged spin correlations resulting from a regular self-consistent iteration for seed A. If the CRA is accurate, it should not make a big difference, whether we insert the correlations of the cluster of seed A or seed B into it. Hence, this procedure can be used to estimate the error of the CRA.

The second disadvantage of the CRA is the numerical effort implied by it. Although we are mainly interested in the central spins autocorrelation, applying the CRA requires computing all $n(n+1)/2$ correlations on the cluster of size n. If it is not important which specific set of correlations is inserted to the CRA, i.e., if the above test is successful, the computational cost of seed farming can be significantly reduced. To this end, one should perform the entire self-consistent computation for one or a few seeds to obtain a sufficiently large set of correlations. Subsequently, one performs the actual seed farming by using this set to construct the second mean-field moments for the new simulations. In this way, one needs to perform only one iteration step per seed (instead of about 4) and compute only the central-spin autocorrelation for each seed. With such an extension, the maximum cluster sizes and time scales could be considerably increased.

5.4.4 Extending the spin model

One of the advantages of spinDMFT and CspinDMFT is their versatility. As demonstrated in Ref. [Grä+21] (Sec. IV), a Gaussian on-site potential can be easily included in the mean-field framework. In this way, one could also use CspinDMFT to simulate the longitudinal relaxation in the singly-rotating frame (T_1), which is affected by a proton-noise source at the diamond surface. A comparison with the experimental data ([Rez22; Rez+23]) could provide a deeper insight into the obtained deviation between experiment and theory in the doubly-rotating frame. Furthermore, it may be promising to consider the relaxation of the NV spin directly, as this is probably easier to measure in experiment [Rez22; Rez+23; Dwy+22]. The NV spin may be simply included in the simulations as an additional special spin.

6 Simulating NMR experiments with spinDMFT and extensions

The main goal of nuclear magnetic resonance spectroscopy is to understand the chemical structure of a sample by resonantly addressing its nuclear spins. A brief introduction to this topic has been given in Sec. 2.5, where we also introduced the FID and the spin echo as basic NMR measurements. Theoretical calculations of such signals are challenging due to the large number of particles involved. Finite-size simulations, such as ED [Ble21] or CET [Wei+06; Ble21] are typically not reliable, as they only capture a few tens of spins.

The short-time behavior of the FID of a regular crystal is well captured by its first moments in the frequency domain[1]. As such, the importance of the second moments has been elaborated by van Vleck already in the 1940s [Van48]. Since that time, numerous approaches to compute FIDs have been developed [LN57; Tjo66; JP73; PL73; PL74; EC75; BPS76; Sha91; Jen95; Fin97; Zha+07; Sav+14]. But despite their accuracy for the specific considered example (usually calcium fluoride), they are not widely used at present. This may be attributed to the challenges in applying and extending the corresponding method to the scenario under study. With the nowadays available computational resources, fully classical simulations [EF15; SF18], hybrid quantum-classical simulations [SF18; SF20] and coupled quantum-cluster simulations [SF20] represent powerful alternatives to calculate FIDs. However, one may question whether these approaches can be easily extended. It is unclear if they can be successfully adapted to different measurement protocols, systems with smaller coordination numbers, or interactions beyond the standard homonuclear Hamiltonian.

The dynamic mean-field framework given by spinDMFT can prove to be an accurate and flexible tool for the various possible setups in NMR spectroscopy, complementing the currently used toolset [Con20]. We recall that spinDMFT has been developed to access the dynamics of spin ensembles at infinite temperature. This makes it less general than other mean-field theories, but at the same time perfectly tailored to NMR because nuclear spin ensembles are completely disordered at ambient conditions due to the smallness of the nuclear gyromagnetic ratios. In Ref. [GHU24], we established spinDMFT and its extensions as alternative tools for simulating NMR signals. The mean-field framework is not necessarily more accurate than the above-listed methods, but it appears to be highly versatile due to its description via an effective Hamiltonian. This versatility has been demonstrated in the above reference by considering two rather distinct examples. The corresponding findings will be summarized in this chapter.

First, we introduce nl-spinDMFT to compute homonuclear FIDs in Sec. 6.1 and to apply it to calcium fluoride in Sec. 6.2. In section Sec. 6.3, we use spinDMFT to compute NMR

---

[1] These correspond to time derivatives of the FID at $t = 0$ and are essentially nested sums of dipolar couplings.

signals of ^{13}C in adamantane. A conclusion and an outlook are provided in Sec. 6.4. As indicated above, several contents of this chapter are based on Ref. [GHU24][2].

6.1 Computing homonuclear free induction decays with non-local spinDMFT

6.1.1 The role of pair correlations

In Eq. (2.32), we related the FID to a double sum of spin correlations. The sum includes autocorrelations as well as pair correlations at infinite-temperature. In the derivation of spinDMFT in Ch. 4, we used the fact that pair correlations are suppressed by the coordination number and can be neglected if z is large [Grä+21; Zob88]. It turns out, however, that the pair correlations appear in such large numbers in the FID that they actually remain relevant. This can be seen directly in the example of a Bethe lattice, if we reorder the correlation sum according to

$$\mathcal{F}(t) \propto \sum_{i,j} \langle \mathbf{S}_i^x(t)\mathbf{S}_j^x(0)\rangle = \sum_i \Big(\underbrace{\langle \mathbf{S}_i^x(t)\mathbf{S}_i^x(0)\rangle}_{\propto 1} + \sum_{p=1}^{\infty} \underbrace{\sum_{j:\lambda(i,j)=p}}_{\propto z^p} \underbrace{\langle \mathbf{S}_i^x(t)\mathbf{S}_j^x(0)\rangle}_{\propto 1/z^p} \Big). \tag{6.1}$$

The outer sum implies a factor of N and is thus not relevant to us. The first inner sum runs over all sets of p-th nearest-neighbor sites. The second inner sum runs over all sites j of a set, that is, all sites j with a relative distance of $p = \lambda(i,j)$ links with respect to site i. In Tab. 4.1, we can read off that pair correlations, that extend over p links on the Bethe lattice, are suppressed by $1/z^p$. At the same time, their multiplicity is z^p. Consequently, these factors cancel each other so that each order p is relevant for the FID on a Bethe lattice. Thus, there is no argument to neglect them, neither on the Bethe lattice nor for other geometries. Still, the FID can be accessed as will be discussed in the next subsection.

It is noteworthy that the sum in Eq. (6.1) is different from the sum by which the mean-fields are constructed, see for example Eq. (4.19). In the latter sum, each spin correlation acquires a coupling-dependent weight. If the couplings fall of quickly with the distance and z is large, pair correlations are negligible for the mean-fields, although they are not negligible for the FID. This has been demonstrated for the Bethe lattice with NN interactions in Ref. [Grä+21] and is discussed for a general lattice with NN interactions in App. B. The physical explanation for this behavior is that the FID measures the far field of the system, while a mean-field measures the local field at a single site.

---

[2] We highlight the different naming of the cluster size, n vs. l, and the order (introduced later), o vs. n, in this thesis and in the cited article.

6.1.2 Non-local spinDMFT

Strategy

The relevance of pair correlations rules spinDMFT out for the computation of the FID. Concurrently, the usage of CspinDMFT appears to be an overkill, since spinDMFT already reliably estimates the mean-fields if the coordination number is large. Consequently, we proposed an in-between approach in Ref. [GHU24], which separates the computation of the mean-fields from the computation of the FID. As detailed in Fig. 6.1, step (1) is to compute the spin autocorrelations self-consistently by spinDMFT. In step (2), we compute the different spin correlations required for the FID by performing simulations of quantum clusters in a mean-field background, which is constructed using the spin autocorrelations from the first step. This step is referred to as nl-spinDMFT because it efficiently accesses **n**on-**l**ocal spin correlations. We use the index c to categorize the different kinds of spin correlations similar to the idea of correlation replicas presented in Sec. 5.1.4. Eventually, the calculated correlations are superposed to obtain the FID.

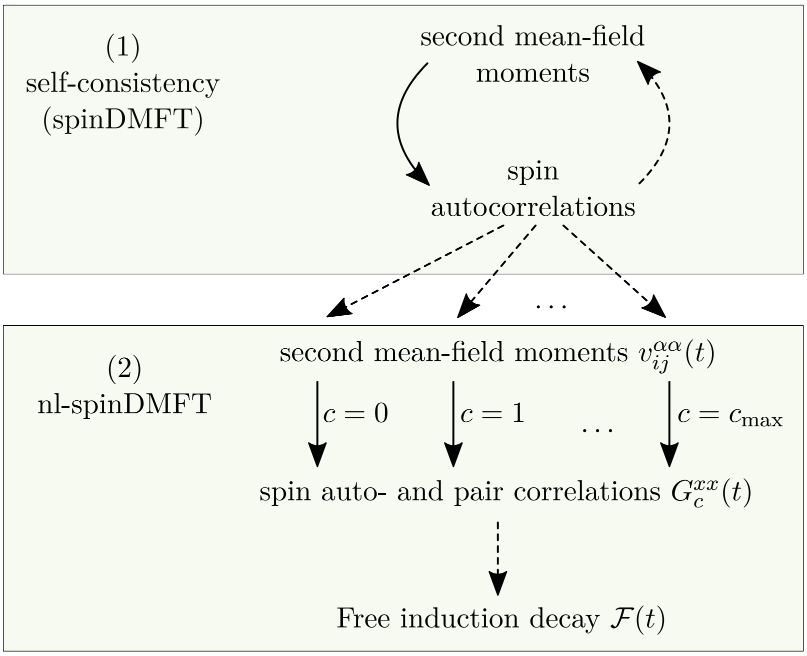

Figure 6.1: Strategy to compute the FID using spinDMFT and nl-spinDMFT. The dashed arrows correspond to computationally cheap operations. The solid arrows correspond to computationally demanding Monte-Carlo simulations.

The simulations in step (2) are analogous to CspinDMFT, but we do not consider a self-consistency loop anymore. In particular, we consider the mean-field Hamiltonian

$$\mathbf{H}_\Gamma^{\mathrm{mf}} = \frac{1}{2}\sum_{i,j\in\Gamma} d_{ij}\vec{\mathbf{S}}_i^\top \underline{\underline{D}}\vec{\mathbf{S}}_j + \sum_{i\in\Gamma}\vec{\mathbf{S}}_i\cdot\vec{V}_i(t), \qquad \underline{\underline{D}} = \begin{pmatrix} 1 & 0 & 0 \\ 0 & 1 & 0 \\ 0 & 0 & -2 \end{pmatrix}, \tag{6.2}$$

where Γ denotes the cluster, which contains n spins. Note that we considered the homonuclear Hamiltonian from Eq. (2.24) as the underlying spin model assuming a secular dipolar interaction. We recall the definition of the secular couplings[3],

$$d_{ij}(\vec{n}_B) = d_{\vec{R}_{ij}}(\vec{n}_B) = \frac{1 - 3\,(\vec{n}_{ij} \cdot \vec{n}_B)^2}{2} \frac{\mu_0}{4\pi} \frac{\gamma_i \gamma_j}{|\vec{R}_{ij}|^3}. \tag{6.3}$$

The second mean-field moments are generally given by[4]

$$\overline{V_i^\alpha(t) V_j^\beta(0)}^{\text{mf}} = \delta^{\alpha\beta}\,(D^{\alpha\alpha})^2 \sum_{k,l \notin \Gamma} d_{ik} d_{jl} \langle \mathbf{S}_k^\alpha(t) \mathbf{S}_l^\alpha(0) \rangle \tag{6.4}$$

with $\alpha, \beta \in \{x, y, z\}$. It is important to note that the spins in Γ are excluded from the sum. This means that each spin contributes only once to the Hamiltonian in Eq. (6.2), either quantum mechanically or classically via the mean-fields. According to the scheme in Fig. 6.1, our only building block for the mean-fields are the autocorrelations. Hence, we neglect any non-local correlation so that we eventually obtain

$$\overline{V_i^\alpha(t) V_j^\beta(0)}^{\text{mf}} \approx \delta^{\alpha\beta}\,(D^{\alpha\alpha})^2\, J^2_{(0),ij} \langle \mathbf{S}^\alpha(t) \mathbf{S}^\alpha(0) \rangle, \tag{6.5a}$$

$$J^2_{(0),ij} := \sum_{k \notin \Gamma} d_{ik} d_{jk}. \tag{6.5b}$$

Similar to spinDMFT, this approximation is justified for large coordination numbers. With this, the second mean-field moments can be straightforwardly computed from the spin autocorrelations obtained in step (1). The remaining ingredient for step (2) is the choice of the clusters.

Generating the clusters order by order

We remind the reader that different correlations are accessed by separate simulations of a spin cluster in a mean-field background. For an optimal performance, the cluster should be varied from simulation to simulation. A phenomenologically motivated procedure for the choice of the cluster has been proposed in [GHU24]. The basic idea is that the correlation $\langle \mathbf{S}_i^\alpha(t) \mathbf{S}_j^\alpha(0) \rangle$ between site i and j does not only result from the direct spin-spin coupling J_{ij}, but also from indirect couplings via one or several intermediate spins. In order to account for these effects, the intermediate spins have to be included in the cluster[5].

This is formalized by decomposing the pair correlation between site i and j into different contributions, each of them representing a path from i to j on the lattice. We define an *order o* of a contribution as the number of links on the corresponding path as illustrated in Fig. 6.2. A valid link connects two sites that have a finite coupling between them, e.g., in case of NN interactions we consider only links between nearest neighbors. In case of long-range interactions, each site couples to an infinite number of sites. To keep

---

[3] For details, see Secs. 2.3 and 2.4.

[4] Note that any off-diagonal correlations ($\alpha \neq \beta$) and thus any off-diagonal mean-field moments are zero due to Eq. (2.16b).

[5] Note that the mean-fields cannot generate correlations between two spins, since back actions of the cluster on the mean-fields are neglected by construction.

the number of paths per order tractable, we truncate long-range couplings at a certain J_{crit}, i.e., we consider as relevant only those links that connect two sites k and l with $|J_{kl}| > |J_{\mathrm{crit}}|$. The proposed procedure adds the presumably most important intermediate spins order by order to the cluster starting from the lowest relevant order, $o = 2$. Note that the spins i and j are added by default so that the first order ($o = 1$) is automatically accounted for.

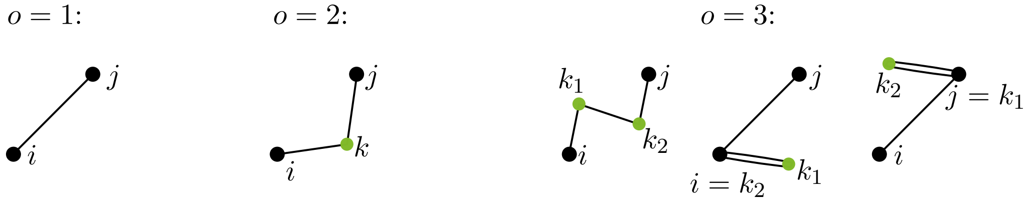

Figure 6.2: Schematic plot of the first three orders. A process of order o consists of o links, shown as black lines between site i and j, which are shown as black dots. The green dots represent intermediate sites, for which there are several options on the lattice. Note that the intermediate sites can be i and j themselves as indicated in the order $o = 3$.

The procedure for the o-th order reads as follows:

- Determine all paths from site i to site j with o links.
- Collect the sites of all paths in a set K. Add all spins in K to the cluster, if this does not exceed the desired cluster size n, and proceed with the next order. If adding all spins would exceed n, consider the next step instead.
- Let f be the number of spins that are still missing in the cluster to reach its full size n. Consider all possibilities to add f spins to K. For each possibility, compute

$$(J_{i-\Sigma_o-j})^{2o}(\Gamma) \coloneqq \sum_{k_1,k_2,\ldots,k_{o-1}\in\Gamma} d_{ik_1}^2 d_{k_1k_2}^2 \ldots d_{k_{o-1}j}^2. \tag{6.6}$$

  Here, k_i can be any spin in the cluster with the f spins added (total size is n) and one has to consider truncated couplings in case of long-range interactions. Then, accept the cluster Γ with the highest value for $(J_{i-\Sigma_o-j})^{2o}$ and stop the procedure.

Aside from the cluster size there is another free parameter in this procedure, namely, the truncation parameter J_{crit}. This parameter indirectly determines the number L of finite couplings that correspond to a valid link. Henceforth, we will rather provide the value for L since that is easier to interpret.

Summary

In summary, the following three steps have to be carried out:

(i) Categorize the correlations that enter into the FID by making use of the symmetries of the system. In practice, one starts with the short-range correlations and ignores any correlation that exceeds a certain maximum range $|\vec{R}_{ij}| > R_{\mathrm{max}}$. The different categories are numbered from $c = 0$, which corresponds to the autocorrelation, to a maximum index $c = c_{\mathrm{max}}$.

(ii) Choose a proper cluster size n depending on the available numerical resources and determine the clusters for each class c by means of the procedure presented above. Remember to truncate the dipolar couplings for this step.

(iii) Having the clusters determined, compute the coupling sums required for Eq. (6.5). Then, perform the two steps of nl-spinDMFT to compute the correlations G_c^{xx} with $c \in [0, \dots, c_{\mathrm{max}}]$. The latter are superposed to obtain the FID according to

$$\mathcal{F}(t) = \sum_{c=0}^{c_{\mathrm{max}}} m_c G_c^{xx}(t), \tag{6.7}$$

where m_c is the multiplicity of class c, i.e., how often the corresponding correlation occurs in the lattice.

We consider an explicit example in the following.

6.2 Free induction decay of calcium fluoride

6.2.1 Modeling

Calcium fluoride, CaF_2, is a crystal composed of calcium ions forming an fcc-lattice and fluoride ions forming an sc-lattice, which is intertwined with the former. For NMR purposes, only the fluoride nuclei ^{19}F are relevant. They have a natural abundance of 100 % and carry a spin of $S = 1/2$. During the NMR experiment, the spin system is subject to a strong external magnetic field leading to the secular Hamiltonian in Eq. (2.24). The secular couplings $d_{ij} \propto (1 - 3\cos^2 \vartheta_{ij})$ depend on the angle ϑ_{ij} that is enclosed by the magnetic field and the distance vector between site i and j. Correspondingly, the orientation of the magnetic field is crucial. In the following, we focus on the [100]-direction, that is, the magnetic field is parallel to one of the crystal axes. As usual, we choose this axis to be the z-axis. We apply nl-spinDMFT by following the three steps listed above.

6.2.2 Applying nl-spinDMFT

Step (i)

First, we categorize the correlations entering the FID. The more short-ranged a correlation is, the earlier it becomes relevant in the FID. Consequently, we sort the correlations with regard to the pair distance, that is, first the autocorrelations, second the NN pair correlations, third the NNN pair correlations and so on. Due to the easy-axis anisotropy, two pair correlations with the same pair distance may not be equivalent, for example, the NN pair correlation with $\vec{R}_{ij} \parallel z$ is different from the one with $\vec{R}_{ij} \parallel x, y$. Therefore, we sort the pair correlations of equal distance once more, this time according to the modulus of the pair coupling. This leads to the categorization presented in Tab. 6.1, wherein we used the definition

$$d_0 \coloneqq \frac{\mu_0 \gamma_{\mathrm{F}}^2}{4\pi a_{\mathrm{sc}}^3}. \tag{6.8}$$

The corresponding distance vectors are indicated by the orange lines in Fig. 6.3.

Table 6.1: List of correlations considered for the FID of $\mathrm{CaF_2}$-[100]. The first entry ($c = 0$) is the autocorrelation, $G_{ii}^{\alpha\alpha}(t)$ and the other entries correspond to pair correlations, $G_{ij}^{\alpha\alpha}(t)$ with $i \neq j$. The second column contains an exemplary distance vector, $\vec{r}_c$, between the two sites i and j of the pair correlation and $|d_c|/d_0$ is the absolute of the direct spin-spin coupling with d_0 given in Eq. (6.8). By m_c we denote the multiplicity of the correlation, i.e., the number how often this correlation occurs per site.

c	$\vec{r}_c^{\top}/a_{\mathrm{sc}}$	$\lvert\vec{r}_c\rvert/a_{\mathrm{sc}}$	$\lvert d_c\rvert/d_0$	m_c
0				1
1	(0 0 -1)	1.0	2.0	2
2	(-1 0 0)	1.0	1.0	4
3	(-1 -1 0)	1.4142	0.3535	4
4	(-1 0 -1)	1.4142	0.1768	8
5	(-1 -1 -1)	1.732	0.0	8
6	(0 0 -2)	2.0	0.25	2
7	(-2 0 0)	2.0	0.125	4
8	(-1 0 -2)	2.2361	0.1252	8
9	(-2 -1 0)	2.2361	0.0894	8
10	(-2 0 -1)	2.2361	0.0358	8
11	(-1 -1 -2)	2.4495	0.068	8
12	(-2 -1 -1)	2.4495	0.034	16
13	(-2 -2 0)	2.8284	0.0442	4
14	(-2 0 -2)	2.8284	0.0221	8
15	(0 0 -3)	3.0	0.0741	2
16	(-3 0 0)	3.0	0.037	4
17	(-2 -2 -1)	3.0	0.0247	8
18	(-2 -1 -2)	3.0	0.0124	16
19	(-1 0 -3)	3.1623	0.0538	8

Step (ii)

We choose a cluster size of $n = 9$ spins. The clusters are chosen individually for each correlation category listed in Tab. 6.1 according to the procedure presented in the previous section. The dipolar couplings are truncated behind the nearest neighbors, which entails $L = 6$ (two times $d = 2d_0$ and four times $d = d_0$). We display the resulting clusters in Fig. 6.3.

Step (iii)

Step (1) of the strategy in Fig. 6.1 is very general because the converged results from spinDMFT depend only on a single free parameter, the quadratic coupling constant. Thus, we can simply adapt the correlations shown in Fig. 4.5 by setting

$$J_{\mathrm{Q}} = 3.655\, d_0, \tag{6.9}$$

which results from a numerical evaluation of the coupling sum.

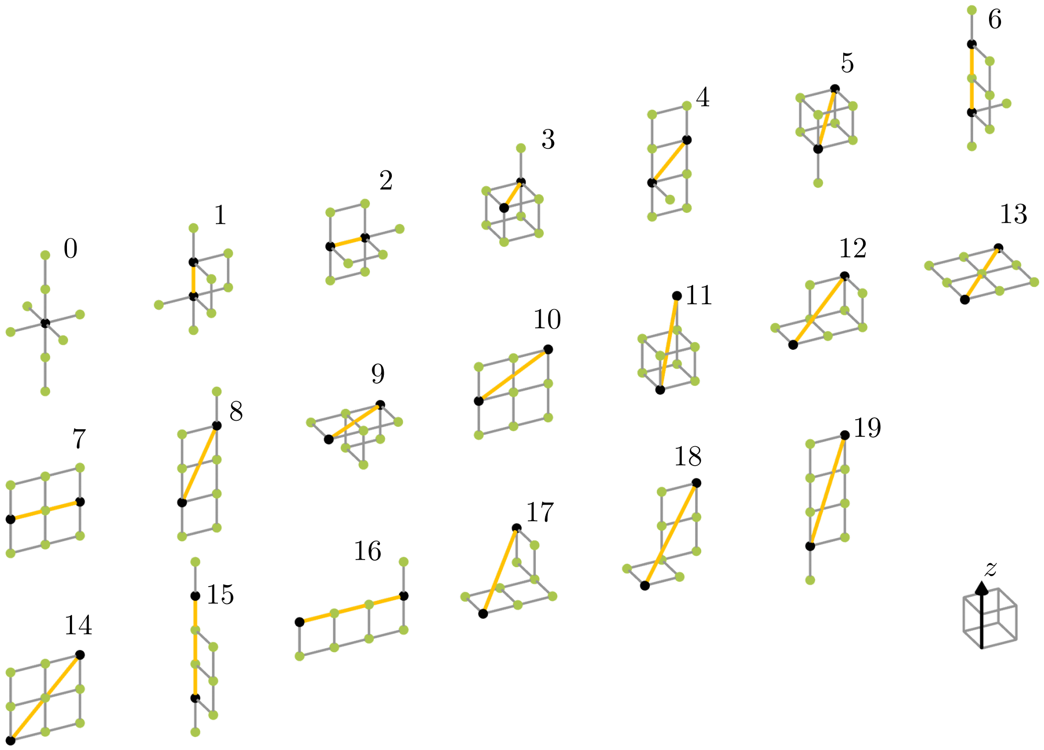

Figure 6.3: Clusters for computing the FID of CaF_2-[100]. The numbers correspond to the category indices c in Tab. 6.1. The black spheres connected by the orange line represent the sites of the corresponding pair correlation. The green spheres are the remaining sites of the cluster and the gray lines represent NN connection lines and multiples of them.

In step (2) of Fig. 6.1, we compute each correlation categorized in Tab. 6.1 by performing a simulation of the corresponding cluster shown in Fig. 6.3 considering a mean-field background generated by the second moments given in Eq. (6.5)[6]. Some numerical details of this procedure are given in App. C.2. Having the pair correlations determined, the FID is computed by Eq. (6.7) considering the multiplicities m_c provided in Tab. 6.1.

6.2.3 Results

The resulting FID is shown in Fig. 6.4 versus the time for different values of $c_{\max}$. In addition, we plot the longitudinal magnetization

$$M^z(t) = \sum_{c=0}^{c_{\max}} m_c G_c^{zz}(t), \tag{6.10}$$

which is conserved in the absence of any approximation. The deviation of $M^z(t)$ from 1 is a measure for the accuracy of the approximation. The simulation results agree better

---

[6] Note that no self-consistency is considered in this step which entails that each simulation involves only a single iteration step in which only the correlation of interest must be computed. This is in contrast to the CRA considered in Ch. 5, which requires computing all $n(n+1)/2$ correlations of a cluster of size n per iteration step.

and better with the experimental FID upon adding more correlations. At the same time, $M^z(t)$ becomes more and more constant as expected. For the final result, $c_{\max} = 19$, the agreement of the FIDs is remarkably good up to about $t = 40\,\mu\text{s}$ demonstrating the success of nl-spinDMFT.

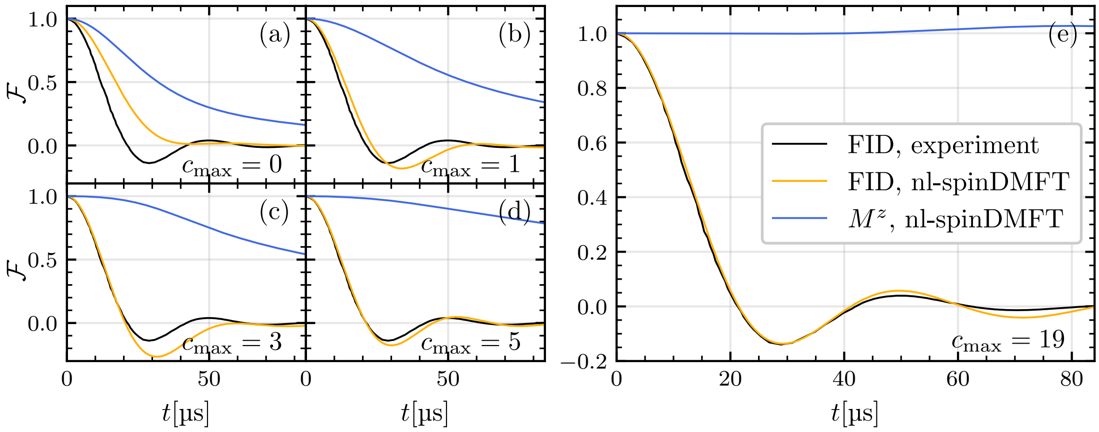

Figure 6.4: FID of CaF_2-[100] simulated by nl-spinDMFT and measured in experiment [EL74]. The simulation results correspond to a cluster size of $n = 9$ and increasing truncation value $c_{\max}$ from panel (a) to panel (e). In addition, we plot the longitudinal magnetization provided in Eq. (6.10). The absolute numerical error tolerance of the individual spin correlations entering $\mathcal{F}$ and M^z is $\epsilon = 2 \times 10^{-3}$. The experimental data were measured at 4 K where the lattice constant takes the value $a_{\text{sc}} = 2.724\,\text{Å}$.

At larger times, the amplitude of the oscillation of the FID is slightly overestimated. We can rule out numercial errors as the origin of this deviation, since they are about an order of magnitude smaller. We also tried adding correlations beyond $c_{\max} = 19$ by the same method, but this yielded the same results. A plausible explanation for the deviation is that the cluster size n is not sufficiently large. This is corroborated by the convergence plot shown in Fig. 6.5. The simulation results clearly tend towards the experiment as the cluster size is increased and the changes upon adding a single spin are significant. We recall that pair correlations cannot be generated by the mean-fields because back actions of the cluster are neglected by construction. The notable changes upon adding a single spin mainly result from additional correlation processes that are made available by extending the cluster. This can be also directly seen in the individual pair correlations as demonstrated in Ref. [GHU24] (App. A). We expect more accurate simulation results at moderate times, if the cluster size is increased further. The currently employed numerical resources are only moderate[7]. In future calculations, cluster sizes with $2-3$ additional spins are realistic.

---

[7] The computation of the entire FID requires in the order of 10^3 single-core hours and is perfectly parallelizable.

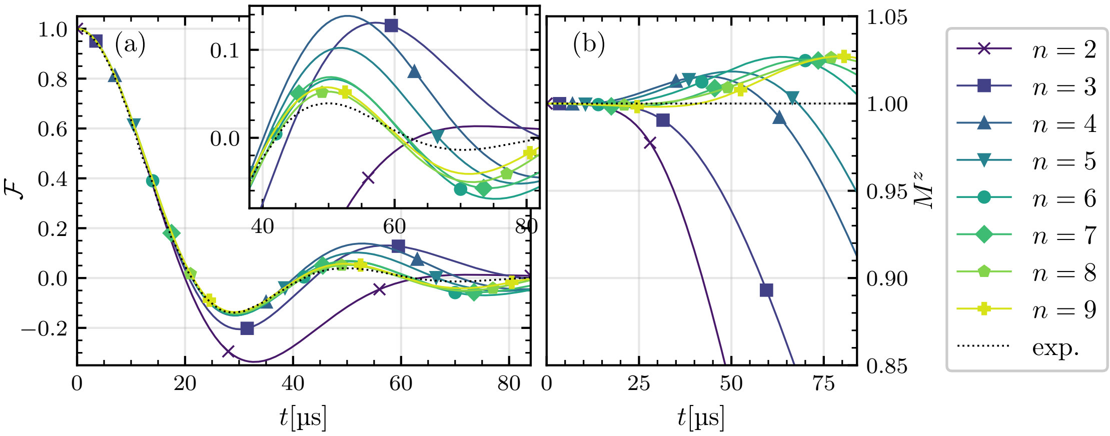

Figure 6.5: NMR signals of CaF_2-[100] simulated by nl-spinDMFT and measured in experiment [EL74]. Panel (a) shows the FID and panel (b) the longitudinal magnetization according to Eq. (6.10). The simulation results have been produced considering $c_{\max} = 19$ and varying cluster sizes n shown by different colors. The dotted line in panel (a) represents the experimental results. The dotted line in panel (b) has not been explicitly measured, but it is the expected result in the absence of any approximations.

In App. E.1, we present the simulation results for CaF_2-[110] and CaF_2-[111] and compare them to experiment. The observations are qualitatively the same as for the [100]-direction, that is, the approach performs excellent at short times and less well at moderate and larger times. However, it should be noted that the deviations are even larger for the other two directions. We attribute this observation to the fact that the coordination number is much larger, $z_{\mathrm{eff}}^{[110]} = 9.2$ and $z_{\mathrm{eff}}^{[111]} = 22.5$ versus $z_{\mathrm{eff}}^{[100]} = 4.9$. This is counterintuitive, because the mean-field approximation is generally better justified if z_{eff} is large. But we stress that the validity of the approximation depends strongly on the choice of the clusters. The number of intermediate spins relevant for a pair correlation increases with the coordination number. Hence, an appropriate, compact choice of the cluster becomes more and more difficult for increasing z_{eff}. At the same time, the local dynamics are already well captured for CaF_2-[100], so that the larger coordination numbers do not offer an advantage in this regard. Consequently, we expect a sweet-spot for the validity of nl-spinDMFT somewhere below $z_{\mathrm{eff}}^{[100]} = 4.9$.

6.2.4 Remarks on the procedure

The presented sorting scheme for the correlations leads to a unique categorization. Indeed, each category contains indistinguishable correlations that need to be computed only once. This is true for any crystals with monoatomic basis, but should be reconsidered in case of a polyatomic basis.

The first step of the strategy to compute the FID is certainly reasonable in case of moderate or high coordination numbers, $z_{\mathrm{eff}} \gtrapprox 5$. In these cases, spinDMFT yields a good approximation for the autocorrelations[8] and, thus, also for the mean-fields. If

---

[8] This can be well seen in the convergence plot for the autocorrelation, see Ref. [GHU24] (App. A).

z_{eff} is small, however, one should replace spinDMFT by CspinDMFT to increase the accuracy of the self-consistency and, perhaps, to compute some of the pair correlations already in step (1) in order to regard them for the mean-field background used in step (2). The latter aspect requires an adaption of Eq. (6.5). This could be important, for example, in a system of spin dimers such as silicon-enriched diamond with magnetic field in [111]-direction [Ver+03; SF20].

6.3 NMR signals of polycrystalline adamantane

6.3.1 Modeling

To demonstrate the versatility of the mean-field framework, we consider polycrystalline adamantane, which forms another common test substance in NMR [Álv+10; AÁS11; ÁS11; SÁS11; SÁS12; Hof22]. The adamantane molecule consists of carbon and hydrogen atoms ($C_{10}H_{16}$), which are located at spherical shells around the center of mass of the molecule as indicated in Fig. 6.6, panel (b). There are two different spheres for carbon (CA and CB) and two different spheres for hydrogen (HA and HB). As a simplified model, we set all bond angles to the tetrahedral angle, $\alpha = 109.5°$, and consider the atoms to be located at the averaged sphere radii [HH71][9]

$$r_{\mathrm{H}} = 2.60(3)\,\text{Å}, \qquad\qquad r_{\mathrm{C}} = 1.68(12)\,\text{Å}. \tag{6.11}$$

For NMR purposes, the hydrogen nuclei ^{1}H ($\approx 99.99\,\%$) and the carbon nuclei ^{13}C ($\approx 1.11\,\%$) are relevant. Both carry a spin of $S = 1/2$. Henceforth, we denote the hydrogen spins by S and the carbon spins by I. Since the carbon spins are so rare, we consider them to be completely isolated from one another and to be irrelevant for the hydrogen-spin relaxation.

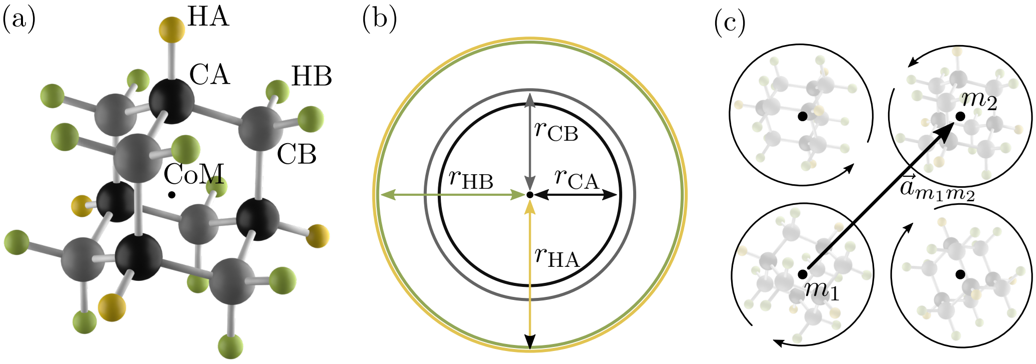

Figure 6.6: **(a)** Sketch of the adamantane molecule ($C_{10}H_{16}$) with carbon atoms in black (CA) and gray (CB) and hydrogen atoms in orange (HA) and green (HB). CoM stands for center of mass. **(b)** Schematic representation of the spheres at which the different sorts of atoms are located. The circles are to scale with each other. **(c)** Sketch of crystalline adamantane. The molecules are fixed at the fcc-lattice points and rotate rapidly and randomly around their centers of mass.

---

[9] This is justified *a posteriori*: we will observe that even the considerable difference between r_{H} and r_{C} hardly matters for the coupling constants required for spinDMFT.

In line with the experiment in Ref. [Álv+10], we consider polycrystalline adamantane at ambient conditions. In this case, the adamantane molecules form an fcc-lattice with lattice constant $a_{\text{fcc}} = 9.426(8)\,\text{Å}$ and four molecules per unit cell [FS64]. Adamantane is a plastic crystal, which entails that the centers of mass of the molecules are fixed, but the molecules rapidly and randomly change their orientations as indicated in Fig. 6.6, panel (c) [Lev01]. These molecular rotations are isotropic and happen on a much smaller time scale than the dipolar relaxation so that only their time average matters. This can be easily modeled by replacing any secular couplings by their motional average. It can be shown that this leads to the vanishing of all intramolecular couplings due to complete averaging [Lev01]. To formalize the motional averaging for the intermolecular couplings, we introduce the double indices $(mX) \coloneqq i$, where $m \in \{1, 2, 3, \dots\}$ is the molecule and $X \in \{\text{H}, \text{C}\}$ is the nucleus type. The averaged couplings read

$$\overline{d_{ij}}^{\text{ma}}(\vec{n}_B) \eqqcolon \overline{d_{(m_1X_1),(m_2X_2)}}^{\text{ma}}(\vec{n}_B) \tag{6.12a}$$

$$= (1 - \delta_{m_1m_2}) \int \frac{\mathrm{d}\Omega_1 \mathrm{d}\Omega_2}{(4\pi)^2}\, d_{\vec{a}_{m_1m_2} - r_{X_1}\vec{n}(\Omega_1) + r_{X_2}\vec{n}(\Omega_2)}(\vec{n}_B), \tag{6.12b}$$

where Ω_1 and Ω_2 describe the solid angles of the two molecules and $\vec{n}_B$ describes the orientation of the magnetic field. The orientation of a molecule is given by

$$\vec{n}(\Omega) = \vec{n}(\vartheta, \varphi) \coloneqq \begin{pmatrix} \sin\vartheta\cos\varphi \\ \sin\vartheta\sin\varphi \\ \cos\vartheta \end{pmatrix}. \tag{6.13}$$

By $\vec{a}_{m_1m_2}$ we denote the lattice vector from center to center of molecule and r_{X_1}, r_{X_2} are the sphere radii according to Eq. (6.11). We emphasize that despite the motional averaging, the orientation of the magnetic field with respect to the lattice is relevant for the intermolecular couplings. Since we consider a polycrystalline substance, the final NMR signal corresponds to an average over any possible orientation $\vec{n}_B$. This is called powder average and denoted by the shorthand “pa” henceforth.

6.3.2 Hydrogen-spin dynamics

The hydrogen-spin dynamics within a single crystallite are captured by the homonuclear Hamiltonian

$$\mathbf{H}_{\text{H}} = \frac{1}{2} \sum_{m_1, m_2} \overline{d_{(m_1\text{H}),(m_2\text{H})}}^{\text{ma}} \sum_{i \in m_1, j \in m_2} \left(-\mathbf{S}_i^x \mathbf{S}_j^x - \mathbf{S}_i^y \mathbf{S}_j^y + 2\mathbf{S}_i^z \mathbf{S}_j^z \right). \tag{6.14}$$

Computing the exact FID by nl-spinDMFT is not possible because a single molecule contains already 16 spins, which exceeds the maximum possible cluster size. On the other hand, the mean-field approximation itself is very well justified because the coordination number of the system is immensely large in the absence of any intramolecular couplings. Hence, we can at least compute the spin autocorrelations reliably by spinDMFT. To this end, we require the quadratic coupling constant,

$$J_{\text{Q,H}}^2(\vec{n}_B) = N_{0,\text{H}} \sum_{m>1} \left(\overline{d_{(1\text{H}),(m\text{H})}}^{\text{ma}}(\vec{n}_B) \right)^2, \tag{6.15}$$

where $N_{0,\mathrm{H}} = 16$ is the number of hydrogen atoms per molecule. This can been computed numerically for different orientations $\vec{n}_B$, see Ref. [GHU24] (Sec. 4.) for details. The obtained distribution $\rho(J_{\mathrm{Q,H}})$ is shown in Fig. 6.7, panel (a). To determine the powder-averaged spin autocorrelations, we simply superpose the generic results from Sec. 4.2.3 for different $J_{\mathrm{Q,H}}(\vec{n}_B)$ weighted by their distribution. The results of this procedure are displayed in Fig. 6.7, panel (b), together with the experimentally measured FID.

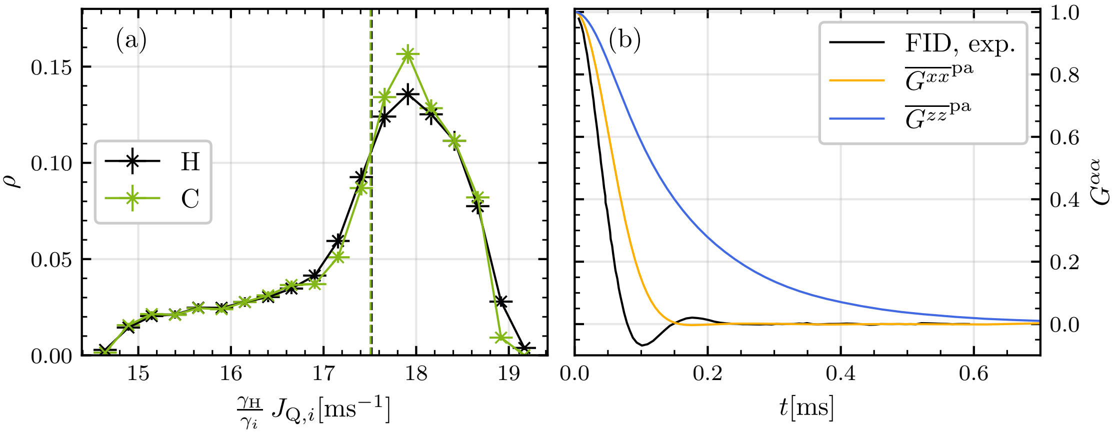

Figure 6.7: **(a)** Distribution of the quadratic coupling constant, which varies from crystallite to crystallite. The main difference between the distribution for hydrogen and carbon results from their different gyromagnetic ratios, see the scaling of the x-axis. **(b)** Powder-averaged spin autocorrelations simulated by spinDMFT compared to the experimentally measured FID [Álv+10] in polycrystalline adamantane.

Unsurprisingly, the FID drops notably faster than the transverse autocorrelation due to the presence of pair correlations in the former. The same behavior has been seen for calcium fluoride, see panel (a) of Fig. 6.4. The difference in the decays can be already understood from the difference in the second time derivatives at $t = 0$, which are given by $-5J_\mathrm{Q}^2/16$ and $-9J_\mathrm{Q}^2/16$ for autocorrelation and FID, respectively. Consequently, we expect a good agreement between theory and experiment if pair correlations are added, but as pointed out before this is not possible for numerical reasons within the current formulation of nl-spinDMFT. The situation is much more favorable for the carbon NMR signals which will be considered in the following section.

6.3.3 Carbon-spin dynamics

In principle, the NMR signals of carbon contain pair correlations as well, see for example the general formula for heteronuclear FID, Eq. (2.33). However, due to the low ^{13}C-abundance, the carbon atoms can be considered completely isolated from one another [Álv+10] making these pair correlations negligible. This allows us to compute the FID and the spin-echo signal by spinDMFT. The dynamics of a carbon spin are captured by the Hamiltonian

$$\mathbf{H}_\mathrm{C} = \mathbf{H}_\mathrm{H} + 2\mathbf{I}^z \sum_{m>1} \overline{d_{(1\mathrm{C}),(m\mathrm{H})}}^{\mathrm{ma}} \sum_{j\in m} \mathbf{S}_j^z, \tag{6.16}$$

assuming that the ^{13}C nucleus sits on the molecule with index 1. Replacing the hydrogen field by a dynamic mean-field $\vec{V}^z(t)$ leads to the effective Hamiltonian

$$\mathbf{H}_{\mathrm{C}}^{\mathrm{mf}}\left[\vec{V}^z(t)\right] = \mathbf{I}^z \vec{V}^z(t) \tag{6.17}$$

including the condition

$$\overline{V^z(t)V^z(0)}^{\mathrm{mf}} = 4J_{\mathrm{Q,C}}^2 \left\langle \mathbf{S}^z(t)\mathbf{S}^z(0)\right\rangle. \tag{6.18}$$

It is noteworthy that the trick to separate the bath dynamics (^{1}H) from the central-spin dynamics (^{13}C) is commonly used if back actions are neglible. The exact same semiclassical model for the central-spin dynamics is, for example, considered in Ref. [WYD14]. But the bath dynamics is computed by the CE method instead of spinDMFT in that reference.

Note that in Eq. (6.18), $J_{\mathrm{Q,C}}^2$ and $\langle \mathbf{S}^z(t)\mathbf{S}^z(0)\rangle$ both depend on $\vec{n}_B$. The quadratic coupling constant $J_{\mathrm{Q,C}}(\vec{n}_B)$ is defined analogous to Eq. (6.15) and yields essentially the same result except for a relative factor of $r_\gamma := \gamma_{\mathrm{C}}/\gamma_{\mathrm{H}} \approx 0.251$ due to the different gyromagnetic ratios. This can be seen in Fig. 6.7, where the corresponding distribution $\rho(r_\gamma^{-1}J_{\mathrm{Q,C}})$ is plotted[10]. Therefore, we can calculate any powder-averaged NMR signal by computing the corresponding signal for several $J_{\mathrm{Q,C}}$ and superpose the results considering the density $\rho(J_{\mathrm{Q,C}}) \approx \rho(r_\gamma J_{\mathrm{Q,H}})$. Performing this leads to the FID and spin-echo signal shown in Fig. 6.8, panel (a) and (b).

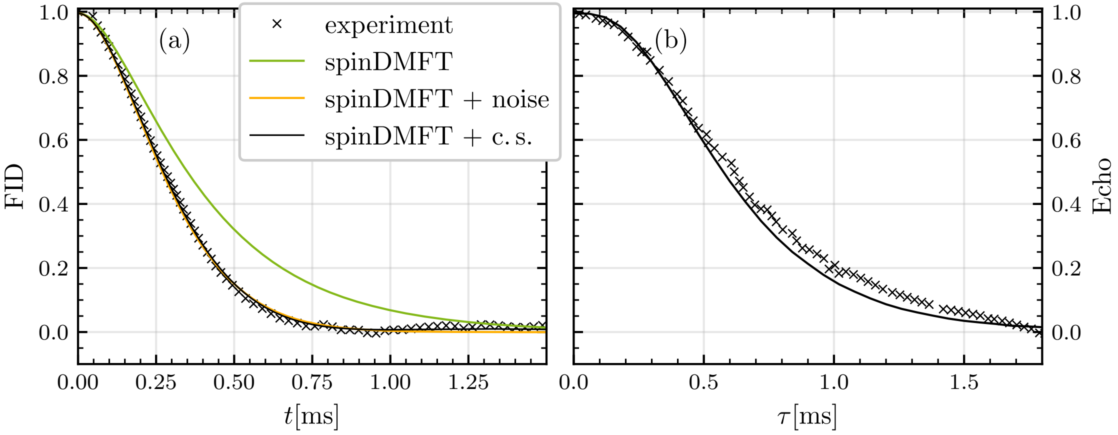

Figure 6.8: **(a)** FID of rare carbon atoms in polycrystalline adamantane simulated by spinDMFT and measured in experiment [Álv+10]. Adding a phenomenological static noise to the simulation leads to a remarkably good agreement (orange line). Alternatively, one can add the chemical shifts (c. s.) measured in Ref. [Hof22] to the simulation. This approach is more physically justified and yields a good agreement as well (black line). **(b)** Carbon-spin-echo signal versus the sequence time τ. The simulation results are independent of local static fields. Consequently, the black line is representative of spinDMFT with and without noise or chemical shifts.

---

[10] To be on the safe side, we checked the equality of $r_\gamma^{-1}J_{\mathrm{Q,C}}(\vec{n}_B)$ and $J_{\mathrm{Q,H}}(\vec{n}_B)$ also for individual orientations $\vec{n}_B$ observing the same behavior. The radii at which the atoms are located play only a minor role for the quadratic coupling constant [GHU24].

We obtain a significant deviation for the FID, which is unexpected in view of the large coordination number of the system. On the other hand, the agreement is excellent for the spin-echo signal in panel (b). A possible explanation for this observation is the presence of inhomogeneous broadening due to local fluctuations of the magnetic susceptibility. This effect would amplify the dephasing of the carbon spins, while being precisely canceled in the spin-echo signal [Lev01; Sli90]. In Ref. [GHU24], the inhomogeneous broadening was phenomenologically modeled by adding a static Gaussian noise source coupling to the carbon spins z-component. A good agreement was obtained for a noise width of $\omega_{\text{noise}} = 0.29(6)\,\text{ms}^{-1}$, the result of which is displayed in panel (a).

Yet the question of the source of the inhomogeneous broadening remains unanswered. A plausible explanation for the discrepancy in the FIDs of experiment and theory is the different chemical shifts of the two types of carbon, CA (from CH) and CB (from CH_2) [Lev01][11]. The chemical shift is induced by the electrons and essentially describes a local variation of the global NMR field. It depends on the electronic environment of a nuclear spin and therefore varies depending on the molecular bonds of the considered atom. From Ref. [Hof22], we extract the relative chemical shift between CA and CB at room temperature,

$$\Delta\delta(25\,^\circ\text{C}) = \delta_{\text{CA}}(25\,^\circ\text{C}) - \delta_{\text{CB}}(25\,^\circ\text{C}) = 9.047\,\text{ppm}, \tag{6.19}$$

which translates to

$$\Delta\omega = \Delta\delta \frac{\gamma_{\text{C}}}{\gamma_{\text{H}}} 2\pi\nu_0 = 4.289\,\text{ms}^{-1} \tag{6.20}$$

where $\nu_0 = 300\,\text{MHz}$ is the ^{1}H resonance frequency of the spectrometer in experiment [Álv+10]. This value is close to the average quadratic coupling constant $\overline{J_{\text{Q,C}}}^{\text{pa}} = 4.403\,\text{ms}^{-1}$ and thus not negligible. Therefore, the chemical shifts need to be included in the simulations. While the relative frequency between the two types of carbon is known with relatively high precision according to Eq. (6.20), the reference frequency ω_{ref} required to compute the absolute chemical shifts in the rotating frame is not precisely known in experiment[12]. Consequently, we regard the position of the chemical shifts relative to the reference frequency as a fit parameter. It is determined by minimizing the square error between theory and experiment. This procedure yields the absolute chemical shifts

$$\omega_{\text{CA}} = -3.611(46)\,\text{ms}^{-1}, \qquad \omega_{\text{CB}} = 0.678(46)\,\text{ms}^{-1} \tag{6.21}$$

along with the distribution sketched in Fig. 6.9. These can be straightforwardly included in spinDMFT by simulating the adapted Hamiltonian

$$\mathbf{H}^{\text{mf}}_{\text{CX}}\left[\vec{V}^z(t)\right] = \mathbf{I}^z\left(\vec{V}^z(t) + \omega_{\text{CX}}\right), \tag{6.22}$$

for $\text{CX} \in \{\text{CA}, \text{CB}\}$ and different values of the quadratic coupling constant so that the powder average can be carried out. The simulation results are depicted in Fig. 6.8,

---

[11] In Ref. [GHU24], we listed also the chemical-shift anisotropy as a potential origin. This effect can be relevant in a solid, but it is highly suppressed in a plastic crystal such as adamantane [Lev01] and, therefore, probably not relevant here.

[12] At least it is not provided in Ref. [Álv+10].

panel (a). The inclusion of the chemical shifts leads to a very good agreement with the experimental data demonstrating the validity of spinDMFT once more. In fact, the agreement is even slightly better than for the Gaussian noise which was motivated only phenomenologically. It should be noted that similar to inhomogeneous broadening, the chemical shifts do not affect the spin echo, i.e., the result in panel (b) of Fig. 6.8 remains unchanged. Furthermore, it is noteworthy that the chemical shift difference of the two types of hydrogen is much smaller, $\Delta\delta \approx 0.1\,\mathrm{ppm}$, and thus irrelevant for the hydrogen signal in Fig. 6.7.

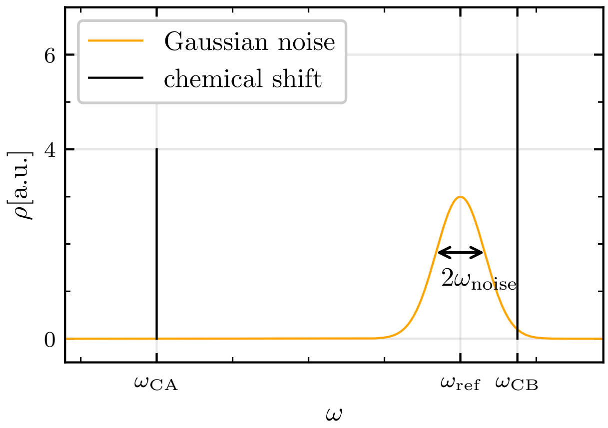

Figure 6.9: Two different ways of including static local fields in the simulation. The Gaussian noise is phenomenologically motivated and has a width of $\omega_{\mathrm{noise}} = 0.29(6)\,\mathrm{ms}^{-1}$. The chemical shift difference $\omega_{\mathrm{CA}} - \omega_{\mathrm{CB}}$ results from the different electronic environments of CA (from CH) and CB (from CH_2). The values ω_{CA} and ω_{CB} with respect to $\omega_{\mathrm{ref}} := 0$ are provided in Eq. (6.21).

6.4 Chapter conclusion and outlook

6.4.1 Improvement of nl-spinDMFT

We already mentioned the possibility to extend step (1) of the strategy in Fig. 6.1 by replacing spinDMFT with CspinDMFT. This is expected to be relevant for systems with rather small effective coordination numbers z_{eff}. It turns out to be more important to choose a proper cluster for each pair correlation. In particular, the size of the clusters appears to play a significant role, as can be seen in the convergence plot in Fig. 6.5. Larger cluster sizes could be reached by enhancing the efficiency of the entire cluster simulation, for example, by employing quantum typicality [Whi09; EF13; Sta24]. In this approach, the evaluation of a trace over the Hilbert space of the cluster would be replaced by an expectation value with respect to one or a couple of pure states, which would require much less computational effort. As previously mentioned, fully classical [EF15; SF18] or hybrid quantum-classical [SF18; SF20] methods are very powerful for computing the FID at high temperatures. The strength of nl-spinDMFT in capturing short-range correlations in a systematically controlled way could be combined with these approaches to develop a universal simulation tool. It is conceivable that long-range correlations behave more classically because they involve many spins. Consequently, one could, for example, simulate short-range correlations by nl-spinDMFT and long-range correlations classically. The results can then be superposed using Eq. (6.7) to compute the FID.

6.4.2 Advantages and disadvantages of the mean-field framework

As discussed in the introduction of this chapter, a variety of successful approaches to compute FIDs exist. In the current formulation, nl-spinDMFT is not the most accurate theory, especially at larger times because of the difficulty to describe long-range pair correlations. Moderate (and perhaps small) coordination numbers, $z_{\mathrm{eff}} \lessapprox 5$, are accessed well, but the results become less accurate for large z_{eff} as can be seen in the cases of CaF_2-[110] and CaF_2-[111], see App. E.1. We emphasize, however, that the limits of spinDMFT and its extensions are by far not explored and some promising improvements have been proposed in the previous section. Furthermore, we wish to highlight a significant advantage of the mean-field framework. Due to its microscopic description via an effective Hamiltonian it is highly versatile and can be extended to include magnetic fields or noises of any kind as well as quadrupolar interactions. In addition, explicit time dependencies, such as trains of pulses, can be readily incorporated as has been demonstrated by the spin echo for the example of adamantane.

The presented examples serve as excellent benchmarks for the mean-field framework. However, it should be noted that direct FID measurements as considered above are not particularly relevant in modern solid-state NMR. In fact, the dipolar interactions lead to line broadening in the NMR spectra which corresponds to relaxation in the time domain. This is generally impractical when trying to gain insight into the chemical structure of a sample. In the following section, we will briefly discuss a method to reduce the line broadening in practice and how spinDMFT can be relevant in such a scenario.

6.4.3 Magic-angle spinning

MAS is a widely-used technique in solid-state NMR [ABE58; Low59; Meh83]. The basic idea is straightforward. In liquids, the rapid random molecular motions and rotations average the anisotropic dipolar interactions to zero. The same effect can be achieved in a solid by rotating the sample rapidly around a specific axis during the measurement as detailed in Fig. 6.10. As a consequence, the secular couplings obtain a periodic time dependence, $d_{ij} \to d_{ij}(t)$. If the rotation axis of the sample encloses the magic angle $\vartheta_{\mathrm{m}} \approx 54.7°$ with $\vec{n}_B$, it can be shown that the long-time average of $d_{ij}(t)$ vanishes completely. Consequently, the dipolar relaxation becomes more or less irrelevant.

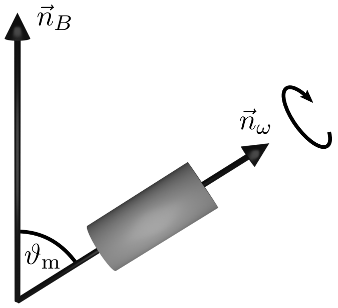

Figure 6.10: Basic setup of MAS. The sample (gray cylinder) rotates around the axis $\vec{n}_\omega$, which encloses the magic angle ϑ_{m} with the magnetic-field orientation $\vec{n}_B$. The reachable spinning frequencies nowadays are in the order of $100 - 200\,\mathrm{kHz}$.

This can be analyzed by capturing the effect of the time dependence in an effective-Hamiltonian expansion, as is done in average-Hamiltonian theory (AHT) [Mag54; HW68;

Pen+19], or in Floquet theory [SBE10; Chá+21]. In both cases, the leading order contribution of the dipolar interactions is eliminated. In practice, however, the effects of higher orders are still visible as *residual line broadening* for realistic spinning frequencies. The precise physics behind this is subject of ongoing research [Mal+19; Pen+19; Chá+21].

Indeed, the dynamic mean-field approach could be adapted to this scenario. One could, for example, apply spinDMFT directly to the time-dependent secular Hamiltonian. While this is conceptually straightforward, it may not be numerically feasible due to the necessity of resolving the rapid spinning by the time discretization. An alternative is to apply spinDMFT and its extensions to an effective time-independent Hamiltonian generated by AHT or Floquet theory. To date, spinDMFT has only been applied to bilinear spin Hamiltonians, for which the mean-field substitution is straightforward. Higher orders of the above-listed expansions contain also terms with three or more spin operators, for example[13],

$$\mathbf{H}^{\mathrm{eff}}_{(2)} = \mathtt{i} \sum_{p,q,r} C_{pqr}\, \mathbf{S}^z_p \left(\mathbf{S}^+_q \mathbf{S}^-_r - \mathbf{S}^-_q \mathbf{S}^+_r \right) \tag{6.23}$$

with constant C_{pqr}. In order to address such terms, we remind the reader of a key ingredient of the mean-field approach: Fields comprising a large number of uncorrelated spins behave classically and follow a Gaussian distribution in accordance with the central limit theorem. This statement can be simply extended to fields with constituents that are multi-linear in spin operators. By employing this argument, the spin dynamics under MAS could be accessed within the mean-field framework.

---

[13] This term arises in second order Floquet theory, if the secular Hamiltonian contains homonuclear interactions as well as chemical shifts (local magnetic fields in z-direction) [Chá+21].

7 Conclusion

This theoretical thesis was devoted to the development and application of a numerical method in condensed-matter physics. We established a dynamic mean-field theory for spins at infinite temperature, short spinDMFT [Grä+21]. The key idea of the approach is to capture a dense spin system by an effective single-site model which describes a spin in a classical, dynamic mean-field following a Gaussian distribution. Relating the second moments of this distribution to spin autocorrelations leads to a self-consistency problem which can be solved numerically with minor computational effort. Apart from studying spinDMFT, a considerable part of this thesis dealt with the extension to a cluster version, dubbed CspinDMFT [Grä+23], and a non-local version, dubbed nl-spinDMFT [GHU24]. CspinDMFT treats several spins quantum-mechanically which increases the accuracy and allows for the study of inhomogeneous systems. Nl-spinDMFT efficiently accesses pair correlations required to compute FIDs in the context of NMR.

Spin systems occur frequently in nature and are typically disordered at room temperature. Hence, the seemingly abstract requirement for infinite temperature is a highly-relevant scenario. Corresponding reseach areas such as NV centers in diamond or NMR have been highlighted in the introduction (Ch. 1). Although spin models can be written down straightforwardly, see Ch. 2, their simulation remains a notoriously difficult task due to the exponentially large Hilbert spaces. Mean-field approaches form one class of approximate methods that tackle this issue. As such, spinDMFT can be considered a dynamic extension of Weiss mean-field theory[1] similar to the fermionic DMFT being a dynamic extension to Hartee-Fock theory. As we pointed out in Ch. 3, there are other mean-field theories and many different methods to deal with large spin systems, each coming along with different advantages and disadvantages. Which method to use is always a question of the specific scenario under study.

In Ch. 4, we presented the microscopic derivation of spinDMFT. Based on the limit $z \to \infty$, we argued that the spin environments can be replaced by classical, time-dependent mean-fields, that back actions of a single spin onto its mean-field are negligible, and that the mean-fields follow a Gaussian distribution due to the central limit theorem. For homogeneous systems, the derivation results in an effective single-site model as sketched in Fig. 4.2. In this case, the only relevant energy scale is the quadratic coupling constant. The form of the resulting autocorrelations solely depends on the spin model and not on the geometry. This allowed us to provide universal results for the Heisenberg, Ising and XXZ model. Subsequent benchmarks revealed that spinDMFT is already an acceptable approximation on a square lattice with $z = 4$.

We emphasize that spinDMFT can be modified in many ways. For example, the assumption of spatial homogeneity is actually not a requirement. The computational cheapness of the approach allows for solving the self-consistency problem for several sites with

---

[1] Admittedly, for infinite temperatures only.

distinct environments. Note that in contrast to CspinDMFT, the computational cost of spinDMFT scales only linearly with the number of sites allowing for the explicit simulation of moderately large systems. Employing this, one could use spinDMFT to simulate the macroscopic spatial diffusion of a conserved spin polarization [Zu+21]. This requires the explicit inclusion of conservation laws in the approach as sketched in App. F. If this turns out to be successful, one could also study systems with approximate conservation laws by introducing a small conservation-breaking parameter [LLR17; LLR18a; LLR18b].

The self-consistency problem defined by spinDMFT yields solutions homogeneous in time[2]. However, time translation invariance can be broken by applying time-dependent external fields. In this way, spinDMFT could be also used to study discrete time-crystalline behavior [Cho+17b; Zha+17]. Probably one of the greatest challenges to spinDMFT is the extension to finite temperatures. Mean-field-approaches for spin glasses provide an idea of how this may be accomplished [GR98; GPS00]. A central ingredient will be to formulate the approach in imaginary time.

Ch. 5 was devoted to the extension of spinDMFT to CspinDMFT, which was mainly developed to access systems with positional randomness. The derivation is very similar to spinDMFT. An additional important aspect is the choice of the cluster as well as the adaption of the self-consistency conditions. For inhomogeneous systems, we introduced the CRA which maps out-of cluster correlations to in-cluster correlations based on similarity-measuring quantities. The CRA forms an additional approximation, but it has the advantage that, in the end, only a single cluster needs to be simulated. Therefore, simulations with a cluster size up to $n = 10$ are still feasible.

In Sec. 5.2, we benchmarked CspinDMFT and concluded that the accuracy increases with the cluster size as long as the border between cluster and environment contains no strong quantum bonds. Subsequently, we applied CspinDMFT to a spin ensemble with positional randomness to capture the experiment described in Sec. 2.6, which uses an NV center to probe the dynamics of defect spins on a diamond surface [Rez22; Rez+23]. The simulation of the autocorrelations of a central surface spin yielded a vast difference between the longitudinal and transverse relaxation, the same phenomenon that had been observed experimentally. Still, theory and experiment could be compared only on a very qualitative level. This is, amongst others, due to slow convergence of the numerics with the cluster size, due to uncertainties regarding the surface geometry and due to large fluctuations and error bars in the experimental data. The discrepancy between theory and experiment is summarized by a factor of four in the characteristic relaxation time of the theoretical, configuration-averaged, longitudinal autocorrelation relative to the experimental one. Interestingly, the convergence plot implies an even slower relaxation in theory for $n \to \infty$. This suggests that the current modeling of the surface spins is not completely adequate. It is conceivable that some spins are mobile [Dwy+22] and form another fast channel of decoherence that is not captured by the model.

The key aspect explaining the difference between the two relaxations is a conservation law. While the transverse polarization also undergoes dephasing, the longitudinal polarization is globally conserved and can thus only decay locally by being transported to other spins. Indeed, such a diffusive process can be moderately fast for the considered spin model on

---

[2] Although we cannot generally rule out solutions that spontaneously break time translation invariance.

a different geometry, as we demonstrated with the example of a triangular lattice. But the inhomogeneous system tends to form well-separated clusters[3] of spins between which transfer of polarization can be suppressed. To validate this explanation, the geometry or the spin model could be varied in future studies. Does a lattice of spatially separated clusters of spins exhibit the same behavior as the inhomogeneous system? How stable is the obtained phenomenon to perturbations that break the conservation law? What role does the dimensionality of the system play? These and further questions could be straightforwardly studied by CspinDMFT. We also like to mention that simulations of the surface-spin ensemble including the NV spin should be possible in the framework of CspinDMFT. In this way, the numerics could be compared with direct measurements of the NV spin, which are probably more reliable.

In Sec. 5.3.6, we gave a brief overview of the state of research of many-body localization concluding that it is not entirely clear where or whether the phase exists. Whether or not MBL could be observed in the framework of CspinDMFT is also unclear because, for instance, the cluster would need to be larger than the localization length, which is not known *a priori*. Yet, the numerical results impressively show that CspinDMFT is capable of describing very slow dynamics [Grä+23; Mar+23] and perhaps capturing a prethermal MBL phase [Lon+23]. Further research in this context should be preceeded by validating and adjusting the CRA as described in Sec. 5.4.3. This is likely to significantly reduce the computational effort so that larger cluster sizes and larger times can be reached. The latter would allow to distinguish stretched-exponential from logarithmic behavior, both of which currently fit the numerical data well, see Fig. 5.20. Besides this, it is worth mentioning that the coupling between the cluster and the mean-fields is usually weak compared to the couplings within the cluster, which suggests the usage of perturbation theory. However, it is difficult to formulate the latter because there is no simple analogy to Wick's theorem for spin expectation values.

Ch. 6 was devoted to simulating NMR signals. We showed that the FID of a dense spin system includes pair correlations and we extended spinDMFT to nl-spinDMFT in order to access them. The success of nl-spinDMFT has been demonstrated on the example of a simple-cubic spin lattice hosted by CaF_2. However, the results for CaF_2-[110] and CaF_2-[111] revealed a certain weakness of the mean-field approach. The reachable cluster sizes are too small to access long-range correlations in case of large coordination numbers reliably. Therefore, counterintuitively, FIDs in denser spin systems are accessed less well by nl-spinDMFT. But having a detailed look into how pair correlations develop, one might find a way to eliminate this issue in the future. An interesting observation in this context is that small correlation effects add up linearly to a good approximation [GHU24]. Furthermore, one can try to formulate a hybrid approach, in which short-range correlations are simulated by nl-spinDMFT and long-range correlations by a fully classical simulation. Considering the success of entirely classical simulations [EF15; SF18], it is conceivable that such a combination yields accurate results for both short and long times.

By considering the FID and the spin echo of ^{13}C in adamantane, we demonstrated the versatility of the mean-field approach once more. The agreement with the experimental

---

[3] In this context, the term "cluster" refers to a group of proximate spins and not to the cluster in CspinDMFT.

results is remarkably good if the chemical shifts of the two kinds of carbon are added to the simulation. We are convinced that many scenarios in NMR can be captured by spinDMFT and its extensions. As such, we sketched how the mean-field approach can be applied to the nowadays very relevant MAS experiments, see Sec. 6.4.3. Finally, we mention that the usage of quantum typicality can reduce the computational effort of nl-spinDMFT enormously.

SpinDMFT and its extensions are now part of the large toolset of numerical methods in condensed-matter physics. In order to decide, whether a method is suitable for solving a certain problem, it is essential to know its advantages and disadvantages:

A strength of spinDMFT is its versatility, which stems from the fact that the approach is semiclassical[4] and computationally cheap. Translational invariance in case of a lattice can be straightforwardly included. Long-range interactions, which are particularly challenging for brute-force methods, justify the application of spinDMFT even more due to the increased effective coordination number. The mean-field approach can be adapted to describe anisotropies, external fields or quadrupolar interactions[5]. Explicit time-dependencies, for example, from trains of pulses can be incorporated without increasing the numerical effort much. Therefore, spinDMFT is a suitable tool for exploring non-equilibrium physics. Another noteworthy advantage of spinDMFT is its exactness in the limit $z \to \infty$, a property it shares with other mean-field theories. As with the self-energy in DMFT, the spin correlations in spinDMFT become site-local in the limit of an infinite coordination number justifying the description via an effective single-site model. Therefore, the mean-field framework is expected to be successful especially in high-dimensional systems where brute-force quantum simulations are not reliable. But there are also several disadvantages.

Systems with small coordination numbers, e.g., chains or star-like topologies, are not captured well. CspinDMFT can help out if the system can be well separated into clusters, but the convergence with the cluster size can be slow. Another disadvantage of the mean-field approach is that it does not automatically keep track of conservation laws. To illustrate that, a polarization that is conserved in the exact system can be absorbed by the mean-fields where it is immediately lost in spinDMFT, since they are zero on average[6]. CspinDMFT and nl-spinDMFT allow for computing non-local correlations, but only over a limited spatial range because of the neglect of back actions of the cluster onto the mean-fields. In contrast to related mean-field approaches [KF98; GR98; GPS00], spinDMFT and its extensions are currently formulated exclusively for the infinite-temperature regime. Consequently, temperature-induced phase transitions are not accessible.

We emphasize, however, that some of these disadvantages may just be challenges that can be overcome in future research. As previously mentioned, the applicability and extendability of the method have yet to be fully explored. This thesis not only paves the way for numerous applications of spinDMFT to specific problems, but also provides a foundation for further methodological research.

---

[4] In fact, spinDMFT is equivalent to a mean-field approach for classical spins in case of $S = 1/2$. But in contrast to a fully classical model, additional quantum degrees of freedom are easily incorporated, as is demonstrated by the cluster-extension CspinDMFT.

[5] The latter has not yet been tried out.

[6] It should be noted, however, that this behavior naturally follows from the neglect of back actions and is thus well justified for large z.

A Notations

Units

- We set $\hbar = 1$ in all equations.
- Frequencies are provided in Hz and angular frequencies in s^{-1}.

Symbols

- Matrices are indicated by doubly-underlined symbols, e.g., $\underline{\underline{M}}$.
- Vectors are indicated by vector arrows, e.g., $\vec{r}$.
- Quantum-mechanical operators are indicated by boldface symbols, e.g., $\mathbf{O}$, except for density operators, which are denoted by ρ.
- The letter D is reserved for the real-space dimension and d for the Hilbert-space dimension.
- The letter ν is reserved for frequencies and the letter ω or Ω for angular frequencies.
- $\Theta(x)$ is the Heaviside function and $\delta(x)$ is the delta distribution.

Conventions

- Traces are denoted by "Tr". If the trace is carried out only on a subspace, this is indicated by an additional index, for example, Tr_i denotes a local trace at site i.
- The expectation value of an operator $\mathbf{O}$ is generally defined as

  $$\langle \mathbf{O} \rangle_\rho := \mathrm{Tr}\left(\mathbf{O}\rho\right), \tag{A.1}$$

  with ρ being the density operator. For brevity, we occasionally omit ρ as an index, if the state we are referring to is either not specified or automatically clear from the context.

- Besides the quantum average, there are five other types of averages in this thesis, which are denoted by

$$\overline{O}^{\mathrm{mf}} \quad - \quad \text{mean-field average,} \tag{A.2a}$$

$$\overline{O}^{\mathrm{cf}} \quad - \quad \text{configuration average,} \tag{A.2b}$$

$$\overline{O}^{\mathrm{ma}} \quad - \quad \text{motional average,} \tag{A.2c}$$

$$\overline{O}^{\mathrm{pa}} \quad - \quad \text{powder average,} \tag{A.2d}$$

$$\overline{O}^{\mathrm{ta}} \quad - \quad \text{time average,} \tag{A.2e}$$

  where O is a placeholder for the function being averaged over.

- In case of a lattice system, we occasionally use the notation

$$\delta_{\langle i,j\rangle} := \begin{cases} 1, & \text{if } i \text{ and } j \text{ are nearest-neighbor (NN) sites,} \\ 0, & \text{else.} \end{cases} \tag{A.3}$$

- Directional indices (mostly $\alpha, \beta \in \{x, y, z\}$) in Kronecker deltas are indicated by *upper* indices, e.g., $\delta^{\alpha\beta}$, for better distinction from other Kronecker deltas.

- If a sum or integral has no limits, it runs over any possible value of the sum or integral variable, e.g., an ensemble sum with sites $i \in \{1, \ldots, N\}$ reads

$$\sum_i := \sum_{i=1}^{N}. \tag{A.4}$$

- Spin-spin interaction Hamiltonians are written as

$$\mathbf{H} = \frac{1}{2} \sum_{i,j} \mathbf{h}(i,j) \underset{\text{for 3 sites}}{=} \mathbf{h}(1,2) + \mathbf{h}(1,3) + \mathbf{h}(2,3). \tag{A.5}$$

  The prefactor $1/2$ accounts for double countings of the couplings. Self interactions, $\mathbf{h}(i,i)$, are always ruled out by setting the self couplings, e.g., J_{ii}, to zero.

- NN interaction sums are occasionally indicated by

$$\frac{1}{2} \sum_{\langle i,j\rangle} := \frac{1}{2} \sum_{i,j} \delta_{\langle i,j\rangle}. \tag{A.6}$$

- Involved constraints on sums are occasionally denoted by a double dot according to

$$\sum_{i:C}. \tag{A.7}$$

  Here, i is the index being summed over and C represents the constraint.

- For lattices, we denote the taxicab distance between two sites i and j by $\lambda(i,j)$. It counts the minimum number of NN links required to move from i to j.

B Relevance of pair correlations for the second mean-field moments

A crucial ingredient of the derivation of spinDMFT is that pair correlations are suppressed by the inverse coordination number. This has been explicitly shown on a Bethe lattice at infinite temperature, see Tab. 4.1 for the results and Ref. [Grä+21] (App. A) for more details. An extension to lattice systems has not yet been considered because the occurrence of loops makes such a proof notoriously difficult. But, at least the simplification of the second mean-field moments can be reconsidered easily, if we adapt the general scaling arguments. We demonstrate this for lattices with NN interactions in this appendix.

The second mean-field moments in case of NN interactions $J_{ij} = \delta_{\langle i,j \rangle} J$ are given by

$$\frac{1}{J^2} \overline{V_i^\alpha(t_1) V_i^\beta(t_2)}^{\mathrm{mf}} = \sum_{j,k} \delta_{\langle k,i \rangle} \delta_{\langle j,i \rangle} \langle \mathbf{S}_j^\alpha(t_1) \mathbf{S}_k^\beta(t_2) \rangle. \tag{B.1}$$

This can be rewritten as

$$\begin{aligned} \frac{1}{J^2} \overline{V_i^\alpha(t_1) V_i^\beta(t_2)}^{\mathrm{mf}} &= \underbrace{\sum_{k} \delta_{\langle k,i \rangle}}_{\propto z} \underbrace{\langle \mathbf{S}_k^\alpha(t_1) \mathbf{S}_k^\beta(t_2) \rangle}_{\propto 1} \\ &+ \underbrace{\sum_{j,k} \delta_{\langle j,i \rangle} \delta_{\langle k,i \rangle} \delta_{\langle j,k \rangle}}_{z\tilde{z}} \underbrace{\langle \mathbf{S}_j^\alpha(t_1) \mathbf{S}_k^\beta(t_2) \rangle}_{\propto \frac{1}{z}} + \underbrace{\sum_{j,k} \delta_{\langle k,i \rangle} \delta_{\langle k,j \rangle} (1 - \delta_{\langle j,k \rangle})}_{z(z-\tilde{z})} \underbrace{\langle \mathbf{S}_j^\alpha(t_1) \mathbf{S}_k^\beta(t_2) \rangle}_{\propto \frac{1}{z^2}} . \end{aligned} \tag{B.2}$$

The first sum contains the autocorrelations, which are not suppressed. The second sum contains the pair correlations of two neighbors of site i that are also neighbors to one another. Such correlations are suppressed by $1/z$ and they do not occur in the mean-field sums on a Bethe lattice because the latter is loop-free. Here, we consider a general lattice and must take them into account. To determine their relevance, we introduce $\tilde{z} < z$ as the number of shared nearest neighbors of two NN sites as illustrated in Fig. B.1. The third sum contains the remaining pair correlations, which are suppressed by $1/z^2$.

The third sum can be generally neglected in the limit $z \to \infty$ because it is suppressed by at least $1/z$ relative to the autocorrelation sum. This has been used already in the considerations for the Bethe-lattice. However, the second sum is suppressed only by $\tilde{z}/z$ relative to the autocorrelation sum. This does not play a role in a square lattice, where $\tilde{z} = 0$, but it is relevant in a triangular lattice, where $\tilde{z} = 2$. Here, the neglect of pair correlations in the mean-field sum is justified only by $\tilde{z}/z = 1/3$ and not by $1/z = 1/6$ as one would have expected from the Bethe-lattice consideration. An extreme case for this phenomenon is a spin system on complete graphs. In this case, $\tilde{z}/z = (z-1)/z$, so that the neglect of pair correlations in the mean-field sum is not well justified. However, the benchmark on complete graphs in Sec. 4.3 indicates that the error from this approximation is still not large.

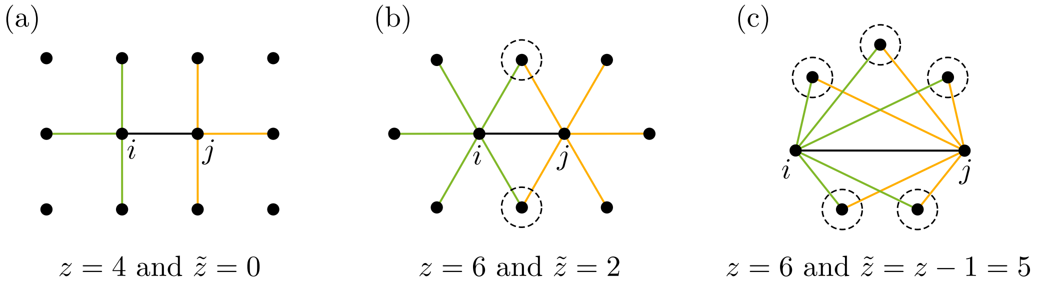

Figure B.1: Illustration of the number of shared nearest neighbors $\tilde{z}$ in different lattices. Panel (a) shows a square lattice, panel (b) a triangular lattice and panel (c) a complete graph with $N = 7$. The two sites i and j are nearest neighbors which is indicated by the black connection line. The links from site i to its remaining neighbors are shown by green lines and the ones from site j to its remaining neighbors by orange lines. The shared neighbors are highlighted by the dashed circle.

C Implementation and sources of numerical error

In this appendix, we discuss the implementation, the numerical errors and the choice of the associated numerical parameters in spinDMFT, CspinDMFT and nl-spinDMFT. Throughout the chapter, we assume time translation invariance, i.e., all correlations and errors depend only on a single time $t \coloneqq t_1 - t_2$. The time-inhomogeneous case is easily accessible by replacing $(t) \to (t, 0) \to (t_1, t_2)$.

C.1 spinDMFT

Implementation and computational cost

The iteration procedure for solving the self-consistency problem of spinDMFT is given in Fig. 4.3. Its numerical implementation is sketched by the pseudocode in Alg. 1.

Algorithm 1: Pseudocode for solving the self-consistency problem of spinDMFT.

```
[1]  Guess the initial spin autocorrelations $g^{\alpha\beta}_{(0)}(t)$
[2]  $p = 0$                                                          // iteration step
[3]  do
[4]      $p \leftarrow p + 1$
[5]      determine $v^{\alpha\beta}_{(p)}(t)$ from $g^{\alpha\beta}_{(p-1)}(t)$ using the self-consistency conditions
[6]      construct the covariance matrix from $v^{\alpha\beta}_{(p)}(t)$ and diagonalize it
[7]      draw $M$ different mean-field samples over time
[8]      for each mean-field sample $\mathcal{X}$                        // Monte-Carlo simulation
[9]      do
[10]         for all time points $t'$                                   // time propagation
[11]         do
[12]             compute the short-step propagator $\mathbf{U}(t'+\delta t, t')[\mathcal{X}]$
[13]             compute the full propagator $\mathbf{U}(t'+\delta t, 0)[\mathcal{X}] = \mathbf{U}(t'+\delta t, t')[\mathcal{X}]\mathbf{U}(t', 0)[\mathcal{X}]$
[14]             compute and store the autocorrelations $g^{\alpha\beta}_{(p)}(t'+\delta t)[\mathcal{X}]$
[15]     determine $g^{\alpha\beta}_{(p)}(t)$ for all times by averaging over the samples
[16]     compute the iteration error $\Delta I_{(p)}$ between the steps $p$ and $p-1$
[17] while $\Delta I_{(p)} > \Delta I_{\mathrm{threshold}}$                   // termination condition
```

First, the initial spin autocorrelations have to be guessed as described by line 1. A simple choice is to set the diagonal correlations ($\alpha = \beta$) to Gaussian or exponential functions in time and the off-diagonal correlations ($\alpha \neq \beta$) to zero. The better the initial guess, the faster the algorithm will converge. Note that one could also formulate a guess for the mean-field moments as indicated in Fig. 4.3, but in practice, it is easier to guess the spin autocorrelations, since they are fixed by $g^{\alpha\beta}(0) = \delta^{\alpha\beta}/4$ (for $S = 1/2$). The corresponding mean-field moments are straightforwardly computed using the self-consistent equations.

The construction of the covariance matrix in line 6 is discussed in Ref. [Grä+21] (Sec. II, D and App. B, 4). Once constructed, the covariance matrix must be diagonalized to obtain the set of eigenvalues and the corresponding orthogonal transformation. These two can be used to draw time-correlated Gaussian mean-field samples in line 7[1]. A detailed description of this procedure is also given in Ref. [Grä+21] (Sec. II, D).

Due to the dynamic mean field, the Hamiltonian is explicitly time dependent which complicates the computation of time propagators. The latter must be sliced into short-step propagators, which describe the time evolution over a single time step δt. These can be computed efficiently by using CFETs [AF11][2]:

$$\mathbf{U}^{(2)}_{\text{CF:1}}(t' + \delta t, t') = \mathrm{e}^{\mathbf{A}_1}, \tag{C.1a}$$

$$\mathbf{U}^{(4)}_{\text{CF:3,Opt}}(t + \delta t, t') = \mathrm{e}^{\frac{11}{40}\mathbf{A}_1 + \frac{20}{87}\mathbf{A}_2 + \frac{7}{50}\mathbf{A}_3} \times \mathrm{e}^{\frac{9}{20}\mathbf{A}_1 - \frac{7}{25}\mathbf{A}_3} \times \mathrm{e}^{\frac{11}{40}\mathbf{A}_1 - \frac{20}{87}\mathbf{A}_2 + \frac{7}{50}\mathbf{A}_3} \tag{C.1b}$$

where

$$\mathbf{A}_j = -\mathtt{i}(2j - 1)\frac{\delta t}{2}\Big(\mathbf{H}(t' + \delta t) - (-1)^j \mathbf{H}(t')\Big). \tag{C.2}$$

The expression for A_j results from approximating time integrals by the trapezoidal rule, which has to be used because the mean field and thus the Hamiltonian is known only at time t' and $t' + \delta t$ and not in between[3]. The exponents in Eq. (C.1) are always linear combinations of the Pauli matrices in case of $S = 1/2$. Therefore, the exponentials can be simplified according to

$$\mathrm{e}^{-\mathtt{i}\frac{\varphi}{2}\vec{n}\cdot\vec{\sigma}} = \cos\left(\frac{\varphi}{2}\right)\sigma^0 - \mathtt{i}\sin\left(\frac{\varphi}{2}\right)(\vec{n}\cdot\vec{\sigma}) \tag{C.3}$$

where φ is a real number, $\vec{n}$ is a normalized 3D vector and $\vec{\sigma} = (\sigma^x, \sigma^y, \sigma^z)^\top$. This also reveals two advantages of using CFETs: unitarity is automatically ensured, i.e., $\mathbf{U}^\dagger\mathbf{U} = \mathbf{1}$, and the Lie group structure of the spin is preserved. Multiplying the resulting short-step propagators leads to the full time propagator as indicated in line 13. The square brackets indicate that the propagators depend on a single mean-field sample $\mathcal{X}$.

The algorithm for spinDMFT contains three computational bottlenecks: the diagonalization of the covariance matrix, the mean-field sampling and the time propagation. The diagonalization only needs to be performed once per iteration step. Nevertheless, it can consume a lot of computational resources if the number of time steps L is large, since its computational cost roughly grows as $\mathcal{O}(d^3)$, where $d = 3(L + 1)$ is the matrix dimension. The sampling of the mean field requires, amongst other things, a matrix-vector multiplication, which grows only as $\mathcal{O}(d^2)$. However, this multiplication must be done for each sample, which results in an additional factor of M. The cost of computing the time

---

[1] This step requires a pseudo-random number generator. For all results in this thesis, we use the Mersenne Twister generator mt19937 implemented in the C++ standard library.

[2] Note that the second order CFET is equivalent to the first order Magnus expansion.

[3] We assume that the discretization is fixed and equal for the mean-field moments and the spin autocorrelations.

propagators and autocorrelations is linear in M and L and is only relevant for rather coarse discretizations[4].

In the following subsections, we will provide the definition of the numerical errors, i.e., the statistical error Σ, the time-discretization error ΔQ, and the iteration error ΔI. We will also discuss the choice of the numerical parameters, i.e., the sample size M, the step width δt, and the iteration-error threshold $\Delta I_{\text{threshold}}$.

Statistical error and sample size

As mentioned previously, the spin autocorrelations are computed by Monte-Carlo simulation, which involves a statistical error. The latter can be estimated in each iteration step of a simulation with little computational cost. Suppose the single-sample spin autocorrelation[5] $G^{\alpha\beta}(t)[\chi]$ is given for a set of mean-field samples χ. The statistical error of the mean value, which reads

$$G^{\alpha\beta}(t) \coloneqq \frac{1}{M}\sum_{\chi} G^{\alpha\beta}(t)[\chi], \tag{C.4}$$

can be estimated by

$$\Sigma^{\alpha\beta}(t) \coloneqq \sqrt{\frac{1}{M}\sum_{\chi}\left(G^{\alpha\beta}(t)[\chi] - G^{\alpha\beta}(t)\right)^2} \tag{C.5}$$

where M is the sample size. We define the general statistical error Σ of a simulation result as the maximum value of Eq. (C.5) considering all directions α, β and times t.

There are several strategies for choosing an appropriate sample size M. In Ref. [Grä+21] (App. B, 1), it was shown analytically and numerically that the statistical error in Eq. (C.5) converges to $1/\sqrt{3M}$ in the limit $t \to \infty$. For shorter times, $\Sigma^{\alpha\beta}(t)$ is typically smaller than this limit. Based on this observation, we can formulate a conservative estimate of the statistical error,

$$\Sigma \lessapprox \frac{c}{\sqrt{3M}}, \qquad c \coloneqq 2. \tag{C.6}$$

The choice of the parameter c is simply based on practical experience. Using Eq. (C.6), an appropriate sample size can be determined by

$$M \coloneqq \frac{c^2}{3\epsilon^2}, \tag{C.7}$$

where ϵ is the desired error tolerance. Alternatively, the sample size can be changed adaptively during the iterations which can increase the efficiency. This strategy has only been tried out for CspinDMFT, but there is no reason why it should not work for spinDMFT as well.

---

[4] It becomes more relevant, however, when the correlations have to be computed for pairs of times, t_1 and t_2, i.e., when time translation invariance does not hold.

[5] We remind the reader that the capital letter "G" is used for the normalized spin correlations, i.e., $G^{\alpha\beta}(0) = \delta^{\alpha\beta}$.

It is worth noting that the statistical fluctuations due to the Monte-Carlo simulation can lead to small violations of the semidefiniteness of the covariance matrix required to sample the mean field. This issue is simply solved by truncating the negative eigenvalues. More information on this can be found in Ref. [Grä+21] (App. B, 1).

Time-discretization error and step width

Another key ingredient of the numerical implementation is the time discretization, which entails another source of numerical error. Note that for the purposes of this thesis, the time points in all simulations are chosen to be equidistant. Suppose the simulation results $G_\lambda^{\alpha\beta}(t)$ are given for two different discretizations, $\lambda = \mu$ (coarser) and $\lambda = \nu$ (finer), and the number of time steps of ν is an integer multiple of μ. We define the quantity

$$\Delta Q_{\mu\to\nu}^{\alpha\beta}(t) \coloneqq |G_\nu^{\alpha\beta}(t) - G_\mu^{\alpha\beta}(t)| \tag{C.8}$$

for all directions α, β and all times t of the coarser discretization μ. Its maximum value is an estimate of the discretization error $\Delta Q_{\mu\to\nu}$ of μ.

A modified version of this error has been studied numerically in Ref. [Grä+21] (App. B, 2[6]) and yields a dependence on δt^2. This is consistent with the expectation from using the trapezoidal rule to compute the exponents of short-step propagators as mentioned earlier. It should be noted, however, that the prefactor of the error depends strongly on the spin model under consideration. Furthermore, the dependence on δt^2 is only valid on a finite interval, since the errors upper bound is 2 (due to the limits of the correlation) and its lower bound is the statistical error (which is inherent in Eq. (C.8)).

In practice, the simulation of a given effective Hamiltonian must be performed for at least two different step widths in order to estimate the discretization error. Comparisons between different data sets and intuition can help to decide on an appropriate choice of δt. For instance, if Larmor oscillations are expected to enter the mean field, one should resolve each Larmor period by at least $5 - 10$ time steps. In general, if the desired tolerance ϵ is exceeded by the discretization error, the step width should be successively reduced until the tolerance is met. We recall that $\Delta Q_{\mu\to\nu}$ refers to the discretization error of the coarser discretization. The error of the finer discretization can be estimated by

$$\Delta Q_\nu \coloneqq \left(\frac{\delta t_\nu}{\delta t_\mu}\right)^2 \Delta Q_{\mu\to\nu} \tag{C.9}$$

where δt_ν and δt_μ are the corresponding step widths. In practice, we always show the results of the finest discretization $\nu_{\min}$. Consequently, $\Delta Q \coloneqq \Delta Q_{\nu_{\min}}$ is the relevant error for the tolerance ϵ. From our experience, we recommend decreasing δt in powers of 2. It is conceivable that the step width can be changed adaptively during the iteration steps of a single simulation in order to maintain the tolerance ϵ, but this has not been tested yet.

---

[6] In that reference, we considered the time-averaged discretization error instead of Eq. (C.8), but the behavior is essentially the same.

Iteration error

The self-consistency problem posed by spinDMFT is solved iteratively, i.e., we introduce an initial guess for the spin autocorrelations and improve it iteration by iteration as explained in Alg. 1. The termination of this procedure after a finite number of steps entails another source of numerical error, which we denote as the iteration error. Suppose the Monte-Carlo-averaged results $G^{\alpha\beta}_{(q)}(t)$ of two adjacent iteration steps $q = p - 1$ and $q = p$ are given. We define the quantity

$$\Delta I^{\alpha\beta}_p := \overline{|G^{\alpha\beta}_{(p)}(t) - G^{\alpha\beta}_{(p-1)}(t)|}^{\text{ta}} \tag{C.10}$$

where "ta" stands for time average[7]. The maximum value of $\Delta I^{\alpha\beta}_p$ with respect to the directions α, β is considered the iteration error ΔI_p of step p.

If the iteration error falls below a certain threshold value $\Delta I_{\text{threshold}}$, the self-consistency iteration is terminated. It is important to note that ΔI_p contains the statistical error. Consequently, $\Delta I_{\text{threshold}}$ must be chosen larger than the latter for an efficient termination condition. According to Eq. (C.6), a reasonable choice for the threshold is

$$\Delta I_{\text{threshold}} := \frac{c}{\sqrt{3M}}. \tag{C.11}$$

Alternatively, $\Delta I_{\text{threshold}}$ could be defined directly by the estimated statistical error Σ in each iteration step, but this has not been tried yet.

General numerical error and error tolerance

The general numerical error ε is calculated *a posteriori* as the maximum of the statistical error Σ and the discretization error ΔQ estimated in the simulation. The iteration error is considered implicitly, since it is directly linked to the statistical error via Eq. (C.11). If a data set is given an error tolerance ϵ, we have explicitly checked that the estimated general numerical error ε does not exceed it.

The main numerical parameters of spinDMFT are the sample size M and the step width δt. The proper sample size for a desired error tolerance can be estimated *a priori* by Eq. (C.7), while the proper step width can only be guessed. As an example, for the generic result of the Heisenberg model, see Fig. 4.4, the sample size is $M = 10^6$ and the step width is $\delta t = 2 \times 10^{-2}\, J_{\text{Q}}^{-1}$ ($L = 10^3$ steps), which leads to an error tolerance $\epsilon < 10^{-3}$. The corresponding computational cost is in the order of one core hour[8].

---

[7] The average is taken over t_1 and t_2 if time translation invariance does not hold.

[8] Note that the tolerance is relatively small. Increasing it by a factor of two reduces the computation time approximately by a factor of 10.

C.2 CspinDMFT and nl-spinDMFT

Implementation and computational cost

The implementation of CspinDMFT is essentially the same as that of spinDMFT except for the inclusion of an additional tensor dimension due to the different sites in the cluster. This additional dimension enters the spin correlations, the mean-field moments and the covariance matrix in CspinDMFT. The dimensionality of the latter is increased by the cluster size n making its diagonalization and the subsequent sampling more expensive. But the cost of computing a spin correlation increases even more because it involves matrix-matrix products on the local Hilbert space, the dimension of which is 2^n in CspinDMFT. The cost of computing these products grows with the cube of the dimension, i.e., $2^{3n} = 8^n$. The computation of the time propagators is also more involved because Eq. (C.3) can no longer be used to evaluate the CFET exponentials. In the current implementation of CspinDMFT, these exponentials are computed by diagonalizing the exponent, which is also computationally expensive[9]. Furthermore, the self-consistency condition of CspinDMFT typically includes several spin correlations, all of which must be computed in each iteration step. The number of these correlations can be quite large, e.g., $n(n+1)/2$ in case of the CRA (assuming T-symmetry and ignoring the multiplicity due to the different directions α, β). Because of all these aspects, the computational bottleneck of CspinDMFT shifts more from the diagonalization and sampling to the computation of spin correlations. This strongly motivates to minimize the number of correlations computed per iteration step, see for example the proposed improvement of the CRA in Sec. 5.4.3 or nl-spinDMFT, which will be briefly discussed below.

The idea of nl-spinDMFT is to access the individual correlations required to compute the FID by simulating a cluster in an *a priori* given mean-field background. The latter is computed by spinDMFT, for which numerical details have already been discussed. The implementation of nl-spinDMFT is essentially the same as for CspinDMFT, but no self-consistency is required, i.e., only a single iteration step is performed. It should be noted, however, that each correlation that enters the FID requires an individual simulation of a particular cluster. The computational effort (CE) of a FID-simulation with respect to a self-consistent simulation by CspinDMFT is thus approximately given by

$$\frac{\mathrm{CE(nl\text{-}spinDMFT)}}{\mathrm{CE(CspinDMFT)}} = K \frac{\text{\#correlations for FID (nl-spinDMFT)}}{\text{\#iteration steps (CspinDMFT)}}. \tag{C.12}$$

The factor $K < 1$ accounts for the fact that the self-consistency in CspinDMFT requires the computation of several correlations during each iteration step.

Adapted statistical and time-discretization error

The additional dimension due to the site dependence must also be regarded in the numerical errors of CspinDMFT and nl-spinDMFT. This basically means to consider the

---

[9] Note that there are more efficient ways to evaluate exponentials of antihermitian operators, for example, the Krylov technique [AF11]. This should be considered in future implementations of CspinDMFT.

extended quantities

$$\Sigma^{\alpha\beta}(t) \to \Sigma^{\alpha\beta}_{ij}(t), \qquad \Delta Q^{\alpha\beta}_{\mu\to\nu}(t) \to \Delta Q^{\alpha\beta}_{ij,\mu\to\nu}(t). \tag{C.13}$$

However, in many cases we are only interested in one or a small number of correlation functions and not all of them. For example, in nl-spinDMFT, each individual simulation aims at a single pair correlation only, i.e., the tuple ij is fixed. Therefore, only this specific pair correlation is considered for the numerical errors.

In CspinDMFT the situation is more subtle. Often, we are only interested in a single correlation (usually $ij = 11$, see Ch. 5), but several more correlations are needed to close the self-consistency. However, numerical errors entering the mean fields via the self-consistency are negligible for the simulated spin correlations to a very good approximation. Therefore, it is reasonable to consider only the correlations of interest (the ones that are plotted and analyzed) as being relevant for the numerical errors. Nevertheless, the errors of the remaining correlations that enter the self-consistency should at least be tracked. If these errors are of a different order of magnitude, the numerical parameters should be adjusted accordingly to be on the safe side[10].

Another noteworthy aspect of CspinDMFT is that the mapping of correlations via the CRA can lead to violations of the semidefiniteness of the covariance matrix *beyond statistical fluctuations*. In practice, the resulting negative eigenvalues can nevertheless be truncated as explained in Ref. [Grä+23] (App. D, 1).

Adapted iteration error

In nl-spinDMFT, an iteration error occurs only in the process of generating this mean-field background by means of spinDMFT. This error was discussed before. In CspinDMFT, the situation is more complicated. Similar to Eq. (C.13), we have to consider the extended quantity

$$\Delta I^{\alpha\beta}_{p} \to \Delta I^{\alpha\beta}_{ij,p}. \tag{C.14}$$

While the statistical and discretization errors behave rather generically, the behavior of the iteration error is difficult to predict. It is conceivable that it varies greatly from correlation to correlation in certain examples. Since the correlations affect each other through the self-consistency condition, the value of $\Delta I^{\alpha\beta}_{ij,p}$ may not be representative of the iteration error, not even for that of $G^{\alpha\beta}_{ij,(p)}$. However, if $\Delta I^{\alpha\beta}_{ij,p}$ is small for all pairs of directions and all pairs of sites, this is a good indicator of numerical convergence. Consequently, we define the iteration error ΔI_p in CspinDMFT as the maximum of $\Delta I^{\alpha\beta}_{ij,p}$ for all $\alpha\beta$ and ij, and terminate the iteration when ΔI_p falls below a predefined threshold $\Delta I_{\text{threshold}}$. This implies that all correlations must converge. The threshold should be set to the desired error tolerance. However, it is important to note that the iteration error still contains the statistical error and is thus bounded from below. Thus, the threshold can only be surpassed if the statistical error is sufficiently small. Notably, the required sample size for this is typically considerably smaller for CspinDMFT than for spinDMFT, as will be discussed in the subsequent section.

---

[10] Significant numerical errors in certain correlations can result, for example, from cutting strong dimer bonds at the edge of the cluster, see Fig. 5.8.

Reduced sample size for larger clusters

As previously stated, the infinite-time value of the statistical error in spinDMFT can be derived analytically. It is given by[11]

$$\lim_{t\to\infty} \Sigma^{\alpha\beta}(t) = \frac{1}{\sqrt{3M}}. \tag{C.15}$$

The basic idea of the derivation is to describe the time evolution of the spin vector by a rotation matrix that rotates the spin in real space. With the help of this and the assumption that all initial information in the system is lost at infinite time, it can be deduced that all directions are equally probable, which explains the factor of 3 in the square root. The additional factor M simply represents the difference between the standard deviation of a single mean-field sample and the standard deviation of the average over M samples (the latter being the proper statistical error of the Monte-Carlo simulation).

This derivation can be extended to CspinDMFT. Here, the Hilbert space extends to several spins (with $S = 1/2$) and the Hamiltonian is partly bilinear in spin operators as can be seen for example in Eq. (5.5). The corresponding time evolution transforms a single Pauli matrix into a linear combination of products of Pauli matrices at different sites according to

$$\sigma_i^\gamma(t)[\mathcal{X}] = \sum_{\alpha_1,\ldots,\alpha_n} c^\gamma_{i,\alpha_1\ldots\alpha_n}(t)[\mathcal{X}] \prod_j \sigma_j^{\alpha_j}, \qquad \alpha_j \in \{0,x,y,z\} \wedge j \in \{1,\ldots,n\}, \tag{C.16}$$

where $c^\gamma_{i,\alpha_1\ldots\alpha_n}(t)[\mathcal{X}]$ are real-valued coefficients, n is the cluster size, and $\mathcal{X}$ represents a single mean-field sample[12]. Note that this expression is completely general in the Hilbert space of the cluster. Successive actions of the Liouville operator (commutations with the Hamiltonian) connect all possible products of Pauli matrices with one other except for the identity σ^0. Consequently, all coefficients can be finite except for $c^\gamma_{i,0\ldots0}(t)[\mathcal{X}]$, which is strictly zero if $\gamma \in \{x,y,z\}$ ($\gamma = 0$ is trivial). In addition, we know that

$$\left(\sigma_i^\gamma(t)[\mathcal{X}]\right)^2 = \sum_{\substack{\alpha_1,\ldots,\alpha_n\\ \beta_1,\ldots,\beta_n}} c^\gamma_{i,\alpha_1\ldots\alpha_n}(t)[\mathcal{X}]\, c^\gamma_{i,\beta_1\ldots\beta_n}(t)[\mathcal{X}] \left(\prod_j \sigma_j^{\alpha_j}\right)\left(\prod_j \sigma_j^{\beta_j}\right) \overset{!}{=} \sigma^0. \tag{C.17}$$

For this to hold, only terms $\propto \sigma^0$ can survive in the double sum so that we can effectively ignore all contributions except for $\alpha_j = \beta_j, \forall j$ arriving at

$$\sum_{\alpha_1,\ldots,\alpha_n} \left(c^\gamma_{i,\alpha_1\ldots\alpha_n}(t)[\mathcal{X}]\right)^2 = 1. \tag{C.18}$$

Similar to the procedure for spinDMFT, we now assume that any initial information in the system is lost at infinite time. This is reasonable if the dynamic mean fields act as a bath for the cluster removing information from it over time. However, no general statement can be made about the time scale of this process. Following our assumption,

---

[11] See Ref. [Grä+21] (App. B, 1) for the step-by-step derivation.

[12] Note that $\mathcal{X}$ comprises the time evolution of *all* n mean fields interacting with the cluster.

all of the coefficients should behave equal on average at infinite time. Considering this and $c^{\gamma}_{i,0\dots0}(t)[\mathcal{X}] = 0$, the normalization condition in Eq. (C.18) can be rewritten as

$$\lim_{t\to\infty} \overline{\left(c^{\gamma}_{i,\alpha_1\dots\alpha_n}(t)[\mathcal{X}]\right)^2}^{\mathrm{mf}} = \frac{1}{4^n-1}. \tag{C.19}$$

Total information loss at infinite time also implies that every spin correlation vanishes so that

$$\lim_{t\to\infty} G^{\alpha\beta}_{ij}(t) = \lim_{t\to\infty} \overline{G^{\alpha\beta}_{ij}(t)[\mathcal{X}]}^{\mathrm{mf}} = \lim_{t\to\infty} \overline{c^{\alpha}_{i,0\dots0\,\alpha_j=\beta\,0\dots0}(t)[\mathcal{X}]}^{\mathrm{mf}} = 0. \tag{C.20}$$

By means of this, we obtain the single-sample standard deviation

$$\lim_{t\to\infty} \left(\sigma^{\alpha\beta}_{ij}(t)\right)^2 = \lim_{t\to\infty} \overline{\left(G^{\alpha\beta}_{ij}(t)[\mathcal{X}] - G^{\alpha\beta}_{ij}(t)\right)^2}^{\mathrm{mf}} \tag{C.21a}$$

$$= \lim_{t\to\infty} \overline{\left(G^{\alpha\beta}_{ij}(t)[\mathcal{X}]\right)^2}^{\mathrm{mf}} = \lim_{t\to\infty} \overline{\left(c^{\alpha}_{i,0\dots0\,\alpha_j=\beta\,0\dots0}(t)[\mathcal{X}]\right)^2}^{\mathrm{mf}}. \tag{C.21b}$$

Together with Eq. (C.19), this yields

$$\lim_{t\to\infty} \sigma^{\alpha\beta}_{ij}(t) = \frac{1}{\sqrt{4^n-1}}. \tag{C.22}$$

To compute the proper statistical error $\Sigma^{\alpha\beta}_{ij}(t)$, this expression must be multiplied by $1/\sqrt{M}$. Including this factor, Eq. (C.22) reproduces the result of spinDMFT for $n = 1$, see Eq. (C.15). For $n \geq 2$, the formula can be tested numerically. To this end, we consider a Heisenberg model with spins on a triangular lattice and couplings $\propto {}^1\!/_{R^3}$. In Fig. C.1, the mean and the standard deviation of the central spins autocorrelation are plotted against time.

As can be seen in panel (a), the mean does not change much upon increasing the cluster size, which is not surprising due to the relatively large coordination number. As for the results in Sec. 5.2, we obtain a fast convergence to zero, which justifies our assumption of total information loss at infinite time in Eq. (C.20). The standard deviation shown in panel (b) behaves differently. It is zero at $t = 0$ because the initial value of the correlation is fixed. After that, it increases rapidly, followed by a slow convergence to a fixed value. This value agrees with our prediction in Eq. (C.22) confirming the assumption of total information loss once more. Interestingly, the statistical error in CspinDMFT ($n \geq 2$) relaxes considerably slower than the autocorrelation, suggesting that information is concealed in higher order correlation functions. Another surprising aspect of CspinDMFT is that σ^{xx}_{11} peaks significantly above the limit at short times. Therefore, in contrast to spinDMFT, the bound cannot be used as a conservative estimate of the statistical error. Nevertheless, the statistical error decreases significantly with the cluster size. We can therefore conclude that simulations of larger clusters require smaller sample sizes.

As mentioned above, the statistical error should always be tracked in a simulation in order to verify that the desired precision is achieved with the selected sample size. Instead of choosing a fixed sample size in advance, one can adaptively change it based on the statistical error computed at each iteration step. This strategy has been tested and found to be very effective, but it comes at the cost of having no strict bound on the computation time.

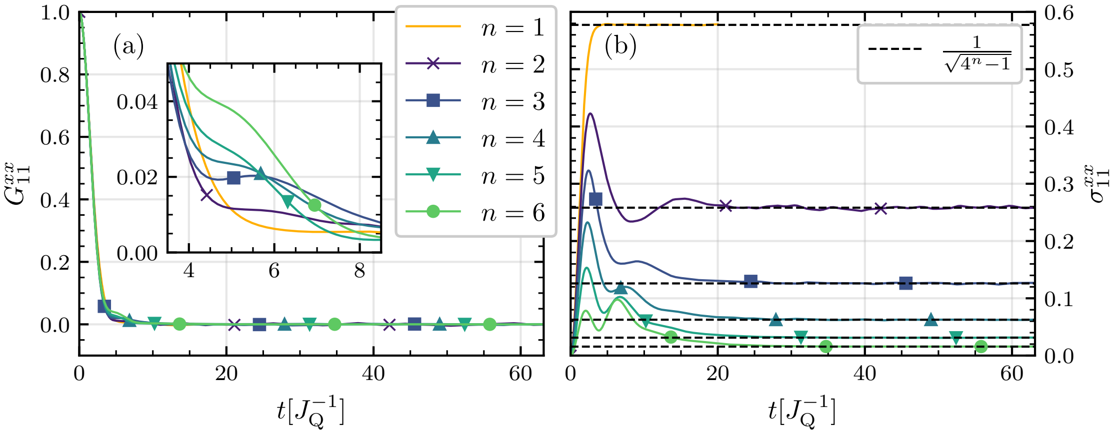

Figure C.1: Plot of the mean G_{11}^{xx} (a) and the single-sample standard deviation $\sigma_{11}^{xx} = \sqrt{M}\Sigma_{11}^{xx}$ (b) of the central spins autocorrelation considering a Heisenberg model on a triangular lattice with couplings $\propto R^{-3}$ and varying cluster sizes n. The time is measured in units of the inverse quadratic coupling constant of the lattice. The orange line results from spinDMFT ($n = 1$) and the remaining colored lines (supported by markers for better distinction) result from CspinDMFT. The dashed lines in panel (b) result from the predicted limit value from Eq. (C.22). For the sake of completeness, we note that the statistical error of other correlations (for $n \geq 1$) behaves qualitatively the same.

General numerical error

In spinDMFT, the general numerical error ε is calculated *a posteriori* as the maximum of the statistical error Σ and the discretization error ΔQ estimated in the simulation. This is done exactly the same way in nl-spinDMFT. In CspinDMFT, however, we also consider the iteration error for ε, since the relation of the latter to the statistical error is not entirely clear.

D Choosing an appropriate cluster in CspinDMFT

One, if not the most important part of CspinDMFT, is a reliable choice of the cluster, which shall be discussed in this appendix. We recall that the main goal of the approach is to estimate the autocorrelation of the central spin $\vec{\mathbf{S}}_1$ as reliable as possible. In accordance with the derivation of CspinDMFT in Sec. 5.1, a successful cluster-finding strategy considers the following two aspects:

- The most important interaction partners of $\vec{\mathbf{S}}_1$ are included in Γ.
- The border between Γ and the environment does not contain strong couplings.

The first aspect is easily fulfilled by the *central-spin-based* strategy, which fills the cluster with the spins that are strongest coupled to $\vec{\mathbf{S}}_1$. The strength of a coupling is measured by the modulus

$$\Delta_k^{\mathrm{cs}} := |J_{1k}|. \tag{D.1}$$

This strategy is certainly plausible in regular one-atomic lattices as detailed in Fig. D.1, panel (a)[1]. However, since it only considers the couplings with the central spin, there is no control about the second aspect, i.e., the border between cluster and environment at all. This can be problematic in inhomogeneous systems, for example, if spin dimers are “cut” at the edge of Γ, see Fig. D.1, panel (b).

The *cluster-based* strategy circumvents this problem by adding the spins one by one to the cluster. The next spin to be added is determined from maximizing the sum

$$\Delta_k^{\mathrm{cluster}} := \sum_{i\in\Gamma} |J_{ik}| \tag{D.2}$$

with respect to k. In this way, strong couplings between cluster and environment are prevented if the cluster size is chosen properly, see Fig. D.1, panel (c). The drawback of this strategy is that the clusters depend rather strongly on the initially added neighbors. The latter contribute to the condition in Eq. (D.2) and therefore strongly bias the cluster finding, see for example panel (d). This is sometimes in contrast to the first aspect, i.e., some relatively important interaction partners of the central spin are not added to the cluster.

The central-spin-based and the cluster-based strategy have been derived and studied in Ref. [Grä+23]. The conclusion was drawn that the cluster-based strategy performs a bit better because of a quicker convergence of the central-spin autocorrelations with the cluster size. It should be noted, however, that a quick convergence can be misleading

---

[1] The strategy can break down in the special case of NN interactions because the condition becomes useless as soon as all neighbors of the central spin are part of the cluster. In this case, an additional condition is needed.

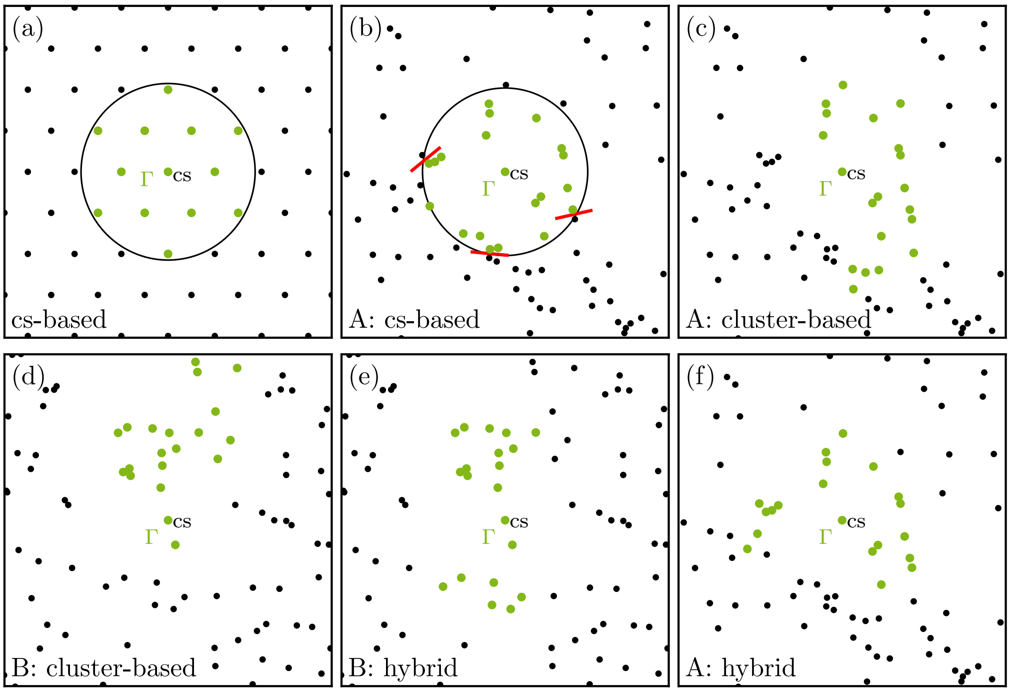

Figure D.1: Triangular spin lattice (a) and two different seeds for an inhomogeneous spin system, denoted by A (b,c,f) and B (d,e), considering dipolar-like interactions, $J = R^{-3}$. The shorthand "cs" stands for central spin. The green dots correspond to spins that are assigned to the cluster Γ according to the different strategies (names provided in the lower left corner of each panel). The cluster sizes have been fixed to 13 in panel (a) and 20 in panels (b-f). Such large cluster sizes are not realistic for an actual simulation, but they are advantageous for observing the characteristics of the different strategies. In panel (a), the displayed cluster is obtained for all considered strategies, if one considers the extra rule that all strongest-coupled spins are added at once. Due to the radial symmetry of the couplings, the cluster can be always separated from the environment by a sphere in case of the central-spin-based strategy. This is indicated by the black circle in panel (a) and (b). The red lines in panel (b) indicate "cuts" through dimers of strongly-coupled spins emphasizing the disadvantage of the central-spin-based strategy. This problem occurs only rarely in the cluster-based and hybrid strategy and can be eliminated by varying the cluster size. The cluster-based strategy has the drawback that it tends to push the cluster into a certain direction, see especially panel (d). This does not happen in the hybrid strategy, which gives the central spin a special weight, see panels (e) and (f).

particularly for the cluster-based strategy. Spins that are far away from the central spin are often preferred over nearby spins, but they hardly affect the central spins autocorrelation. Considering the latter for different cluster sizes could mistakenly imply numerical convergence although some presumably important, nearby spins of the central spin are not yet added to the cluster. Therefore, a clear statement about the performance of the strategies cannot be made. The convergence of the central-spin autocorrelation is certainly a more reliable indicator in the central-spin based strategy. Yet it is important to respect the local geometry when selecting a cluster, as is done in the cluster-based strategy. Consequently, we propose an intermediate strategy that strives to balance both strategies.

In the *hybrid* strategy, the next spin to be added is determined from maximizing

$$\Delta_k^{\text{hybrid}} \coloneqq (1-\mu_n)|J_{1k}|, \qquad \mu_n \coloneqq n^{-k/D} + \mu_n \sum_{i\in\Gamma} |J_{ik}|. \tag{D.3}$$

Here, n is the *current* size of Γ, D is the system dimension and k is the power by which the couplings decrease, i.e., $k = 3$ for dipolar interactions. The specific choice of μ_n results from the demand to keep the central spin equally important in the criterion as the cluster size is increased. As a consequence, the cluster is built around the central spin, but the border between cluster and environment is still minimized, see panels (e) and (f) of Fig. D.1. Note that the hybrid strategy can be used for both lattices and inhomogeneous systems. For lattices, we define an extra rule that requires all spins with maximum Δ_k^{hybrid} to be added at once, i.e., the spins are added shell by shell. This prevents random behavior during the construction of the cluster. In case of NN interactions, μ_n is simply set to one.

We stress that the cluster size is limited by the available numerical resources. Due to the importance of the border between cluster and environment it is not always the best option to set n to the maximum possible value. In a system of spin dimers, for example, n should be chosen even because otherwise a spin dimer would be cut in half. In inhomogeneous systems, it is reasonable to create the cluster for several sizes n. Then, the best choice is determined by minimizing[2]

$$\rho_n \coloneqq \max_{k\notin\Gamma} \Delta_k^{\text{hybrid}}. \tag{D.4}$$

with respect to n. A minimization of ρ_n corresponds to finding an optimal cut between cluster an environment. Note that, overall, this quantity decreases with n so that larger clusters are preferred. This is completely plausible because we expect better results for the central spin, if n is larger. In lattice systems, this criterion yields the maximum possible cluster size for all cases considered in this thesis. This is not astonishing because the border between cluster and environment does not vary much in periodic lattices. All calculations in this thesis are done with the hybrid approach unless stated otherwise.

---

[2] This criterion is different from the one used in Ref. [Grä+23].

E nl-spinDMFT

E.1 FID of calcium fluoride for other field directions

In this appendix, we provide the results for CaF_2-[110] and CaF_2-[111]. The procedure is the same as in Sec. 6.2. We begin with sorting the pair correlations according to the distance and, if the distance is equal, according to the modulus of the pair coupling, see Tab. E.1 and Tab. E.2. Subsequently, we generate the clusters for each category, see Fig. E.1 and Fig. E.3. Then, we calculate the pair correlations by simulating the corresponding cluster in a mean-field background generated by spinDMFT. The results are superposed to obtain the FID, which is plotted in Fig. E.2 and Fig. E.4. As explained in the main text, the choice of adequate clusters is more difficult for CaF_2-[110] and CaF_2 -[111] due to the larger coordination numbers. This explains the more notable deviations from the experiment.

Table E.1: Sorted list of correlations considered for the FID. Same content as in Tab. 6.1, but for CaF_2-[110].

c	$\vec{r}_c^{\top}/a_{\mathrm{sc}}$	$\lvert\vec{r}_c\rvert/a_{\mathrm{sc}}$	$\lvert d_c\rvert/d_0$	m_c
0				1
1	(0 0 -1)	1.0	1.0	2
2	(-1 0 0)	1.0	0.5	4
3	(-1 -1 0)	1.4142	0.7071	2
4	(-1 1 0)	1.4142	0.3535	2
5	(-1 0 -1)	1.4142	0.0884	8
6	(-1 -1 -1)	1.732	0.1924	8
7	(0 0 -2)	2.0	0.125	2
8	(-2 0 0)	2.0	0.0625	4
9	(-2 -1 0)	2.2361	0.152	4
10	(-2 1 0)	2.2361	0.0626	12
11	(-2 0 -1)	2.2361	0.0179	8
12	(-2 -1 -1)	2.4495	0.085	8
13	(-1 1 -2)	2.4495	0.068	4
14	(-2 1 -1)	2.4495	0.051	8
15	(-1 -1 -2)	2.4495	0.0	4
16	(-2 -2 0)	2.8284	0.0884	2
17	(-2 2 0)	2.8284	0.0442	2
18	(-2 0 -2)	2.8284	0.0111	8
19	(-2 -2 -1)	3.0	0.0617	4
20	(-2 2 -1)	3.0	0.037	6

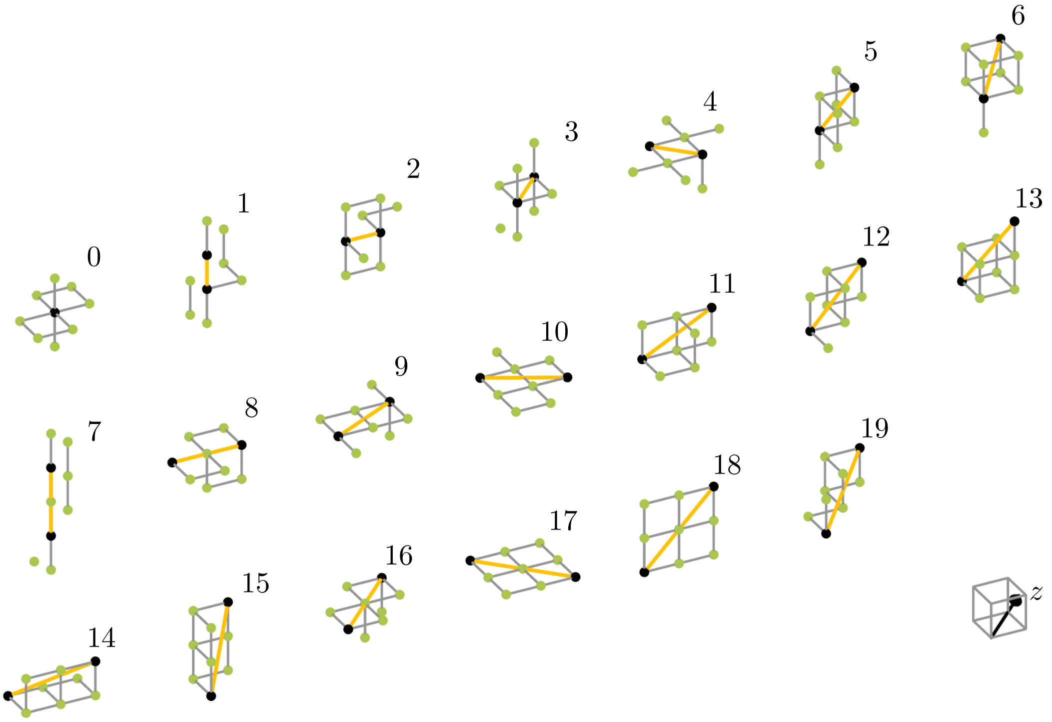

Figure E.1: Clusters to compute the correlations entering the FID. Same content as in Fig. 6.3, but for CaF_2-[110]. The dipolar couplings were truncated behind the $L = 8$ strongest couplings.

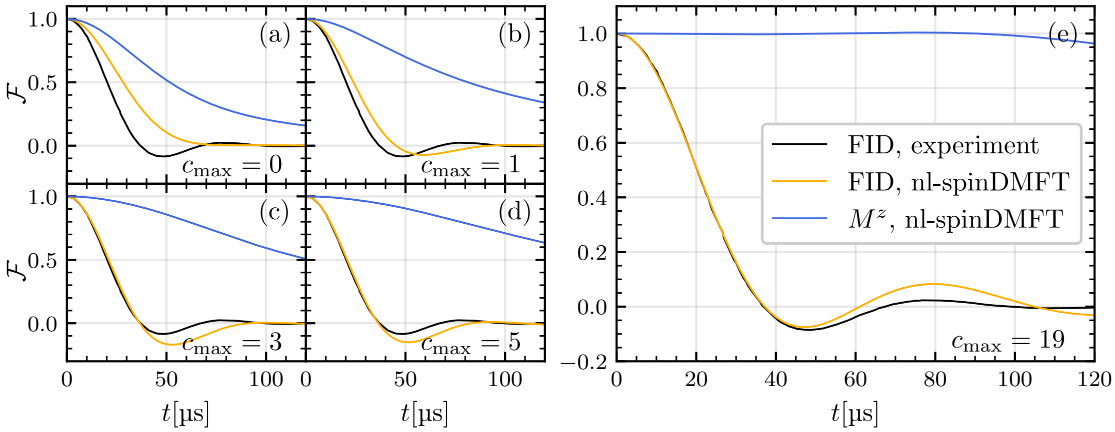

Figure E.2: Free-induction decay of CaF_2-[110] for different truncation values $c_{\max}$. The experimental data were taken from Ref. [EL74]. Nl-spinDMFT captures the experiment less well than for CaF_2-[100] (see Fig. 6.4), but the agreement is still satisfactory.

Table E.2: Sorted list of correlations considered for the FID. Same content as in Tab. 6.1, but for CaF_2-[111].

c	$\vec{r}_c^{\top}/a_{\mathrm{sc}}$	$\lvert\vec{r}_c\rvert/a_{\mathrm{sc}}$	$\lvert d_c\rvert/d_0$	m_c
0	(0 0 0)	0.0	0.0	1
1	(-1 0 0)	1.0	0.0	6
2	(-1 -1 0)	1.4142	0.3535	12
3	(-1 -1 -1)	1.732	0.3849	2
4	(-1 -1 1)	1.732	0.1283	6
5	(-2 0 0)	2.0	0.0	6
6	(-2 -1 0)	2.2361	0.0716	24
7	(-2 -1 -1)	2.4495	0.1134	6
8	(-2 1 1)	2.4495	0.068	6
9	(-2 -1 1)	2.4495	0.0227	12
10	(-2 -2 0)	2.8284	0.0442	12
11	(-2 -2 -1)	3.0	0.0658	6
12	(-2 -1 2)	3.0	0.0329	12
13	(-3 0 0)	3.0	0.0	12
14	(-3 -1 0)	3.1623	0.019	24
15	(-3 -1 -1)	3.3166	0.0349	6
16	(-3 1 1)	3.3166	0.0249	6
17	(-3 -1 1)	3.3166	0.005	12
18	(-2 -2 -2)	3.4641	0.0481	2
19	(-2 -2 2)	3.4641	0.016	6
20	(-3 -2 0)	3.6056	0.0197	24

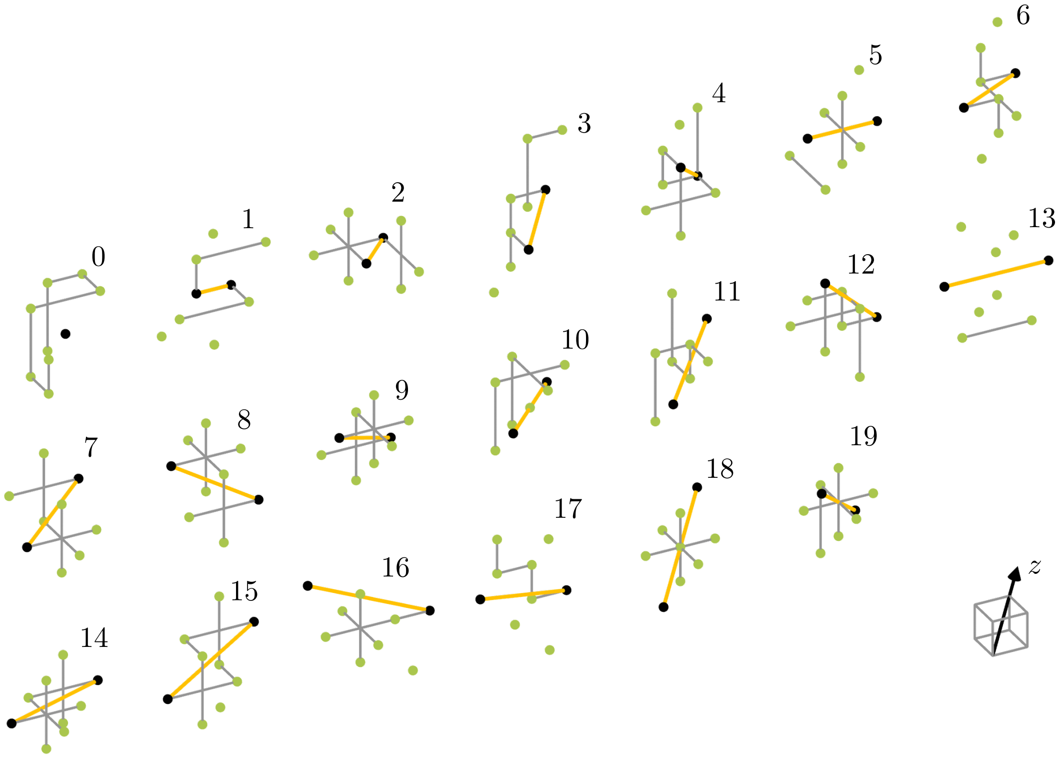

Figure E.3: Clusters to compute the correlations entering the FID. Same content as in Fig. 6.3, but for CaF$_2$-[111]. The dipolar couplings were truncated after the $L = 14$ strongest couplings. Some clusters do not look very compact, but this is expected due to the magnetic-field direction. The two strongest couplings are the ones in [111]-direction, see the entry $|d_3|/d_0$ in Tab. E.2. A clear and unambiguous illustration of the clusters is difficult; we decided that showing only the NN connection lines (and multiples of them) is the least confusing representation.

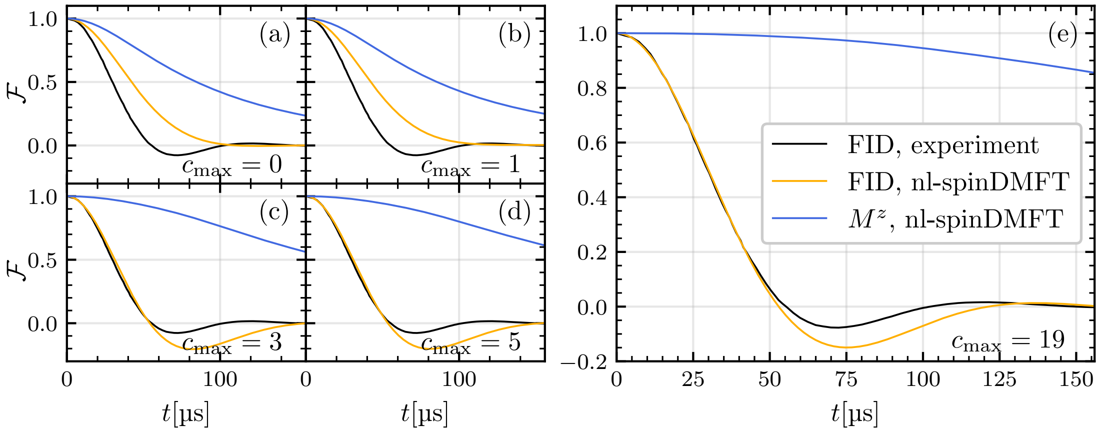

Figure E.4: Free-induction decay of CaF$_2$-[111] for different truncation values $c_{\max}$. The experimental data were taken from Ref. [EL74]. The agreement is worse than for CaF$_2$-[100] (see Fig. 6.4) and CaF$_2$-[110] (see Fig. E.2).

F Preliminary results: Including a globally conserved polarization in spinDMFT

Throughout this thesis, spinDMFT is exclusively considered at infinite temperature, i.e., for completely disordered spins. In this limit, a global conservation law such as the total spin conservation are not particularly relevant for the dynamics at a single site. However, the situation changes drastically when a global polarization is introduced to the system. This appendix presents some preliminary results of spinDMFT for this scenario. We use the shorthand $\mathbf{S}^\alpha := \mathbf{S}^\alpha(0)$ for spin operators at time $t = 0$.

F.1 Violation of total spin conservation in the Heisenberg model

We consider an ensemble of N interacting spins with $S = 1/2$ described by the Heisenberg model

$$\mathbf{H} = \frac{1}{2} \sum_{i,j} J_{ij} \vec{\mathbf{S}}_i \cdot \vec{\mathbf{S}}_j \tag{F.1}$$

The couplings J_{ij} are not specified for now, but we assume a homogeneous spin system with one-atomic basis. Analogous to the quadratic coupling constant J_Q, we define the linear coupling sum

$$J_\mathrm{L} := \mathcal{J}_{1,i} = \sum_j J_{ij}. \tag{F.2}$$

The system is considered in the paramagnetic regime $\beta^{-1} \gg J_\mathrm{L}$ and prepared in a polarized state[1]

$$\rho = \frac{1}{\mathcal{Z}} \mathrm{e}^{h \sum_i \mathbf{S}_i^z}, \qquad \mathcal{Z} = \left(\cosh \frac{h}{2}\right)^N, \qquad h = B\beta. \tag{F.3}$$

Since $\mathbf{H}$ commutes with the total spin $\vec{\mathbf{S}}_\mathrm{tot} := \sum_i \vec{\mathbf{S}}_i$, it also commutes with the density operator in Eq. (F.3). Hence, any spin expectation values are time independent. Transferring this situation to spinDMFT forms a problem because the naïve mean-field model does not conserve the total spin according to

$$\mathbf{H}^\mathrm{mf}\left[\vec{V}_1(t), \dots, \vec{V}_N(t)\right] = \sum_i \vec{\mathbf{S}}_i \cdot \vec{V}_i(t). \tag{F.4a}$$

$$\left[\vec{\mathbf{S}}_\mathrm{tot}, \mathbf{H}^\mathrm{mf}\right] = \sum_i \vec{V}_i(t) \times \vec{\mathbf{S}}_i \neq \vec{0}. \tag{F.4b}$$

---

[1] In experiment, such a state can be achieved by applying magnetic fields much stronger than the order of magnitude of the couplings, i.e., $B \ll J_\mathrm{L}$, see for example NMR.

For non-zero mean-fields, this description always contains some leakage: From time to time the spins and thus the mean-fields change their orientations leading to a decay of the initial polarization[2]. Hence, spinDMFT violates the conservation law of the original model. However, it is possible to include the total spin conservation by hand as will be discussed the following section.

F.2 Including total spin conservation by hand

The idea is to split the observables of interest into a conserved and a time-dependent fraction. For obvious reasons, the conserved fraction does not change over time, while the time-dependent fraction is allowed to fluctuate. The latter can decay to zero on average even if the whole observable doesn't. This means that the fluctuating dynamics could be captured by a semiclassical noise model that violates any conservation laws. We follow the strategy proposed in Ref. [Uhr+14] and Ref. [SRU14] to formulate this mathematically.

We begin by expressing the spin operator at an arbitrary site i by a fraction of the total spin operator and a fluctuating part, that is,

$$\mathbf{S}_i^\alpha = c_\alpha \mathbf{S}_{\text{tot}}^\alpha + \Delta\mathbf{S}_i^\alpha. \tag{F.5}$$

The coefficients c_α can be computed either by using the operator scalar product

$$(\mathbf{A}|\mathbf{B}) := \text{Tr}\left(\mathbf{A}^\dagger \mathbf{B}\rho\right) \tag{F.6}$$

or, in this special case, simply by taking the sum over all N sites on both sides of the equation, which yields

$$\mathbf{S}_{\text{tot}}^\alpha = c_\alpha N \mathbf{S}_{\text{tot}}^\alpha + \sum_i \Delta\mathbf{S}_i^\alpha \tag{F.7}$$

Since the fluctuations $\Delta\mathbf{S}_i^\alpha$ do not contain $\mathbf{S}_{\text{tot}}^\alpha$ anymore by construction, we can deduce

$$c_\alpha = \frac{1}{N}. \tag{F.8}$$

and thus

$$\mathbf{S}_i^\alpha = \frac{1}{N}\mathbf{S}_{\text{tot}}^\alpha + \Delta\mathbf{S}_i^\alpha = \mathbf{m}^\alpha + \Delta\mathbf{S}_i^\alpha, \tag{F.9}$$

where $\mathbf{m}^\alpha$ is the polarization.

Now we apply spinDMFT to the Hamiltonian. To this end, we replace the environment fields by time-dependent Gaussian mean-fields $\vec{\mathbf{V}}_i \to \vec{V}_i(t)$, the moments of which are connected to quantum expectation values of the original fields. For the first moments, we obtain

$$\overline{\mathbf{V}_i^\alpha(t)}^{\text{mf}} = \langle \mathbf{V}_i^\alpha(t)\rangle = J_{\text{L}}\langle \mathbf{S}^\alpha\rangle = \delta^{\alpha z} J_{\text{L}}\langle \mathbf{S}^z\rangle \tag{F.10}$$

---

[2] This behavior is confirmed numerically (not shown).

Following this procedure, it seems reasonable to use the autocorrelations of the fields $\vec{\mathbf{V}}_i(t)$ to define the second moments. However, the latter need to be real and symmetric unlike the correlation functions

$$\langle \mathbf{AB} \rangle = \mathrm{Tr}\left(\mathbf{AB}\rho\right) \neq \langle \mathbf{BA} \rangle, \tag{F.11}$$

which are, in general, allowed to be non-symmetric and complex. This issue can be solved by employing the anticommutator according to

$$\langle \mathbf{A}, \mathbf{B} \rangle_{\mathrm{sc}} \coloneqq \frac{1}{2} \langle \{\mathbf{A}, \mathbf{B}\} \rangle = \frac{1}{2} \langle \{\mathbf{B}, \mathbf{A}\} \rangle = \langle \mathbf{B}, \mathbf{A} \rangle_{\mathrm{sc}}, \tag{F.12}$$

where "sc" stands for **s**ymmetrized **c**orrelation[3]. With the aid of this, the second moments yield

$$\overline{V_i^\alpha(t_1) V_j^\beta(t_2)}^{\mathrm{mf}} = \langle \mathbf{V}_i^\alpha(t_1), \mathbf{V}_j^\beta(t_2) \rangle_{\mathrm{sc}} = \sum_{kl} J_{ik} J_{jl} \, \langle \mathbf{S}_k^\alpha(t_1), \mathbf{S}_l^\beta(t_2) \rangle_{\mathrm{sc}} \tag{F.13a}$$

$$\approx \delta^{\alpha z} \delta^{\beta z} \langle \mathbf{S}^z \rangle^2 \left(J_{\mathrm{L}}^2 - J_{\mathrm{Q}}^2 \delta_{ij} \right) + J_{\mathrm{Q}}^2 \delta_{ij} \, \langle \mathbf{S}^\alpha(t_1), \mathbf{S}^\beta(t_2) \rangle_{\mathrm{sc}}, \tag{F.13b}$$

where we used

$$\langle \mathbf{S}_k^\alpha(t_1), \mathbf{S}_l^\beta(t_2) \rangle_{\mathrm{sc}} \approx \langle \mathbf{S}_k^\alpha, \mathbf{S}_l^\beta \rangle_{\mathrm{sc}}, \tag{F.14}$$

for $k \neq l$, i.e., we neglect any evolving dynamical correlations between different sites[4]. Moreover, we left out site indices in the expectation values of the final expression because they are redundant according to translational invariance in space.

Replacing the environment fields by the mean fields leads to the Hamiltonian

$$\mathbf{H}^{\mathrm{aux}} \left[\vec{V}_1(t), \ldots, \vec{V}_N(t) \right] = \sum_i \vec{\mathbf{S}}_i \cdot \vec{V}_i(t), \tag{F.15}$$

which has been already provided in the previous section. The dynamics described by this semiclassical, effective model does not conserve the polarization, but it may capture the fluctuating dynamics appropriately. Therefore, our strategy is to use it as an auxiliary model to simulate the fluctuations. Henceforth, we distinguish between expectation values of the auxiliary model ("aux") and the mean-field model ("mf"). The latter corresponds to the actual mean-field approximation of the exact system, i.e., it captures any observables (not only the fluctuations) correctly for large z. The models are connected through

$$\langle \Delta \mathbf{S}^\alpha(t) \rangle^{\mathrm{mf}} = \langle \Delta \mathbf{S}^\alpha(t) \rangle^{\mathrm{aux}}, \tag{F.16a}$$

$$\langle \Delta \mathbf{S}^\alpha(t_1) \Delta \mathbf{S}^\beta(t_2) \rangle^{\mathrm{mf}} = \langle \Delta \mathbf{S}^\alpha(t_1), \Delta \mathbf{S}^\beta(t_2) \rangle_{\mathrm{sc}}^{\mathrm{aux}}. \tag{F.16b}$$

To clarify this concept, we summarize the relationship between the exact model, the mean-field model, and the auxiliary model in Fig. F.1.

---

[3] A similar trick is used, for example, in the TWA, which also faces the issue of relating classical to quantum observables [Pol10].

[4] This is plausible from the Bethe lattice consideration summarized in Tab. 4.1, but a rigorous extension of the latter has not yet been done.

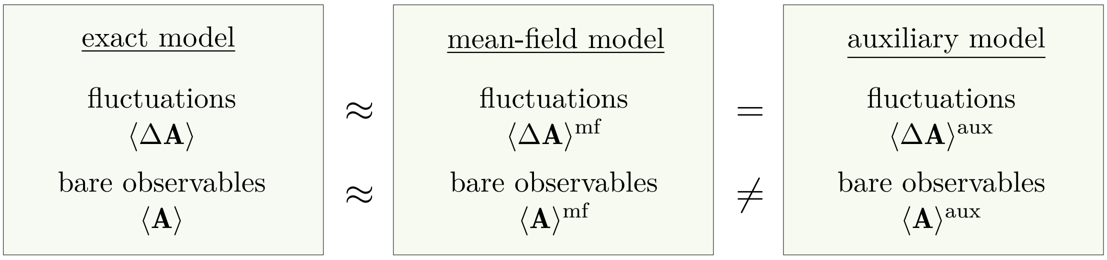

Figure F.1: Relationship between the different models introduced in the main text.

The spin operators in Eq. (F.15) are fully decoupled from one another. Due to spatial homogeneity, the auxiliary model can be reduced to a single-site,

$$\mathbf{H}_i^{\mathrm{aux}}\left[\vec{V}_i(t)\right] = \vec{\mathbf{S}} \cdot \vec{V}_i(t), \tag{F.17}$$

as usual in spinDMFT. In the next step, we close the self-consistency.

The first mean-field moments have been already determined in Eq. (F.10). To compute the second moments, we approximate the exact correlations in Eq. (F.13) by correlations of the mean-field model, which, in turn, can be expressed by correlations of the auxiliary model. For $\alpha \neq z$ or $\beta \neq z$, we obtain

$$\overline{V_i^\alpha(t_1) V_j^\beta(t_2)}^{\mathrm{mf}} = \delta_{ij} J_{\mathrm{Q}}^2 \, \langle \mathbf{S}_i^\alpha(t_1), \mathbf{S}_i^\beta(t_2) \rangle_{\mathrm{sc}}^{\mathrm{mf}} \tag{F.18a}$$

$$= \delta_{ij} \delta^{\alpha\beta} \frac{J_{\mathrm{Q}}^2}{4N} + \delta_{ij} J_{\mathrm{Q}}^2 \, \langle \Delta \mathbf{S}_i^\alpha(t_1), \Delta \mathbf{S}_i^\beta(t_2) \rangle_{\mathrm{sc}}^{\mathrm{aux}} \tag{F.18b}$$

$$\begin{aligned} = \delta_{ij} J_{\mathrm{Q}}^2 \Bigg(& \frac{\delta^{\alpha\beta}}{4N} + \langle \mathbf{S}_i^\alpha(t_1), \mathbf{S}_i^\beta(t_2) \rangle_{\mathrm{sc}}^{\mathrm{aux}} - \frac{1}{N} \sum_j \langle \mathbf{S}_i^\alpha(t_1), \mathbf{S}_j^\beta(t_2) \rangle_{\mathrm{sc}}^{\mathrm{aux}} \\ & - \frac{1}{N} \sum_j \langle \mathbf{S}_j^\alpha(t_1), \mathbf{S}_i^\beta(t_2) \rangle_{\mathrm{sc}}^{\mathrm{aux}} + \frac{1}{N^2} \sum_{jk} \langle \mathbf{S}_j^\alpha(t_1), \mathbf{S}_k^\beta(t_2) \rangle_{\mathrm{sc}}^{\mathrm{aux}} \Bigg) \end{aligned} \tag{F.18c}$$

$$= \delta_{ij} J_{\mathrm{Q}}^2 \Big(\langle \mathbf{S}^\alpha(t_1), \mathbf{S}^\beta(t_2) \rangle_{\mathrm{sc}}^{\mathrm{aux}} - \langle \mathbf{S}^\alpha(t_1) \rangle^{\mathrm{aux}} \langle \mathbf{S}^\beta(t_2) \rangle^{\mathrm{aux}} \Big). \tag{F.18d}$$

Note that expectation values at $t = 0$ are equivalent in all models allowing to leave out the index “mf” or “aux”, respectively. To get from Eq. (F.18b) to Eq. (F.18c), we inserted the fluctuations using Eq. (F.9) and, subsequently, the total spin (polarization), which is not conserved in the auxiliary model. In the last step, we considered spatial homogeneity and the thermodynamic limit, $N \to \infty$. In a similar fashion, we find

$$\overline{V_i^z(t_1) V_j^z(t_2)}^{\mathrm{mf}} = J_{\mathrm{L}}^2 \langle \mathbf{S}^z \rangle^2 + \delta_{ij} J_{\mathrm{Q}}^2 \Big(\langle \mathbf{S}^z(t_1), \mathbf{S}^z(t_2) \rangle_{\mathrm{sc}}^{\mathrm{aux}} - \langle \mathbf{S}^z(t_1) \rangle^{\mathrm{aux}} \langle \mathbf{S}^z(t_2) \rangle^{\mathrm{aux}} \Big). \tag{F.19}$$

Alltogether, this yields the covariances

$$\mathrm{Cov}\left[V_i^\alpha(t_1), V_j^\beta(t_2)\right] = \delta_{ij} J_{\mathrm{Q}}^2 \Big(\langle \mathbf{S}^\alpha(t_1), \mathbf{S}^\beta(t_2) \rangle_{\mathrm{sc}}^{\mathrm{aux}} - \langle \mathbf{S}^\alpha(t_1) \rangle^{\mathrm{aux}} \langle \mathbf{S}^\beta(t_2) \rangle^{\mathrm{aux}} \Big), \tag{F.20}$$

for $\alpha, \beta \in \{x, y, z\}$. Note that they are zero for $i \neq j$, i.e., all sites are decoupled from one another[5].

---

[5] In Sec. 4.1.3, we discussed that correlations between different mean-fields do not matter for the single-site model, since they do not enter the marginal distribution. Hence, the fact that the covariances vanish for $i \neq j$ is actually not required to decouple the sites.

The auxiliary model in Eq. (F.17) together with the self-consistency condition described by Eqs. (F.10) and (F.20) can be solved numerically by iteration. Afterwards, the true spin correlations in mean-field approximation can be computed straightforwardly by

$$\langle \mathbf{S}^\alpha(t_1), \mathbf{S}^\beta(t_2)\rangle_{\mathrm{sc}}^{\mathrm{mf}} = \langle \mathbf{S}^\alpha(t_1), \mathbf{S}^\beta(t_2)\rangle_{\mathrm{sc}}^{\mathrm{aux}} - \langle \mathbf{S}^\alpha(t_1)\rangle^{\mathrm{aux}}\langle \mathbf{S}^\beta(t_2)\rangle^{\mathrm{aux}} + \delta^{\alpha z}\delta^{\beta z}\langle \mathbf{S}^z\rangle^2. \quad \text{(F.21)}$$

It is noteworthy that this approach can alternatively be derived starting from the adapted equation of motion,

$$\frac{\mathrm{d}}{\mathrm{d}t}\Delta\vec{\mathbf{S}}(t) = \vec{V}(t) \times \Delta\vec{\mathbf{S}}(t) = \vec{V}(t) \times \left(\vec{\mathbf{S}}(t) - \vec{\mathbf{m}}\right), \quad \text{(F.22)}$$

but this is not discussed further here. Moreover, one should note that mean-field model and auxiliary model are equivalent for $h = 0$ because all spin expectation values vanish. Hence, the disordered spinDMFT is reproduced in this case.

Aside from the polarization field h, the autocorrelations also depend on the linear and quadratic coupling sums J_{L} and J_{Q}, since the latter enter the self-consistency condition in Eqs. (F.10) and (F.20). As a consequence, the results will intricately depend on the considered lattice. This is in contrast to the disordered spinDMFT, where only the overall time scale J_{Q}^{-1} is affected by the geometry. It should be noted that the ratio between the coupling sums can be expressed by the coordination number of the lattice according to

$$\frac{J_{\mathrm{L}}}{J_{\mathrm{Q}}} = \sqrt{z}. \quad \text{(F.23)}$$

Consequently, if the time is measured in units of J_{Q}^{-1}, the relevant parameters are the coordination number z and the polarization field h. Preliminary results for the autocorrelations of the presented approach are shown in Fig. F.2 for a square lattice with NN interactions, i.e., $z = 4$, and different polarization fields. Several aspects are different with respect to the disordered spinDMFT. The polarization reduces the full spherical symmetry to a cylindrical symmetry leading to a difference between the diagonal autocorrelations, $G^{xx} = G^{yy}$ (transverse, see panel (a)) and G^{zz} (longitudinal, see panel (c)). An important feature is that G^{zz} does not decay to zero, but to a finite value given by $4\langle \mathbf{S}^z\rangle^2 = \tanh^2(h/2J_{\mathrm{Q}})$ due to the included conservation law. Furthermore, the polarized state entails a non-zero off-diagonal correlation G^{xy}, which is plotted in panel (b).

As a benchmark, we consider the results from ED on a finite-size system for comparison. The agreement is very good at short times, which is not suprising since both approaches are exact at $t = 0$ and capture the static parts of the spin environments correctly. Deviations between the approaches are clearly visible in all correlations after about $t = 2J_{\mathrm{Q}}^{-1}$. The ED with $N = 9$ shows coherent oscillations over the whole time interval which are not obtained in spinDMFT. Increasing the system size to $N = 12$ leads to a significantly better agreement, although the deviations are still not small. To highlight the relevance of finite-size errors in the ED, we also plotted the lower bound of the long-time average of the longitudinal autocorrelation according to Mazur's inequality,

$$\lim_{T\to\infty} \frac{1}{T}\int_0^T \mathrm{d}t G^{zz}(t) \geq \frac{1}{N}\left(1 + 4(N-1)\langle \mathbf{S}^z\rangle^2\right) = \frac{1}{N}\left(1 + (N-1)\tanh^2 \frac{h}{2J_{\mathrm{Q}}}\right), \quad \text{(F.24a)}$$

which slowly converges to the limit value of spinDMFT for $N \to \infty$. We conclude that a clear statement about the validity of the extension presented in this appendix cannot yet be made.

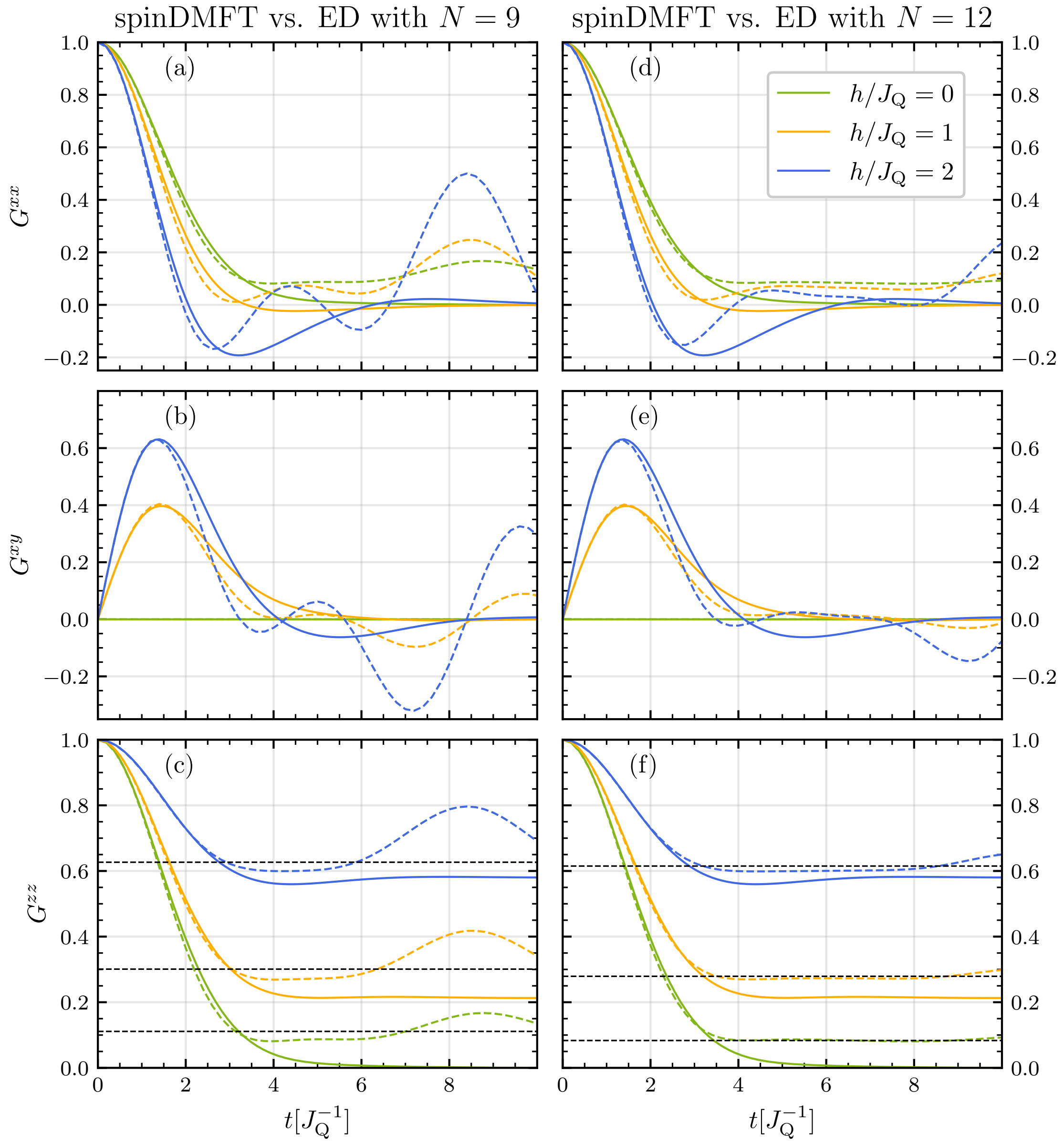

Figure F.2: Autocorrelations from spinDMFT (solid lines) and from ED (dashed lines) on a NN square lattice for different strengths of the initial polarization h. The left column (a-c) shows spinDMFT in comparison to ED with $N = 9$ and the right column (d-f) in comparison to ED with $N = 12$ (the spinDMFT results are the same for both columns). Panels (c) and (f) show also the lower bound of the long-time average of the ED according to Mazur's inequality (dashed black lines), see Eq. (F.24a).

F.3 Outlook

This appendix entails several next steps. First, one can extend the above derivation to the XXZ model with finite polarization in z-direction and benchmark this case as well. In doing so, the system sizes for the ED should be increased beyond $N = 12$ for more meaningful conclusions. If spinDMFT captures the scenario of an exactly conserved polarization well, one can pass to the more subtle case of an almost conserved polarization. This scenario is exemplified by an XXZ model

$$\mathbf{H} = \frac{1}{2} \sum_{ij} J_{ij} \left(\mathbf{S}_i^x \mathbf{S}_j^x + \mathbf{S}_i^y \mathbf{S}_j^y + \lambda \mathbf{S}_i^z \mathbf{S}_j^z \right) \tag{F.25}$$

with weak anisotropy $0 < |\lambda - 1| \ll 1$. The equation of motion of a component of the polarization is given by

$$\mathtt{i} \left[\mathbf{H}, \mathbf{m}^\alpha \right] = \frac{1-\lambda}{N} \sum_{ij} J_{ij} \sum_{\beta} \epsilon^{\alpha\beta z} \mathbf{S}_i^\beta \mathbf{S}_j^z, \tag{F.26}$$

which implies a slow decay of the transverse components ($\alpha \in \{x, y\}$) in case of λ being close but unequal to 1. Equivalently to separating the observables into a conserved and fluctuating part as described by Eq. (F.9), one can separate them into a slowly and fastly evolving part. Under assumptions similar to the ones made in the Lindblad formalism [Man20], e.g., well-separated time scales, one could derive an effective model for the slow dynamics. An interesting aspect in this context is that, in contrast to the Lindblad formalism, there is no separation into system and bath here, i.e., the slow and fast dynamics are both experienced by the exact same spins.

Bibliography

The reference abbreviation scheme is based on the authors' last names and the publication year. For works with three or fewer authors, the first letters of their last names are appended. For works with more than three authors, the first three letters of the first author's last name are used, followed by a '+' symbol.

[AÁS11] A. Ajoy, G. A. Álvarez, and D. Suter. "Optimal pulse spacing for dynamical decoupling in the presence of a purely dephasing spin bath." Physical Review A **83**, 032303 (2011).

[Aba+19] D. A. Abanin et al. "Colloquium: Many-body localization, thermalization, and entanglement." Review of Modern Physics **91**, 021001 (2019).

[ABE58] E. R. Andrew, A. Bradbury, and R. G. Eades. "Nuclear Magnetic Resonance Spectra from a Crystal rotated at High Speed." Nature **182**, 1659 (1958).

[AF11] A. Alvermann and H. Fehske. "High-order commutator-free exponential time-propagation of driven quantum systems." Journal of Computational Physics **230**, 5930 (2011).

[Alt18] E. Altman. "Many-body localization and quantum thermalization." Nature Physics **14**, 979 (2018).

[Álv+10] G. A. Álvarez et al. "Performance comparison of dynamical decoupling sequences for a qubit in a rapidly fluctuating spin bath." Physical Review A **82**, 042306 (2010).

[And+11] P. Anders et al. "Dynamical mean-field theory for bosons." New Journal of Physics **13**, 075013 (2011).

[And58] P. W. Anderson. "Absence of Diffusion in Certain Random Lattices." Physical Review **109**, 1492 (1958).

[And61] P. W. Anderson. "Localized Magnetic States in Metals." Physical Review **124**, 41 (1961).

[And72] P. W. Anderson. "More Is Different." Science **177**, 393 (1972).

[AS05] F. B. Anders and A. Schiller. "Real-Time Dynamics in Quantum-Impurity Systems: A Time-Dependent Numerical Renormalization-Group Approach." Physical Review Letters **95**, 196801 (2005).

[ÁS11] G. A. Álvarez and D. Suter. "Measuring the Spectrum of Colored Noise by Dynamical Decoupling." Physical Review Letters **107**, 230501 (2011).

[ASK15] G. A. Alvarez, D. Suter, and R. Kaiser. "Localization-delocalization transition in the dynamics of dipolar-coupled nuclear spins." Science **349**, 846 (2015).

[Bal+08] G. Balasubramanian et al. “Nanoscale imaging magnetometry with diamond spins under ambient conditions.” Nature **455**, 648 (2008).

[BCP08] R. Bulla, T. A. Costi, and T. Pruschke. “Numerical renormalization group method for quantum impurity systems.” Review of Modern Physics **80**, 395 (2008).

[BCS57] J. Bardeen, L. N. Cooper, and J. R. Schrieffer. “Theory of Superconductivity.” Physical Review **108**, 1175 (1957).

[BF04] H. Bruus and K. Flensberg. *Many-Body Quantum Theory in Condensed Matter Physics: An Introduction.* Oxford University Press Inc., New York, 2004.

[BHP46] F. Bloch, W. W. Hansen, and M. Packard. “The Nuclear Induction Experiment.” Physical Review **70**, 474 (1946).

[Bil+08] J. Billy et al. “Direct observation of Anderson localization of matter waves in a controlled disorder.” Nature **453**, 891 (2008).

[Bla+09] S. Blanes et al. “The Magnus expansion and some of its applications.” Physics Reports **470**, 151 (2009).

[Ble21] P. Bleicker. *The Fermi-Hubbard model and its limiting cases as a testbed for techniques and phenomena.* PhD thesis (Technische Universität Dortmund, 2021).

[Ble24] Thanks to Philip Bleicker for providing the CET data.

[BM80] A. J. Bray and M. A. Moore. “Replica theory of quantum spin glasses.” Journal of Physics C: Solid State Physics **13**, L655 (1980).

[BPS76] K. W. Becker, T. Plefka, and G. Sauermann. “Spin correlation function for free-induction decay in dipolar systems.” Journal of Physics C: Solid State Physics **9**, 4041 (1976).

[Bra+19] C. E. Bradley et al. “A Ten-Qubit Solid-State Spin Register with Quantum Memory up to One Minute.” Physical Review X **9**, 031045 (2019).

[Bro60] R. Brout. “Statistical Mechanical Theory of Ferromagnetism. High Density Behavior.” Physical Review **118**, 1009 (1960).

[Bur07] A. L. Burin. “Energy delocalization in strongly disordered systems induced by the long-range many-body interaction.” arXiv:cond-mat/0611387 [cond-mat.dis-nn] (2007).

[BV08] K. Byczuk and D. Vollhardt. “Correlated bosons on a lattice: Dynamical mean-field theory for Bose-Einstein condensed and normal phases.” Physical Review B **77**, 235106 (2008).

[Cas+02] F. Castellani et al. “Structure of a protein determined by solid-state magic-angle-spinning NMR spectroscopy.” Nature **420**, 99 (2002).

[Chá+21] M. Chávez et al. “Residual dipolar line width in magic-angle spinning proton solid-state NMR.” Magnetic Resonance **2**, 499 (2021).

[Cho+05] H. Cho et al. “Multispin dynamics of the solid-state NMR free induction decay.” Physical Review B **72**, 054427 (2005).

[Cho+16] J.-Y. Choi et al. "Exploring the many-body localization transition in two dimensions." Science **352**, 1547 (2016).

[Cho+17a] J. Choi et al. "Depolarization Dynamics in a Strongly Interacting Solid-State Spin Ensemble." Physical Review Letters **118**, 093601 (2017).

[Cho+17b] S. Choi et al. "Observation of discrete time-crystalline order in a disordered dipolar many-body system." Nature **543**, 221 (2017).

[Cho+23] J.-P. Chou et al. "Ab Initio Study of (100) Diamond Surface Spins." Physical Review Applied **20**, 014040 (2023).

[CK94] M. Caffarel and W. Krauth. "Exact diagonalization approach to correlated fermions in infinite dimensions: Mott transition and superconductivity." Physical Review Letters **72**, 1545 (1994).

[Con20] M. G. Concilio. "Large-scale magnetic resonance simulations: A tutorial." Magnetic Resonance in Chemistry **58**, 691–717 (2020).

[Coo+19] A. Cooper et al. "Environment-assisted Quantum-enhanced Sensing with Electronic Spins in Diamond." Physical Review Applied **12**, 044047 (2019).

[Cur95] P. Curie. *Propriétés magnétiques des corps a diverses températures.* Gauthier-Villars et fils, 1895.

[Czy08] G. Czycholl. *Theoretische Festkörperphysik: Von den klassischen Modellen zu modernen Forschungsthemen.* Springer-Verlag, Berlin Heidelberg, 2008.

[DAl+16] L. D'Alessio et al. "From quantum chaos and eigenstate thermalization to statistical mechanics and thermodynamics." Advances in Physics **65**, 239 (2016).

[Dat+23] A. Datta et al. "Heavy quasiparticles and cascades without symmetry breaking in twisted bilayer graphene." Nature Communications **14**, 2041 (2023).

[Dav+23] E. J. Davis et al. "Probing many-body dynamics in a two-dimensional dipolar spin ensemble." Nature Physics **19**, 836 (2023).

[Deu91] J. M. Deutsch. "Quantum statistical mechanics in a closed system." Physical Review A **43**, 2046 (1991).

[DiV00] D. P. DiVincenzo. "The Physical Implementation of Quantum Computation." Fortschritte der Physik **48**, 771 (2000).

[DL91] R. Dekeyser and M. H. Lee. "Nonequilibrium statistical mechanics of the spin-$1/2$ van der Waals model. II. Autocorrelation function of a single spin and long-time tails." Physical Review B **43**, 8131 (1991).

[Doh+13] M. W. Doherty et al. "The nitrogen-vacancy colour centre in diamond." Physics Reports **528**, 1 (2013).

[DSP17] S. M. Davidson, D. Sels, and A. Polkovnikov. "Semiclassical approach to dynamics of interacting fermions." Annals of Physics **384**, 128 (2017).

[DSR21] J. Dubois, U. Saalmann, and J. M. Rost. "Semi-classical Lindblad master equation for spin dynamics." Journal of Physics A: Mathematical and Theoretical **54**, 235201 (2021).

[Dwy+22] B. L. Dwyer et al. "Probing Spin Dynamics on Diamond Surfaces Using a Single Quantum Sensor." PRX Quantum **3**, 040328 (2022).

[EA07] P. Echenique and J. L. Alonso. “A mathematical and computational review of Hartree–Fock SCF methods in quantum chemistry.” Molecular Physics **105**, 3057 (2007).

[EA75] S. F. Edwards and P. W. Anderson. “Theory of spin glasses.” Journal of Physics F: Metal Physics **5**, 965 (1975).

[EC75] M. Engelsberg and N.-C. Chao. “Continued-fraction approximants to spin correlation functions. Application to NMR line shapes.” Physical Review B **12**, 5043 (1975).

[EF13] T. A. Elsayed and B. V. Fine. “Regression Relation for Pure Quantum States and Its Implications for Efficient Computing.” Physical Review Letters **110**, 070404 (2013).

[EF15] T. A. Elsayed and B. V. Fine. “Effectiveness of classical spin simulations for describing NMR relaxation of quantum spins.” Physical Review B **91**, 094424 (2015).

[EL74] M. Engelsberg and I. J. Lowe. “Free-inducation-decay measurements and determination of moments in CaF_2.” Physical Review B **10**, 822 (1974).

[EMB23] F. Evers, I. Modak, and S. Bera. “Internal clock of many-body delocalization.” Physical Review B **108**, 134204 (2023).

[Fin97] B. V. Fine. “NMR Spin-Spin Relaxation as Kinetics in Spin Phase Space.” Physical Review Letters **79**, 4673 (1997).

[Fis75] K. H. Fischer. “Static Properties of Spin Glasses.” Physical Review Letters **34**, 1438 (1975).

[Foc30] V. Fock. “Näherungsmethode zur Lösung des quantenmechanischen Mehrkörperproblems.” Zeitschrift für Physik **61**, 0044 (1930).

[FS64] R. C. Fort and P. V. R. Schleyer. “Adamantane: Consequences of the Diamondoid Structure.” Chemical Reviews **64**, 277 (1964).

[FSW08] H. Fehske, R. Schneider, and A. Weiße, eds. *Computational Many-Particle Physics*. Springer-Verlag, Berlin Heidelberg, 2008.

[Geb+03] F. Gebhard et al. “Fourth-order perturbation theory for the half-filled Hubbard model in infinite dimensions.” The European Physical Journal B - Condensed Matter and Complex Systems **36**, 491 (2003).

[Geo+96] A. Georges et al. “Dynamical mean-field theory of strongly correlated fermion systems and the limit of infinite dimensions.” Review of Modern Physics **68**, 13 (1996).

[GHU24] T. Gräßer, T. Hahn, and G. S. Uhrig. “Microscopic understanding of NMR signals by dynamic mean-field theory for spins.” Solid State Nuclear Magnetic Resonance **132**, 101936 (2024).

[Gin04] V. L. Ginzburg. “Nobel Lecture: On superconductivity and superfluidity (what I have and have not managed to do) as well as on the “physical minimum” at the beginning of the XXI century.” Review of Modern Physics **76**, 981 (2004).

[GK92] A. Georges and G. Kotliar. “Hubbard model in infinite dimensions.” Physical Review B **45**, 6479 (1992).

[Gla18] M. M. Glazov. *Electron & Nuclear Spin Dynamics in Semiconductor Nanostructures.* Oxford University Press, 2018.

[GPS00] A. Georges, O. Parcollet, and S. Sachdev. “Mean Field Theory of a Quantum Heisenberg Spin Glass.” Physical Review Letters **85**, 840 (2000).

[GR98] D. R. Grempel and M. J. Rozenberg. “Fluctuations in a Quantum Random Heisenberg Paramagnet.” Physical Review Letters **80**, 389 (1998).

[Grä+21] T. Gräßer et al. “Dynamic mean-field theory for dense spin systems at infinite temperature.” Physical Review Research **3**, 043168 (2021).

[Grä+23] T. Gräßer et al. “Understanding the dynamics of randomly positioned dipolar spin ensembles.” Physical Review Research **5**, 043191 (2023).

[Gri+14] M. S. Grinolds et al. “Subnanometre resolution in three-dimensional magnetic resonance imaging of individual dark spins.” Nature Nanotechnology **9**, 279 (2014).

[Gro+11] B. Grotz et al. “Sensing external spins with nitrogen-vacancy diamond.” New Journal of Physics **13**, 055004 (2011).

[Gro+15] V. P. B. Grover et al. “Magnetic Resonance Imaging: Principles and Techniques: Lessons for Clinicians.” Journal of Clinical and Experimental Hepatology **5**, 246 (2015).

[Gul+11] E. Gull et al. “Continuous-time Monte Carlo methods for quantum impurity models.” Review of Modern Physics **83**, 349 (2011).

[Häb+15] T. Häberle et al. “Nanoscale nuclear magnetic imaging with chemical contrast.” Nature Nanotechnology **10**, 125 (2015).

[Hah50] E. L. Hahn. “Spin Echoes.” Physical Review **80**, 580 (1950).

[Har28] D. R. Hartree. “The Wave Mechanics of an Atom with a Non-Coulomb Central Field. Part II. Some Results and Discussion.” Mathematical Proceedings of the Cambridge Philosophical Society **24**, 111 (1928).

[Her24] Thanks to Dag-Björn Hering for providing the iEoM data.

[HH71] I. Hargittai and K. Hedberg. “Electron-diffraction Investigation of the Molecular Structures of Adamantane.” Journal of the Chemical Society D: Chemical Communications, 1499 (1971).

[HJO00] T. Helgaker, P. Jorgensen, and J. Olsen. *Molecular Electronic-Structure Theory.* John Wiley and Sons, Ltd, 2000.

[HNO14] D. A. Huse, R. Nandkishore, and V. Oganesyan. “Phenomenology of fully many-body-localized systems.” Physical Review B **90**, 174202 (2014).

[Hof22] Roy Hoffman. “Solid-state chemical-shift referencing with adamantane.” Journal of Magnetic Resonance **340**, 107231 (2022).

[HT09] W.-J. Hu and N.-H. Tong. “Dynamical mean-field theory for the Bose-Hubbard model.” Physical Review B **80**, 245110 (2009).

[HW68] U. Haeberlen and J. S. Waugh. “Coherent Averaging Effects in Magnetic Resonance.” Physical Review **175**, 453 (1968).

[Imb16] J. Z. Imbrie. “On Many-Body Localization for Quantum Spin Chains.” Journal of Statistical Physics **163**, 998 (2016).

[Isi25] E. Ising. “Beitrag zur Theorie des Ferromagnetismus.” Zeitschrift für Physik **31**, 253 (1925).

[Jaz+19] F. Jazaeri et al. “A Review on Quantum Computing: From Qubits to Front-end Electronics and Cryogenic MOSFET Physics.” 2019 MIXDES - 26th International Conference (Mixed Design of Integrated Circuits and Systems), 15 (2019).

[Jen95] J. Jensen. “Dipolar broadening of $I = 1/2$ NMR spectra of solids.” Physical Review B **52**, 9611 (1995).

[Jin+16] J. Jin et al. “Cluster Mean-Field Approach to the Steady-State Phase Diagram of Dissipative Spin Systems.” Physical Review X **6**, 031011 (2016).

[JP73] S. J. K. Jensen and O. Platz. “Free-Induction-Decay Shapes in a Dipolar-Coupled Rigid Lattice of Infinite Nuclear Spins.” Physical Review B **7**, 31 (1973).

[JW06] F. Jelezko and J. Wrachtrup. “Single defect centres in diamond: A review.” physica status solidi (a) **203**, 3207 (2006).

[KF98] Y. Kuramoto and N. Fukushima. “Dynamical Effective Medium Theory for Quantum Spins and Multipoles.” Journal of the Physical Society of Japan **67**, 583 (1998).

[Kie+22] M. Kiefer-Emmanouilidis et al. “Particle fluctuations and the failure of simple effective models for many-body localized phases.” SciPost Physics **12**, 034 (2022).

[Kle79] R. A. Klemm. “Quantum effects in spin glasses.” Journal of Physics C: Solid State Physics **12**, L735 (1979).

[Koh99] W. Kohn. “Nobel Lecture: Electronic structure of matter—wave functions and density functionals.” Review of Modern Physics **71**, 1253 (1999).

[Kot+01] G. Kotliar et al. “Cellular Dynamical Mean Field Approach to Strongly Correlated Systems.” Physical Review Letters **87**, 186401 (2001).

[Koz22] I. V. Kozitsin. “A general framework to link theory and empirics in opinion formation models.” Scientific Reports **12**, 2045 (2022).

[KRU08] M. Karski, C. Raas, and G. S. Uhrig. “Single-particle dynamics in the vicinity of the Mott-Hubbard metal-to-insulator transition.” Physical Review B **77**, 075116 (2008).

[Kuc+18] G. Kucsko et al. “Critical Thermalization of a Disordered Dipolar Spin System in Diamond.” Physical Review Letters **121**, 023601 (2018).

[Kuz15] A. L. Kuzemsky. “Variational principle of Bogoliubov and generalized mean fields in many-particle interacting systems.” International Journal of Modern Physics B **29**, 1530010 (2015).

[KV04] G. Kotliar and D. Vollhardt. “Strongly Correlated Materials: Insights From Dynamical Mean-Field Theory.” Physics Today **57**, 53 (2004).

[LBB19] T. L. M. Lezama, S. Bera, and J. H. Bardarson. “Apparent slow dynamics in the ergodic phase of a driven many-body localized system without extensive conserved quantities.” Physical Review B **99**, 161106 (2019).

[LBJ02] D. D. Laws, H.-M. L. Bitter, and A. Jerschow. “Solid-State NMR Spectroscopic Methods in Chemistry.” Angewandte Chemie International Edition **41**, 3096 (2002).

[LD17] T. Li and P. Deng. “Nuclear Magnetic Resonance technique in tumor metabolism.” Genes & Diseases **4**, 28 (2017).

[Lev01] M. H. Levitt. *spin dynamics: Basics of Nuclear Magnetic Resonance*. John Wiley and Sons, Chichester, 2001.

[LLA16] D. J. Luitz, N. Laflorencie, and F. Alet. “Extended slow dynamical regime close to the many-body localization transition.” Physical Review B **93**, 060201 (2016).

[LLR17] F. Lange, Z. Lenarcic, and A. Rosch. “Pumping approximately integrable systems.” Nature Communications **8**, 15767 (2017).

[LLR18a] F. Lange, Z. Lenarcic, and A. Rosch. “Time-dependent generalized Gibbs ensembles in open quantum systems.” Physical Review B **97**, 165138 (2018).

[LLR18b] Z. Lenarcic, F. Lange, and A. Rosch. “Perturbative approach to weakly driven many-particle systems in the presence of approximate conservation laws.” Physical Review B **97**, 024302 (2018).

[LN57] I. J. Lowe and R. E. Norberg. “Free-Induction Decays in Solids.” Physical Review **107**, 46 (1957).

[Lon+23] D. M. Long et al. “Phenomenology of the Prethermal Many-Body Localized Regime.” Physical Review Letters **131**, 106301 (2023).

[Low59] I. J. Lowe. “Free Induction Decays of Rotating Solids.” Physical Review Letters **2**, 285 (1959).

[Luk+19] A. Lukin et al. “Probing entanglement in a many-body-localized system.” Science **364**, 256 (2019).

[Mag54] W. Magnus. “On the Exponential Solution of Differential Equations for a Linear Operator.” Communications on Pure and Applied Mathematics **7**, 649 (1954).

[Mai+05] T. Maier et al. “Quantum cluster theories.” Review of Modern Physics **77**, 1027 (2005).

[Mal+19] A. A. Malär et al. “Quantifying proton NMR coherent linewidth in proteins under fast MAS conditions: a second moment approach.” Physical Chemistry Chemical Physics **21**, 18850 (2019).

[Man20] D. Manzano. “A short introduction to the Lindblad master equation.” AIP Advances **10**, 025106 (2020).

[Mar+17] A. Marchetti et al. “Understanding Surface and Interfacial Chemistry in Functional Nanomaterials via Solid-State NMR.” Advanced Materials **29**, 1605895 (2017).

[Mar+23] L. S. Martin et al. “Controlling Local Thermalization Dynamics in a Floquet-Engineered Dipolar Ensemble.” Physical Review Letters **130**, 210403 (2023).

[Maz+08] J. R. Maze et al. “Nanoscale magnetic sensing with an individual electronic spin in diamond.” Nature **455**, 644 (2008).

[Meh83] M. Mehring. *Principles of High Resolution NMR in Solids.* Springer-Verlag, Berlin Heidelberg New York (2nd edn.), 1983.

[MER02] I. A. Merkulov, A. L. Efros, and M. Rosen. “Electron spin relaxation by nuclei in semiconductor quantum dots.” Physical Review B **65**, 205309 (2002).

[Mot49] N. F. Mott. “The Basis of the Electron Theory of Metals, with Special Reference to the Transition Metals.” Proceedings of the Physical Society. Section A **62**, 416 (1949).

[Mül89] E. Müller-Hartmann. “Correlated fermions on a lattice in high dimensions.” Zeitschrift für Physik B Condensed Matter **74**, 507 (1989).

[MV89] W. Metzner and D. Vollhardt. “Correlated Lattice Fermions in $d = \infty$ Dimensions.” Physical Review Letters **62**, 324 (1989).

[NH15] R. Nandkishore and D. A. Huse. “Many-Body Localization and Thermalization in Quantum Statistical Mechanics.” Annual Review of Condensed Matter Physics **6**, 15 (2015).

[Nol15] W. Nolting. *Grundkurs Theoretische Physik 7: Viel-Teilchen-Theorie.* Springer-Verlag, Berlin Heidelberg (8th edn.), 2015.

[OK13] J. Otsuki and Y. Kuramoto. “Dynamical mean-field theory for quantum spin systems: Test of solutions for magnetically ordered states.” Physical Review B **88**, 024427 (2013).

[Pan+20] R. K. Panda et al. “Can we study the many-body localisation transition?” Europhysics Letters **128**, 67003 (2020).

[Pav+11] E. Pavarini et al, eds. *The LDA+DMFT approach to strongly correlated materials.* Forschungszentrum Jülich GmbH, Institute for Advanced Simulations, 2011.

[Pen+19] S. Penzel et al. “Spinning faster: protein NMR at MAS frequencies up to 126 kHz.” Journal of Biomolecular NMR **73**, 19 (2019).

[PL73] G. W. Parker and F. Lado. “Calculation of NMR Line Shapes Using the Memory-Function Approach.” Physical Review B **8**, 3081 (1973).

[PL74] G. W. Parker and F. Lado. “Calculation of NMR line shapes in calcium fluoride from modified moment expansions.” Physical Review B **9**, 22 (1974).

[Pol10] A. Polkovnikov. “Phase space representation of quantum dynamics.” Annals of Physics **325**, 1790 (2010).

[PTP46] E. M. Purcell, H. C. Torrey, and R. V. Pound. “Resonance Absorption by Nuclear Magnetic Moments in a Solid.” Physical Review **69**, 37 (1946).

[PV19] R. Puthenveetil and O. Vinogradova. “Solution NMR: A powerful tool for structural and functional studies of membrane proteins in reconstituted environments.” Journal of Biological Chemistry **294**, 15914 (2019).

[Rab+38] I. I. Rabi et al. “A New Method of Measuring Nuclear Magnetic Moment.” Physical Review **53**, 318 (1938).

[RDO08] M. Rigol, V. Dunjko, and M. Olshanii. “Thermalization and its mechanism for generic isolated quantum systems.” Nature **452**, 854 (2008).

[Rez+23] K. Rezai et al. “Probing dynamics of a two-dimensional dipolar spin ensemble using single qubit sensor.” arXiv:2207.10688v2 [quant-ph] (2023).

[Rez22] K. Rezai. *Probing dynamics of a two-dimensional dipolar spin ensemble.* PhD thesis (Harvard University Graduate School of Arts and Sciences, 2022).

[Rig14] M. Rigol. “Quantum Quenches in the Thermodynamic Limit.” Physical Review Letters **112**, 170601 (2014).

[Roa+08] G. Roati et al. “Anderson localization of a non-interacting Bose-Einstein condensate.” Nature **453**, 895 (2008).

[Rom+15] Y. Romach et al. “Spectroscopy of Surface-Induced Noise Using Shallow Spins in Diamond.” Physical Review Letters **114**, 017601 (2015).

[RS24] Thanks to Kristine Rezai and Alex O. Sushkov for providing the experimental data.

[San+19] S. Sangtawesin et al. “Origins of Diamond Surface Noise Probed by Correlating Single-Spin Measurements with Surface Spectroscopy.” Physical Review X **9**, 031052 (2019).

[SÁS11] A. M. Souza, G. A. Álvarez, and D. Suter. “Robust Dynamical Decoupling for Quantum Computing and Quantum Memory.” Physical Review Letters **106**, 240501 (2011).

[SÁS12] A. M. Souza, G. A. Álvarez, and D. Suter. “Robust dynamical decoupling.” Philosophical Transactions of the Royal Society A **370**, 4748 (2012).

[Sav+14] D. V. Savostyanov et al. “Exact NMR simulation of protein-size spin systems using tensor train formalism.” Physical Review B **90**, 085139 (2014).

[SBE10] I. Scholz, J. D. van Beek, and M. Ernst. “Operator-based Floquet theory in solid-state NMR.” Solid State Nuclear Magnetic Resonance **37**, 39 (2010).

[Sch+07] T. Schwartz et al. “Transport and Anderson localization in disordered two-dimensional photonic lattices.” Nature **446**, 52 (2007).

[Sch+11] M. Schaffry et al. “Proposed Spin Amplification for Magnetic Sensors Employing Crystal Defects.” Physical Review Letters **107**, 207210 (2011).

[Sch+14] R. Schirhagl et al. “Nitrogen-Vacancy Centers in Diamond: Nanoscale Sensors for Physics and Biology.” Annual Review of Physical Chemistry **65**, 83 (2014).

[Sch+15] M. Schreiber et al. “Observation of many-body localization of interacting fermions in a quasirandom optical lattice.” Science **349**, 842 (2015).

[Sch+17] L. Schlipf et al. “A molecular quantum spin network controlled by a single qubit.” Science Advances **3**, e1701116 (2017).

[Sch05] U. Schollwöck. “The density-matrix renormalization group.” Review of Modern Physics **77**, 259 (2005).

[Sch07] F. Schwabl. *Statistische Mechanik.* Springer-Verlag, Berlin Heidelberg (3rd edn.), 2007.

[Sch26] E. Schrödinger. “An Undulatory Theory of the Mechanics of Atoms and Molecules.” Physical Review **28**, 1049 (1926).

[Ser+16] M. Serbyn et al. “Power-Law Entanglement Spectrum in Many-Body Localized Phases.” Physical Review Lett. **117**, 160601 (2016).

[SF18] G. A. Starkov and B. V. Fine. “Hybrid quantum-classical method for simulating high-temperature dynamics of nuclear spins in solids.” Physical Review B **98**, 214421 (2018).

[SF20] G. A. Starkov and B. V. Fine. “Free induction decays in nuclear spin-$1/2$ lattices with a small number of interacting neighbors: The cases of silicon and fluorapatite.” Physical Review B **101**, 024428 (2020).

[Sha91] R. N. Shakhmuratov. “Nuclear magnetic dephasing in solids.” Journal of Physics: Condensed Matter **3**, 8683 (1991).

[Sim+23] B. Simões de Almeida et al. “Barriers to resolution in ^{1}H NMR of rotating solids.” Journal of Magnetic Resonance **355**, 107557 (2023).

[SK75] D. Sherrington and S. Kirkpatrick. “Solvable Model of a Spin-Glass.” Physical Review Letters **35**, 1792 (1975).

[Sli90] C. P. Slichter. *Principles of Magnetic Resonance.* Springer-Verlag, Berlin Heidelberg New York (3rd edn.), 1990.

[SLZ20] P. Sierant, M. Lewenstein, and J. Zakrzewski. “Polynomially Filtered Exact Diagonalization Approach to Many-Body Localization.” Physical Review Letters **125**, 156601 (2020).

[SP21] D. Sels and A. Polkovnikov. “Dynamical obstruction to localization in a disordered spin chain.” Physical Review E **104**, 054105 (2021).

[SP23] D. Sels and A. Polkovnikov. “Thermalization of Dilute Impurities in One-Dimensional Spin Chains.” Physical Review X **13**, 011041 (2023).

[SPA13a] M. Serbyn, Z. Papić, and D. A. Abanin. “Local Conservation Laws and the Structure of the Many-Body Localized States.” Physical Review Letters **111**, 127201 (2013).

[SPA13b] M. Serbyn, Z. Papić, and D. A. Abanin. “Universal Slow Growth of Entanglement in Interacting Strongly Disordered Systems.” Physical Review Letters **110**, 260601 (2013).

[Sre94] M. Srednicki. “Chaos and quantum thermalization.” Physical Review E **50**, 888 (1994).

[SRU13] D. Stanek, C. Raas, and G. S. Uhrig. “Dynamics and decoherence in the central spin model in the low-field limit.” Physical Review B **88**, 155305 (2013).

[SRU14] D. Stanek, C. Raas, and G. S. Uhrig. “From quantum-mechanical to classical dynamics in the central-spin model.” Physical Review B **90**, 064301 (2014).

[SS04] J. Stolze and D. Suter. *Quantum Computing: A Short Course from Theory to Experiment.* Wiley-VCH GmbH and Co. KGaA, Weinheim, 2004.

[Sta+15] T. Staudacher et al. “Probing molecular dynamics at the nanoscale via an individual paramagnetic centre.” Nature Communications **6**, 8527 (2015).

[Sta+19] A. Stacey et al. “Evidence for Primal sp^2 Defects at the Diamond Surface: Candidates for Electron Trapping and Noise Sources.” Advanced Materials Interfaces **6**, 1801449 (2019).

[Sta14] D. Stanek. *Dynamics and decoherence in the central spin model.* PhD thesis (Technische Universität Dortmund, 2014).

[Sta24] Thanks to Grigory Starkov for this hint.

[Šun+20] J. Šuntajs et al. “Quantum chaos challenges many-body localization.” Physical Review E **102**, 062144 (2020).

[Sus+14] A. O. Sushkov et al. “Magnetic Resonance Detection of Individual Proton Spins Using Quantum Reporters.” Physical Review Letters **113**, 197601 (2014).

[SYS07] S. K. Saikin, W. Yao, and L. J. Sham. “Single-electron spin decoherence by nuclear spin bath: Linked-cluster expansion approach.” Physical Review B **75**, 125314 (2007).

[Tam+14] T. H. Taminiau et al. “Universal control and error correction in multi-qubit spin registers in diamond.” Nature Nanotechnology **9**, 171 (2014).

[TAP77] D. J. Thouless, P. W. Anderson, and R. G. Palmer. “Solution of ’Solvable model of a spin glass’.” The Philosophical Magazine: A Journal of Theoretical Experimental and Applied Physics **35**, 593 (1977).

[Tjo66] J. A. Tjon. “Quantum Theory of Magnetic-Resonance Line Shape in a Rigid Lattice.” Physical Review **143**, 259 (1966).

[Uhr+14] G. S. Uhrig et al. “Conservation laws protect dynamic spin correlations from decay: Limited role of integrability in the central spin model.” Physical Review B **90**, 060301 (2014).

[Van48] J. H. Van Vleck. “The Dipolar Broadening of Magnetic Resonance Lines in Crystals.” Physical Review **74**, 1168 (1948).

[Ver+03] A. S. Verhulst et al. “Double and single peaks in nuclear magnetic resonance spectra of natural and ^{29}Si-enriched single-crystal silicon.” Physical Review B **68**, 054105 (2003).

[VHA15] R. Vosk, D. A. Huse, and E. Altman. “Theory of the Many-Body Localization Transition in One-Dimensional Systems.” Physical Review X **5**, 031032 (2015).

[WD06] W. M. Witzel and S. Das Sarma. “Quantum theory for electron spin decoherence induced by nuclear spin dynamics in semiconductor quantum computer architectures: Spectral diffusion of localized electron spins in the nuclear solid-state environment.” Physical Review B **74**, 035322 (2006).

[Wei+06] A. Weiße et al. “The kernel polynomial method.” Review of Modern Physics **78**, 275 (2006).

[Wei07] P. Weiss. “L’hypothèse du champ moléculaire et la propriété ferromagnétique.” Journal of Physics: Theories and Applications **6**, 661 (1907).

[Whi09] S. R. White. “Minimally Entangled Typical Quantum States at Finite Temperature.” Physical Review Letters **102**, 190601 (2009).

[Wig32] E. Wigner. “On the Quantum Correction For Thermodynamic Equilibrium.” Physical Review **40**, 749 (1932).

[WPS19] T. B. Wahl, A. Pal, and S. H. Simon. “Signatures of the many-body localized regime in two dimensions.” Nature Physics **15**, 164 (2019).

[WRC18] K. X. Wei, C. Ramanathan, and P. Cappellaro. “Exploring Localization in Nuclear Spin Chains.” Physical Review Letters **120**, 070501 (2018).

[WSD05] W. M. Witzel, R. de Sousa, and S. Das Sarma. “Quantum theory of spectral-diffusion-induced electron spin decoherence.” Physical Review B **72**, 161306 (2005).

[WYD14] W. M. Witzel, K. Young, and S. Das Sarma. “Converting a real quantum spin bath to an effective classical noise acting on a central spin.” Physical Review B **90**, 115431 (2014).

[Yao+14] N. Y. Yao et al. “Many-Body Localization in Dipolar Systems.” Physical Review Letters **113**, 243002 (2014).

[Yar+23] M. Yarmohammadi et al. “Truncated Wigner approximation for the bosonic model of large spin baths.” Physical Review B **107**, 125421 (2023).

[YL08] W. Yang and R.-B. Liu. “Quantum many-body theory of qubit decoherence in a finite-size spin bath.” Physical Review B **78**, 085315 (2008).

[YL09] W. Yang and R.-B. Liu. “Quantum many-body theory of qubit decoherence in a finite-size spin bath. II. Ensemble dynamics.” Physical Review B **79**, 115320 (2009).

[Zha+07] W. Zhang et al. “Modelling decoherence in quantum spin systems.” Journal of Physics: Condensed Matter **19**, 083202 (2007).

[Zha+17] J. Zhang et al. “Observation of a discrete time crystal.” Nature **543**, 217 (2017).

[Zha+24] Y. Zhao et al. “NMR and MS reveal characteristic metabolome atlas and optimize esophageal squamous cell carcinoma early detection.” Nature Communications **15**, 2463 (2024).

[ZML20] G.-L. Zhang, W.-L. Ma, and R.-B. Liu. “Cluster correlation expansion for studying decoherence of clock transitions in spin baths.” Physical Review B **102**, 245303 (2020).

[Zob88] V. E. Zobov. “Autocorrelation function of a Heisenberg paramagnet in the approximation of a self-consistent fluctuating field.” Theoretical and Mathematical Physics **77**, 1573 (1988).

[ŽPP08] M. Žnidarič, T. Prosen, and P. Prelovšek. “Many-body localization in the Heisenberg XXZ magnet in a random field.” Physical Review B **77**, 064426 (2008).

[ZRS19] B. Zhu, A. M. Rey, and J. Schachenmayer. “A generalized phase space approach for solving quantum spin dynamics.” New Journal of Physics **21**, 082001 (2019).

[Zu+21] C. Zu et al. “Emergent hydrodynamics in a strongly interacting dipolar spin ensemble.” Nature **597**, 45 (2021).

Acronyms

AHT average-Hamiltonian theory. 102, 103

CaF_2-[hkl] calcium fluoride with magnetic field in [hkl]-direction. 92–95, 102, 106, 125–128, 157, 159, 161

CE cluster-expansion. 31, 99

CET Chebyshev expansion technique. 31, 46–48, 60, 61, 86, 153, 154

CFET commutator-free exponential time propagator. 43, 113, 117

CRA correlation-replica approximation. 58, 60, 66, 70, 82–84, 93, 105, 106, 117, 118, 157

CSM central-spin model. 35, 36, 54

CspinDMFT cluster dynamic mean-field theory for spin ensembles. 6, 9, 41, 48, 50–56, 58–71, 73–77, 81–84, 88, 96, 101, 104–107, 112, 114, 117–122, 153–156, 158

DEER double-electron-electron-resonance. 19, 67

DFT density-functional theory. 27, 29

DMFT dynamic mean-field theory. 5, 23, 27–30, 104, 107, 152

DMRG density-matrix renormalization group. 28, 31, 79

ED exact diagonalization. 28, 31, 46–48, 60, 62–65, 86, 133–135, 153, 154, 160

ETH eigenstate thermalization hypothesis. 3, 78, 79, 81, 156

FID free induction decay. 5, 6, 15–17, 31, 86–88, 90–95, 97–102, 104, 106, 117, 125–128, 151, 157–159, 161

FMBL fully many-body localized. 79

iEoM iterated equations of motion. 46, 47, 60, 153

LIOM quasi-local integral of motion. 79

MAS magic-angle spinning. 4, 102, 103, 107, 158

MBL many-body-localized/many-body localization. 3, 4, 6, 51, 77, 79, 80, 82, 83, 106, 156

ND N-dimensional/N dimension(s). 3, 47, 60, 63, 79, 82, 113, 151, 153

nl-spinDMFT non-local dynamic mean-field theory for spin ensembles. 6, 14, 50, 86, 88, 91, 94, 95, 97, 98, 101, 102, 104, 106, 107, 112, 117, 118, 121, 126, 157, 159

NMR nuclear magnetic resonance. 4–7, 9, 11, 13, 14, 16–18, 21, 31, 32, 40, 50, 86, 91, 95–100, 102, 104, 106, 107, 129, 151, 157

NN nearest-neighbor. 10, 33, 34, 37, 46, 47, 56, 60–62, 87, 89, 91, 93, 109, 110, 122, 124, 128, 133, 134, 153, 154, 157, 159–161

NNN next-nearest-neighbor. 56, 91, 153

NV nitrogen-vacancy. 2, 6, 9, 18–20, 50, 68, 72, 74, 83, 85, 104–106, 151, 152

PBC periodic boundary conditions. 47, 61, 62, 64, 153, 154

RF radio-frequency. 14, 18, 19

RWA rotating-wave approximation. 12–14, 16, 20, 22, 83

SIAM single-impurity Anderson model. 28, 152

SKM Sherrington-Kirkpatrick model. 29

spinDMFT dynamic mean-field theory for spin ensembles. 5–7, 9, 14, 16–18, 23, 29–32, 34–41, 43–56, 58–61, 64, 65, 73, 75, 81, 82, 84, 86–89, 92, 95–107, 110, 112–114, 116–121, 125, 129, 130, 132–135, 152, 153, 157, 158, 160

TWA truncated Wigner approximation. 31, 131

List of Figures

List of Tables

Danksagung

Ich habe mal gelesen, dass das Arbeiten an einer Doktorarbeit wie eine Achterbahnfahrt ist, denn es besteht aus ganz vielen Höhen und Tiefen. Und nach viereinhalb Jahren kann ich sagen: Ja, das stimmt! Aber woran liegt das? – Sicherlich spielen die folgenden Punkte eine Rolle: Man kann unmöglich vorhersehen was die eigene Forschung bringt, sonst müsste man sie ja nicht machen. Gleichzeitig trägt man eine große Verantwortung für das eigene Projekt und definiert sich darüber. Wenn etwas gut läuft, ist die Welt in Ordnung, aber wenn mal etwas nicht klappt, hinterfragt man sofort Einiges. Ein zentraler Aspekt um die Fahrt weniger holprig zu gestalten, ist es, sich ständig darauf zu besinnen, dass der Freizeitpark des Lebens noch wesentlich mehr beinhaltet. Darüber hinaus ist es enorm wichtig, sich immer wieder über das eigene Projekt auszutauschen, und zwar sowohl mit Experten, als auch mit Nicht-Experten. Insofern muss betont werden, dass eine Doktorarbeit niemals durch eine einzige Person entsteht. Der häufig verwendete *pluralis auctoris*, also das ständig benutzte "we", soll daher nicht nur den Leser sondern in gewisser Weise auch diese vielen anderen Menschen mit einschließen.

Als erstes möchte ich mich bei meinem Betreuer, Prof. Dr. Götz S. Uhrig, bedanken, mit dem mir die Zusammenarbeit über inzwischen mehr als fünf Jahre hinweg sehr gefallen hat. Ich habe es genossen, dass ich stets die Freiheit hatte, mein Projekt selbst mitzugestalten und gleichzeitig immer Hilfe bekam, wenn ich sie brauchte. Danke für die Unterstützung beim Forschen und beim Anfertigen dieser Arbeit. Ich danke außerdem Herrn Prof. Dr. Frithjof Anders und Herrn Prof. Dr. Matthias Ernst für die Übernahme des Zweit- und Drittgutachtens.

Als nächstes möchte ich mich bei all meinen Mitstreiterinnen und Mitstreitern am Lehrstuhl für die stets entspannte Atmosphäre bedanken. Danke für die regelmäßigen gemeinsamen Kaffeepausen mit interessanten Gesprächen – nicht nur über Physik. Besonderer Dank gilt in diesem Zuge auch einem der angenehmsten Bürokollegen, die man sich vorstellen kann, namens Asliddin Khudoyberdiev. Darüber hinaus möchte ich mich auch bei Prof. Dr. Joachim Stolze bedanken, unter anderem für seine hilfreichen Ratschläge und die Bereitschaft, mein erstes großes Paper zu lesen (immerhin gut 30 Seiten).

Der nächste Dank geht an Kristine Rezai und Prof. Dr. Alex O. Sushkov, mit denen ich über mehrere Jahre das Vergnügen hatte, Theorie und Experiment unter einen Hut zu bekommen. Danke vor Allem an Kristine für die zahlreichen beantworteten Fragen. Ein weiteres Dankeschön geht an Philip Bleicker, Dag-Björn Hering, Mohsen Yarmohammadi und Thomas Hahn für die tolle Zusammenarbeit inklusive Sahnehäubchen, sprich, Veröffentlichungen.

Ein ganz großer Dank gilt den Korrekturleserinnen und Korrekturlesern dieser Arbeit, die es auch alle verdient haben, namentlich aufzutauchen (Reihenfolge kapitelweise): danke an Götz Uhrig, Hannah Rolf, meine Schwester Melanie, Alina Joch, Kristine Rezai, Sinja Behrensmeier, Asliddin Khudoyberdiev, Dag-Björn Hering, Lars Funke, Joshua Althüser, Thomas Hahn und an Padmé Nalbach für den Plagiats-Check.

Zuletzt, aber nicht weniger, möchte ich mich bei meinen Freunden und bei meiner Familie, also Melanie, Raphael, Mama und Papa, bedanken. Danke für die stetige Unterstützung, für die Geduld, wenn ich mal Stress hatte, und schlichtweg für das Da sein.